Self-Assembling Nanocomposite Tectons for Ordered Superlattices

by
Peter J. Santos
B.S. Materials Science and Engineering, Northwestern University (2015)

Submitted to the Department of Materials Science and Engineering
in Partial Fulfillment of the Requirements for the Degree of
Doctor of Philosophy
at the
MASSACHUSETTS INSTITUTE OF TECHNOLOGY
May 2020

Signature of Author ……...
Department of Materials Science and Engineering
April 24, 2020

Certified by ……...
Robert J. Macfarlane
Assistant Professor of Materials Science
Thesis Supervisor

Accepted by …….
Frances M. Ross
Professor of Materials Science and Engineering
Chair, Departmental Committee on Graduate Studies

Self-Assembling Nanocomposite Tectons for Ordered Superlattices

by
Peter J. Santos

Submitted to the Department of Materials Science and Engineering
on April 24, 2020 in partial fulfillment of the
requirements for the degree of
Doctor of Philosophy in Materials Science and Engineering

ABSTRACT
Nanocomposites, materials of heterogeneous composition with at least one of the phases having dimensions between 1-100 nm, can be produced with unique properties dependent on their composition and geometric configuration. However, it is a major challenge to precisely and simultaneously design the structure of synthetic nanocomposites at the nanoscale, microscale, and macroscale. To create advanced nanocomposites in which both structure and composition can be programmed across these disparate size regimes, we have developed a new nanoparticle-based building block, the Nanocomposite Tecton (NCT). An NCT consists of an inorganic nanoparticle core and a polymeric shell, with each chain terminating in a supramolecular binding group at the periphery of the NCT. As each NCT contains both an inorganic nanoparticle and a polymer phase, each building block is itself a nanocomposite, and the incorporation of supramolecular binding groups allows for the directed assembly of NCTs that contain complementary binding groups. These reversible supramolecular interactions enable the assembly of NCTs into ordered arrays, and the collective behavior of the binding groups can be regulated by the dynamics of the polymer chains. The NCTs are capable of rapidly self-assembling into several different crystalline phases that are determined by the design of the building block, and are resilient against dispersity in the molecular weight of the polymer brush and the diameter of the nanoparticle cores. NCTs have been synthesized with both gold and iron oxide nanoparticle cores, indicating the ability to produce NCTs at reasonable scales. Moreover, the incorporation of multiple nanoparticle compositions allows for the synthesis of NCT-based materials with plasmonic and magnetic properties that can affect, as well as be affected by, the assembly process. We further demonstrate that the crystallization kinetics can be modulated to induce the assembly of NCTs into faceted crystallites with micron-sized diameters, and the resulting NCT crystallites can be post-processed into bulk solids with arbitrary macroscopic shape and controlled grain size. The NCT design concept is therefore a highly modular and versatile building block capable of fabricating materials with controlled structures at the levels of atomic composition and molecular geometry, nanoscale organization, microstructure, and macroscopic form.

Thesis Supervisor: Robert J. Macfarlane
Title: Assistant Professor of Materials Science and Engineering

Acknowledgements

First, I want to thank my cat Kirill, who has been my most significant source of scientific, spiritual, and emotional guidance throughout my degree. Thank you Jackie for being a wonderful partner and the absolute best part of my life here in Cambridge. Thank you Mom, Dad, Johanna, Grandma, Grandpa, Granddad, and Gram for getting me into science in the first place, and supporting me throughout my entire journey.

Thank you Hugo, Quantum, Scott, and Bitzy for being excellent roommates at 9 Seckle (or Seckel), and a further thank you to the whole Potlucks crew for making sure I have at least a bit of fun and something to look forward to every week. Also, thanks to the best team at Thirsty Ear Trivia.

Thank you to my entire DMSE cohort, without which I definitely would not have passed my classes or quals.

Thank you to Alex and everyone who came to Stir Friday at Northwestern and made up my favorite part of undergrad. Also, thank you Carson and Taner for being exceptional graduate student mentors.

Thank you to Rob's parents for buying us a coffee maker, and thank you to the barista at Dunkin' who kept accidentally giving me large cold brews when I ordered smalls. Thank you to Lamplighter, Jack's Abbey, and the Homebrew Emporium for obvious reasons. Thank you to the Boston Red Sox for winning the 2018 World Series.

I would also like to explicitly NOT thank COVID19 for being a pretty major buzzkill.

Thank you Rob for being the best PhD advisor I've ever had. When you approached me about being one of your first students, I may have been a bit apprehensive about building a group from the ground up, but working with you has been one of the most rewarding experiences in my life, and I could not have imagined how much I would learn with you. I have been exceptionally lucky that you had my back throughout broken elevators at E-34, samples not getting shipped, and results not making sense.

Thank you to my crew of undergrads/UROPS: Caroline, Tom, Joyce, and Mae. I am always impressed with how quickly you learn, and I'm certain you all have a bright future in science ahead of you!

Thank you to my labmates for all the help terrorizing Rob. Also, for being a great group to brainstorm ideas, find non-broken equipment, and teach me things I ought to already know. Special thanks to Paul, Jianyuan, and Diana for being there from the (more or less) beginning, and to Yuping, Leo, and Margaret for being excellent collaborators that will hopefully keep some of these projects alive.

Thank you Alfredo and Zhen for their computational collaboration. Also, thank you Alfredo and Julia for being on my thesis committee, and offering helpful advice.

Professional Acknowledgements

I would like to acknowledge support by the NSF Graduate Research Fellowship Program under Grant 1122374. This work was further supported by an NSF CAREER Grant, award number CHE-1653289 and made use of the MRSEC Shared Experimental Facilities at MIT, supported by the NSF under Award DMR 14-19807. SAXS experiments at beamline 12-ID-B at the Advanced Photon Source at Argonne National Laboratory were supported by the U.S. Department of Energy, Office of Science, Office of Basic Energy Sciences, under contract DE-AC02-06CH11357. Additionally, thank you Charlie and Byeongdu for their expertise with SAXS.

Table of Contents

List of Figures

List of Supplementary Figures

List of Supplementary Tables

Chapter 1. Nanoparticles as a Material Building Block

1.1 Nanocomposites are a Strategy for Materials by Design

One of the fundamental objectives of materials science is to gain control over structure-property relationships. However, it is often desirable to produce materials with properties or combinations of properties that are not present in any conventional material, such as high strength without increased brittleness. Composites are a method to create these enhanced properties by blending together multiple different materials such that the final product incorporates the beneficial aspects of the constituent parts. A particularly interesting class of composites are nanocomposites,[1] where the different blended phases have dimensions less than 100 nm. As a result, on the macroscopic length scale these materials appear homogenous, and the small size of the domains is capable of significantly affecting properties.

Some of the most striking examples of nanocomposites are found in nature. For instance, bone (**Figure 1-1A**) is a nanocomposite consisting primarily of hydroxyapatite crystallites hierarchically structured in a complex configuration with collagen, other proteins, and living cells.[2] Bone is able to provide a rigid structure for animals because it its high strength, which primarily stems from the rigid hydroxyapatite crystallites. However, bone is unique in that it is significantly more fracture resistant than the pure hydroxyapatite mineral, and is therefore a simultaneously strong and tough material, which are properties that are typically difficult to combine. In the case of bone, the collagen proteins, a soft polymer with high toughness and low strength, interconnect the rigid inorganic components. As a consequence of this composite architecture, energy is efficiently dissipated and cracks are less likely to form in the material, which explains their widespread biological adaptation.[3,4]

Another common example of natural nanocomposites is nacre, the material that makes up the shells of many mollusks, such as the abalone (**Figure 1-1B**).[5] As in bone, nacre consists of both hard, inorganic crystallites and an elastic biopolymer, and exhibits exceptional strength and toughness relative to its constituent parts. In particular, platelets of aragonite, a calcium carbonate polymorph, are interconnected in a "brick and mortar" structure by chitin and other proteins (**Figure 1-1C**).[6] A notable feature of nacres is their vibrant iridescence, which is surprising given the colorlessness of both aragonite and chitin. Instead of color stemming from any pigments, the iridescent effect in nacres is a result of the microscale structure of the material. Aragonite crystallites are regularly

spaced on the order of the wavelength of light, which causes a periodic variation in the dielectric constant of the material, and therefore is able to open a photonic bandgap that strongly reflects light of certain wavelengths in a similar manner to opals.[7]

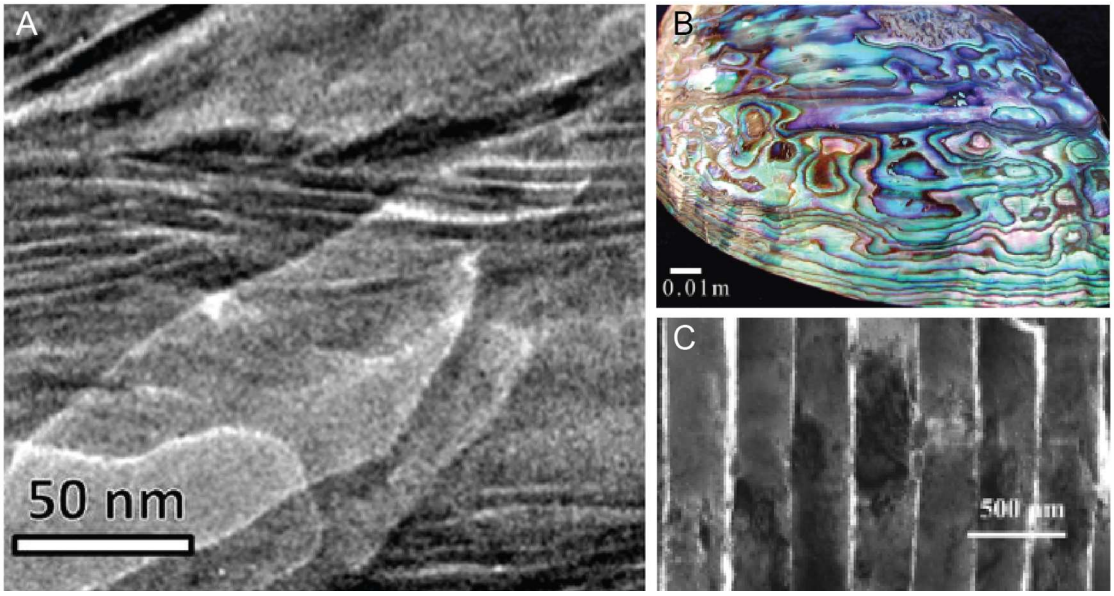

Figure 1-1. Examples of natural nanocomposites. A) TEM micrograph of bone, highlighting the complex structure of crystallites connected by proteins. Adapted from Reznikov et al[3]. B) Optical photograph of an abalone shell, demonstrating its iridescent coloration. C) SEM of nacre. The inorganic plates are periodically spaced on the order of the wavelength of light. Adapted from Snow et al.[5]

Consequently, the properties of nanocomposites are strongly dependent on both their composition and their nano and microscale structure. Advances in nanoscience have demonstrated a number of exotic phenomena that can be controlled by careful design of matter at the nanometer lengthscale including photonic materials that can control the propagation of light through themselves due to their periodic dielectric constant,[8] plasmonic materials that can control the flow of light at dimensions smaller than the wavelength of light,[9] and magnetic materials where the coupling and propagation of magnetic fields can be precisely designed.[10–12]

Synthetic nanocomposites have the potential to feature these exotic properties to a degree not found in natural materials because of the ability to use elements and processing conditions not available to biological systems. However, natural materials still dramatically outstrip synthetic efforts to control structure at the nanoscale.

Many synthetic nanocomposites are blends of polymers and nanoparticles that seek to take advantage of the high toughness of polymers while increasing their strength.[13–16] A canonical examples is the rubber in tires that consist of carbon black stochastically mixed into an elastomer. The hard carbon particles enhance the strength of the rubber, but their localization within the composite is entirely uncontrolled. Consequently, at elevated concentrations the carbon particles aggregate together, limiting the degree of mechanical enhancement while simultaneously providing a potential point of failure.[17] Some manmade composites do utilize structure control to enhance their properties, such as aligned carbon fiber composites, where hard fibers are physically aligned in one dimension to anisotropically enhance mechanical properties.[18] However, macroscopic processing methods are unable to generate the complex, three-dimensionally structured nanocomposites found in nature.

Complex and arbitrary structural control at the nanoscale has been achieved by sophisticated lithographic, or "top-down" techniques.[19,20] However, these processes are limited to making small amounts of samples and require expensive equipment, making them unsuitable for bulk material fabrication. An alternative method is a "bottom-up" approach, where nanoscale building blocks are designed so as to spontaneously self-assemble into a desired nanoscale pattern.[21] Self-assembly is an attractive method for materials fabrication because it is inherently scalable as the whole system can assemble in a parallel manner with a minimal need for any sophisticated equipment, and self-assembly has the potential to make a diverse array of nanoscale structures. In order to create a successful self-assembling system, it is necessary to fully understand the thermodynamic landscape, and therefore the major challenge in self-assembly is to appropriately design the nanoscale building block so that its most energetically stable state is the wanted structure.

1.2 Nanoparticles as a Designable Nanoscale Platform

Nanoparticles are a promising building block for the next generation of self-assembled nanocomposites because they can be produced in a wide variety of compositions and shapes with excellent uniformity, and they are capable of being modified in a number of different manners to be incorporated into various self-assembly schemes. Designing a universal method for producing well-structured nanocomposites from nanoparticles will expand the functionality of the nanoparticles and enable their fabrication into useful materials.

1.2.1 Synthesis and Properties of Nanoparticles

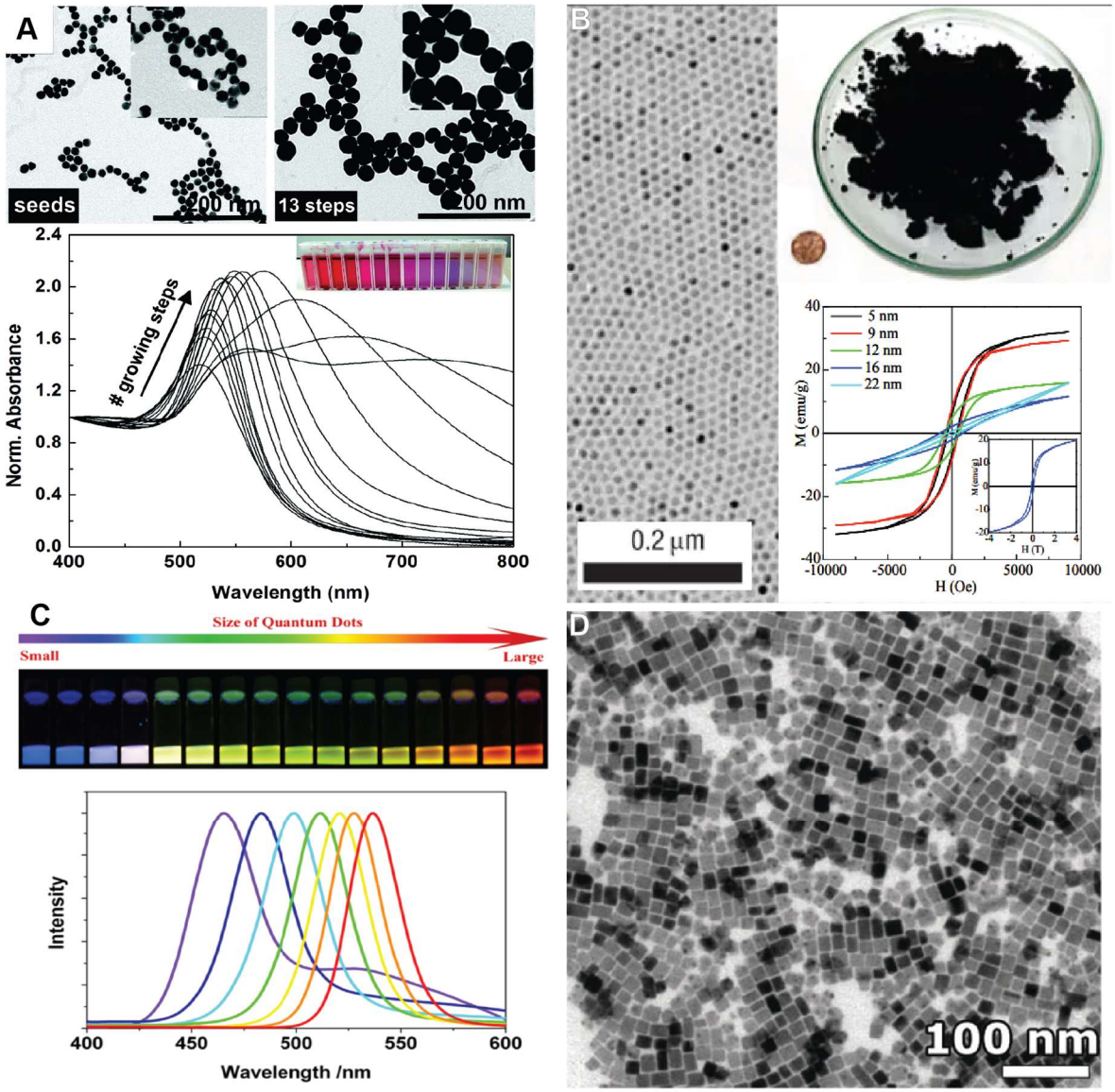

Figure 1-2. Examples of different types of nanoparticles. (A) Citrate stabilized gold nanoparticles are simple to synthesize at multiple sizes through seeded growth protocols. Larger particles see a red shift in their surface plasmon resonance. Adapted from Bastus et al.[29] (B) Uniform iron oxide nanoparticles can be synthesized at large scales. Changing the size of the particles can change their magnetic properties. Adapted from Noh et al.[54] (C) Quantum dots will photoluminesce at longer wavelengths when their diameter is increased. Adapted from Bera et al.[63] (D) Perovskite nanoparticle cubes. Adapted from Tong et al.[70]

Nanoparticles are a broad classification that refers to matter with sizes in all dimensions between 1 and 100 nanometers. Metals, oxides, semiconductors, or polymers can be made in nanoparticle form, and they can be spherical or anisotropic. Importantly, the particles must be stable during synthesis, post-processing, and application. In other words, there must be a mechanism keeping the nanoparticles from fusing together and becoming a bulk material. Some nanoparticle compositions remain stable because they are highly non-reactive, such as silica particles prepared with the Stöber process or ball-milled oxides.[22] However, for more reactive compositions, including many metals and oxides, the nanoparticle surface must be modified to maintain their stability. Most commonly, this is accomplished by the use of capping ligands, organic molecules that bind to the surface of a nanoparticle. Many nanoparticle syntheses rely on capping ligands to regulate the size of the particles as they grow, or even determine the nanoparticle shape by preferentially binding to certain crystallographic planes of the particles and favoring faceting. These capping ligands maintain nanoparticle stability by either introducing a charge, causing the nanoparticles to repel via coulombic forces, or the ligands may act as a steric barrier.

There has been significant recent progress in the synthesis of nanoparticles, with the primary objectives being: 1) increasing the diversity of possible compositions, 2) increasing the diversity of shapes, and 3) decreasing the size variation of the particles. The wide variety of nanoparticles will not be comprehensively reviewed here, but nanoparticles that may in the near future make interesting self-assembled composite materials will be highlighted.

1.2.1.1 Plasmonic Nanoparticles

Metallic nanoparticles with a localized surface plasmon resonance (LSPR) are some of the most studied, in particular those made of gold or silver. An LSPR is a collective oscillation of the conduction band electrons in a material due to incident electromagnetic radiation. These oscillations occur at sizes smaller than the wavelength of light, resulting in a dramatic enhancement in the local electromagnetic field.[9,23] Consequently, these plasmonic nanomaterials absorb light very strongly at select frequencies, dependent on the composition and nanoscale structure of the material. As a result, plasmonic nanoparticles are extensively studied because nanoscale changes can beneficially modify their properties, and the dramatic response is often easy to characterize. Furthermore, gold is resistant to oxidation, easy to functionalize, and there are a number of

established routes to synthesize high quality nanoparticles without any specialized equipment or toxic reagents, simplifying research.[24,25]

Citrate capped gold and silver nanoparticles can be synthesized through the Turkevich method,[26–28] which involves reducing a metal halide precursor with sodium citrate (**Figure 1-2A**). Under optimal conditions, the nucleation of nanoparticles occurs in a quick burst, leading to a narrow size distribution of spheres with diameters ranging between 10 and 300 nm.[29] After synthesis, the citrate ions are weakly bound to the surface of the nanoparticles, and can be easily replaced by more strongly coordinating groups, in particular thiols.

Gold nanoparticles can also be synthesized with a capping thiol ligand already installed through the Brust-Schiffrin method.[30] Typically, an aqueous gold chloride salt solution is prepared, and added to an organic phase solution containing a thiolated compound and a phase transfer catalyst like tetraoctylammonium bromide. A reducing agent such as sodium borohydride is added to result in fairly uniform, organic phase particles. The Brust-Schiffrin and other similar methods[31,32] are often preferred for making smaller nanoparticles (1-10 nm), and can load a wide variety of ligands onto the particles at a high grafting density without the need for an additional functionalization step.

Another synthetic route, a seeded growth process, can produce gold nanoparticles with a narrow size distribution, and through careful selection of the capping ligands the faceting can be controlled to produce either isotropic or anisotropic particles. In this synthesis, gold salts are reduced, typically with a mild reducing agent like ascorbic acid. Then, with cetyltrimethylammonium bromide (CTAB) used as a capping ligand additional gold salt is added to the seeds to grow larger particles.[33] Importantly, the presence of small amounts of additives is capable of favoring the growth of anisotropic particles, for instance silver nitrate is often used to generate gold nanorods, or trace amounts of iodine impurity in the CTAB capping ligand can dramatically affect the resulting morphology.[34,35] This seeded growth strategy has been modified to synthesize a large number of different structures including spheres, rods, triangular prisms, cubes, concave rhombic dodecahedra, octahedra, tetrahexahedra, truncated ditetragonal prisms, cuboctahedra, and more.[24,35–37]

The manipulation of plasmonic effects can create materials with new optical near-field and far-field properties, such as asymmetrically reflective films from alternating layers of gold and silver nanoparticles.[38] The vibrant colors of plasmonic particles could make high quality displays,[39] the

thermal energy released by exciting plasmonic nanoparticles at their resonant frequency can be used to kill cancer cells in photothermal therapy,[40] and the enhanced electric fields have been demonstrated to improve catalysis performance.[41] Additionally, in surface enhanced Raman spectroscopy (SERS), the field enhancement of plamonic particles has enabled ultra-sensitive chemical detection.[42]

1.2.1.2 Magnetic Nanoparticles

Nanoparticles made from magnetically active materials exhibit several unique properties as compared to their bulk counterparts, which make them an attractive building block for functional nanocomposites. Bulk ferromagnetic materials can have a permanent magnetic field due to the alignment of spins stabilized by the lattice and the formation of magnetic domains. However, below a certain critical volume to magnetic domains can no longer be stabilized and the particles become single domain. At even smaller sizes, depending on the chemical composition of the nanoparticle on the order of 10's of nanometers, the particles become superparamagnetic, meaning ambient thermal energy will be sufficient to cause the orientation of the spins in the nanoparticle to spontaneously realign and so a permanent magnetic field is no longer held.[43,44] Beyond the size of the nanoparticle itself, their magnetic response can be tuned by controlling the coupling between the particles, as each particle functions as a magnetic dipole that can interact over distances of a few nanometers.[45] Furthermore, if the magnetic nanoparticles are appropriately positioned, several exotic properties, such as dipolar ferromagnetism, are expected to arise.[46,47]

A large number of synthetic routes exist for magnetic nanoparticles, with established methods for varying composition, uniformity, and size.[48] Both magnetic oxides including magnetite[49,50] and other spinel-type ferromagnetic oxides,[51] and metals such as cobalt[52] and iron platinum alloys[53] can be synthesized. Some syntheses can be performed at multi-gram or even kilogram scale, though typically at the expense of uniformity, such as the precipitation of magnetite from aqueous solution.[43] Other syntheses can produce particles of exceptionally low dispersity with diameters ranging from 5-50 nm at scales of a few grams using the thermal decomposition of a metal-organic precursor (**Figure 1-2B**).[54–56]

The unique response of magnetic nanoparticles and the ability to easily tune their properties makes them ideal for several promising applications. First, there is interest in using their magnetic

moment for data storage applications, as a dense assembly of particles could be a cheaper and more efficient method of creating computer hard drives.[57] Moreover, their superparamagnetic properties have made them an attractive material for manipulating electromagnetic waves.[11,12,58,59] Biomedical researchers have developed magnetic hyperthermia therapies based on rapidly oscillating a magnetic field around superparamagnetic nanoparticles to generate heat and kill cancer cells.[60] Finally, more sophisticated assemblies of magnetic nanoparticles may find use in advanced spintronic devices.[61,62]

1.2.1.3 Semiconducting Nanoparticles

Semiconducting materials also possess interesting properties when their dimensions are shrunk to the nanoscale. Semiconductors are a class of material with a narrow bandgap, meaning that the most energetic electrons in the material only need a small input of energy to become excited. As bulk materials, they have found use as transistors, solar cells, and light emitting diodes.

Semiconducting particles with nanometer dimensions are known as "quantum dots" due to their ability to exhibit quantum confinement. Their small size results in a discontinuous density of states near their bandgap, or in other words their electronic structure more closely resembles that of a molecule than a bulk material. As the diameter of the quantum dot changes there is a dramatic effect on its density of states, which modifies the bandgap of the quantum dot.[63]

One of the most useful properties of quantum dots is their ability to luminesce: if an electron is excited from the valence band to the conducting band, it will decay and emit a photon with energy equal to the bandgap. Quantum dots typically display a very high quantum yield, which refers to the number of emitted photons relative to the number of incident photons, because excited electrons are trapped inside the quantum dot which limits the number of possible non-radiative decay processes.[64]

An important consequence of the quantum confinement effects is that quantum dots of different sizes will have different bandgaps, and therefore emit photons of different energies. Frequently, it is possible to tune a sample of quantum dots to emit light across the entire visible spectrum (**Figure 1-2C**). Therefore, most applications of quantum dots tend to exploit their unique optoelectronic properties, including displays,[65] solar cells,[66] and sensors.[67]

Quantum dots have been prepared from a wide variety of different semiconductors. Some of the most common include PbS, CdSe, ZnS, CdTe, and ZnSe.[63] Several synthesis routes are available, but the most popular involves the hot injection of organometallic precursors that easily decompose into high temperature solutions of capping ligands.[68] These processes often yield very uniform solutions of quantum dots, which can be further refined by size-selective precipitation methods, in order to measure the size-dependent electronic properties.

An additional noteworthy class of semiconducting material that has been recently formed into nanoparticles are perovskites (**Figure 1-2D**).[69,70] These materials are ionic crystals with the chemical formula ABX_3, where A is a monovalent cation, B is a divalent cation, and X is a halide, and can be synthesized by the precipitation of appropriate precursors in organic solvent.[71] These materials have received intense interest due to their excellent optical properties, often exceeding those of more traditional quantum dots.[72] However, a major barrier to their more widespread adoption is their poor stability; perovskite nanocrystals rapidly degrade when exposed to water, excessive heat, or repeated exposure to UV light.[73] A number of processes are being developed to combat their poor stability by either post-synthetically or during synthesis coating the particles in a protective layer, such as a polymer brush.[74,75]

1.2.2 Polymer Brush Particles

Many nanoparticles are capped with a surface ligand to prevent them from coalescing, but the presence of this ligand provides an opportunity to add further functionality to the nanoparticle. The grafting of polymer brushes to nanoparticles is a method for stabilizing the particles via steric interactions, is a promising strategy for designing novel nanocomposites.

1.2.2.1 Preparation of Polymer Brush Particles

Polymer-coated nanoparticles are most often prepared by either "grafting to", attaching a pre-synthesized polymer to the surface of the particle, or "grafting from", growing polymer chains from an initiator affixed to the surface of a particle.[76]

In a "grafting to" procedure, a polymer is synthesized with an appropriate anchor group that can strongly adhere to a nanoparticle surface. The choice of anchor group is highly dependent on the surface chemistry of the nanoparticle, with some common anchor groups include thiols,[77] catechols,[78] phosphonates,[79] silanes,[80] and carboxylic acids.[81] The key advantage of a "grafting to"

procedure is the ability to synthesize the polymer separately from the nanoparticle, which allows for easier characterization, and greater control over chemical composition and dispersity. However, the grafting reaction is frequently low yielding, requiring a significant excess of polymer and making the method unsuitable for industrial-scale production.

Alternatively, "grafting from" involves attaching an initiator to the surface of a nanoparticle and using the resulting conjugate as a macroinitiator.[82] Initiators can be affixed to nanoparticles using the above-mentioned anchor groups, but importantly in this synthesis strategy the nanoparticle surface can be saturated with the less expensive initiator making materials synthesized by "grafting-from" easier to scale. A consequence of the "grafting from" method is that the polymers cannot be modified separately from the particle, and most characterization requires the decomposition of the nanoparticle, which may affect the polymer chains themselves. Furthermore, growing polymers from the surface of a particle increases the probability of side-reactions such as chain-chain termination occurring during synthesis, which limits types of polymerizations that can be performed and can result in a decrease in polymer quality.

Research into polymer-grafted nanoparticles has recently dramatically increased due to the invention of several controlled radical polymerization reactions. It is important to note that polymer-grafted nanoparticles can be prepared by both the "grafting to"[83] and "grafting from"[84] method from uncontrolled polymerizations, but the resulting products tend to face limitations such as low molecular weight, poor grafting density, and high dispersity. Conventional uncontrolled radical polymerizations occur very rapidly as free radicals form and being reacting with monomer. However, because the free radicals are quite unstable, and are capable of reacting with other free radicals, a number of termination events such as reacting with an impurity or another free radical on a different polymer chain are possible. Anionic[85] and cationic[86] polymerizations are known as "living polymerizations" because the reactive species repel each other through Coulombic forces, suppressing termination, and allowing for further reaction steps (for instance the synthesis of a block copolymer) to occur after the first monomer is consumed. The drawback of these living polymerizations is that the active species tend to be so reactive that they are incompatible with many common functional groups, and pose safety risks. Controlled radical polymerizations, which include nitroxide mediated polymerization (NMP),[87] atom transfer radical polymerization (ATRP),[88] and reversible addition-fragmentation chain-transfer (RAFT),[89] instead prevent unwanted termination reactions by regulating the active radical species. In NMP, the carbon-

oxygen bond in an alkoxyamine initiator homolytically cleaves to generate a carbon centered radical and a nitroxide radical. The reverse reaction between the nitroxide and carbon radicals is much faster than the termination reaction between two carbon radicals. As a result, there is a persistent, but low population of carbon radicals available at any moment in the reaction mixture, and so chain growth becomes a much more likely reaction than termination. ATRP works by a similar principle, where a carbon-halide bond in an initiator is homolytically cleaved by a copper catalyst, but the reverse reaction reattaching the halide proceeds at a much faster rate. ATRP has grown in favor relative to NMP because of its compatibility with a larger number of monomers, the increased simplicity of integrating the initiator into other molecular designs, and the fact that the chain end of polymers made by ATRP is often a halide group that can be easily substituted for easy end-group modification. RAFT differs slightly from these two methods, in that initiation is performed in the same manner as a typical uncontrolled free radical polymerization. However, a thiocarbonylthio "RAFT agent" is also present in the reaction mixture to serve as a trap for radicals. In the main RAFT equilibrium, growing polymer chains will be released from the RAFT agent as a radical, and given the opportunity to grow by an additional monomer or be trapped again by the RAFT agent. Like the other controlled radical techniques, the deactivation reaction is faster than the activation reaction, and so polymer growth is slow and the population of radicals is kept at a small and regulated level. Importantly, these controlled radical polymerizations are "living" similar to anionic or cationic polymerizations; the reaction can be halted, the monomer exchanged, and then restarted to synthesize block copolymers.

These controlled radical polymerizations offer several advantages for the synthesis of polymer coated nanoparticles. First, these methods decrease the probability of branching, and provide options for synthetically installing a wide variety of chemical functionalities at the chain ends of the polymers.[90,91] For "grafting to" approaches, this enables good control over the presence of the anchor groups, and for both synthetic routes it is possible to dictate the chemical composition of the brush as it extends away from the particle. Furthermore, because controlled radical polymerizations allow for the synthesis of polymers with narrow dispersity, it is possible to make brushes with well-known distributions of polymer chains which decreases the number of variables in the system. Additionally, "grafting from" syntheses require some form of a controlled polymerization to produce high molecular weight polymers. On the surface of a particle with growing polymer chains, there are a large number of radical species in close confinement, which

would typically lead to a significant degree of chain-chain termination. Because the population of radicals is kept low, surface initiated (SI)[92] ATRP,[93] RAFT,[94] and NMP[95] are able to grow polymers of significant lengths.

1.2.2.2 Behavior of Polymer Brushes

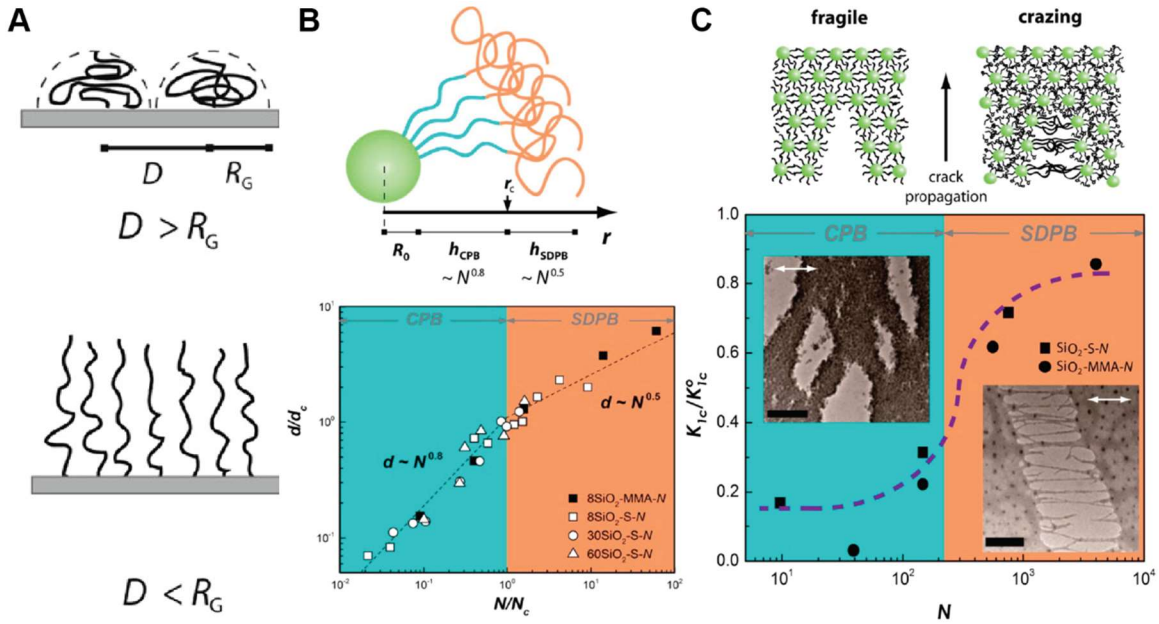

Figure 1-3. Properties of polymer brushes. (A) Polymer brush conformation is highly dependent on grafting density. If the grafting density is low enough that the distance between chains greatly exceeds the radius of gyration of the polymer, it will adopt the "mushroom" configuration. If the polymers are densely grafted onto a surface, it will adopt an extended conformation. (B) On curved surfaces, the density of a polymer brush decreases as the chain end extends. Near the surface the polymer will be in the concentrated particle brush regime, but longer polymers may enter the semidilute polymer brush regime. (C) Materials made from concentrated polymer brushes act like hard spheres, and are brittle. Semidilute polymer brushes can entangle, which enhances the toughness of the material. Adapted from Hui et al.[82]

Surfaces grafted with polymer chains, known as "polymer brushes", were first explored in the context of star polymers and micelles.[96,97] The most notable differences between free polymers in the melt or in solution involve the grafting density of polymers per unit area and the relationship between the polymer's contour length and the curvature of the surface they are present on.

In the dilute limit, individual polymer chains will be unable to affect their neighbors, and it takes places when the distance between grafting points is greater than twice the radius of gyration (R_g) of the polymer.[76] Here, the polymers will behave similarly to star polymers, with the height of the brush (extension away from the surface) scaling with $N^{1/2}$ in a theta solvent and $N^{3/5}$ in a good solvent, where N is the number of Kuhn segments in the polymer. In this conformation, known at the "mushroom" regime, the presence of the interface has a minimal effect on polymer behavior as the chains simply maximize their configurational entropy by adopting a random walk shape.[98] Conversely, in the concentrated brush regime, excluded volume interactions between polymer chains prevent the polymer from adopting a random walk in the z-dimension extending away from the interface, instead providing a linear relationship between the number of monomers in the molecule and the height of the brush (**Figure 1-3A**).[99]

Importantly, on a curved surface, like a nanoparticle, the areal density of polymer will decrease as the brush extends away from the interface and splays out. Consequently, a polymer brush will transition from the concentrated brush regime to the semidilute regime at higher molecular weights. Models adapted from star polymers[100] suggest this transition is dependent of the curvature of the particle, the grafting density, and the chemical composition of the polymer.[101–103] The experimental data largely corroborates the theory, however a scaling exponent of $\sim N^{0.8}$ is typically observed in the concentrated brush regime, which is likely due to the fact that the transition between concentrated and semidilute brushes is continuous (**Figure 1-3B**).[104]

1.2.2.3 Properties of Materials Made from Polymer Brush Particles

Polymer brush particles are an attractive building block for nanocomposites because the organic and inorganic components are chemically bonded together, therefore preventing undesirable aggregation in the material.[105] Furthermore, the ease of synthetically modifying polymer brushes makes them an interesting platform for making functional materials with novel thermal, chemical, and optical responses.[106]

Integrating nanoparticles into polymers has long been known to enhance their mechanical properties, but at high volume fractions the aggregation of particles provides a failure mechanism instead. Polymer grafted nanoparticles, by contrast, are better able to integrate into a polymer matrix because of the favorable mixing energies of the polymer brush with the matrix.[107] However,

the compatibility of polymer grafted particles with the matrix is highly dependent on particle size, polymer molecular weight, and grafting density. As a rule of thumb, a dense brush (> 0.1 chains per nm^2) is capable of completely shielding the nanoparticle core, making the interactions of the polymer coated nanoparticle completely dependent on the properties of the brush.[108] Alternatively, lower grafting densities enable some degree of interaction between the core and the matrix, and the competition between the cores, brush, and bulk polymer can result in assemblies of strings or sheets of particles.[109] Similarly, the polymer brush on the nanoparticle must be of sufficient length to favorably interact with the matrix; at shorter polymer lengths in the particle brush the conformational differences between the brush particle and the matrix cause dewetting and phase segregation.[110] Overall, the mechanical properties of these composite materials such as Young's modulus and fracture strain tend to be optimized in the case of well dispersed particles.[111]

Interestingly, the optical properties of these polymer matrix – polymer grated nanoparticle composites are also dependent on the brush morphology. Aggregates of nanoparticles inside a polymer become large enough to scatter significant amounts of light, turning the composite opaque. Researchers addressed this by grafting a bimodal polymer brush to the surface of titania nanoparticles, so that the short polymers still protected the cores from aggregating, but the longer polymer was fully in the dilute polymer brush regime as it had an artificially lowered grafting density. As a result, it was able to successfully mix with matrix polymer, disperse the particles with minimal aggregation, and maintain optical transparency in the composite.[112] Alternatively, choosing an appropriate polymer, polymer molecular weight, and nanoparticle composition can allow for matching of the refractive indices of the filler and matrix, resulting in effectively transparent particles.[113]

Polymer grafted nanoparticles can also be used to form single component nanocomposites, without any additional matrix polymer, and therefore undesirable particle aggregation is impossible. In this case, the key interaction is between the polymer brushes of adjacent particles, as opposed to polymer chains in a matrix. When the polymer is in the concentrated particle brush regime, the dense chains are not capable of entangling with one another. Consequently, the polymer coated nanoparticles act like hard spheres, undergo brittle fracture, and due to the weak interactions between particles have unremarkable mechanical properties. Alternatively, if the polymer chains are long enough to enter the semidilute polymer brush regime they are capable of entangling with one another. These materials deform more like polymers, with behavior like crazing clearly evident

in samples after mechanical testing is performed (**Figure 1-3C**). Brush particles capable of entangling with one another are quite tough, and also have increased toughness relative to pure polymer.[114–118]

1.3 Nanoparticle Self-Assembly Creates Structural Control across Length Scales

Nanoparticles are a promising platform for nanocomposite design due to their unique composition and size dependent properties. In order to create the most sophisticated next-generation nanocomposites, it will be necessary to simultaneously control the structure of these materials at the nanoscale, microscale, and macroscale. The only way to achieve the desired level of geometric complexity in a scalable fashion is through self-assembly. Significant progress has been made in designing self-assembling nanoparticle systems, which can be built upon to make nanocomposites by design.

1.3.1 Drying-Mediated Assembly

Non-specific, non-directional supramolecular interactions are typically not very strong, but are quite commonplace. A common and illustrative case is micelle self-assembly;[119] when molecules with both a hydrophobic and hydrophilic component, called amphiphiles, arrange themselves into aggregates so that the component of the molecule that interacts favorably with the solvent, typically a charged group interacting favorably with water, is exposed and the component that interacts unfavorably, typically an alkyl chain, is sequestered to the interior of the micelle. The force that drives micelle assembly, the hydrophilic-hydrophobic force, is particularly interesting because unlike chemical forces, such as covalent bond formation, the dominant free energy contribution comes from entropy instead of enthalpy. In typical micelles with water as a solvent, the shell of water molecules surrounding the amphiphiles adopts a limited set of conformations so as to minimize the polar-nonpolar mismatch between the alkyl chain and the strong dipole of water. However, above a critical concentration, many amphiphiles arrange themselves into a closed geometry so that only their hydrophilic ends are exposed to water, giving both the hydrophobic tails and the water molecules increased conformational freedom. This force is non-specific because each amphiphile can interact with every other, and non-directional because the interaction is largely isotropic. Micelles have some limits on the complexity they can exhibit, but the structure

can be dictated to some degree by changing the sizes and chemical identity of the components of the molecule in order to form spheres, cylinders, bilayers, or occasionally more exotic shapes.

Colloidal self-assembly is a common way to define structure, and it can do so to create fascinating macroscopic results, an example being the opal gemstone which is known for its striking iridescence due to the partial photonic bandgap of the structure.[120] One-dimensional photonic bandgaps can be made by alternating layers of components with different dielectric constants, which exhibit strong reflectivity at certain angles, but not others. Potentially more interesting are higher order two and three dimensional photonic bandgaps, which can perfectly reflect certain wavelengths at any viewing angle. Artificial opals have been synthesized from periodic arrays of face centered cubic (fcc) close-packed monodisperse particles have been studied since the 1950's,[121] but for photonic applications inverse opals, where colloidal assemblies are used as a template for another material to fill their negative space, are preferred because they can form a complete, as opposed to partial, three-dimensional photonic bandgap if made with high refractive index materials.[122] Colloidal photonic crystals have been assembled by methods including centrifugation,[123] drying,[124] Langmuir-Blodget methods,[125] sedimentation,[126] spin coating,[127] and shear alignment,[128] and inverse opals have been formed by infiltrating these assemblies with a wide array of materials, such as silica,[122] polymers,[129] metals,[130] and semiconductors[131] allowing for responsive crystals.[132] Assemblies of close packed colloids rely on non-specific, non-directional depletion forces where the entropy of the solvent is maximized by minimizing the surface area and thus volume of the particles, not too dissimilar from the interactions that form micelles. Unfortunately, the lack of complexity of the assembly mechanism means that it remains a challenge to produce alternative geometries, and additionally there is no ability to program the arrangement of different particle types inside the lattice.

To produce more intricate particle arrangements, additional parameters must be introduced to drive assembly to phases other than an fcc packing. It is possible to synthesize highly monodisperse small nanoparticles (around 10 nm), and to functionalize them with small molecule organic ligands. By slowly drying mixtures of different nanoparticles, many different highly ordered crystalline nanoparticle superlattices can be reliably formed (**Figure 1-4A**).[133,134] The assembly is primarily directed by depletion forces as nanoparticles of different sizes configure themselves to form the densest possible lattice, not dissimilarly from amphiphiles packing into different arrangements depending on their size, while additional small magnitude coulombic forces are

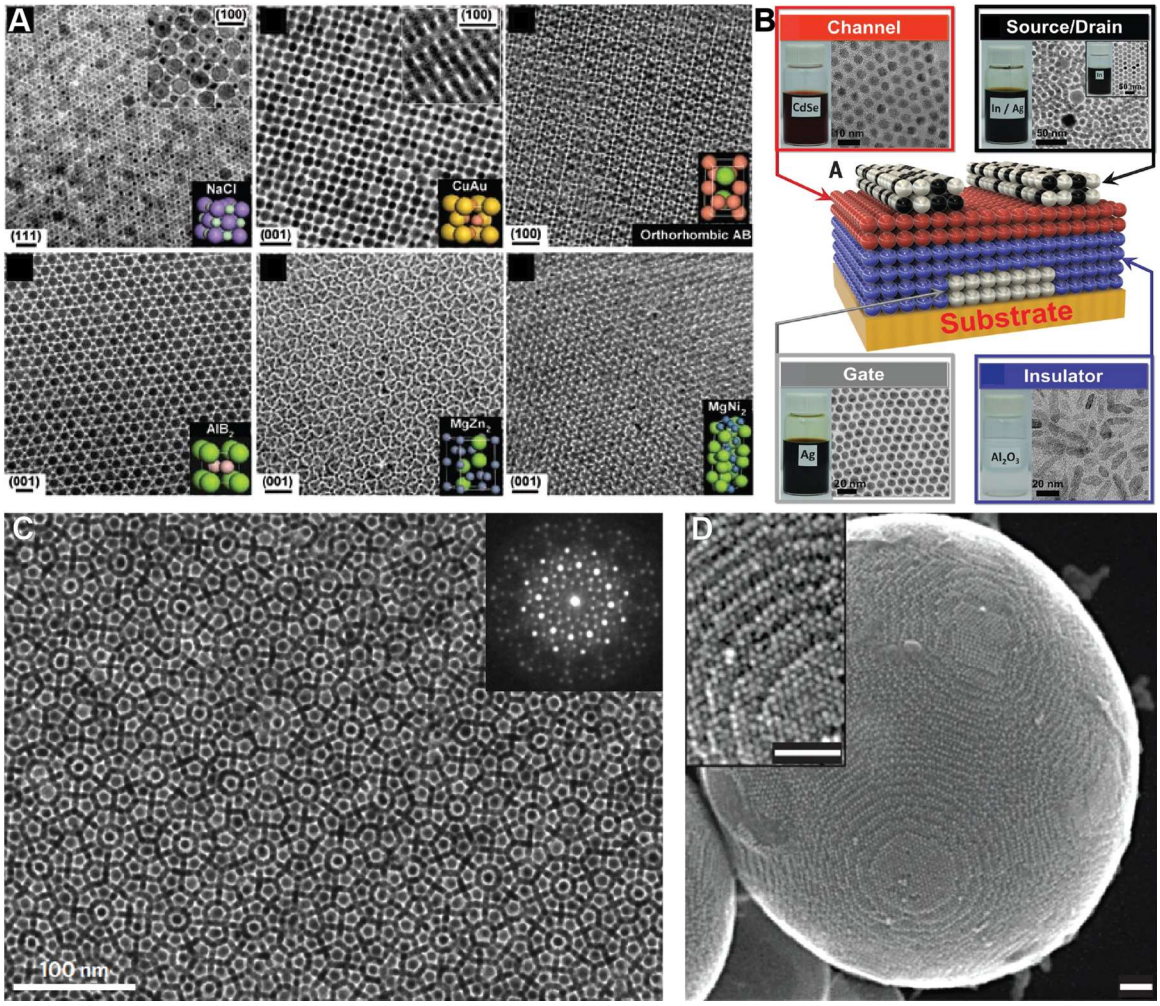

Figure 1-4. Drying mediated assembly can generate complex nanoparticle superlattices. (A) Binary mixtures of nanoparticles can result in a large number of different crystallographic phases. Adapted from Shevchenko et al.[133] (B) A transistor made entirely from colloidal components. Adapted from Choi et al.[147] (C) A quasi-crystalline superlattice prepared from drying-mediated assembly. Adapted from Ye et al.[135] (D) Assembly in droplets can create complex meso-scale structures. Adapted from Nijs et al.[143]

introduced through the ligands on the nanoparticle surface. The slow drying procedure ensures that the nanoparticles reach their thermodynamic minimum which is designed to be the ordered phase. The modularity of nanoparticle assembly can form ordered structures with binary, ternary, or more complex nanoparticle mixtures as well as interchanging the chemical identity of the nanoparticle core. This technique has been expanded to produce quasicrytals (**Figure 1-4C**)[135] and other

complex lattices,[136,137] it has integrated doping techniques to introduce tunable chemical composition,[138] and to expand the number of design handles by using anisotropic nanoparticles,[139] and by diversifying the ligand composition to include dendrons[140] and polymers.[141] Beyond films, some three-dimensional structures can be produced,[142] for instance by assembling the nanoparticles in droplets (**Figure 1-4D**).[143–145] The well-controlled nanoparticle lattices have been explored for application for lithium-ion storage[146] and as modular building blocks for electronics (**Figure 1-4B**).[147] Although the slow drying approach has had significant success at generating diverse superlattice structures, it faces challenges producing scalable and applicable materials. It is difficult to produce the monodisperse nanoparticles at a large enough scale within an acceptable tolerance limiting the diverse structures to periodicities too small to be useful, and the slow drying procedure may be cumbersome for industry to adapt. A further complication is that, since the assembly force is non-specific, changing the size or chemical identity of the components will alter the crystal structure adapted by the lattice, which makes it difficult to determine design rules and arbitrarily produce predicted arrangements of matter. Additionally, the assembly force is non-directional, making it challenging to limit the force to only bonding the particles together in a programmed manner. This complicates the use of the slow drying technique for the larger lengthscales needed for photonic applications because the weak and isotropic depletion force produces many similar energy states that cannot be differentiated between and so larger particles form disordered aggregates.

1.3.2 Assembly through Coulombic Interactions

Coulombic interactions are a force that is specific, in that a positively charged component can be specifically designed to interact with a negatively charged component, but non-directional, in that the force is isotropic. Because of their chemical simplicity and compatibility with aqueous environments, Coulombic forces are often found in nature, such as in proteins to direct their folding. Furthermore, chemists have used this biologic inspiration to design ordered peptide structures.[148] In comparison to the depletion force that directs micelle assembly, Coulombic forces are significantly stronger, on the order of 100 kJ/mol versus 10 kJ/mol,[149] and so also apply over a longer range than weaker forces. This makes bonds formed by ionic forces effectively non-reversible, and thus it is easier to form kinetically trapped states and more difficult to form large, ordered, and designed structures governed by ionic interactions. However, the high strength of

ionic interactions can be tempered by combining large numbers of oppositely charged ions that result in a neutrally charged material. At a smaller lengthscale than supramolecular interactions, this is taken advantage of by nature in the formation of ionic crystals. Since the coulombic force is so strong, there is a large driving force to maximize the number of oppositely charged neighbors each ion has that leads to a set of design rules for making different crystal structures. Different ions have different ionic radii based on their position in the periodic table, and so the multiple species that make up a compound will take on a different number of nearest oppositely charged neighbors, their coordination number, to maximize interactions for simple compounds. For more complicated compositions with multiple different charged ions present, such as aluminosilicates, the ionic packing requires each species to maintain local charge electroneutrality, while also maximizing the distance between like-charged components, which can result in more complex geometries. Together, these considerations can reliably predict the lowest energy arrangement of ions, and thus the most prevalent crystal structure.[150]

To assemble nanoparticles with a higher degree of specificity, coulombic forces can be used to drive nanoparticle assembly.[151] Researchers functionalized nanoparticles with small molecule alkanes terminated in ammonium or carboxylate groups. In water the charges can be screened by salts, but in a water-DMSO mixture the water can be evaporated so that the electrostatic attraction associates the two particle types, and if performed slowly enough a thermodynamically stable crystal can form. Interestingly, the particles arrange into a non-close packed diamond-like sphalerite lattice, primarily because the screening length (2.7 nm) is comparable to the nanoparticle size (5 nm) and so like-charge repulsions prevent a denser packing. However, the lack of directionality of the coulombic force causes larger particles to behave differently and pack more closely when their size exceeds the interaction length. The specificity of the electrostatic force does allow precise positioning of nanoparticles with arbitrary core compositions, in this case the researchers co-assembled both gold and silver nanoparticles, meaning this force can add an element of programmability to superlattice design. This approach is able to grow crystals several microns in diameter, but interestingly enough the largest crystals were found in samples with fairly non-uniform (10-20%) nanoparticles. It was determined that the particles on the smaller end of the distribution served to screen and stabilize the larger aggregates, and so delayed their precipitation.[152] Using ionic forces to assemble nanoparticles also faces some limitations in creating alternative crystal structures. Mixtures of different sized nanoparticles are unable to be

stabilized by charge screening, and larger particles with less charge exclusively form a limited number of close packed structures. This diminishes the applicability of this method because it can only access smaller size regimes without a broad variety of crystal structures, and so although electrostatic forces increase programmability they can decrease structural diversity. Furthermore, free floating micron sized crystals are difficult to integrate into devices, and the slow evaporation of water would complicate industrial fabrication impeding scalability.

1.3.3 Assembly through Watson-Crick Base Pairing of DNA

Specific and directional forces arguably provide the most reliable method for generating nanoscale ordering because they most strictly define molecular arrangement. Biology uses the most common specific and directional force, hydrogen bonding, for some of its most precise requirements, such as the self-assembly of DNA. A hydrogen bond consists of a hydrogen bond donor, which provides a loosely bonded proton, and a hydrogen bond acceptor, which can coordinate to the loosely bonded proton. Complimentary hydrogen bond motifs of arrays of donors and acceptors, such as the adenine-thymine and cytosine-guanine pairs in DNA, can further enhance their specificity and modulate their binding strength.[153] Hydrogen bonding is particularly well-suited to supramolecular chemistry because the bond-strength is typically between that of coulombic and depletion forces, and so hydrogen bonds are strong enough to hold together an assembly but weak enough to rearrange themselves to make an ordered structure. Beyond nature, chemists have found many creative uses for hydrogen bonding motifs, for example they have synthesized molecules with bifunctional bonding groups which when mixed with their compliments form condensation polymers, but with hydrogen bonds instead of covalent bonds connecting the monomers.[154] Because hydrogen bonds are directional, these supramolecular polymers possess one dimensional anisotropy forming a backbone very similar to conventional polymers. Moreover, the specific nature of hydrogen bonds lets chemists synthesize monomers that only polymerize when mixed with their compliment. Additionally, hydrogen bond motifs are specific enough that several orthogonal motifs or other types of specific and directional bonding like metal coordination can be combined to add more complexity to the polymer.[155]

In order to enhance the capability to rationally design nanoparticle crystal symmetry, a more refined assembly method is necessary. DNA, the biopolymer used to precisely convey genetic

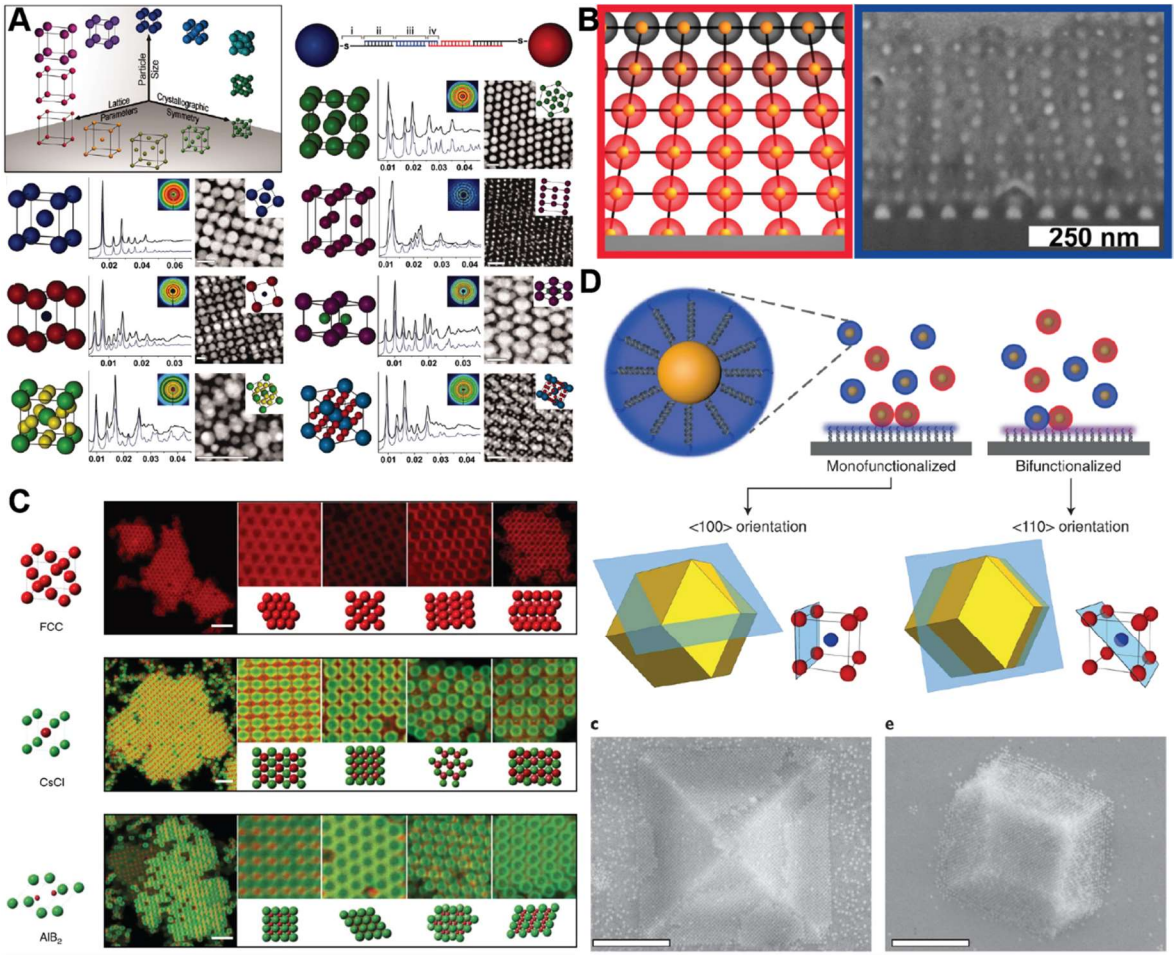

Figure 1-5. Complex crystals can be assembled using DNA as a structure directing agent. (A) The programmable atom equivalent (PAE) system consisting of nanoparticles grafted with DNA are capable of forming a large number of lattices symmetries by varying the relative sizes and grafting densities of the PAEs. Adapted from Macfarlane et al.[162] (B) PAE crystals can be grown off of substrates using a layer by layer method. The substrate can be patterned so as to have lattice mismatch with the PAEs, generating strain and defects. Adapted from Gabrys et al.[176] (C) DNA can also be grafted to micron sized colloidal particles to direct their assembly into a similar set of lattices. Adapted from Wang et al.[168] (D) PAEs annealed in the presence of a substrate will form Winterbottom constructions as the crystallites grow from the surface. Changing the surface functionality can tune the resulting morphology. Adapted from Lewis et al.[178]

information uses hydrogen bonding as a specific and directional force to co-assemble complementary strands. Nanoparticles can be functionalized by DNA ligands, which aggregate

when mixed together with a complimentary crosslinker.[156,157] The specificity of the DNA hydrogen bonding motifs allows for the synthesis of stable, individual building blocks that only aggregate when mixed with the complimentary crosslinker, and the directionality of hydrogen bonding confines the interactions to the periphery of the nanoparticles which separates the aggregation mechanism from the rest of the building block. Importantly, hydrogen bonding is a strong enough force that it can hold nanoparticles together at room temperature, but at elevated yet accessible temperatures (<100°C) the aggregates can be "melted". This melting behavior can be tuned: diluting the complimentary strands broadens and lowers the melting transition (T_m), larger particles sharpen and slightly lower T_m, higher salt concentrations (and thus enhanced screening of the negative electrostatic charge of DNA) raises T_m, and longer crosslinker spacer lengths raise T_m.[158,159] By modifying the DNA design so that each of two nanoparticles expresses a short DNA sequence that is complimentary to the other building block, known as programmable atom equivalents (PAEs),[160] the nanoparticles can be annealed near their melting temperature to drive self-assembly into ordered crystalline lattices.[161] Equally sized PAEs form fcc lattices for self-comlimentary DNA strands and body centered cubic (bcc) lattices for a binary system. However, the size of the nanoparticles and the DNA shell can both be modified to create building blocks of different proportions which pack together in unique but predictable ways to provide multiple new crystal symmetries (**Figure 1-5A**),[162] including complex structures like clathrates.[163] Moreover, the number of possible superlattices is further enhanced by the ability to introduce multiple binding capabilities or ternary particle systems.[164] The nanoparticle core can be replaced with an anisotropic particle, such as plates[165] or cubes,[166] that thereby affect the resulting lattice symmetry. Recent work has introduced the concept of the "electron equivalent," where multiple short DNA segments will connect particles to create lattices, more resembling a metallic bond than more traditional PAEs that more closely mimic ionically bonded materials.[167] The sophistication of DNA nanotechnology has allowed for many creative methods for controlling nanoparticles that can even form non close-packed crystal symmetries, for instance DNA origami has been used to form tetrahedral cages around nanoparticles that then assemble into a diamond lattice.[168] Furthermore, the DNA strategy has been extended to micron sized colloidal particles (**Figure 1-5C**).[169] Interestingly, the PAEs also allow for significant control over the micron-scale structure. When slow cooled, the PAEs will crystallize into faceted Wulff polyhedra, where the faceting is determined by the type of lattice the PAEs assemble into.[170–172] Alternatively, the PAEs crystallites

can be grown off of substrates, which could be beneficial for future applications because it would be possible to macroscopically manipulate the crystalline material and give it a controlled orientation.[173–175] Interestingly, the substrates used for surface growth can be prepared with different periodicities than the PAE crystal, forcing a lattice mismatch and introducing strain and defects to the system (**Figure 1-5C**).[176] The presence of PAEs on a surface opens the possibility of alternative processing methods, for instance annealing them by excitation of the surface plasmon resonance of gold PAEs with laser light.[177] Furthermore, the slow cooling technique used to prepare single crystals of PAEs can be applied to substrates, and results in crystallites that follow the Winterbottom construction (**Figure 1-5D**)[178] Thus, using hydrogen bonding to assemble nanoparticles can impart a high degree of programmability and also permit a broad range of structural diversity.

However, DNA assembled nanoparticles suffer from several key deficiencies that prevent them from being a scalable and therefore useful nanomaterial. First, DNA is expensive and difficult to precisely synthesize in the bulk quantities needed for mass production. Furthermore, DNA is not amenable to many processing methods; it is incompatible with organic solvents, and moreover requires carefully controlled salt concentration and pH to maintain the fidelity of the nanoparticle assemblies. Finally, this approach forces the use of DNA as the ligand, which limits the design space for the resulting materials. This could be crucial because generating more complex non-close packed structures may require more comprehensive processing.

Hydrogen bonding is a promising method for driving nanoparticle assembly, but must be implemented in an industrially relevant method. However, this has remained a challenge, leading to the introduction of several other promising techniques.[179,180] Assembling nanoparticle superlattices from scalable components using a specific and directional binding force can be used to make nanocomposites with a diverse array of possible structural configurations that can be precisely tuned to make functional devices.

Chapter 2. Self-Assembling Nanocomposite Tectons

Adapted from Zhang, J.; Santos, P. J.; Gabrys, P. A.; Lee, S.; Liu, C.; Macfarlane, R. J. Self-Assembling Nanocomposite Tectons. *J. Am. Chem. Soc.* **2016**, *138* (50), 16228–16231. https://doi.org/10.1021/jacs.6b11052.

The physical characteristics of composite materials are dictated by both the chemical composition and spatial configuration of each constituent phase. A major challenge in nanoparticle-based composites is developing methods to precisely dictate particle positions at the nanometer length scale, as this would allow for complete control over nanocomposite structure-property relationships. In this work, we present a new class of building blocks called nanocomposite tectons (NCTs), which consist of inorganic nanoparticles grafted with a dense layer of polymer chains that terminate in molecular recognition units capable of programmed supramolecular bonding. By tuning various design factors including particle size and polymer length, we can use the supramolecular interactions between NCTs to controllably alter their assembly behavior, enabling the formation of well-ordered body centered cubic superlattices consisting of inorganic nanoparticles surrounded by polymer chains. NCTs therefore present a modular platform enabling the construction of composite materials where the composition and three-dimensional arrangement

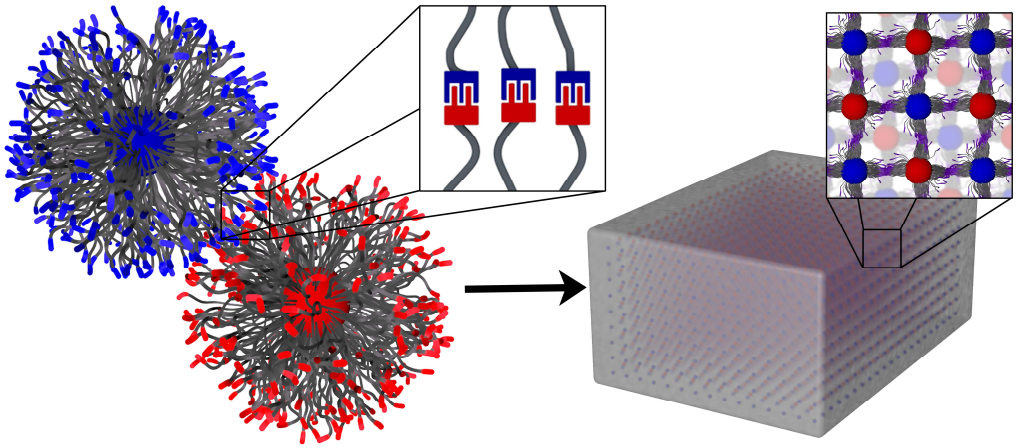

Figure 2-1. Nanocomposite tectons (left) use supramolecular binding interactions to form nanocomposite materials with spatial control over particle placement in three dimensions.

of different constituents within the composite can be independently controlled.

Nanocomposites are an important class of materials based on integrating two or more disparate phases to achieve physical characteristics that cannot be realized with a single-phase material.[1,107,181,182] The properties of these composites are dictated by their chemical compositions, as well as the relative three-dimensional arrangements of each component. While structure control in macroscopic composites can be easily achieved via direct approaches like mechanical processing, top-down methods to control nanoscale composite structure either provide limited spatial resolution or are undesirably inefficient. Alternatively, self-assembly can produce nanocomposite materials with well-defined geometries in a parallelizable manner that is amenable to scale-up. Indeed, many sophisticated nanoscale assembly techniques have been developed to synthesize materials with unique photonic, plasmonic, electronic, and mechanical properties,[183–185] making use of multiple types of nanoscale building blocks including polymers,[186–188] biological materials,[189,190] and inorganic nanocrystals.[133,139,191,192] However, the major limitations of current nanocomposite self-assembly techniques are that they either 1) focus on ensuring compatibility of the different phases but lack hierarchical structural organization of all constituent components,[193–196] or 2) utilize directing agents or processing conditions that are not amenable to functional composite architectures.[141,162,197] Here, we circumvent these challenges by developing a class of nanocomposite "tectons"[198,199] (NCTs, **Figure 2-1**) – irreducible nanocomposite building blocks that are themselves composite materials. An NCT consists of a nanoparticle grafted with polymer chains that terminate in functional groups capable of supramolecular binding, where supramolecular interactions between polymers grafted to different particles enable programmable bonding that drives particle assembly (**Figure 2-1**). Importantly, these interactions can be manipulated separately from the structure of the organic or inorganic components of the NCT, allowing for independent control over the chemical composition and spatial organization of all phases in the nanocomposite via a single design concept.

2.1 Design and Assembly of Nanocomposite Tectons

NCTs represent a versatile class of building blocks for nanocomposite synthesis, as the inorganic nanoparticle core provides a basic scaffold that dictates the size and shape of the NCT, while the polymeric ligands define its solubility, the stiffness of its corona, and the interparticle distances in the final structure; together, these two components also dictate the overall chemical composition of the NCT. Conversely, the assembly process, and thus the final mesoscale ordering of particles

within the composite, are dictated by the interactions between supramolecular binding groups. Indeed, the unique aspect of the NCT architecture is the use of these molecularly-programmed interactions to enable more sophisticated control over particle assembly in the macroscopic composite than previous polymer-grafted nanoparticle systems.

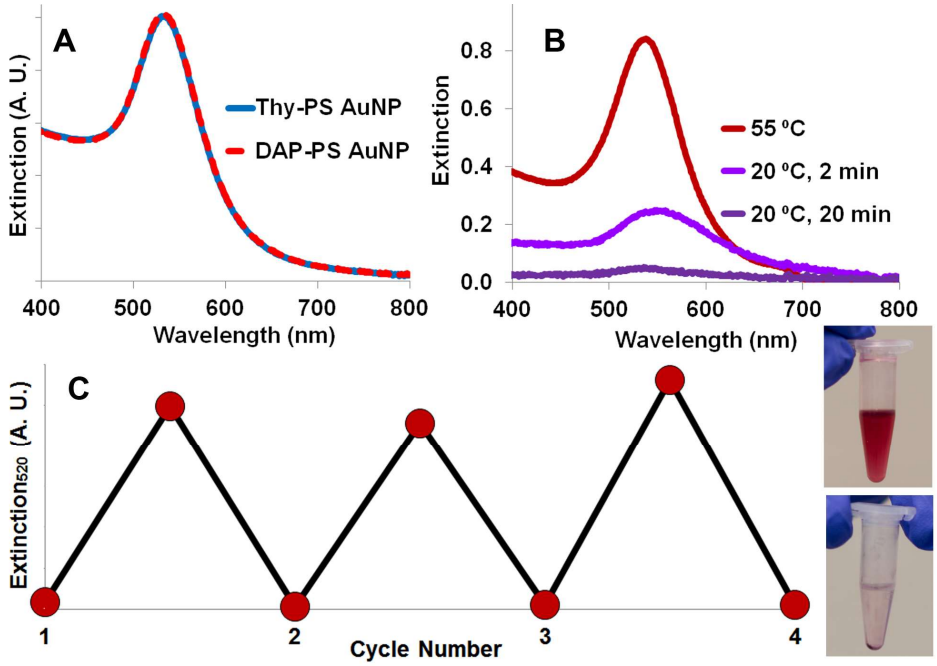

Figure 2-2. (A) Normalized UV-vis spectra of NCT dispersions in toluene (20 nm AuNPs, 11.0 kDa DAP-PS or Thy-PS). (B) UV-vis spectra of mixtures of complementary NCT dispersions. The three traces represent the spectrum 2 minutes after mixing, 20 minutes after mixing, and after heating at 55 ˚C for ~1-2 min. (C) Normalized extinction at 520 nm for a mixture of complementary NCTs undergoing multiple heat-cool cycles between 20 and 55 ˚C (lower and upper data points, respectively, see SI for details). Insets: optical images of a representative NCT mixture at the given temperatures.

Here, we demonstrate the first example of an NCT by grafting gold nanoparticles (AuNPs) with polystyrene (PS) chains that terminate in molecular recognition units with complementary hydrogen bonding motifs (diaminopyridine, DAP, and thymine, Thy). Gold nanoparticles provide a sensitive spectral probe for particle assembly[200] and are easily functionalized via gold-thiol chemistry, while polystyrene can be synthesized with a wide range of molecular weights and low dispersity using controlled radical polymerization techniques such as atom transfer radical polymerization (ATRP).[201] Complementary hydrogen bonding[202] via the DAP and Thy units

provides a simple means of controlling particle interactions by modulating temperature, as hydrogen bonds break upon addition of heat.

Functionalized PS polymers (DAP-PS and Thy-PS) were made from DAP or Thy modified initiators via ATRP, followed by post-functionalization to install a thiol group that allowed for particle attachment (scheme S1). The polymers synthesized for the current study had three different molecular weights (~3.7, ~6.0, and ~11.0 kDa, **Figure S1-1**) with narrow dispersity (Đ<1.10), and were grafted to nanoparticles of different diameters (10, 15, 20, and 40 nm) via a "grafting-to" approach modified from a previous report.[203]

Once synthesized, NCTs functionalized with either DAP-PS or Thy-PS were readily dispersed in common organic solvents such as tetrahydrofuran, chloroform, toluene, and N,N'-dimethylformamide with a typical plasmonic resonance extinction peak at 530-540 nm (**Figure 2-2A**, **Figure S1-2**) that confirmed their stability in these different solvents. Upon mixing, DAP-PS and Thy-PS coated particles rapidly assembled and precipitated from solution, resulting in noticeable red-shifting, diminishing, and broadening of the extinction peak within 1-2 minutes (example with 20 nm AuNPs and 11.0 kDa polymers, **Figure 2-2B**). Within 20 minutes, the dispersion appeared nearly colorless, and large, purple aggregates were visible at the bottom of the tube. After moderate heating (~55 ˚C for ~1-2 minutes for the example in **Figure 2-2B**), the particles redispersed and the original color intensity was regained, demonstrating the dynamicity and complete reversibility of the DAP-Thy directed assembly process. NCTs were taken through multiple heating and cooling cycles without any alteration to assembly behavior or optical properties, signifying that they remained stable at each of these thermal conditions (**Figure 2-2C**).

2.2 Melting of Nanocomposite Tectons

A key feature of NCTs is that the sizes of their particle and polymer components can be easily modified independent of the supramolecular binding group's molecular structure. However, because this assembly process is driven via the collective interaction of multiple DAP and Thy-terminated polymer chains, alterations that affect the absolute number and relative density of DAP or Thy groups on the NCT surface impact the net thermodynamic stability of the assemblies. In other words, while all constructs should be thermally reversible, the temperature range over which particle assembly and disassembly occurs should be affected by these variables. To better understand how differences in NCT composition impact the assembly process, NCTs were

synthesized using different nanoparticle core diameters (10-40 nm) and polymer spacer molecular weights (3.7–11.0 kDa), and allowed to fully assemble at room temperature (~22 ˚C) (**Figure 2-3**). Particles were then monitored using UV-Vis spectroscopy at 520 nm while slowly heating at a rate of 0.25 ˚C/min, resulting in a curve that clearly shows a characteristic disassembly temperature (melting temperature, T_m) for each NCT composition.

From these data, two clear trends can be observed. First, when holding polymer molecular weight constant, T_m increases with increasing particle size (**Figure 2-3A**). Conversely, when keeping particle diameter constant, T_m drastically decreases with increasing polymer length (**Figure 2-3B**). To understand these trends, it is important to note that NCT dissociation is governed by a collective and dynamic dissociation of multiple individual DAP-Thy bonds, which reside at the periphery of the polymer-grafted nanoparticles. The enthalpic component of NCT bonding behavior is therefore predominantly governed by the local concentration of the supramolecular bond-forming DAP and Thy groups, while the entropic component is dictated by differences in polymer configuration in the bound versus unbound states.

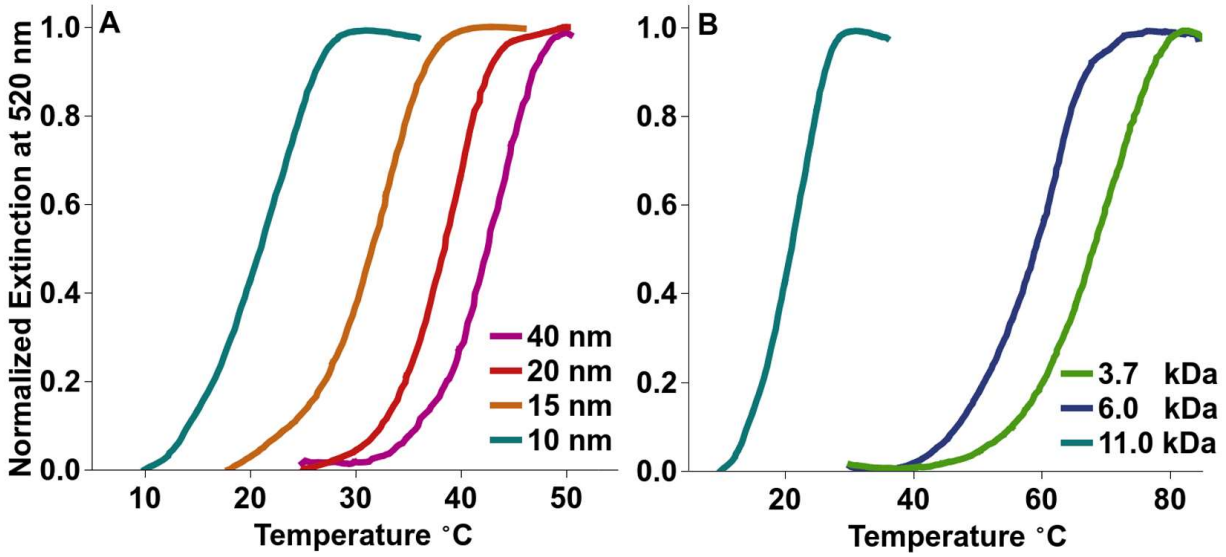

Figure 2-3. Thermal study of complementary NCT mixtures with (A) constant polymer molecular weight (11.0 kDa) and varying NP diameter; (B) constant particle diameter (10 nm) and varying polymer molecular weights.

All NCTs in this study possess similar polymer grafting densities (i.e. equivalent areal density of polymer chains at the inorganic nanoparticle surface, **Figure S1-3**) regardless of particle size or

polymer length. However, the areal density of DAP and Thy groups at the periphery of the NCTs is not constant as a function of these two variables due to NCT geometry. When increasing inorganic particle diameter, the decreased surface curvature of the larger particle core forces the polymer chains into a tighter packing configuration, resulting in an increased areal density of DAP and Thy groups at the NCT periphery;[204] this increased concentration of binding groups therefore results in an increased T_m, explaining the trend in **Figure 2-3A**.[205,206]

Conversely, for a fixed inorganic particle diameter (and thus constant number of polymer chains per particle), increasing polymer length decreases the areal density of DAP and Thy groups at the NCT periphery due to the "splaying" of polymers as they extend off of the particle surface, thereby decreasing T_m in a manner consistent with the trend in **Figure 2-3B**. Additionally, increasing polymer length results in a greater decrease of system entropy upon NCT assembly, due to the greater reduction of polymer configurations once the polymer chains are linked via a DAP-Thy bond; this would also be predicted to reduce T_m. While a more quantitative study on the melting behavior of NCTs is currently underway, we note that within the range tested, all samples were easily assembled and disassembled via alterations in temperature. Inorganic particle diameter and polymer length are therefore both effective handles to control NCT assembly behavior.

2.3 Crystallization of Nanocomposite Tectons

Importantly, because the NCT assembly process is based on dynamic, reversible supramolecular binding, it should be possible to drive the system to an ordered equilibrium state where the maximum number of binding events can occur. We hypothesize that, although the particle cores and polymer ligands are more polydisperse (**Figure S1-7**, **Table S1-1**) than the particles and small molecule ligands used in prior studies to form nanoparticle superlattices,[133,162] ordered arrangements still represent the thermodynamically favored state for a set of assembled NCTs. It is true that, when packing NCTs into an ordered lattice, deviations in particle diameter would be expected to generate inconsistent particle spacings that would decrease the overall stability of the assembled structure. However, the inherent flexibility of the polymer chains should allow the NCTs to adopt a conformation that compensates for these structural defects. As a result, an ordered NCT arrangement would still be predicted to be stable if it produced a larger number of DAP-Thy

binding events than a disordered structure and this increase in binding events outweighed the entropic penalty of reduction in polymer chain configurations.

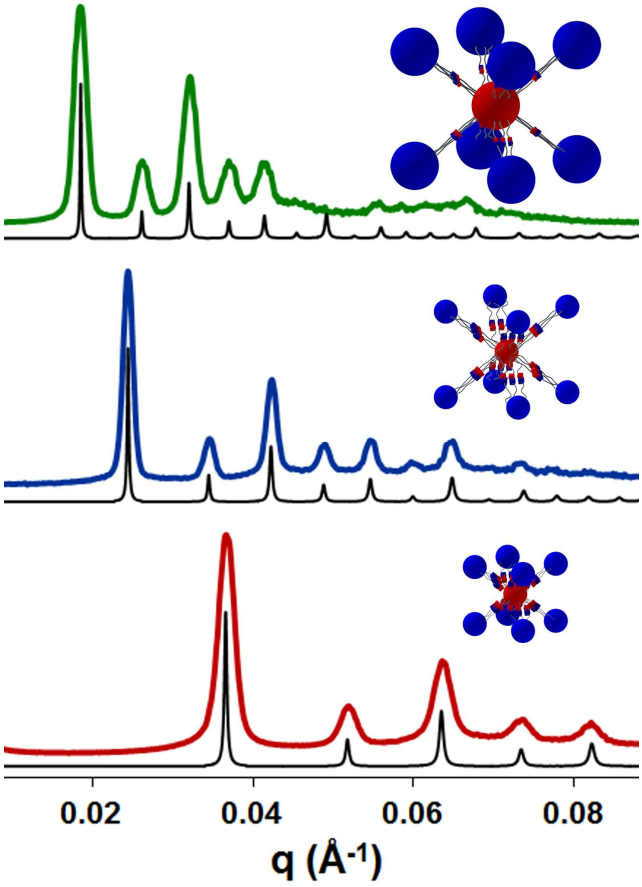

Figure 2-4. SAXS data showing NCT assembly into ordered bcc superlattices: (green trace) 20 nm AuNPs and 11.0 kDa PS; (blue trace) 10 nm AuNPs and 11.0 kDa PS; (red trace) 10 nm AuNPs and 6.0 kDa PS; (black traces) predicted SAXS patterns for corresponding perfect bcc lattices. Insets show the unit cell for each lattice drawn to scale.

To test this hypothesis, multiple sets of assembled NCTs were thermally annealed at a temperature just below their T_m, allowing particles to reorganize via a series of binding and unbinding events (experimental details in the SI) until they reached the thermodynamically most stable conformation. The resulting structures were analyzed with small angle X-ray scattering (SAXS), revealing the formation of highly ordered mesoscale structures where the nanoparticles were arranged in body-centered cubic (bcc) superlattices (**Figure 2-4**, **Figure S1-6**). The bcc structure

was observed for multiple combinations of particle size and polymer length (**Table S1-3**), indicating that the nanoscopic structure of the composites can be controlled as a function of either the organic component (via polymer length), the inorganic component (via particle size), or both, making this NCT scheme a highly tailorable method for the design of future nanocomposites.

In conclusion, we have demonstrated the versatility and programmability of NCTs as controllable nanocomposite building blocks. The data presented here provide the first example of this concept, and we predict that these NCTs should be amenable to multiple different particle core and polymer ligand formulations, as well as different supramolecular binding motifs. Together, these design handles allow for nanocomposite structure control at a level that is unrivaled by previous composite synthesis techniques. Future investigations will both explore the fundamental processes involved in NCT assembly, as well as develop synthesis schemes for making solid and free-standing architectures from NCT building blocks. These structures are predicted to possess unique optical,[207] mechanical,[208] chemical,[82] and electrical phenomena[183] that will make them highly desirable in multiple potential applications.

Chapter 3. Dictating Nanoparticle Assembly via Systems-Level Control of Molecular Multivalency

Adapted from Santos, P. J.; Cao, Z.; Zhang, J.; Alexander-Katz, A.; Macfarlane, R. J. Dictating Nanoparticle Assembly via Systems-Level Control of Molecular Multivalency. *J. Am. Chem. Soc.* **2019**, *141* (37), 14624–14632. https://doi.org/10.1021/jacs.9b04999.

Nanoparticle assembly is commonly regulated by multivalent intermolecular binding events between surface ligands, where the collective interaction of multiple surface-bound molecules dictates the overall thermodynamics of interparticle bonding.[209] A significant amount of effort has therefore been put forth in examining how alterations to these molecular interactions affect nanoparticle behavior, and many strategies have been developed to control particle arrangements by finely tuning the molecular structures that guide nanoparticle assembly.[140,210–212] However, while the manipulation of molecular bonding has been shown to be a powerful means to control the thermodynamics of nanoscale assembly, it is also true that the nanoscale arrangement of these molecular binding groups can affect the overall strength of the bonds being formed.[213–216] In other words, not only can changes to molecular geometry alter material ordering at larger length scales, but changes to these larger scale structures can also cause alterations to molecular behavior. Indeed, manipulating the relative positions of individual chemical moieties is a common design principle used in nature to control the strength and specificity of multivalent intermolecular interactions including avidity in antibody-antigen binding,[217] substrate selectivity at the active site of catalytic enzymes,[218] and strong yet dynamic carbohydrate-regulated cell adhesion.[219] While synthetic materials typically try to general hierarchical ordering from small length scales upwards (e.g. changes to molecular motifs causing different nanoscale behaviors), these examples in nature demonstrate that structural hierarchy can also work in the opposite direction, where large-scale organization alters the behavior of individual components (e.g. nanoscale organization affecting molecular multivalency). Controlling hierarchical organization via interplay between structures at multiple length scales can be referred to as a "systems" approach to materials development.

In principle, it should be possible to develop a systems-level approach to nanoparticle assembly, where structural features at the length scales of individual molecular bonds, nanoscale particle

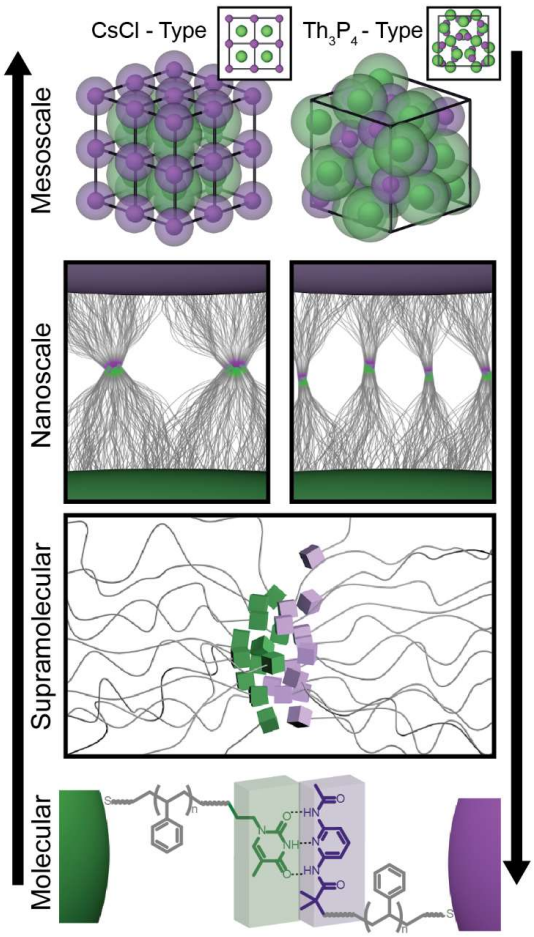

Figure 3-1. Typically, hierarchical structuring is understood as molecular structures causing the organization of larger length scale motifs, but these larger motifs can also influence how the smaller length scale components of a material behave. For example, NCTs functionalized with DAP or Thy terminated polymer chains engage in supramolecular bonding determined by the chemical identity of the ligands (molecular structures, bottom). The binding groups cluster into supramolecular bundles due to differences in intermolecular forces between the head groups, polymer chains, and solvent molecules (supramolecular structures), and this bundling allows multiple molecular groups to act multivalently. Multiple bundles arranged around a nanoparticle surface (nanoscale structures) thereby drive the formation of ordered arrays of nanoparticles (mesoscale structure). However, the organization of particles within a mesoscale lattice can in turn affects the nanoscale arrangement of polymer chains, and these alterations affect polymer chain dynamics, which thereby modulate the thermodynamics of the bundled molecular bonds. Consequently, the structure of the entire system must be considered simultaneously.

geometry, and mesoscale arrangement of particles serve as integrated design handles to control the assembly process.[165,220,221] For example, a systems-level approach to nanomaterials synthesis could use multivalent supramolecular bonding to dictate how nanoscale particles form into mesoscale lattices, but also simultaneously use the nanoparticle coordination environment within those lattices to regulate the multivalency of molecular interactions and alter the strength of these bonds. The advantage of such a complex materials synthesis method would be the ability to more finely tune both particle assembly and supramolecular bonding by design features both above and below the length scales of the nanoparticle bonds themselves. In order to realize this goal, however, it is important first to understand how nanoscale structure affects the thermodynamics of these multivalent interactions in a rational manner. In this work, the hierarchical nature of a nanoparticle building block is used to methodically modify the degree to which supramolecular groups act collectively, and therefore control the overall interaction strength between nanoparticles.

This enables a systems-level approach to materials synthesis, where nanoscale geometry influences molecular organization, and those design parameters in conjunction control mesoscale architecture, affording simultaneous control of material structure across multiple length scales in a programmable manner.

3.1 Multivalent NCT Bonds

We have recently demonstrated a new nanoparticle-based building block capable of directed assembly via complementary hydrogen bonding motifs called the Nanocomposite Tecton (NCT).[222] NCTs consist of rigid nanoparticle cores functionalized with deformable polymer chains in a dense brush architecture (**Figure 3-1**, **Figure S2-1-5**, **Figure S2-8**; NCTs examined here consist of gold nanoparticles coated in polystyrene brushes, suspended in toluene). All polymer chains on the NCTs terminate in either a diaminopyridine or thymine group (DAP and Thy, **Scheme S2-1**), which constitute a complementary supramolecular pair.[223,224] Complementary sets of NCTs can form many DAP-Thy complexes that behave as a collective nanoscale bond linking NCTs together into large superlattices. Indeed, with appropriate thermal annealing, NCTs can even form crystalline lattices with long-range ordering.

Each nanoscale NCT-NCT bond within these lattices is a multivalent structural feature, where the multivalency number (N) is the number of monovalent DAP-Thy complexes that act in a coordinated manner when two adjacent NCTs form an interparticle bond.[225,226] As a result, the free

energy driving NCT assembly can be regulated by modifying NCT structure at either the molecular or nanometer length scales; the former controls the strength of each individual monovalent supramolecular complex, while the latter regulates how many supramolecular interactions constitute a multivalent NCT-NCT bond. These synthetically independent design handles at different size regimes make NCTs ideal for exploring how both nanoparticle assembly and the multivalency of individual NCT-NCT bonds are affected by changes in structure at both the chemical and nanometer length scales. The ability to rationally program multivalency as a function of nanoscale structural features is therefore the first step in understanding and using this systems-level approach to materials design.

Initial work has demonstrated that the collective binding enthalpy of an NCT-NCT bond is significantly greater than an individual DAP-Thy complex,[222] a hallmark of a multivalent interaction. However, the calculated values of multivalency for these NCT systems are surprisingly low. For example, NCTs consisting of 26 nm particle cores functionalized with ~1000 polymer chains exhibit a multivalency value of only 10. While it is possible that each multivalent NCT-NCT bond consists of only 10 DAP-Thy complexes, the high local concentration of 100s of DAP and Thy groups between particles makes this explanation of a low multivalency number unlikely. An alternative reason for this low value of *N* could be that the total number of DAP-Thy complexes comprising each NCT-NCT bond is significantly greater than 10, but there exists a structural feature in between the nanoscale shape of the NCT and the individual molecular groups that regulates the number of complexes that can act in a coordinated, multivalent manner. More simply, each NCT-NCT bond consists of a large number of DAP-Thy complexes, but these complexes are arranged in tiny "bundles", and only complexes within a single bundle could be considered to be multivalent (**Figure 3-2**, right panel). Prior work has demonstrated that given an appropriate driving force, small molecule ligands on the surface of nanoparticles will indeed bundle together.[227,228] Similarly, polymer brushes on nanoparticles have also been shown to engage in bundling when exposed to a strong antisolvent.[229] Based on these prior observations, we hypothesize that the driving force behind bundling of supramolecular complexes here could be differences in the chemical potential between individual DAP and Thy groups and the surrounding solvent molecules. Nonpolar polymers modified with telechelic polar moieties are known to form reverse micelles in low polarity solvents (**Figure S2-11.** DLS measurements of polymer chains in toluene at 5 mg/ mL concentration. The Blank PS curve refers to the 12k polystyrene sample

without any supramolecular functional group (overlaps with the sample containing supramolecular groups in 100% toluene). The other measurements are of mixtures of the 12k DAP and 12k Thy polymers in varying solvent compositions. Each curve was normalized to the small radius peak.), which would be consistent with small clusters forming at the ends of the polymer brush.[230] If such bundling were indeed dictating the multivalency in these NCT systems, the presence of these "bundle bonds" would therefore represent a systems-level emergent phenomenon where the

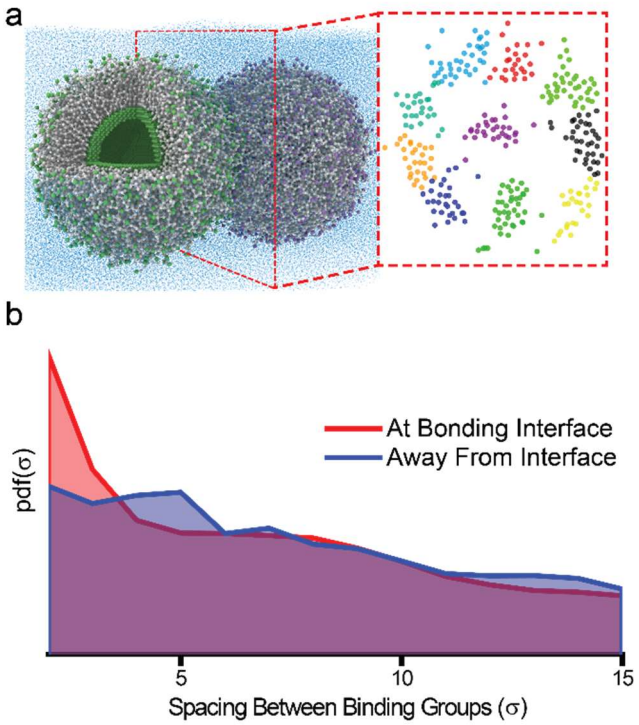

Figure 3-2. Molecular dynamics simulations of NCT assembly. (a) The equilibrium structure of modeled NCTs shows the presence of bundles that emerge at the interface of two complementary NCTs. The dots in the inset denote positions of individual supramolecular groups at the NCT-NCT interface; the different colors denote algorithmically defined bundles that dictate the degree of multivalency (see SI for clustering analysis). (b) A pair distribution function (PDF) analysis of the distance between supramolecular groups both at and away from the NCT-NCT interface. At the interface, the supramolecular binding groups associate into bundles, resulting in a distinct spike in the PDF, which corresponds with the radius of the bundles. The absence of this peak away from the interface confirms that it is the act of forming the nanoscale NCT-NCT bond that drives formation of this emergent structural feature.

nanoscale sizes and shapes of the NCT could be used to regulate thermodynamics of supramolecular complexation.

Because the positions of individual chain ends on an NCT cannot be readily measured due to their small size, their poor electron density contrast with the surrounding polymer and solvent, the presence of the significantly larger and more electron dense nanoparticle cores, and the transient nature of supramolecular complexes, the bundle bond hypothesis was first examined using molecular dynamics simulations to determine the most probable arrangement of individual DAP-Thy complexes within a multivalent NCT-NCT bond (**Figure 3-2**). A full atomistic description of NCTs would be computationally prohibitive, but a coarse-grained model with a consistent mapping of the geometry, volume fraction, and interaction parameters between experiments and simulations (see SI for details, **Figure S2-12**, **Figure S2-20**) is sufficient to provide insight into the configuration of the multivalent NCT-NCT bond interface.[227,228]

In a typical simulation where a pair of complementary NCTs is allowed to reach equilibrium, DAP and Thy groups that are not part of a supramolecular complex are randomly positioned at the periphery of the particles. However, DAP-Thy complexes that are part of a multivalent NCT-NCT bond do indeed coalesce into "bundles" that dynamically change shape throughout the simulation (**Figure 3-2a**, **Figure S2-13-15**). Thus, each multivalent NCT-NCT bond consists of multiple "bundle bonds", where the degree of multivalency is determined by the number of DAP-Thy complexes that comprise a single bundle. Because the bundles are only found at the interface of NCTs connected via a multivalent NCT-NCT bond (**Figure 3-2b**), these data not only confirm the presence of the bundle bonds, but also demonstrate that it is the act of forming a nanoscale NCT-NCT bond *itself* that drives supramolecular bundle formation. NCTs therefore present a previously unexplored opportunity to systematically study how nanoscale structure can be used to modulate molecular multivalency.

It is also important to note that this bundling behavior is distinct from previous examples of spontaneous symmetry breaking in the ligands of nanoparticles being assembled. These differences stem from the fact that the bundles of supramolecular complexes observed here are significantly smaller than the cross-section of the overall NCT-NCT bond, and any given NCT-NCT bond therefore consists of multiple bundles. Moreover, the DAP-Thy connections are dynamic, and the exact sizes and shapes of the bundles are constantly changing. As a result, the bundling phenomenon is not entirely identical to the "patchiness" observed in other systems such

as those that are anisotropically functionalized[229,231] or that form soft skyrmions via ligand rearrangement,[232] as the overall surface of the NCT would still be considered to be largely isotropic even with the bundling phenomena occurring (*vide infra*). This distinction means that NCTs are affecting material structuring at a level *in between* an individual molecular bond and an overall nanoparticle structure. The obvious question that therefore arises is whether design handles at both the molecular and nanoscale can be used in conjunction to modulate the collective size and dynamic behavior of these bundle bonds.

3.2 Thermodynamics of NCT Assembly

In order to properly answer this question, it is important to understand how the thermodynamics of NCT assembly change as a function of different nanoscale structural features. In a standard multivalent bond between NCTs, the strength of each supramolecular complex (each monovalent binding event) is described by the free energy equation:

$$\Delta G_s = \Delta H_s - T\Delta S_s \quad (1)$$

where ΔG_s, ΔH_s, and ΔS_s are the Gibbs free energy, enthalpy, and entropy associated with the formation of a single DAP-Thy complex. The strength of a multivalent "bundle bond" is therefore:

$$\Delta G_m = \Delta H_m - T\Delta S_m \quad (2)$$

where ΔG_m, ΔH_m, and ΔS_m are the Gibbs free energy, enthalpy, and entropy of the collective bundle. By definition, the ratio between the enthalpy values of these reactions is the value of multivalency (i.e. $N = \Delta H_m/\Delta H_s$). More simply, the multivalency number N is the average number of groups within a given bundle.

The most significant contribution to ΔH_m is expected to be the hydrogen bonds formed between DAP-Thy pairs, as these are by far the strongest types of interactions involved in the formation of a DAP-Thy complex. Additional enthalpic contributions such as dispersion forces or polymer mixing within the brush may also be possible, but these are expected to play a much smaller role in dictating the thermodynamics of NCT assembly due to the fact that they are significantly weaker than the hydrogen bonding interactions (additional discussion in SI). The most significant contribution to ΔS_m is expected to come from the reduction in polymer configurations upon forming a DAP-Thy complex that restricts the motion of the two adjoined polymer chains.

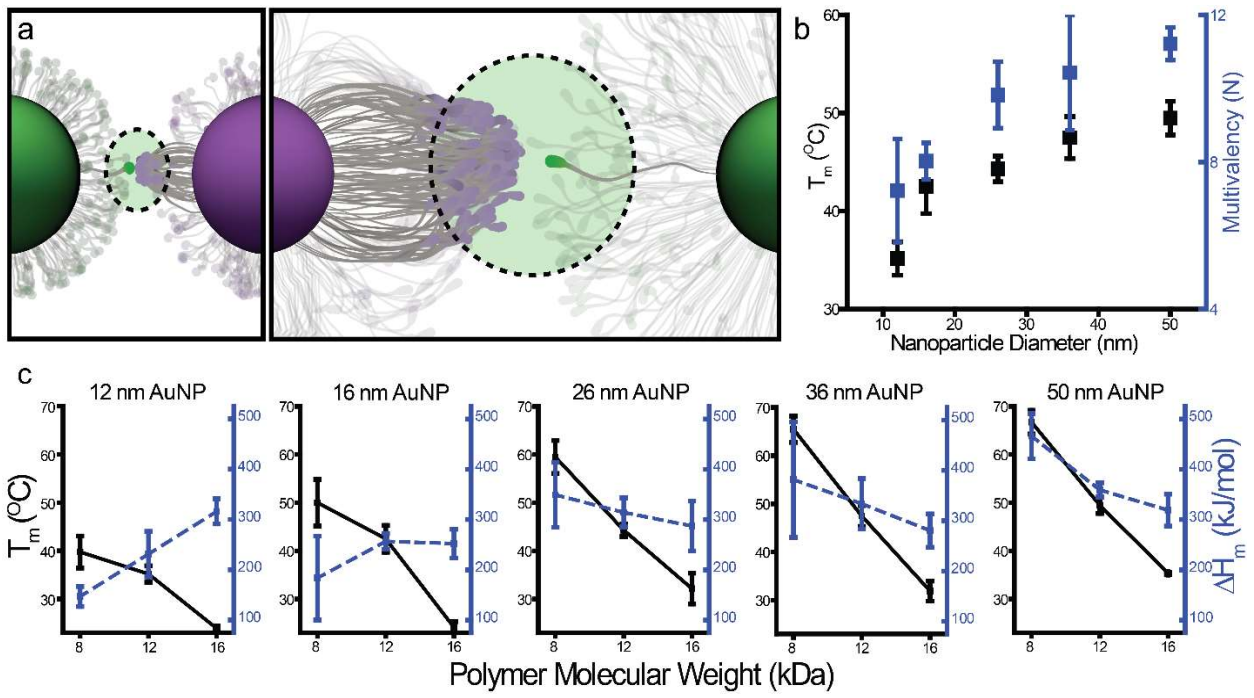

Figure 3-3. Thermodynamics of bundle bond formation are controlled via nanoscale design handles. (a) The thermodynamics of bundle bond formation are dictated by the number of supramolecular groups that can cluster together, as well as the entropy penalty associated with confining polymer chain motion upon forming a supramolecular complex. In the case of a smaller particle with a short polymer the number of supramolecular bonds is limited (left). When a longer polymer is used (right) the multivalency increases, but with an added entropic penalty. (b) Thermal melt analysis shows increases in ΔH_m and T_m with increasing nanoparticle diameter (decreased particle curvature). A decrease in NCT curvature results in a higher density of supramolecular binding groups, and therefore a larger number of hydrogen bonds can bundle together (c) NCT T_m decreases with increasing polymer length for all particle sizes examined (black traces), but the collective ΔH_m of the bonds either increases or decreases depending on the inorganic particle core diameter (blue traces).

The value of ΔH_s for each DAP-Thy complex within a bundle bond can be assumed to be constant based on prior evidence in simpler molecular systems.[225] Thus, ΔH_m should be ΔH_s multiplied by the number of DAP-Thy complexes that comprise a bundle bond (i.e. $\Delta H_m = N\Delta H_s$). However, ΔS_s is not equivalent for all polymers within a bundle bond, as different polymers will have different amounts of conformational confinement upon the formation of a DAP-Thy complex, depending

on where they are anchored on the surface of the nanoparticle core. As a result, expressing the value of ΔG_m as a function of N, ΔH_s, and ΔS_s becomes:

$$\Delta G_m = N(\Delta H_s) - T\left(\sum_i^N \Delta S_i\right) \quad (3)$$

where values of ΔS_i are the entropy changes associated with the different polymer linkers being tethered together via DAP-Thy complexes. As noted above, while there may be additional contributions to this simple approximation, such thermodynamic parameters are small enough so as to not significantly affect the conclusions drawn here, and these assumptions should hold for systems like the NCTs that possess long ligands and directional enthalpic interactions.[233,234]

Based on these thermodynamic parameters, a "bundle bond" therefore represents a collection of DAP and Thy groups where the entropy penalty for linking any given pair of polymer chains comprising that bundle is less than the strength of the DAP-Thy complex that is formed. In other words, if a polymer chain has to stretch so much to become a part of a bundle that the $T\Delta S_i$ is greater than ΔH_s, that polymer will not be a part of that multivalent bundle.

This interplay between enthalpy and entropy explains why bundles of DAP and Thy groups only emerge within an NCT-NCT bond, as the enthalpy benefit of generating a supramolecular complex is necessary to offset the entropic penalty of restricting polymer motion; the reduced chemical potential of clustering the polar head groups is not enough on its own to drive this behavior. Additionally, it indicates that changes to NCT structure at the nanoscale should affect multivalency by altering the extent to which polymer chain conformations are restricted upon formation of a bundle bond. Therefore, because the design of NCTs can be easily varied, a series of well controlled experiments can provide further support of the bundle bond hypothesis, and provide insights into the relationship between nanoscale structure and multivalency.

For example, changing the nanoscale shape of an NCT by modifying particle core diameter is observed to increase the temperature at which NCT-NCT bonds break, as well as values of N and ΔH_m. The thermodynamics of NCTs were studied by monitoring the dissociation of particles with UV-Vis spectroscopy, and the resulting thermal transition was fit to the Van't Hoff equation to extrapolate relevant thermodynamics values (see supporting information, Figs S6, S7, S20 for further details).[158] The increase in T_m and ΔH_m with increasing nanoparticle core diameter can be explained as a function of changes to particle nanoscale curvature. When two curved surfaces approach one another, different sets of points on the opposing surfaces are not necessarily

equidistant. Additionally, the polymer chains extending perpendicularly from the curved surface are not all initially aligned in the same direction as the NCT-NCT bond (**Figure 3-3a**, left). As a result, polymer chains further from the NCT-NCT bond axis need to stretch in order to form a DAP-Thy complex, while polymers directly at the center of the bond will likely compress in order to allow more polymer chain ends to reach one another and form supramolecular complexes (**Figure 3-3**a, right).The more curved the particle surface, the greater the variation in compression and stretching as a function of where the polymers are grafted to the surface. The values of ΔS_i resulting from tethering polymer chains via a supramolecular complex would therefore be expected to vary more as a function of lateral distance between binders when NCT particle cores have more curved surfaces. As a result, lowering particle curvature by increasing particle diameter enables a larger number of polymer chains to bundle together and act multivalently. In other words, the value of N at which $\sum_i^N \Delta S_i$ overcomes ΔH_m is higher for larger diameter cores. This larger value of N correlates to larger bundle bonds and (based on equation 3) explains the fact that values of ΔH_m and T_m increase with particle core size, asymptotically approaching the limit corresponding to a flat surface (**Figure 3-3b**).

Increasing the height of the polymer brush can also use nanoscale geometric influence to modify NCT bonding thermodynamics, but would be expected to have more complex effects on multivalency and bundle bond formation. As polymer length increases, the number of conformations (and thus entropy) of each polymer chain should also increase. This means that tethering two longer polymer chains together should result in a larger entropy penalty, indicating that the value of N at which $\Sigma T\Delta S_i$ exceeds ΔH_m should decrease, resulting in lower T_m. Experiments demonstrate that T_m does indeed decrease with increasing polymer length for all systems studied (**Figure 3-3c**). However, while NCTs with larger particle diameters (26, 36, 50 nm) also show a corresponding decrease in N, NCTs with smaller particle diameters (12 and 16 nm) exhibit values of N that instead *increase* with increasing polymer length.

These data indicate that the number of DAP-Thy complexes that comprise a bundle bond is actually increasing, which can be explained as a function of polymer packing density. Short polymers grafted onto particles form a dense concentrated brush, but longer polymers extend further off of the particle surface into a semidilute brush regime.[99,115] The transition from the concentrated to semidilute regimes is dependent on the degree of particle curvature, with larger

spheres requiring longer polymer lengths to become semidilute. Polymer chain ends in this semidilute regime can occupy a greater number of conformations, which in turn allows a greater number of DAP groups to bind to complementary Thy groups on adjacent particles (**Figure 3-3a**). However, this would also mean that, when comparing two NCT systems with the same bundle bond size, smaller particle cores would require greater amounts of polymer chain confinement in order to form the bundles. These opposing thermodynamic effects explain the contrasting trends in ΔH_m as a function of polymer length on small and large nanoparticle cores. The greater surface curvature of the small cores inherently allows for more polymer flexibility and enables the formation of larger bundle bonds with increasing polymer length (increasing ΔH_m and N), but also requires greater polymer deformation to form these bundles (larger values of ΔS_i, which results in a decreased T_m despite the larger N).

3.3 Saturating Multivalency in Bundles

In order to further show that the multivalent behavior observed in NCTs is an effect of nanostructure-induced bundle bonds and not just an increased local concentration of DAP and Thy groups at the particle surface, NCTs were co-loaded with controlled ratios of "active" polymers terminating in a supramolecular binding group and "inert" polymers without any such functionality (**Figure S2-9-10**). In conventional model systems that explain multivalency solely due to increased local concentration of binding groups, reducing the number of active chains would be predicted to lower the degree of multivalency. However, in the NCT system, the values of N and ΔH_m did not exhibit any significant change as a function of density of DAP and Thy groups (**Figure 3-4a**, **Figure S2-10**). These unexpected results imply that, above a critical fraction of active polymer chains, the local bonding structure of an NCT-NCT connection must be constant, meaning that the size and the shapes of the bundle bonds do not change as a function of the number of "active" polymers within the range studied. The lower melting temperatures for the coloaded samples must therefore arise from a greater polymer entropy penalty for NCT bonding, as greater deformation would be required to maintain a constant multivalency. The importance of this finding is to reiterate the initial discovery that the act of forming a nanoscale bond results in an emergent structure (the bundle bond), where this new structural motif is the determinant factor of the entire system's multivalency. The data and simulations presented above therefore indicate that the degree

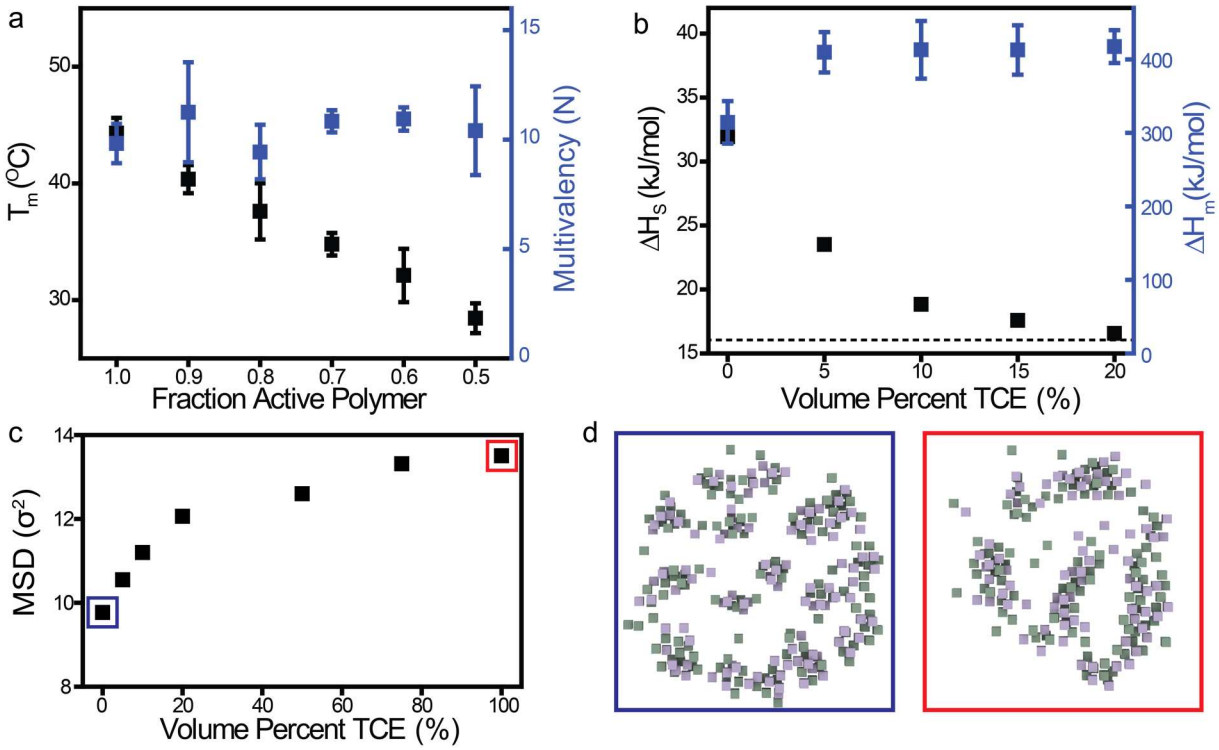

Figure 3-4. NCTs exhibit a maximum multivalency, implying saturated bonding behavior. (a) Decreasing the fraction of polymer chains that have a supramolecular binding group decreases NCT Tm, but with no significant change in ΔH_m. (b) Bundling is hypothesized to originate from the polar supramolecular binding groups phase segregating from the nonpolar toluene solvent. Introducing a polar solvent weakens individual supramolecular bonds (black data, dotted line represents the DAP-Thy binding strength in 100% TCE), but surprisingly increases the binding enthalpy for the collective NCT-NCT interaction (blue data). (c) Molecular dynamics simulations show that increasing solvent polarity decreases the restrictive effect on the supramolecular binding groups. This can be quantified by measuring the mean square displacement (MSD) of the binding groups, which is shown to increase with increasing TCE. (d) Positions of supramolecular groups at a modeled NCT-NCT interface show smaller, less multivalent bundles in low polarity solvent (blue), and larger, more diffuse bundles in higher polarity solvent (red).

of multivalency in an NCT-NCT bond is indeed a complex interplay of building block structure across length scales, and that nanoscale structure can be used to modulate bundle bond behavior. Nevertheless, because each bundle bond still consists of multiple individual supramolecular complexes, it is also important to consider the effects of altering the molecular composition of the

system. While this can be achieved via chemical alterations to the DAP or Thy complexes (as has been examined in previous molecular models[235]), it is also possible to modify the overall structure and chemical behavior of an NCT via alterations to the solvent environment. Individual hydrogen bonding interactions typically weaken in more polar solvents, which would be expected to reduce the value of ΔH_s.[236] However, the chemical potential between DAP and Thy groups and their local environment would also decrease when increasing solvent polarity, reducing the driving force for forming the bundles, which could lead to larger bundle bonds and greater multivalency.[230]

Variable temperature NMR experiments performed on small molecule DAP and Thy analogues demonstrate that adding a more polar solvent (1,1,2,2-tetrachloroethane, TCE) does indeed decrease ΔH_s for individual DAP-Thy complexes. This enthalpy change reaches a minimum value at ~20% TCE, due to preferential solvation[237,238] of the moderately polar DAP-Thy complex (**Figure S2-18-19**). However, although ΔH_s decreases with increasing solvent polarity, the collective ΔH_m of an NCT bond actually increases when TCE is added (**Figure 3-4b**). Because each individual hydrogen bond is weaker, the increase in ΔH_m indicates that N must dramatically increase in the more polar solvent: bundles in the more polar solvents exhibit multivalencies up to ~250% of their value in pure toluene (N = 10 in toluene but 25 in 20% TCE for the system in **Figure 3-4b**). Simulations confirm that adding TCE increases both average bundle bond size and the rate at which DAP-Thy complexes exchange between adjacent bundles (**Figure S2-16-17**). This enhanced mobility affords each supramolecular group a greater number of counterparts on a neighboring particle with which it can complex, enhancing NCT multivalency (**Figure 3-4c, d**). Thus, although each individual hydrogen bond weakens with increased solvent polarity, the increased multivalency results in higher collective binding strength between NCTs. As a result, the hierarchical ordering of an NCT-NCT bond is dictated (and can be controlled) by a complex and integrated set of design variables across multiple size regimes. Alterations to molecular composition of the solvent change the enthalpic driving force for bundle bond formation, while alterations to NCT nanoscale structure alter its associated entropic penalty. NCTs therefore represent a multivalent supramolecular system that, just like natural systems, can only be regulated and understood by considering material structure at the molecular and nanoscale simultaneously.

3.4 Manipulating Nanoscale Structure via Control over Multivalency

Importantly, the fundamental understanding of NCT bond behavior from the experiments above potentially allows for the development of new design principles for systems-level control of assembly as a function of these integrated molecular and nanoscale handles. Prior work has shown that NCTs with symmetric particle sizes and polymer lengths form ordered, crystalline CsCl-type lattices upon thermal annealing.[222] A crystalline lattice is hypothesized to be the thermodynamically favored state because it maximizes the number of NCT bonds that can form and minimizes the entropic penalty associated with polymer confinement upon binding. This implies that manipulating the overall morphology of the "bundled" bonds could allow new phases to be achieved, as these enthalpic and entropic factors that determine which crystal phase is thermodynamically preferred are inherently linked to the sizes and shapes of the bundles. As a result, alterations to nanoscale NCT architecture could be used to regulate both the thermodynamics of supramolecular complex formation and the mesoscale coordination environment of particles within a lattice.

For example, an asymmetric NCT system consisting of complementary large (20 nm diameter core and 12 kDa polymer) and small (12.5 nm core and 7 kDa polymer) NCTs was found to assemble into a lattice isostructural with Th_3P_4 after thermal annealing. The formation of this lattice symmetry is surprising, since it has a lower nanoparticle valency and thus fewer interparticle connections than CsCl-type lattices. It has been postulated in other nanoparticle assembly methods[239,240] that the Th_3P_4 phase is favored over CsCl because it alleviates strain in linkers that are sterically limited in their mobility. This strain on the ligands induced by assembly also connects to the previously described bundling behavior, as increasing polymer strain correlates negatively with the amount of multivalency. In toluene, the strong driving force for segregation of the DAP and Thy groups drives the formation of small bundles ($N \sim 10$ as shown above), which restrict the motion of the supramolecular binding groups. Increasing the solvent polarity would be expected to increase molecular bond mobility and soften nanoscale polymer coronae, expanding the size of the supramolecular bundle bonds and increasing the multivalency of the NCT. In more polar solvents, the higher enthalpic driving force from the collective supramolecular interaction should

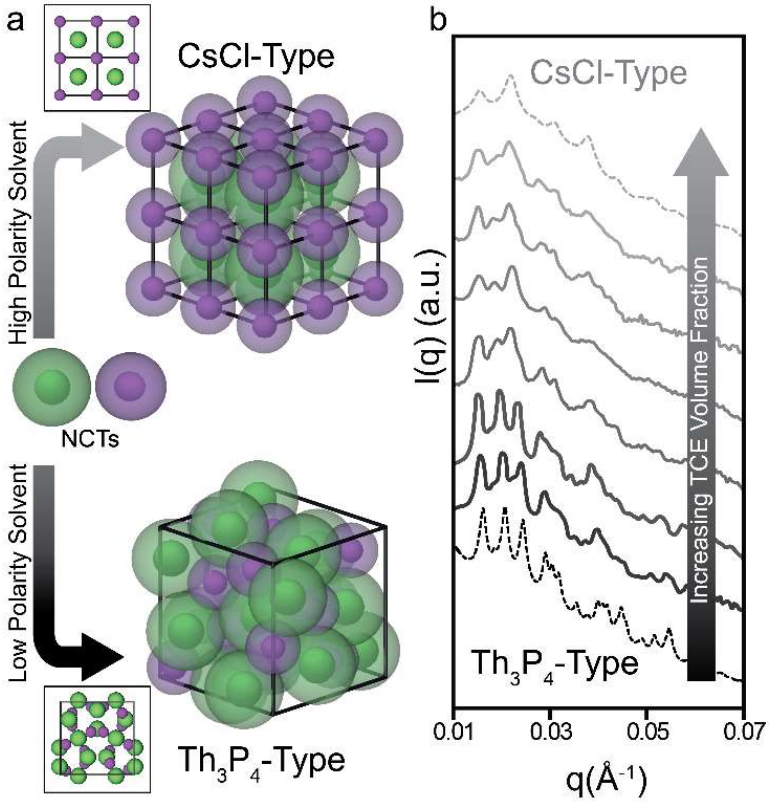

Figure 3-5. Solvent composition manipulates NCT superlattice crystal structure. (a) Schematic diagram showing the unit cell of a Th_3P_4-type NCT superlattice and 8 unit cells of CsCl-Type lattices, which occupy a similar volume. (b) Small angle x-ray scattering measurements of NCT superlattices in toluene with 0 to 10 volume percent 1,1,2,2 tetrachloroethane (TCE) as a cosolvent. The top and bottom dashed patterns are simulated. Increasing TCE modulates the bundle bond size, which then alters the resulting mesoscale structure of the NCTs.

be able to overcome the entropy penalty of straining the polymers, and favor an alternate superlattice structure. To clarify, the collective supramolecular interaction of multiple molecular binding groups arranged around a nanoscale scaffold would result in a mesoscale superlattice architecture, but this mesoscale organization would also control the amount of nanoscale polymer reorganization needed to maintain the lattice, thereby affecting the supramolecular bundle sizes and thus collective molecular thermodynamics—a true "systems" approach to material design (**Figure 3-1**).

Adding TCE to NCT solutions during thermal annealing does indeed favor the formation of the 4% denser CsCl lattice (**Figure 3-5**), demonstrating that a single set of NCT building blocks can be driven down two different assembly pathways using solely changes to solvent composition. The

significance of this result is that the hierarchical ordering in this system cannot be predetermined by simply summing up the interactions of individual molecular binding groups, or considering the larger lattices and NCT bonds to be just a consequence of the behavior of individual molecules. Rather, these structures are indeed an example of a systems-level design process, where the morphology at each length scale (molecular, nano, and meso) is both an effect and a cause of behavior at the others.

It is important to again note that this system-derived change in NCT coordination environment is different than prior particle assembly schemes that use "patchy" particles[229,231,241]. These methods typically control particle coordination numbers by breaking the overall symmetry of the ligand shell around a particle. Here, the overall ligand shell surrounding the particles remains largely isotropic at the nanoscale, as each NCT-NCT bond consists of multiple emergent bundle bonds that are smaller than the length scale of the collective NCT-NCT interactions. Instead of altering the nanoscale symmetry of the particle building blocks, these bundles regulate the degree of multivalency to dictate the equilibrium lattice symmetry. The formation of these two unique superlattices and the ability to drive a single set of NCT building blocks to either crystallographic symmetry therefore demonstrates the potential for materials design using a combination of integrated handles across multiple size regimes.

In order to fully mimic the complexity of naturally occurring materials made via directed assembly, it is imperative to understand how the interactions between design features at multiple length scales dictate material structure. The systems-level design methodology presented here represents a unique platform for exploring the thermodynamics of multivalent behavior in a manner that is more similar to a natural system than a simple molecular model. While this work focuses on the first steps of controlling material structure and molecular assembly in a systems-level approach, the modularity of the NCT design potentially allows future exploration of different design handles (e.g. polymer compositions, supramolecular binding group structures, particle shapes) to further imitate and explore many different types of multivalent natural systems that use nanoscale structure to modulate their behavior and hierarchical ordering across multiple length scales. The understanding gained from the experiments performed here and these future investigations is critical for multiple fields where materials require sophisticated structures and interactions between features at the molecular, nano-, and macroscopic length scales, including catalysis, interface science, and biomimetics. Studying the interplay between molecular makeup and

nanoscale spatial organization therefore presents a powerful opportunity for programming hierarchical ordering and material behavior beyond the limitations of current reductionist design approaches.

Chapter 4. Assembling Ordered Crystals with Disperse Building Blocks

Adapted from Santos, P. J.; Cheung, T. C.; Macfarlane, R. J. Assembling Ordered Crystals with Disperse Building Blocks. *Nano Lett.* **2019**, *19* (8), 5774–5780. https://doi.org/10.1021/acs.nanolett.9b02508.

Colloidal crystallization is an effective means of manipulating material structure at the nanometer length scale, as chemical interactions between nanoparticle building blocks can be used to program their assembly into ordered lattices.[242,243] A wide variety of surface ligands have been used to control these interactions and thereby manipulate particle assembly, where the most stable phases typically maximize either particle packing density or the number of favorable interactions between particles' surface ligands.[244,245] In all of these strategies, particle size and shape dispersity are regarded as a negative factor that must be overcome to create well-ordered crystals, as irregularity in building block shape results in inefficient packing and limitations to interparticle surface contacts.[133,246,247] As a result, many impressive strategies to minimize dispersity in the particle assembly process have been developed, including multiple techniques for the synthesis of monodisperse particles of different shapes,[36,248,249] the use of biopolymer cages to dictate the directionality of interparticle bond formation,[168,250] or even the use of molecularly precise biomacromolecules with controlled surface functionalization as colloidal building blocks.[251–253] However, all of these methods have limits in the composition of the particles that can be used, and tend to result in a trade-off between the quality and quantity of the building blocks that can be made. In contrast to colloidal crystallization approaches that aim to use the least disperse building blocks possible, we have recently reported a new self-assembling particle called the Nanocomposite Tecton (NCT), which uses inherently non-uniform synthetic polymers as surface ligands (**Figure 4-1**).[222] Interestingly, although NCTs have dispersity originating from both their nanoparticle core and their polymer brush, they can still form lattices with long-range order. We hypothesize that the ability of NCTs to spontaneously form crystalline lattices despite their inherent size and shape inhomogeneity arises from the ability of the polymer brush to easily deform as a means of maximizing favorable supramolecular interactions between particles.

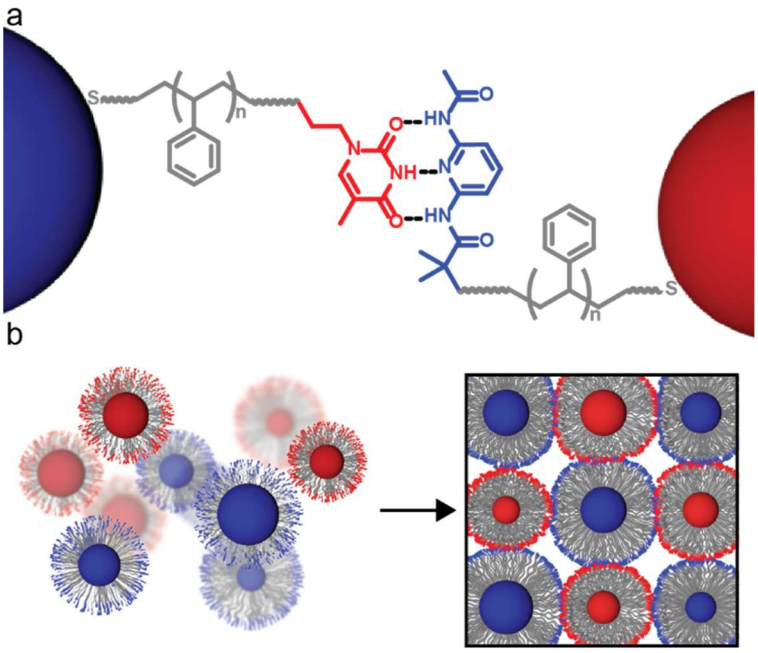

Figure 4-1. Nanocomposite Tecton assembly scheme. a. NCTs consist of a nanoparticle core, a polymer shell, and a supramolecular binding group. When complementary NCTs are combined, hydrogen bonds form between them to drive assembly. b. Particles containing a soft, polymeric shell are more tolerant of dispersity, and when coupled with an enthalpic driving force they can crystallize into well-organized structures.

Thus, the establishment of appropriate design and processing strategies could enable these "soft" building blocks to overcome significant variations in either particle core size or ligand length.[141,254,255] Here we explain how the concept of ligand softness affects the processing pathways used to obtain NCT-based colloidal crystals, as well as how these highly deformable surface ligands can mask imperfections in particle size or shape during assembly.[256] Ultimately, this strategy allows for highly disperse nanoparticle components (up to 23% variation in particle core diameter) to form superlattice architectures without any reduction in crystal quality, well beyond the ~2-10% limit that is typically required for maximizing the quality of other colloidal crystals. As a result, NCTs represent a unique building block for nanomaterials synthesis that has significant potential for making scalable particle-based materials.

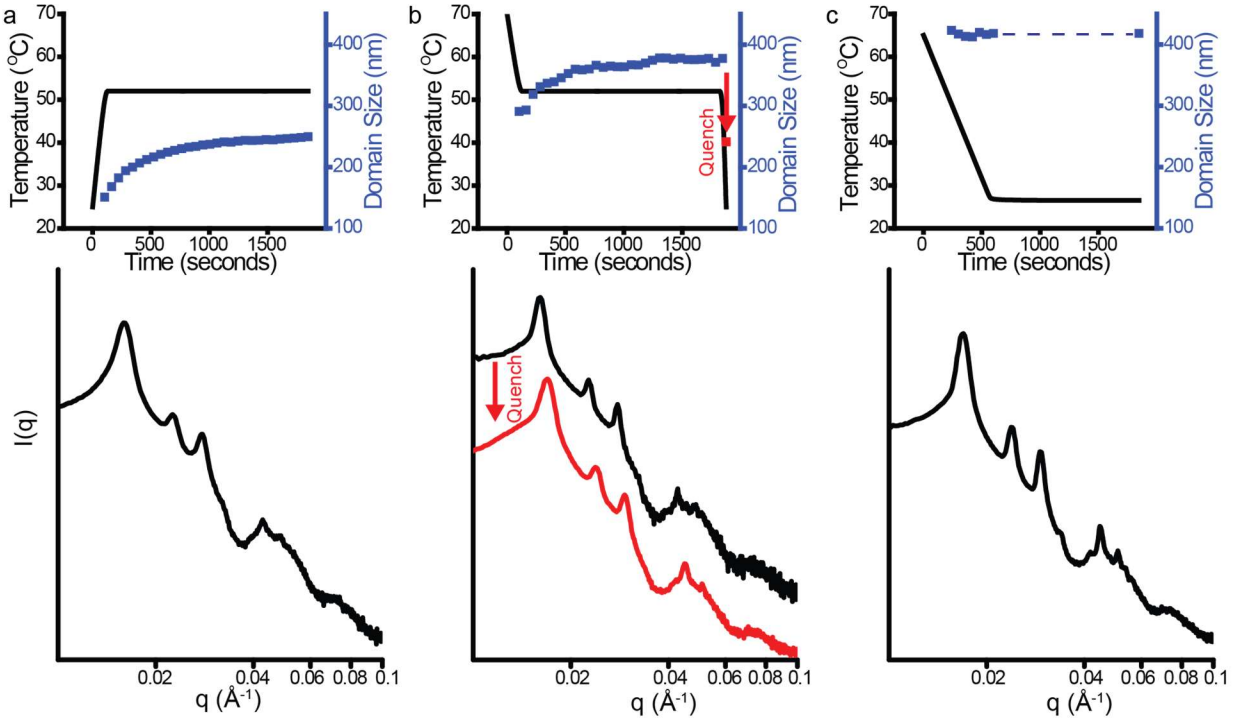

Figure 4-2. In-situ SAXS measurements of NCT crystallization. a. Temperature profile of NCTs heated from room temperature to their Tm, and held there while they crystallize (black trace). Annealing results in a gradual increase in domain size, as estimated by the Scherrer equation, but after a 30 minute treatment the crystal quality is still poor (blue data points). b. When NCTs are cooled from an elevated temperature, the nucleation and growth process results in larger crystalline domains. However, further quenching from Tm to room temperature causes the formation of additional amorphous phase aggregates from unassembled NCTs. c. Cooling the NCTs from an elevated temperature at 4 °C/min results in highly ordered crystals at all temperatures.

4.1 Kinetics of NCT Assembly

The NCTs used in this work consist of gold nanoparticle (AuNP) cores coated with polystyrene brushes (**Figure S3-1**) that terminate in either diaminopyridine (DAP) or thymine (Thy) motifs that constitute a complementary hydrogen bonding pair. When NCTs with complementary supramolecular binding groups are combined, multiple hydrogen bonds form between the particles; these bonding interactions have been demonstrated to drive the formation of bcc-type superlattices when the NCTs are thermally annealed.[222] NCTs are amenable to thermal annealing because the hydrogen bonding is relatively weak, and so heating to mild temperatures (below 80 ^{O}C) is sufficient to break the bonds and enable rearrangement. Given the inherent dispersity in

both the particle sizes and shapes (previous work has demonstrated crystals for particle sizes with a relative standard deviation (RSD) of 15% and polymers with Đ of ~1.1), the ability of NCTs to adopt conformations with long-range order is somewhat surprising. Understanding and controlling how these soft, high dispersity polymer shells affect crystallization therefore requires first determining how crystal formation is affected by processing pathway, as well as any upper bound in crystal quality that may be imposed on these assembled lattices via the use of a non-uniform and deformable polymer ligand coating.

The simplest potential thermal annealing profile to generate ordered NCT arrays is to heat and hold the initially amorphous aggregates at a temperature close to their melting temperature (T_m),[257] analogous to recrystallization and grain growth processes in classical atomic systems (**Figure 4-2a**).[258] When this thermal annealing profile is used, the NCTs are able to form an ordered lattice, but small angle x-ray scattering (SAXS) data indicate that this annealing profile results in highly polycrystalline samples with small grain sizes ~250 nm in diameter. The small average size of these grains is not entirely unexpected, as the dispersity of the polymer brush heights and the flexibility of the polymer chains means that the number of DAP-Thy complexes that can form in a perfectly ordered state and a kinetically trapped state should be similar. Because the driving force for assembling NCTs is the formation of supramolecular complexes, the energy difference between these two states with similar numbers of hydrogen bonds would be predicted to be relatively small, reducing the thermodynamic force for forming large crystallites.

To avoid the formation of the kinetic traps that limit crystal grain size, an alternate annealing pathway would be to heat the NCTs until completely melted, then drop the solution to just below the T_m and hold the NCTs in this state until crystal formation is complete (**Figure 4-2b**). This thermal profile should grow large, high quality crystals because quenching the sample just below its melting temperature suppresses the number of nucleation events, resulting in a small number of initial crystallites that grow to form large grains. Indeed, this formation pathway is commonly used to generate large atomic or molecular crystals.[259] However, while the initial aggregates that formed immediately below T_m were more crystalline than the samples heated from room temperature, quenching from this high T (to 25 °C) resulted in a noticeable reduction in crystal quality (as indicated by the broader peaks in the SAXS pattern). This reduction in quality stems from the fact that NCTs exist in equilibrium between their assembled and melted state across a large thermal window; this broad melting transition arises from the multivalent nature of the

bonding interactions between particles (**Figure S3-5**).[158,170] Therefore, to give the largest domains, the NCT solution must be brought into equilibrium at each temperature between the fully melted and fully aggregated states. Interestingly, when the NCTs are slowly cooled across this thermal window, the resulting crystals exhibit a sharper SAXS diffraction pattern corresponding to larger grain sizes (~400 nm), but these crystal sizes reach a maximum early in the transition and only become more numerous instead of larger (**Figure S3-7a**). This upper limit on domain size is likely due to the fact that crystallites of a given mass can be observed to precipitate out of solution; while some small amounts of additional growth may occur due to individual NCTs attaching to these precipitated structures, grain growth rates are limited compared to the solution-suspended aggregates. Therefore, at temperatures within the thermal window between the fully aggregated and fully melted state, there exists an equilibrium between free NCTs dispersed in solution and precipitated aggregates that are unlikely to either grow or reorganize, indicating that the crystallite sizes observed in **Figure 4-2c** represent a practical maximum. This limitation in domain size was confirmed by controlling the rate of cooling during NCT crystallization. For cooling rates slower than 8 °C/s, only a slight increase in crystal quality or domain size was observed as cooling rate was decreased (**Figure S3-7**). Nevertheless, the kinetic traps caused by both the dispersity in NCT size and the soft nature of their bonding interactions can be minimized by using solution cooling rate to control the nucleation and growth rates of crystals in solution within this fundamental limit.

4.2 NCTs with Disperse Polymer Brushes

Given that NCT crystallization arises from the formation of multiple DAP and Thy hydrogen bonds, it therefore could be hypothesized that altering the dispersity of the polymer brush height could also affect crystallization by altering the ability of DAP and Thy groups on adjacent particles to form supramolecular complexes. Larger variations in polymer chain lengths across the surface of an NCT would be expected to decrease crystallinity, as they would effectively alter the overall shape of each NCT, and therefore the thermodynamic driving forces for forming ordered arrays. To investigate the effects of polymer dispersity on NCT crystallization, a series of DAP terminated polymers ranging in molecular weight from 10 kDa to 16 kDa, each with $Đ < 1.05$, was synthesized by atom transfer radical polymerization (ATRP).[88] Đ of the NCT polymer brushes was varied by combining these batches of low dispersity polymers in different ratios to obtain polymer blends where the average polymer length remained constant at ~12 kDa, but the overall values of Đ varied

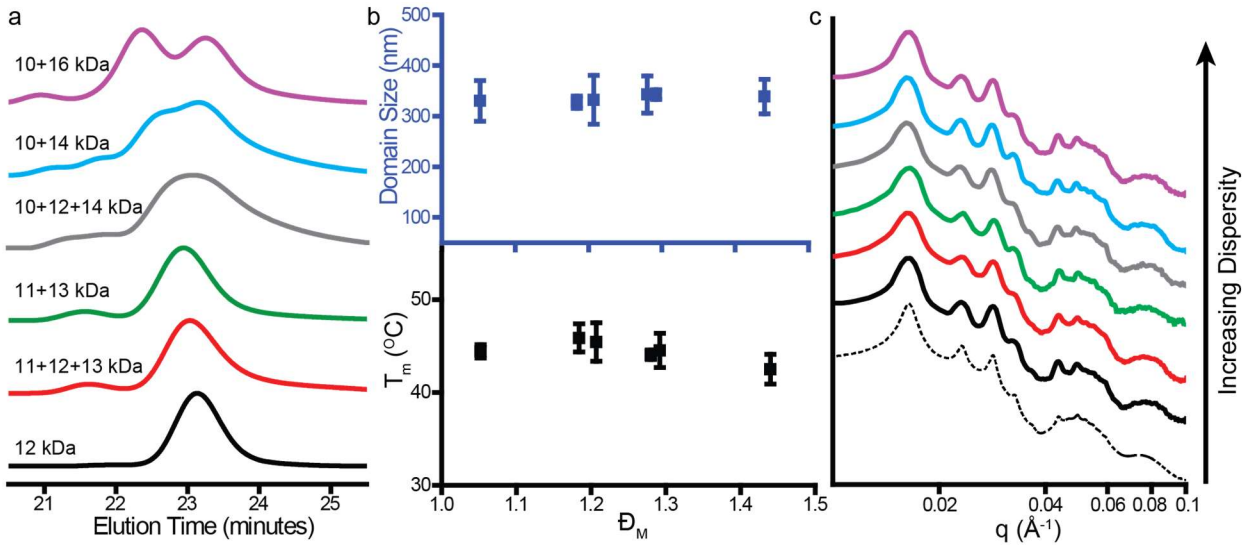

Figure 4-3. NCT assembly is not strongly affected by the dispersity of the polymer shell. a. GPC traces showing the increasingly disperse batches of polymers used in NCT synthesis. All polymer batches have a number average molecular weight of 12 kDa, polymer dispersity is controlled by blending together multiple low dispersity polymers of different molecular weights. b. The melting temperature of the NCTs (bottom), indicative of the strength of NCT-NCT association, does not have a strong relationship with polymer dispersity. Additionally, there is no statistically significant difference in domain size, as estimated by the Scherrer equation (top) for NCTs assembled with polymers of varying dispersity. Error bars represent standard deviations, n = 3. c. SAXS diffraction patterns of NCTs assembled with increasingly disperse polymers. The dashed line is a simulated SAXS diffraction pattern of a bcc crystal structure.

between 1.05 and 1.44 (a value that might be obtained from an uncontrolled free radical polymerization).[260] We would note that control experiments were also performed to ensure that the polymer grafts on the NCTs possessed the same polymer length distributions as the polymer stocks used to functionalize each batch of particles. In other words, the values of Đ for the polymer brushes on each NCT were identical to the values of Đ of the stock solutions (**Figure S3-2**). These samples were then annealed by slowly cooling them from high temperatures to obtain the most ordered lattice possible.

Surprisingly, no correlation between polymer dispersity and crystallinity was observed—all of the samples exhibited indistinguishable SAXS patterns, indicating that the final crystal structures were identical in quality. Even NCTs with a strongly bimodal distribution of polymer lengths showed

no change in their average crystallite domain size, lattice parameter, or degree of long-range ordering (**Figure 4-3b,c**).

Prior theoretical work[261] has described polymer brushes containing chains with varying molecular weight, and can provide an interpretation consistent with the experimental results presented here. Specifically, the preservation of crystallinity suggests the NCTs retain an isotropic configuration, even when loaded with disperse polymer brushes. Prior models and experiments suggest that having high and low molecular weight polymers adjacent to one another is energetically favorable due to a positive entropy of mixing, and therefore no phase segregation or patches of different polymer lengths is expected to occur along the surface of the particle, although there may be differences in the brush conformation.[261–263] More simply, although individual polymer chains lengths can vary, the average brush height remains largely isotropic across the surface of the entire particle.

Nevertheless, individual polymer chains may experience different entropic penalties when confined within an NCT-NCT bond. When adjacent NCTs form DAP-Thy hydrogen bonds, the polymer chains engaged in bonding experience a severe reduction in the number of accessible conformations, resulting in a large decrease in entropy. When an NCT brush consists of polymer chains of varying molecular weight, the magnitude of this change in entropy would be dependent on polymer length, as shorter polymer chains whose ends are not already near the surface of the NCT require additional conformation restriction in order to form hydrogen bonds (i.e. shorter chains need to stretch more to reach their NCT neighbors).

It is therefore surprising that increasing the dispersity of the polymer brush does not affect the binding strength of the NCTs, as indicated by their relatively static T_m regardless of polymer dispersity (**Figure 4-3b**). However, the prior model mentioned above suggests that a polymer brush can minimize its free energy by segregating the chain ends along the brush height coordinate of the system as a function of polymer molecular weight.[261] In other words, it is energetically unfavorable for the longer polymers to bury their chain ends in the interior of the brush, but instead they will on average have their termini further from the surface of the particle than the shorter ones. As a result, interactions between the longest polymer chains on bound NCTs would dominate the thermodynamics of NCT assembly, explaining the lack of significant variation in either crystal quality or melting temperature as a function of brush dispersity.

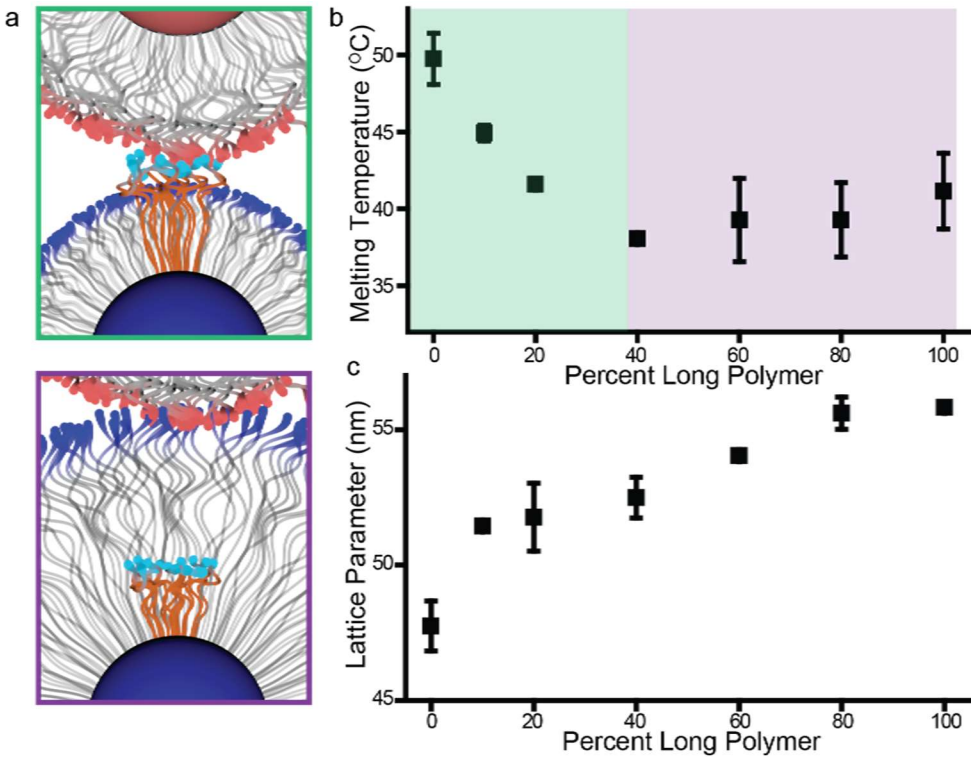

Figure 4-4. Assembling NCTs with bimodal mixtures of long and short polymer chains reveals the dynamics of the polymer brush. a. Polymer chains that are significantly longer than the average brush height are presented at the periphery of the NCT and are thus always able to participate in bonding (top). Conversely, polymer chains that are significantly shorter than the average brush height are buried in the polymer brush and do not readily participate in interparticle bonding (bottom). b. Increasing the fraction of long polymer chains in the bimodal distribution (mixtures of 10 kDa and 16 kDa polymers) decreases the melting temperature of the NCTs, However, when the fraction of long polymer surpasses 40%, the melting temperature plateaus at a value corresponding to the T_m of NCTs functionalized with just the long polymer. This trend suggests the assembly behavior is dominated by only the longer polymer chains. c. Despite the lack of change in T_m above 40% longer polymer, the interparticle spacing consistently increases with the growing fraction of long polymer, signifying the presence of the shorter polymers are still contributing to the overall height of the brush by altering the free volume occupied by the longer polymer chains.

To further verify this hypothesis, NCTs were coloaded with a bimodal mixture of varying fractions of long and short polymer chains. NCTs made with the two different polymers have a stark difference in T_m, (~10 °C difference between the 10 kDa and 16 kDa NCTs), meaning that

monitoring the T_m of NCTs consisting of mixtures of these polymer lengths could potentially indicate which polymer length dictates the strength of inter-NCT bonding (**Figure S3-6**). Interestingly, doping a low molecular weight polymer brush with longer chains has different effects on NCT thermodynamics than doping a high molecular weight brush with shorter polymer chains (**Figure 4-4a**). When shorter polymers are doped into the long-polymer NCTs (right-most data points, **Figure 4-4b**), the T_m remains largely unchanged. This lack of change in T_m is consistent with the hypothesis that shorter chains dispersed among an otherwise high molecular weight brush would be forced to undergo significant stretching to reach the bonding plane between NCTs, and the corresponding entropy penalty associated with this stretching means that it is energetically unfavorable for them to strongly contribute to NCT assembly. Thus, the T_m remains fairly constant with an increasing amount of shorter polymers in a majority long-polymer brush. Alternatively, when longer polymers are added to a low molecular weight brush, the melting temperature quickly drops (left-most data points, **Figure 4-4b**). The supramolecular binding groups on these longer chains are close to the exterior of the NCT, and can readily participate in hydrogen bonding, regardless of the length of the nearby polymer chains. As a result, the height of the brush gradually increases with increasing amounts of longer polymer, as is reflected in the larger lattice parameter (**Figure 4-4c**). The shorter polymers are forced to incur an entropic stretching penalty to participate in bonding, resulting in a lowered T_m. As the necessary degree of stretching increases with a larger fraction of longer polymer, hydrogen bonds between the shorter polymers no longer improve the stability of the lattice. Above this point (~40% long polymer for this system), these longer chains are able to dominate the assembly process, dictating the thermodynamics of NCT assembly (indicating the lack of substantial change in T_m between 40% and 100% long polymer). The observation that longer polymer chains can encapsulate the shorter ones in the brush are in agreement with prior experimental work.[264] Therefore, dispersity in polymer molecular weight has a minimal effect on the overall dimensions of the NCT, as the brush can stretch and compress to account for local variations in polymer length.

4.3 NCTs with Disperse Nanoparticle Cores

While the softness of the polymer brush is observed to aid in NCT crystal formation despite any inherent inhomogeneity in polymer chain length, the nanoparticle core of NCTs is an additional source of dispersity in the NCT architecture, and unlike the polymer brush it is not capable of

dynamically changing its shape. In colloidal crystals formed due to entropically driven close packing, small variations in particle size make the formation of ordered lattices impossible, even in the case of polymer grafted nanoparticles.[265,266] In hard-sphere packing, it has been theoretically calculated and experimentally shown that the order-disorder transition is thermodynamically prohibited above a terminal dispersity between 6 and 11%.[267,268] Prior work has demonstrated that adding bonding interactions that drive lattice formation via enthalpy maximization can enable more disperse building blocks to form ordered arrays. However, these systems still have limitations in the amount of dispersity that can be tolerated. For example, colloids coated with rigid dsDNA typically only form ordered arrays at particle dispersities of ~10% or less, and only when the length of the DNA ligands is comparable to the radius of the particles being assembled.[161] Other examples have also been demonstrated to create mesoscale structures from disperse mixtures of nanoparticles, but these typically occur through fractionalization or self-limiting processes that do not incorporate all particles present in solution or do not control particle coordination environment.[151,212] Given the above-demonstrated ability of the NCT polymer brush to accommodate significant variations in polymer brush height, it could also be hypothesized that NCTs may be able to tolerate greater deviations in particle size or shape than these previous colloidal crystallization methods.

To confirm this prediction, NCTs were synthesized with nanoparticle core diameters of 19 nm, 24 nm, and 28 nm, each with a particle diameter relative standard deviation (RSD) < 11.5%. The three different sizes were combined in ratios that maintained an average diameter of 24 nm, but varied the overall distribution of inorganic particle core sizes up to ~23% (representing a bimodal distribution of 19 and 28 nm spheres, **Figure S3-3**). These samples were annealed by slow cooling through their melting temperature and analyzed with SAXS. Astonishingly, all samples with the exception of the 23% RSD system exhibited crystals of identical quality, and even the 23% RSD sample exhibited only slight traces of a non-uniform crystal structure (evidenced by a slight shoulder in the SAXS pattern at q ~ 0.011) (**Figure 4-5**). There was also no observed shift in the average lattice parameter as a function of particle size dispersity, nor was there any evidence of observable phase segregation of the smaller or larger particles within a crystal. If the larger and smaller particles phase segregated into separate crystallites, this would be noted by a gradual broadening of the SAXS peaks with increasing deviation in particle sizes, as well as a reduced

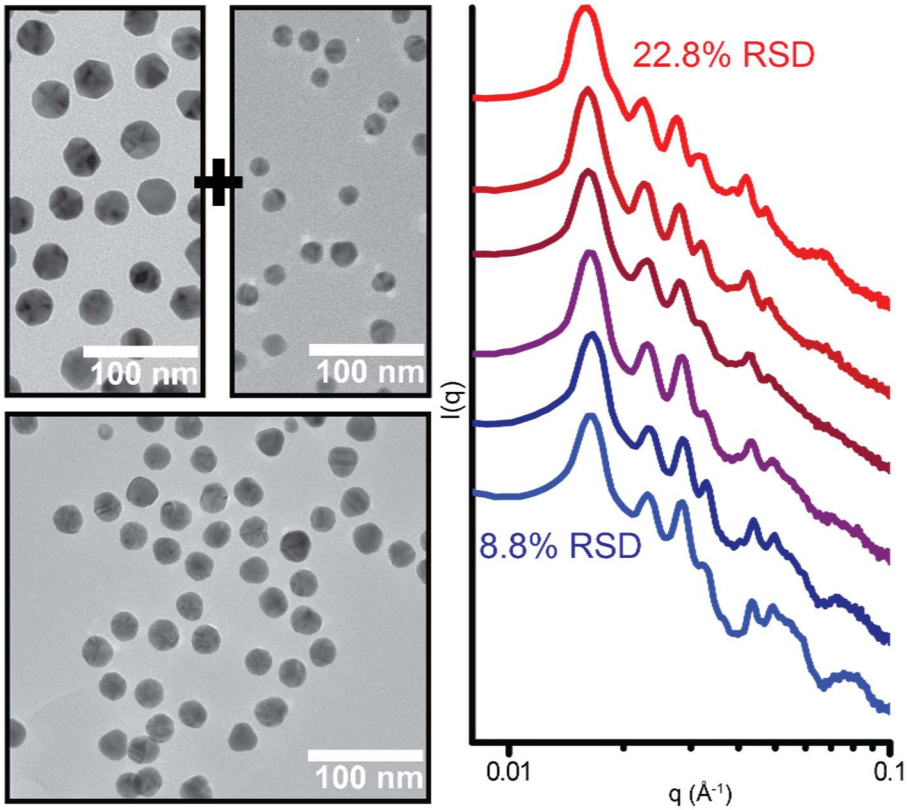

Figure 4-5. SAXS patterns of NCT assemblies synthesized with varying nanoparticle core dispersities. Combinations of 19, 24, and 28 nm AuNPs were used to prepare sets of NCTs where each NCT batch had an average core diameter of 24 nm but RSDs ranged from 8.8% to 22.8% (inset numbers). After thermal processing, all sets of NCTs were able to form bcc crystals with almost no discernable change to crystal quality.

number of observable higher order peaks due to this broadening. In other words, the final state would consist of multiple different crystallites with varying lattice parameters due to the differences in particle core diameters in each crystallite; this is clearly not observed in the SAXS patterns, which all exhibit nearly identical peak widths and number of higher order scattering peaks. Furthermore, the changes in the scattering patterns' form factors at higher q (~0.05 – 0.1) indicate that the dispersity of the particles within the lattices correlates with the dispersity of the NCT stock solutions (**Figure S3-4**).[269] Finally, the fact that all particles in each sample precipitated out of solution, combined with the observation that there was no difference in crystal quality or

lattice parameter at different points within the precipitate also implies that the RSD in particle size within each lattice is comparable to the initial RSD of particle sizes in the stock solutions. In short, the softness of the polymer ligands appears to completely mask variations in particle size or shape within the regime studied, meaning that even at 23% RSD (mixtures of NCTs with 19 and 28 nm average core sizes), the soft polymer brushes adjusted to allow all particles to form an average crystal lattice parameter. The degree of deformation of the polymer brush required to assemble such disperse nanoparticles (~ 5 nm) is comparable to the amount of polymer stretching measured in **Figure 4-4c**, and so is consistent with the above results. It is hypothesized that shorter polymers would be less capable of deforming, and so would only tolerate smaller variations in nanoparticle core size.

The surprising ability of NCTs to crystallize even with particle size deviations several times greater than is typically required by multiple other colloidal assembly methods can be understood by examining how NCT design differs from these more commonly studied nanoparticle superlattice building blocks. Colloidal crystals that assemble through a drying-mediated process require that each particle be as close to uniformity as possible, as these crystals do not have a deep energy minimum and thus variance in particle diameter can significantly reduce the favorability of packing. This trend can even be observed even when assembling polymer brush-coated particles that are soft and capable of deforming to accommodate deviations in particle size, as the lack of an enthalpic driving force means that alterations to packing fraction (and thus entropy) can have a significant destabilizing effect on assembly. However, because NCTs are assembled via supramolecular bonding, the enthalpic driving force for NCT crystallization is much stronger, offsetting some of the entropic considerations that are affected by particle dispersity. NCTs do get stuck in kinetic traps as a result of these enthalpic bonding interactions, but proper thermal processing is effective at overcoming them. Dispersity is therefore hypothesized to mostly affect NCTs through geometric obstruction, where differences in particle size cause such severe lattice strain that the formation of large crystalline domains becomes unlikely.

The ability to synthesize ordered nanomaterials from highly disperse building blocks solves a persistent problem in colloidal self-assembly, as producing uniform nanoparticles is often impractical at the relevant quantities required to synthesize bulk solids.[270] Additionally, the facile manipulation of the various structural features of NCTs allows them to provide insight into how particle crystallization occurs when “soft” bonds drive the assembly process. Moreover, NCTs are

potentially amenable to the use of size- and shape-disperse nanoparticle building blocks that may not form ordered crystals when using other assembly methods.[266–268] NCTs are therefore a useful platform for understanding colloidal self-assembly, and their easy processing and resistance to dispersity make them a valid candidate for the scalable synthesis of ordered nanomaterials.

Chapter 5. Reinforcing Supramolecular Bonding with Magnetic Dipole Interactions to Assemble Dynamic Nanoparticle Superlattices

Adapted from Santos, P. J.; Macfarlane, R. J. Reinforcing Supramolecular Bonding with Magnetic Dipole Interactions to Assemble Dynamic Nanoparticle Superlattices. *J. Am. Chem. Soc.* **2020**, *142* (3), 1170–1174. https://doi.org/10.1021/jacs.9b11476.

Superparamagnetic nanoparticles can serve as building blocks for the synthesis of sophisticated materials, where hierarchical ordering of the nanoparticle constituents can modulate the collective magnetic response of the resulting structures.[46] This tunability results from magnetic dipole interactions being affected by particle composition, size, shape, and local environment. Therefore, controlling particle distribution within an assembled solid is critical for fully manipulating structure-property relationships in these magnetic materials.[58,271–274] A strategy for precisely dictating nanoparticle arrangement involves assembling superlattices, where the particles are driven towards the configuration that represents a thermodynamic minimum through a mixture of intermolecular interactions between the nanoparticles' ligands and the surrounding solvent.[133,275,276] Importantly, because magnetic dipole-dipole coupling between particles depends on the particles' positions relative to one another, these additional magnetic interactions could potentially alter the particle self-assembly pathways.[277–280] In other words, when the dipole-dipole interaction energies and ligand binding energies are balanced to be of comparable strength, the magnetic force competes with the chemical forces driving nanoparticle assembly to produce novel structures and structure-property relationships.[191,281–284] To achieve a self-assembly system with tailorable chemical and magnetic forces, however, a building block is needed where each interaction can be independently tuned. Magnetic coupling can be controlled by using different nanoparticle core sizes or changing interparticle spacings, while chemical interactions can be dictated by using different bonding motifs or regulating the degree of multivalency of the binding groups.[285]

5.1 Preparing NCTs with Iron Oxide Nanoparticle Cores

We have recently described the synthesis of a nanoscale building block capable of dynamic self-assembly, the nanocomposite tecton (NCT) (**Figure 5-1A**).[222] NCTs consist of inorganic nanoparticle cores coated with polymer brushes. Each polymer chain in a brush terminates in a

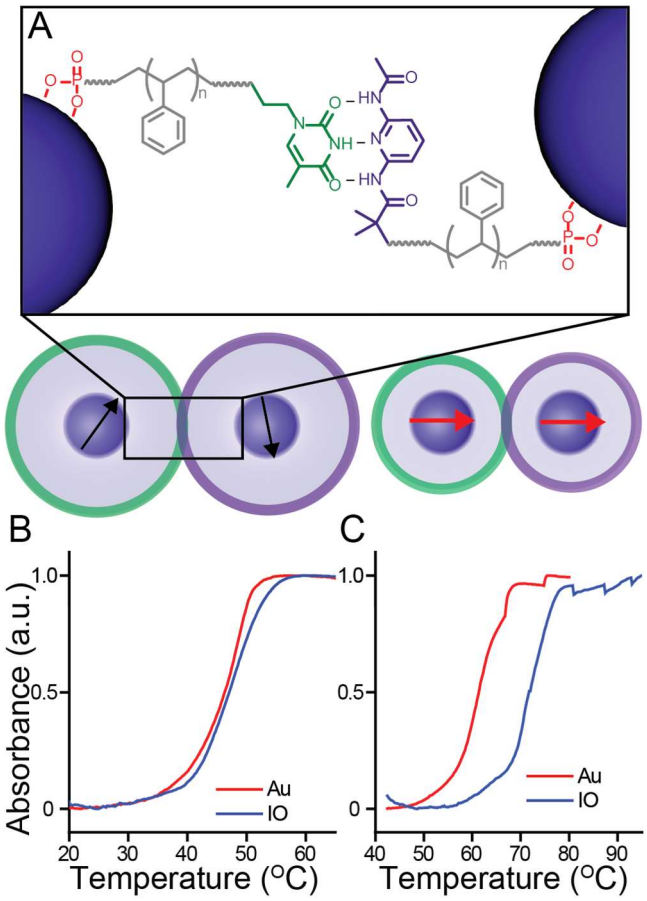

Figure 5-1. A. Nanocomposite tectons (NCTs) consist of a nanoparticle core, polymer brush, and supramolecular binding groups that drive assembly. Here, iron oxide (IO) NCTs are functionalized with polystyrene chains that are modified with a terminal phosphonate anchor. Assembly is subsequently directed via complementary hydrogen bonding moieties, but can be strengthened with magnetic dipole coupling between aligned spins when interparticle distances are short. B. Melt profiles of IO-NCTs containing 16 nm diameter IONPs with 13 kDa polymers and Au-NCTs containing 15 nm diameter AuNPs with 14 kDa polymers; the two sets of NCTs show no significant difference in their melt profiles. C. The melting profile of 16 nm IO-NCTs coated with 8 kDa polymers is shifted ~10°C above that of 15 nm Au-NCTs coated with 9 kDa polymers. Spikes in the data at high temperature are from evaporation and condensation of solvent.

supramolecular binding group, and when NCTs with complementary binding groups are mixed, these bonding interactions drive NCT assembly. Previously reported NCTs have predominantly used diaminopyridine (DAP) and thymine (Thy) groups as the supramolecular binding pair, where the hydrogen bonds between DAP and Thy are thermally labile. As a result, thermal annealing enables reorganization of the assembled lattices, allowing NCTs to form crystalline architectures that maximize the number of DAP-Thy interparticle bonds. In principle, NCTs are an ideal platform for studying the interplay between chemical bonding and magnetic coupling in nanoparticle assembly because the composition of the particle, polymer, and supramolecular binding group components of the NCT can be easily and orthogonally changed.[286] While previous NCTs used gold nanoparticle cores (AuNPs), it is also possible to use magnetically responsive nanoparticle compositions to study how magnetic interactions affect assembly. In this work, NCTs were prepared with both gold and iron oxide nanoparticle cores functionalized with polystyrene brushes that terminated in DAP and Thy groups; the AuNP NCTs served as a non-magnetic control to isolate the effects of dipole-dipole interactions on particle assembly. AuNP based NCTs were synthesized according to prior protocols.[287] The iron oxide nanoparticles (IONPs) were synthesized through the decomposition of an iron oleate precursor, resulting in 9, 14, 16, or 23 nm diameter magnetite spheres with relative standard deviations < 10% (**Figure S4-1-3**, **Table S4-1**).[54] DAP and Thy-terminated polystyrene polymers of 8 kDa and 13 kDa molecular weight with Đ < 1.1 (**Figure S4-4**, **Table S4-2**) were synthesized in the same manner as reported for prior use in AuNP-based NCTs, but were instead modified with a phosphonate group at their terminus to anchor the polymers to the IONPs (further details in the SI).[88,288] TGA measurements indicate the polymers graft at a similar density to both AuNP and IONP NCTs (**Figure S4-5**), meaning that the number of DAP/Thy groups on the particles were equivalent. Isolated solutions of DAP and Thy functionalized IO-NCTs remained stable for at least a week, and did not noticeably respond when exposed to a handheld magnet at the concentrations used in these experiments (~100 nM). After mixing DAP and Thy IO-NCTs, however, the dark solution became turbid within seconds, and aggregates became visible within a minute. The aggregates could be manipulated by a handheld magnet, indicating their collective magnetic force could overcome Brownian motion.

Hydrogen-bonded NCTs can be cycled between assembled and melted states by changing the solution temperature; this process was monitored with UV-Vis spectroscopy (**Figure S4-7-7**).[222] For IO-NCT designs with larger interparticle spacings or smaller nanoparticle cores (e.g. 16nm

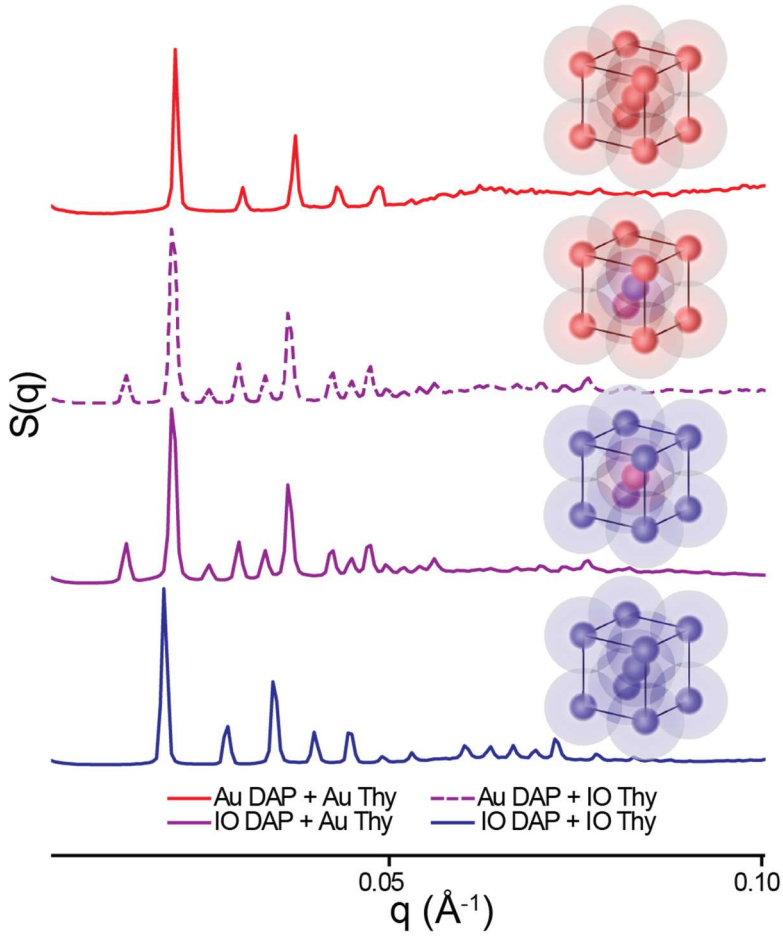

Figure 5-2. NCTs can be synthesized with both gold (AuNP) and iron oxide nanoparticle (IONP) cores. Small angle x-ray scattering (SAXS) patterns of superlattices assembled with IO-NCTs (bottom), Au-NCTs (top), and mixtures of Au and IO-NCTs (middle two). The lattices composed of just IONP or AuNP cores possess bcc crystal symmetry, while the combinations of IONP and AuNP have CsCl symmetry. Notably, the interparticle spacings are nearly identical, demonstrating that the superlattice crystal symmetry and lattice parameters can be independently controlled from the nanoparticle core compositions.

core diameter, 13 kDa polymer molecular weight) their melting temperature (T_m, the melt curve inflection point) was identical to Au-NCTs with similar design parameters (15 nm core diameter, 14 kDa polymer molecular weight) (**Figure 5-1B**). However, in systems where the ratio of particle size to interparticle distance was larger (e.g. 8 kDa polymer on 16 nm IO-NCTs, 9 kDa polymer on 15 nm Au-NCTs), T_m increased significantly (**Figure 5-1C**). We hypothesize that this added attractive energy arises from magnetic dipole coupling between particles, and that these magnetic

interactions are sensitive to various nanoscale structural parameters (i.e. interparticle distance and particle size, see **Figure S4-6** for additional data).[191,282] Dipole-dipole coupling is insufficient to cause particle aggregation on its own, but can supplement the supramolecular interactions to further strengthen NCT-NCT assembly.

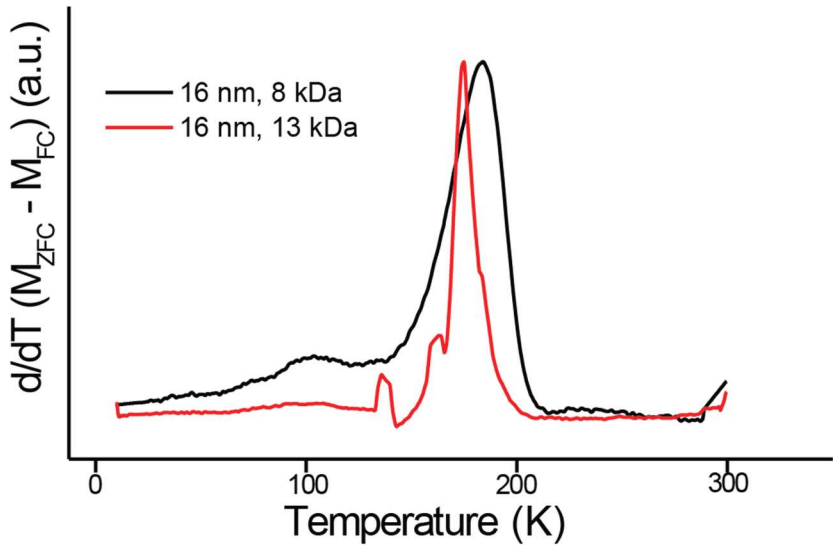

Figure 5-3. Blocking temperature (T_b) determination for IO-NCT assemblies with 8 kDa and 13 kDa polymer shells. T_b is identified as the peak of the derivative of the difference between the zero field cooled (ZFC) and field cooled (FC) curves (see **Figure S4-10** for experimental data). Upon shortening the polymer length, the T_b increases and the transition range broadens, indicating an increase in dipole-dipole interactions.

Because NCT assembly is governed primarily by supramolecular bonding, the two nanoparticle core compositions should be structurally equivalent when constructing nanoparticle superlattices. To confirm this, IO-NCTs and Au-NCTs were thermally annealed to drive them to their thermodynamically preferred configurations, which for complementary NCTs of identical size is a body centered cubic (bcc) lattice (**Figure 5-2** red and blue traces).[222] This crystalline arrangement is the thermodynamic product for a range of particle sizes and polymer lengths in both the Au-NCT and IO-NCT assemblies (**Figure S4-8**).[285] Importantly, this also means that an alternating lattice of Au and IO-NCTs can be assembled if the two NCT compositions are functionalized with complementary binding groups (**Figure 5-2**, purple traces); this results in lattices structurally equivalent to CsCl crystals.[276]

5.2 Controlling Magnetic Dipole Interactions with NCTs

Based on these structural and thermal data, we conclude that although the iron oxide cores of the NCTs are interchangeable with Au-NCTs as a structural element of the superlattices, magnetic coupling between IO-NCTs can affect the strength of interparticle bonding when IONPs are in close proximity. At larger interparticle spacings (surface to surface > 5 nm), the interaction energy is best estimated by the Keesom interaction:[244]

$$U_{dd} = -\frac{1}{3k_BT}\left(\frac{m^2}{4\pi\mu_0 r^3}\right)^2 \quad (5\text{-}1)$$

where m is the magnetic moment (proportional to particle size), r is the interparticle distance, and μ_0 is the magnetic vacuum permeability. When assembled, each NCT is subject to interactions from neighboring particles, but because the interaction energy is approximated to change as r^{-6}, only the first few nearest neighbors would be expected to contribute to the total binding energy between neighboring NCTs. Furthermore, polymer ligand length should significantly affect dipole-dipole coupling strength, as it dictates the surface-to-surface distance between particles.[45] For example, 16 nm IO-NCTs functionalized with 8 kDa polymer were determined by SAXS to have a 29.6 nm interparticle spacing; Equation 5-1 predicts that this interparticle distance should result in a dipole energy of ~5.2 k_BT. When the polymer molecular weight is increased to 13 kDa (38.5 nm interparticle spacing), the calculated interaction energy is 1.1 k_BT. It is important to note that these magnetic dipole interaction energies are significantly weaker than a single DAP-Thy hydrogen bonding pair (12.8 k_BT in toluene),[285] but significant enough to contribute to assembly in conjunction with the supramolecular bonding.

The existence of enhanced dipole-dipole coupling for NCTs with smaller interparticle spacings can be further confirmed using zero field cooled / field cooled (ZFC/FC) measurements to determine the NCT assemblies' blocking temperatures (T_b), the temperature at which unaligned magnetic spins orient to an applied magnetic field (**Figure 5-3**, **Figure S4-10**, see **Figure S4-11** for hysteresis measurements). Dipole-dipole interactions are known to increase T_b and broaden the temperature window of this transition.[49,289] To best determine T_b, the derivative of the difference between the ZFC and FC curves was taken for both the 8 kDa and 13 kDa linked nanoparticle assemblies mentioned above (**Figure 5-3**).[290] The peak, signifying T_b, increased by ~11 K when the shorter polymer was used, and the transition significantly broadened, confirming an enhancement in dipole-dipole interactions.

The observed increases in T_m and T_b are consistent with the notion that shortening the interparticle distance between IO-NCTs allows the magnetic polarization of each particle to interact and increase the interparticle attraction. Adding magnetic coupling therefore contributes another design parameter for controlling nanoparticle assembly, and consequently it may be possible to stabilize particle systems that otherwise may not crystallize. Indeed, IO-NCTs synthesized with the shorter Thy-terminated polymer ligand formed face centered cubic (fcc) lattices when prepared in the absence of DAP-NCTs, the first time this phase has been demonstrated in the NCT system. While Thy-Thy interactions can be stabilized by hydrogen bonding,[291] these interactions are too weak on their own to cause the Thy-coated NCTs to assemble into stable lattices. Accordingly, Au-NCTs functionalized with short Thy polymers (9 kDa) exhibit only a slight scattering peak (**Figure 5-4**, red data). However, the well-defined fcc crystals formed by IO-NCTs imply that an additional magnetic attractive force must be present (**Figure 5-4**, blue data).[162] Consistent with this observation, no assembly occurs between IO-NCTs functionalized with longer Thy-terminated polymers (**Figure S4-9**).

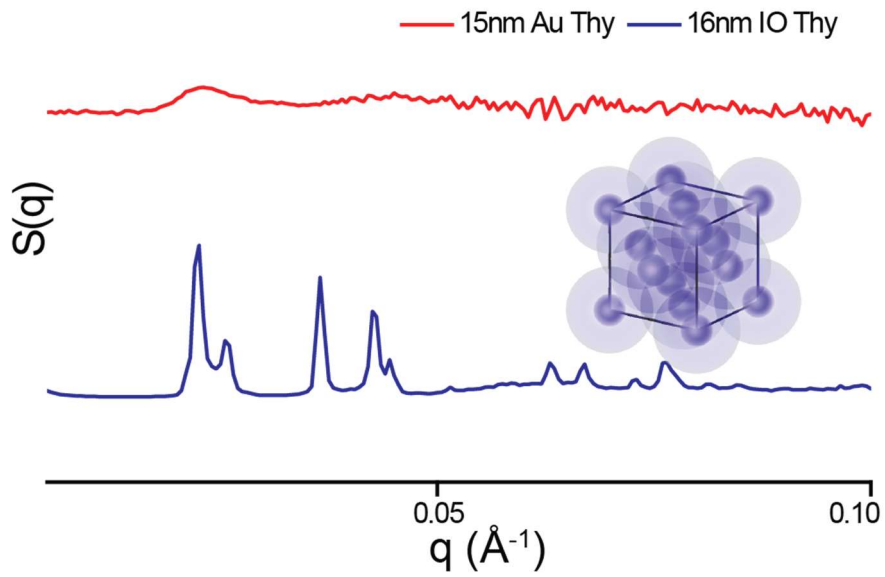

Figure 5-4. 15 nm Au-NCTs functionalized with ~9 kDa Thy-terminated polymers exhibit a slight peak at q = 0.023 $Å^{-1}$ indicating only minor amounts of random aggregation. Conversely, 16 nm IO-NCTs functionalized with ~8 kDa Thy-terminated polymers show the sharp and clear scatting pattern of a face centered cubic (fcc) superlattice.

We have demonstrated that the NCT design concept is easily adapted to magnetic nanoparticles, making NCTs a powerful platform for designing magnetic nanocomposites. NCTs can be appropriately designed to either mask the identity of the core composition, or take advantage of any inherent interparticle interactions, with some limitations based on nanoparticle size and interparticle spacings. Due to the complex sets of interactions governing self-assembly in these magnetic NCTs, magnetic dipole coupling between nanoparticles can reinforce the supramolecular interactions that drive the formation of superlattices. These synergistic interactions can even stabilize previously unachievable crystallographic symmetries. Consequently, NCTs can further clarify the interactions of nanoscale materials, and how the competition between forces affects self-assembly. Furthermore, the ability to engineer the magnetic coupling of nanoparticles is a promising strategy to developing materials with complex metamaterial properties.

Chapter 6. Nanoparticle Composite Materials with Programmed Nanoscale, Microscale, and Macroscale Structure

Adopted from forthcoming work from the forthcoming work: Santos, P. J.; Gabrys, P.A. Zornberg, L.Z.; Macfarlane, R. J. Nanoparticle Composite Materials with Programmed Nanoscale, Microscale, and Macroscale Structure.

One of the promises of nanotechnology is the ability to make designer materials with deterministic control over both composition and 3D spatial organization.[10,292] The self-assembly of nanoparticles[212,293–295] has emerged as a promising method for synthesizing these nanomaterials because they offer a vast array of materials fabrication components of varying sizes, shapes, and chemical compositions.[296,297] A significant accomplishment has been the formation of ordered superlattices of nanoparticles that resemble the crystalline lattices of atomic materials,[133,151,156,157,160,162,169,180,275,298] and even creating unnatural crystallographic symmetries by exploiting the broad design-space of the building blocks.[135–137,146,163,166,299] The resemblance of nanoparticle superlattices to atomic crystals has inspired the development of a number of processing methods for creating thin films[134,173,175,176] and single crystals of precisely arranged nanoparticles.[142,143,170,172,178,280] Although current efforts have therefore succeeded at creating materials with designed nano- and micrometer geometry, the fundamental promise of being able to build a bulk material with controlled structure across the length scales of atomic crystal structure, nanoscale size and organization, and ultimately material microstructure and macroscopic form, has been challenging to realize. Progress towards designed macroscopic nanomaterials has been impeded by the difficulty of producing bulk quantities of the building blocks, the slow processing of the nanoparticle components into assemblies, and the lack of a method for transforming micron sized crystallites and films with well-defined microstructures into a larger material. A major advancement would therefore be a single materials synthesis and processing route that could create free-standing, macroscopic materials of arbitrary three dimensional shapes with precisely controlled nanoparticle positions across the entirety of the material composition.
Here, we address these challenges with a recently developed building block, the Nanocomposite Tecton (NCT),[222] and demonstrate its unique suitability for producing well-ordered macroscopic

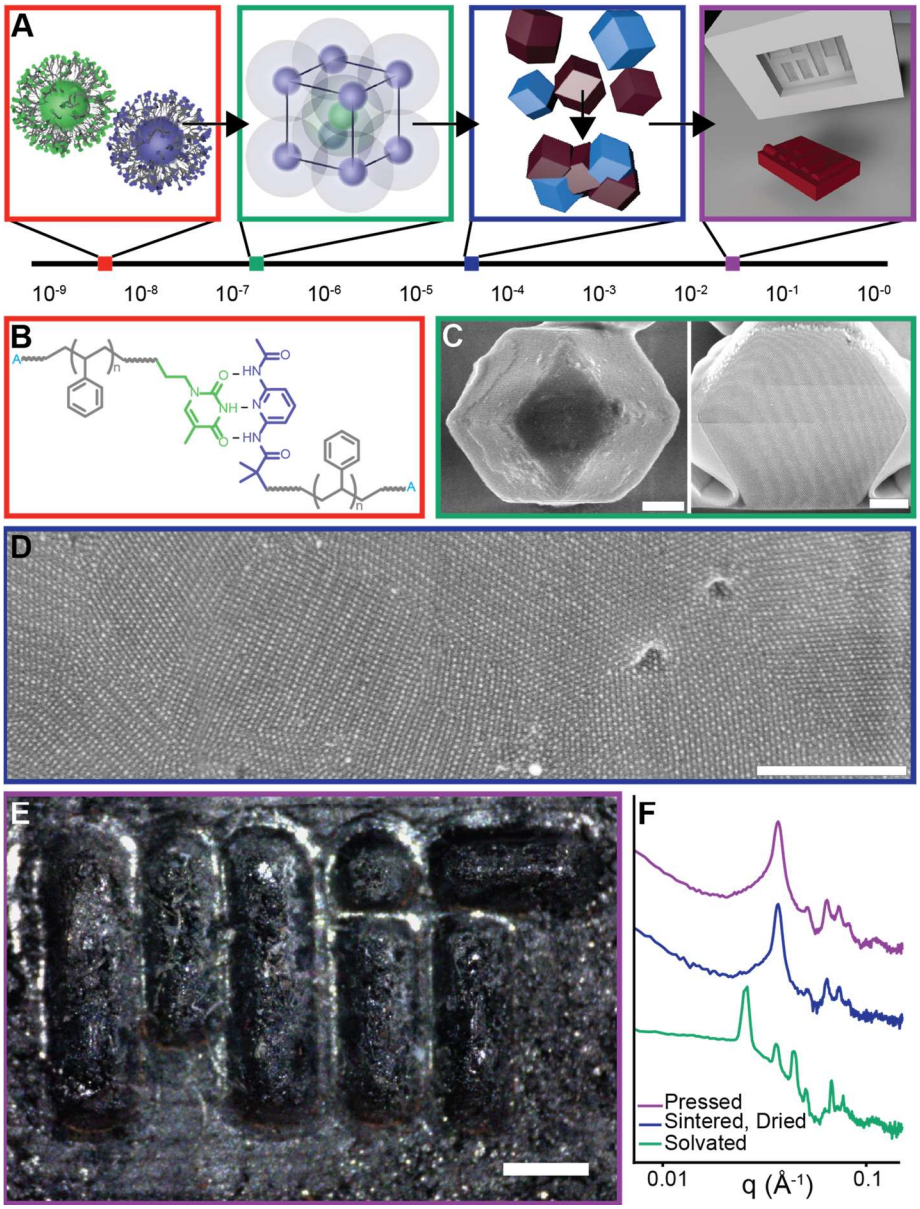

Figure 6-1 The Nanocomposite Tecton (NCT) design concept allows for structural control from the nanoscale to the macroscale. A. Supramolecular interactions drive the assembly of nanoparticles. Under appropriate conditions the NCTs will assemble into ordered superlattices, and form micron-sized crystallites. These crystallites can be sintered together to form a macroscopic solid material. The NCT solid can be mechanically pressed into an arbitrary shape. B. NCTs consist of a nanoparticle core coated with a polymer brush terminated in a supramolecular binding group. In this work, polystyrene was used as the polymer and diaminopyridine (DAP) and thymine (Thy) as a supramolecular binding pair.

Figure 6-1 Continued. C. Scanning electron microscope (SEM) micrographs of the surface morphology (left) and cross-section (right) of a gold nanoparticle NCT (Au-NCT) crystallite that formed a Wulff polyhedra. Scale bar is 500 nm. D. SEM micrograph of the cross-section of a sintered Au-NCT solid. Scale bar is 500 nm. E. Iron Oxide nanoparticle NCTs mechanically shaped into the MIT school logo. Scale bar is 0.5 mm. F. Small angle X-ray scatting (SAXS) of the NCTs in part E while solvated in toluene (green), after being sintered and dried (blue), and after mechanical deformation (purple), demonstrating the body centered cubic (bcc) ordering is preserved throughout the process.

nanomaterials. We investigate the assembly of NCTs into ordered crystallites directed by a simple, enthalpically driven supramolecular interaction, allowing for precise and rapid control over microscale size and distribution. Finally, we extend the analogy between nanoparticles and atoms by devising a processing route akin to the sintering of nanocrystalline powders to fabricate an NCT-based polycrystalline, bulk monolith that can be post-processed (dried and pressed) into large, arbitrarily shaped solids. In other words, we have devised a single materials synthesis and processing route for nanoparticle-based, bulk materials with designed structure at the atomic scale (supramolecular chemistry), nanoscale (crystalline unit cell), microscale (controlled grain size and composition), and macroscale (arbitrary shape) (**Figure 6-1**).

6.1 Manipulating NCTs with Non-Solvents

At the scale of the building block, each NCT consists of an inorganic nanoparticle core covered with a dense polymer brush, and each polymer chain is terminated in a supramolecular binding group (**Figure 6-1B**), which upon the mixing of complementarily functionalized NCTs, directs their assembly.[286] Previous work has shown that after a mild annealing process, NCTs self-assemble into well-ordered superlattices,[287] but no work has been done to either further modify nanoscale behavior or characterize their larger length-scale structure. NCTs are able to crystallize because they are near-equilibrium materials; as they are heated the supramolecular bonds that hold together the lattice are capable of rapidly breaking and reforming until the NCTs freely disperse into solution in a process characterized by a melting temperature (T_m).[285] Upon cooling the binary NCTs through T_m, the nanoparticles organize into body-centered cubic (bcc) crystallites (**Figure 6-1C**).

NCT crystallization occurs in good solvents for the polymer shell, meaning that the brush is in a swollen state. However, the configuration of polymer chains is highly dependent on their enthalpy of mixing with the solvent; introducing a non-solvent causes the polymer to adapt a coiled conformation due to the repulsive interaction energy.[99,300] Because the polymer brushes in NCTs are a dynamic material, it was hypothesized that the conformation of the polymer chains could be modified by the addition of a poor solvent, allowing for actuation of interparticle distance within the crystalline lattice. To study control over polymer brush swelling with solvent, a model NCT system was developed using previously developed chemistries: 15.4 nm gold nanoparticle cores (AuNPs), ~14 kDa polystyrene polymer brushes, and a DAP-Thy hydrogen bonding supramolecular attachment chemistry scheme (**Figure S5-1&2**). During assembly, the NCT system is dispersed in toluene, a good solvent for the polystyrene chains, and therefore the brush is in a fully swollen condition. Simple alkanes (e.g. n-hexane, n-octane, n-decane) can serve as non-solvents for polystyrene while not interfering with hydrogen bonding. When any of these non-solvents are added to the NCTs, the system robustly maintains its bcc crystallinity, but the interparticle spacing decreases in a continuous, monotonic fashion (**Figure 6-2A**, **Figure S5-4**). Interestingly, the polymer brush collapse is reversible, as a lattice can be cycled from solvent to non-solvent and back again without any decrease in crystallinity as determined by SAXS (**Figure S5-5**). This cycling represents a dramatic 40 percent linear compression and expansion of the lattice, changing the interparticle spacing from 38.2 nm in pure toluene to 22.9 nm in pure n-decane. Because this change in lattice parameter is dependent on the behavior of the polymer brush, it is possible to further control interparticle spacing by changing the length of the polymer brush used. For example, NCTs with a smaller 6 kDa polymer were found to create a lattice with a 19.5 nm interparticle spacing in the collapsed state, a notably short surface-to-surface distance of 4.1 nm (**Figure S5-6**).[301,302] Strikingly, polymer conformation can be controlled by solvent content with Angstrom-level precision as measured by small angle x-ray scattering (SAXS). The ability to modulate the distance between nanoparticles and therefore, create high inorganic fraction nanocomposites with NCTs, may have significant implications for materials that could engage in plasmonic or magnetic coupling.

However, solvated NCTs are unsuitable for implementation as bulk materials, because, although their low barrier to rearrangement aids their ability to crystallize, it leaves them susceptible to

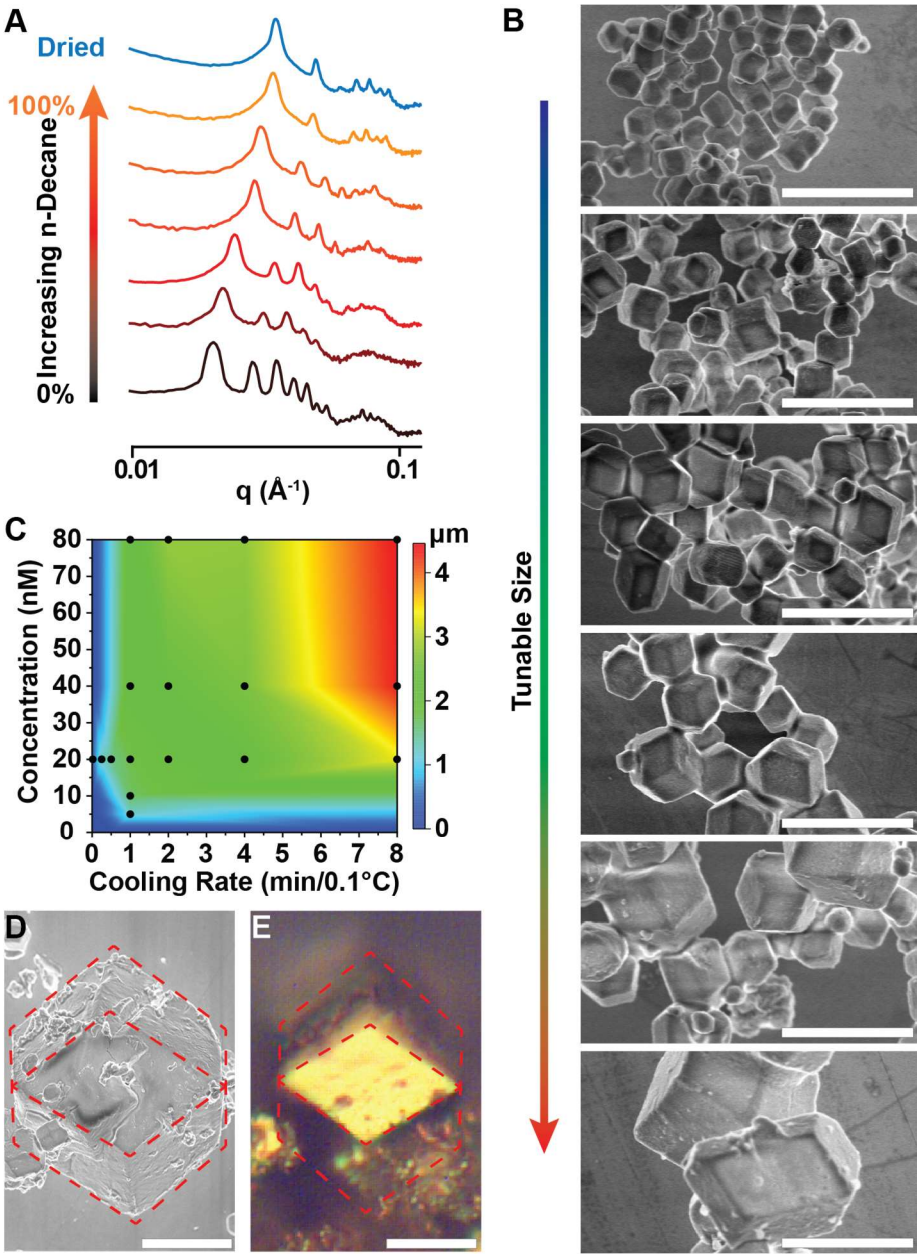

Figure 6-2. The formation of solid Wulff polyhedra from NCTs. A. During crystallization, NCTs are suspended in a solvent compatible with the polymer brush, such as toluene. However, because the polymer brush is swollen, evaporating the solvent causes a loss of ordering and destroys the crystallites. Adding a non-solvent, in this case n-Decane cause the brush to de-swell, preserving ordering, as demonstrated by SAXS, and resulting in a significant (40%) contraction of the lattice parameter. B. During crystallization, the NCTs assemble into Wulff polyhedra. The size of the polyhedra can be tuned by modifying the concentration of NCTs and their cooling rate during crystallization. Scale bars are all 5 microns.

Figure 6-2 Continued. C. The largest polyhedra form when a high concentration of NCTs and a slow cooling rate is used. Under optimal conditions, very large crystallites form, up to 30 microns in diameter. D. SEM and E. Optical image of large Wulff polyhedra. Scale bars are 10 microns.

destabilization upon exposure to adverse thermal or chemical stimuli. Simply evaporating the NCTs from their good solvent (toluene) destroys the ordering as the brush collapses (**Figure S5-3**), indicating that the toluene is a key structural element of the lattice. Therefore, it is hypothesized that the solvent ceases to be a structural component once fully transitioned to the non-solvent, and can be subsequently dried without loss of crystallinity. Indeed, NCT lattices evaporated from n-decane demonstrate near identical ordering to the solvated state (**Figure 6-2A**, **Figure S5-4**). Unlike the existing strategies to transition enthalpy-driven colloidal crystals to the solid-state,[303–305] transitioning NCTs to a solid materials *via* this deswelling of the polymer brush is a promising and powerful technique as it requires no additional reagents that may affect the system, diminish its ordering, or modify its properties.

6.2 Controlling NCT Crystallite Size with Processing Conditions

In addition to providing precise, actuatable control over nanoscale periodic spacing and expanding the accessible environments available to NCTs, the drying process allowed for imaging of NCT assemblies using scanning electron microscopy (SEM). NCTs slowly cooled (standard rate 1 minute per 0.1°C) through their melting transition yield crystallites with consistent, rhombic dodecahedron shapes (**Figure 6-1C**). The highly ordered nanostructure evident in the SAXS data (**Figure 6-2A**) is corroborated by SEM imaging of focused ion-beam (FIB) cross-sections, confirming the materials are highly crystalline throughout even after drying. A rhombic dodecahedron is the predicted Wulff polyhedra for bcc crystallites that forms because the surface is capped with the (110) closest-packed crystal planes and has been observed in other nanoparticle systems.

Other nanoparticle assembly strategies to produce Wulff polyhedra typically require either a slow solvent evaporation over hours to days[142] or a slow cooling through the melting transition with typical speeds of 10min/0.1°C.[170] In contrast, due to the lack of electrostatic repulsion between NCTs and their assembly through an enthalpy-mediated process the NCT system is capable of

crystallizing very quickly; at the fastest rate that could be controllably measured and achieved (1s/0.1℃), NCTs still form highly ordered lattices (**Figure S5-7&8**), and faceting can be clearly observed on crystallites cooled at 15s/0.1℃ (**Figure S5-9**).

The ability of NCTs to rapidly crystallize enables the use of annealing rate as a variable for controlling the resulting crystallize average size and distribution. In more traditional crystallization systems, crystallite size is positively correlated to slower cooling rate and lower precursor concentration, depending on the specific conditions of the system.[306] Consistent with this analogue, slower cooling rates in NCT crystallization were found to produce larger crystallite sizes, and as a result, the crystallite size can be reasonably well controlled with median characteristic lengths between ~500 nm and ~5 μm (**Figure 6-2B&C**, **Figure S5-8**-**Figure S5-27**). Surprisingly, it was also observed that higher concentrations yielded larger crystallites, but with a larger distribution of sizes. This is contrary to what is commonly observed in atomic systems, wherein higher precursor concentrations typically increase the total number of crystallites, thereby reducing the size of individual crystallites. To understand the dependence of crystallite size on concentration and cooling rate, a model was developed treating the cooling NCTs as aggregating clusters of nanoparticles. During cooling, these clusters collapse into an aggregate whose size is determined by the number of particles in a diffusion-limited volume as the system cools through the NCT melting window and crystallizes. Consequently, the model predicts that a slower annealing rate would increase the interaction volume, while a higher concentration would increase the total number of NCTs that would be present within the interaction volume, resulting in a larger aggregate. Furthermore, due to the stochastic nature of the aggregation process, increasing these two parameters would also be expected to broaden the distribution of crystallite sizes, and so the predicted trends of the model are consistent with the experimental data (**Figure 6-2C**, **Figure S5-28**-**Figure S5-31**).

Utilizing the insights garnered from the model, combining the effects of a slow cooling rate and a high NCT concentration, crystallites with a diameter > 30 microns when collapsed can be synthesized (**Figure 6-2D**), equivalent to 50 microns when the polymer brush is extended. These large NCT crystallites have a diameter nearly 2.5 times the largest previously reported nanoparticle Wulff polyhedra, and contain approximately 10 times more particles[307] (**Figure S5-27**). As a result, the crystallites can be easily observed under an optical microscope (**Figure 6-2E**) and

exhibit a highly reflective gold coloration, indicative of strong plasmonic coupling between the particles.

6.3 Preparing Macroscopic Nanocomposite Materials

Although NCTs are capable of producing quite large single crystals, it would take prohibitively onerous processing conditions to grow a macroscopic single crystal. Alternatively, appropriate post-processing methods could be developed to transform micron sized crystallites into a bulk material. After their assembly, the NCTs are a powder of individual, micron sized crystallites with a negligible number of connections between crystallites. Turning to conventional metallic, ceramic, and polymeric materials where nanocrystalline powders are often sintered into macroscopic compacts for inspiration, it is hypothesized that an analogue to 'sintering' within the NCT system could be accomplished. In conventional materials, the application of heat and pressure allows for powder particles to plastically flow and deform in order to densify into a solid.[308–310] When the polymer brush of NCTs is swollen with toluene the system is near its melting transition (within 50°C), and so the dynamic supramolecular bonds of NCTs are hypothesized to be able to break and reform upon NCT crystallite deformation. Pressure was applied to NCT crystallites *via* centrifugation (20,000 RCF for 10 minutes), and, indeed, a monolithic solid was obtained after polymer brush collapse and drying (**Figure S5-32**). SAXS confirms the NCTs maintain their crystalline ordering throughout this processing (**Figure 6-1F**), and SEM imaging of FIB cross-sections reveals the NCTs have been formed into a densified structure with grain boundary-like features (**Figure 6-1D**, **Figure 6-3**). Analysis of the microstructure is consistent with a sintering mechanism for compact formation: necking is evident near remaining void spaces and grains appear to have deformed form their original Wulff shape (**Figure S5-33**-**Figure S5-38**). Combining the control over microscale crystallite size distribution enabled by the understanding of crystallization dynamics with this macroscale processing method, it is hypothesized that a sintered NCT material would retain the size distribution of the initial crystallites in its final grain structure. To investigate this, NCT crystallites were prepared at different cooling rates as per **Figure 6-2**, so as to result in two distinct populations of crystallite sizes which were subsequently exposed to the abovementioned centrifugation compacting protocol (**Figure 6-3A&B**). Indeed, SEM analysis reveals that the NCT bulk solids can be designed to have controllable grain sizes that track with the initial size distribution of crystallites (**Figure 6-3C&D**), indicating the ability

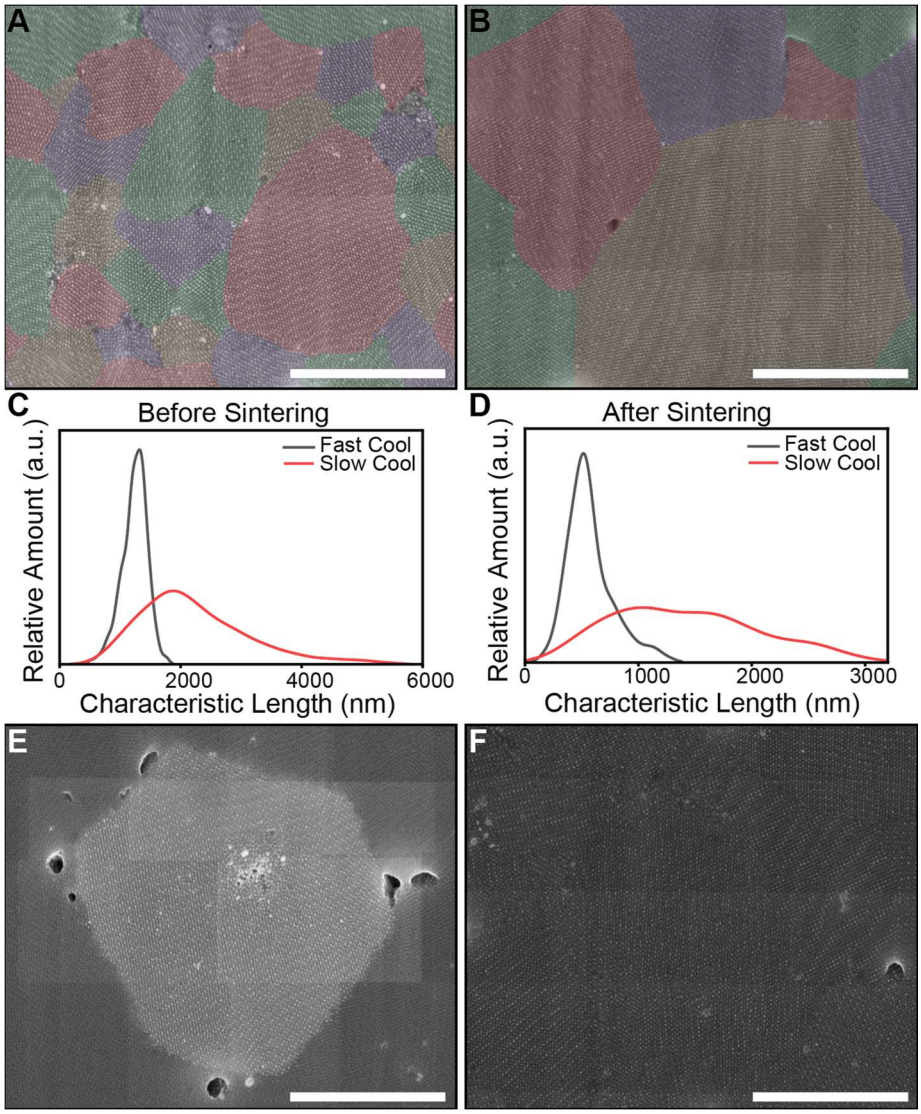

Figure 6-3. The NCT crystallites can be sintered into macroscopic solid materials. These solid NCTs are polycrystalline, with clearly identifiable grain boundaries in cross-sections. The size of the grains in the polycrystalline solid is dependent on the characteristic sizes of the initial NCT crystallites. A. When a faster cooling rate is used, smaller crystallites form, and the resulting solid has smaller grains. B. Conversely, a slower cooling rate results in larger crystallites and bigger grains. The overall distribution of crystallite sizes before sintering (C) matches the distribution after sintering (D), though the average size decreases, hypothesized to be a result of deformation. E. The sintering method can be used to create materials of multiple compositions. Gold and iron oxide NCTs can be separately crystallized, and then blended together and sintered to create a heterogenous microstructure.

Figure 6-3 Continued. F. Gold and iron oxide NCTs can also be assembled together to create a lattice with isostructural symmetry to CsCl where every alternating nanoparticle is gold or iron oxide, sintered into a solid with a homogeneous microstructure. Consequently, depending on the processing route, two materials of equivalent composition but dramatically different microstructure can be fabricated with NCTs. All scale bars are 1 micron.

to dictate microstructure along with nano-ordering and macro-shape. Furthermore, solids prepared from NCTs with larger size distributions were also qualitatively observed to have an increase in void space, supportive of a sintering mechanism (**Figure S5-34&35**).

The microstructure of NCT solids can be further programmed by changing the composition of the nanoparticle constituents. Previous work has demonstrated that NCTs can be synthesized with iron oxide nanoparticle cores (IO-NCTs), and the assembly process is largely unaffected by nanoparticle core identity.[311] Therefore, sintered NCT solids were prepared using a mechanically blended combination of bcc IO-NCT crystallites (**Figure S5-37**, **Figure S5-40**, **Figure S5-42**) and bcc Au-NCTs crystallites. The result is a macroscopic material with control over the composition of microscopic grains (**Figure 6-3D**). Notably, the Au and IO-NCTs remain phase segregated in this sample, suggesting a minimal degree of grain boundary diffusion occurs during the sintering process (**Figure S5-41**). To extend this compositional control to the nanoscale, NCT crystallites co-crystallized with Au and IO-NCTs to form superlattices isostructural with CsCl (**Figure S5-39&40**, **Figure S5-42**) were produced and similarly sintered. The resulting macroscale, continuous material with well-defined, microscale grain size also demonstrates a tailored nanostructure where every-other nanoparticle consists of a different composition (**Figure 6-3E**).

As IO-NCTs consist of iron oxide nanoparticles and polystyrene polymers, each synthesized at gram-scale quantities, it is possible to conveniently produce macroscopic materials from these building blocks and process them into arbitrary three-dimensional shapes. A mold was created by etching the MIT school logo into a bar of polyoxymethylene, and a sintered solid of IO-NCTs was prepared by the abovementioned centrifugation method. The solid was then pressed into the mold with 500 Newtons of force and removed to yield a freestanding block with the embossed logo and dimensions of 3.9 mm x 2.6 mm x 0.25 mm (**Figure 6-1E**, **Figure S5-43**-**Figure S5-47**). SAXS confirms the NCTs remain ordered after processing (**Figure 6-1F, Figure S5-45**), and SEM imaging reveals the microstructure is preserved (**Figure S5-47**).

Here, we have demonstrated a method for manufacturing bulk, solid materials from a nanoparticle-based building block that can be manipulated into arbitrary macroscopic shapes while maintaining nanoscale control over ordering. The observation of sintering and grain development makes the NCT system an excellent platform for future studies into the similarities between colloidal assemblies and atomic materials. Furthermore, NCTs may serve as analogues to atoms in conventional materials, but their larger size will enable their *in-situ* characterization during deformation to allow the visualization of defect formation. Finally, these hierarchically designed NCT solids offer a new opportunity for integrating nanoscale properties into macroscale materials to create advanced nanocomposites with unique plasmonic, magnetic, or mechanical properties.

Chapter 7. Future Work

7.1 The Growth of NCTs Crystallites off of Substrates into Winterbottom Structures

An exciting finding about NCTs is their ability to form single crystalline Wulff polyhedra, as their well-defined facets may result in unique optical properties and their anisotropy may allow for interesting mechanical measurements. However, casting the crystallites onto a substrate from solution results in randomly oriented facets, and the NCTs are capable of easily detaching from the substrate. Therefore, it would be desirable to grow the NCT crystallites from a substrate with controlled crystallographic orientation. Furthermore, although a key accomplishment of the NCT system is the synthesis of bulk, macroscopic colloidal materials with nanoscale ordering, some nanoparticle building blocks can only be synthesized in small quantities, and so substrate bound materials would be more feasible to study.

Recent work on Programmable Atom Equivalents (PAEs, DNA-linked nanoparticle assemblies) has shown that it is possible to grow single crystal colloidal structures off of surfaces, and that they form Winterbottom constructions.[178] The Winterbottom construction forms due to similar thermodynamic considerations as Wulff polyhedra, but the presence of an interface requires the surface energies of the substrate to be accounted for as well, resulting in a truncated polyhedral shape.

Preliminary work has demonstrated that NCTs are also capable of assembling into Winterbottom constructions. This was accomplished by functionalizing a gold coated silicon substrate with thiolated DAP or Thy polymer, and slowly cooling the NCTs through their melting transition, and resulted in similar structures to what was observed in the PAE case.

Notably, two different morphologies were present, depending on whether the NCT surface was functionalized with DAP or Thy polymers (**Figure 7-1**). These two morphologies were also observed in the PAE example, with the “pyramid” shape appearing when the surface was functionalized with DNA only complementary to one particle type, while the “diamond” morphology resulting from a substrate functionalized with DNA complementary to both particle types.

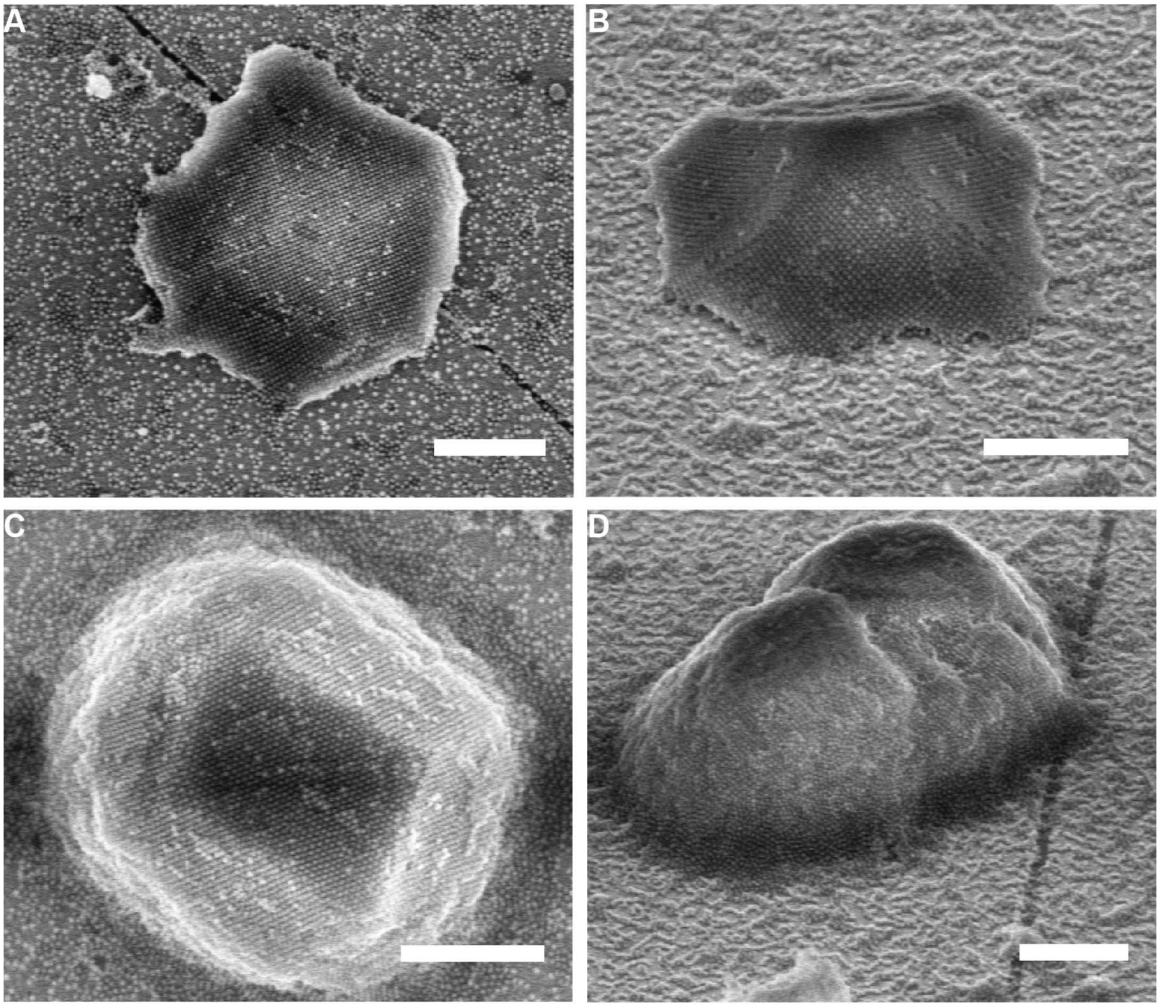

Figure 7-1. NCT crystallites grown from substrates in the Winterbottom construction. (A) Top and (B) side views of the "pyramid" morphology that results from NCTs grown on DAP functionalized surfaces. (C) Top and (D) side views of the "diamond" morphology that results from NCTs grown on Thy functionalized surfaces. All scale bars 500 nm.

Although the substrates used with NCTs were only functionalized with a single polymer type, prior work has shown that the Thy polymers have a mild self-complementary interaction,[311] which could have a similar effect to loading with two types of DNA. The "diamond" morphology has the (110) plane attached to the surface, which for a bcc lattices contains both DAP and Thy functionalized nanoparticles. Conversely, the "pyramid" morphology has the (100) plane on the surface, which only contains a single nanoparticle functionality. The difference in morphology may be a result of the crystallite nucleation kinetics, the DAP functionalized surface only attracts Thy particles, which can form a (100) plane on the surface and continue to grow the pyramid-like structures.

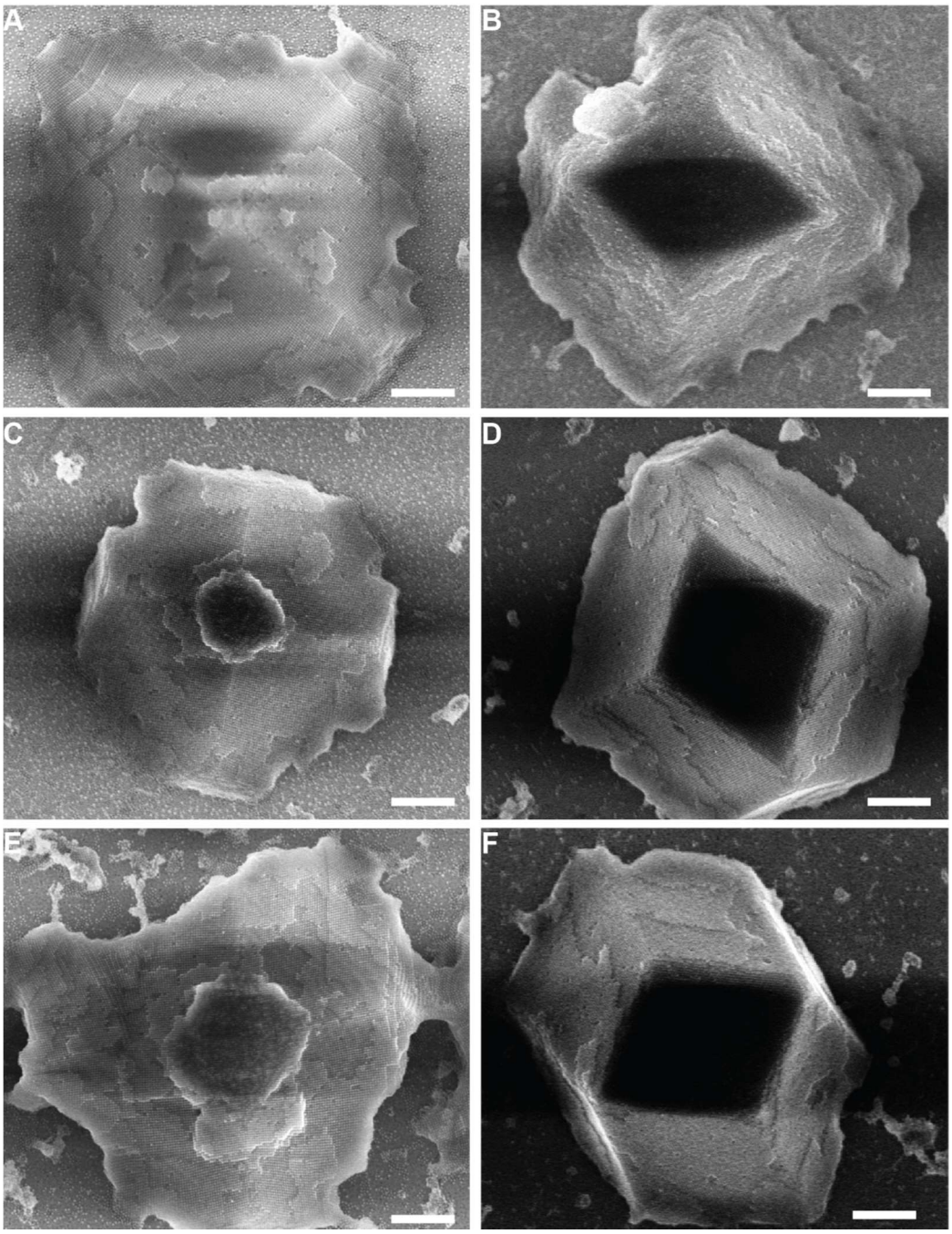

Figure 7-2. SEM micrographs of Winterbottom NCTs grown off substrates with (A and B) 6 kDa polymer grafted (C and D) 14 kDa polymer grafted (E and F) 18 kDa polymer grafted. A, C, and E are DAP substrates, B, D, and F are Thy substrates. Scalebars are 500 nm.

Conversely, the Thy surface attracts both particle types, and so the more closely packed (110) plane is able to form on the substrate and grow into the "diamond" morphology. Notably, if only

the thermodynamics of the interactions between substrate and particle were considered, the "pyramid" morphology would be expected with both substrate functionalities as that would result in the strongest bonds between particle and substrate, and so the differences in behavior are likely due to the kinetics. Another set of data that supports this hypothesis are experiments performed with different polymer lengths grafted to the substrate. All systems generally create crystallites with the expected morphologies (**Figure 7-2**), however, longer polymers frequently display some of the opposite morphology as would be expected. The shorter polymers bind more strongly to the NCTs, and so mismatch would be less likely as there is a greater driving force for the correct particle type to bind to the surface. Further experiments that test different concentrations of the two particle functionalities may be able to provide better evidence for this hypothesis.

An additional feature that is brought into focus by the polymer length survey is the dewetting of crystallites from the substrates. When NCTs are dried, they undergo a significant volumetric contraction as the solvent is exchanged from toluene, which swells the polymer brush, to decane, which causes it to collapse. When grown off a substrate, this becomes most clear when a longer polymer is used, as it must contract the most, and binds to the NCTs with the lowest strength. Many Winterbottom structures have interesting concavities due to the shrinkage, and the surface interface is worth further study.

Along with better studying the formation mechanism for the two different NCT morphologies, there are several other immediate experiments that can be done to better understand how NCTs grow off of surfaces.

First, the grafting density of polymers on the substrates is unknown, and may strongly affect the binding behavior, and could be responsible for some of the differences between different polymer molecular weights. Quartz crystal microbalance experiments could be used to accurately measure the areal loading of thiolated polymer onto a gold surface.

Another unexpected observation was the presence of "hat" like structures on the top of some pyramids synthesized with longer polymers as the substrate polymer. These may be due to the dewetting of NCTs from the substrate upon drying, or an interesting feature that appears during growth. In-situ microscopy techniques could explain these results.

Furthermore, a vigorous study of concentration, cooling rate, and NCT design could reveal more about how growth occurs on the surfaces, and the resilience of NCTs to shrinking. Of particular

interest would be seeing how large a crystallite can be grown and survive the drying process, and how crystallite size compares to those grown in solution.

Finally, the presence of a surface offers many opportunities for complicated experimental design. Substrates can be lithographically patterned to favor growth in certain areas, or perhaps more sophisticated morphologies can be prepared as a result of crystallites growing into one another. The presence of a substrate also will open the possibility of performing interesting measurements, allowing for the study of NCT mechanical or optical properties (see below).

7.2 Assembly of NCTs with Anisotropic Nanoparticle Cores

A unique benefit of the NCT system is its ability to assemble into well-ordered structures, even when the nanoparticle and polymer components lack uniformity, due to the flexible nature of the polymer brush.[287] However, this complicates efforts to synthesize NCT superlattices with different crystallographic symmetry because the polymer chains can easily stretch to allow the system to still form a bcc or CsCl-type lattice, which has a deeper potential well than more exotic structures. A method to overcome the softness of the polymers is to prepare NCTs with anisotropic nanoparticles that can use the shape of the rigid inorganic core to dictate polymer brush behavior. The objective of this work will be to control the coordination environment of NCTs with their nanoparticle cores, and to determine at what ratio of polymer length to nanoparticle core size the soft brush is able to compensate for its anisotropic scaffold and still form an isotropic sphere.

Preliminary work has focused on synthesizing NCTs with FeO cubic nanoparticle cores,[312] which can be functionalized using an identical procedure as magnetite spheres.[311] When longer polymer chains are used (~13 kDa, 25 nm nanoparticle edge length), the NCTs form either bcc or (8 kDa Thy polymers) fcc lattices, depending on if the NCTs are a binary or unary system, identical to the behavior of spherical particles (**Figure 7-3**). However, as the polymer molecular weight shortens (8 kDa), a different phase appears. Efforts to isolate a pure sample of this structure have so far been unsuccessful, but analysis of both SAXS and SEM data indicate a mixture of bcc and bct (body centered tetragonal) are both forming. The region of stability for this phase appears to be small, but small modifications of the nanoparticle size, polymer length, solvent, and annealing conditions should promote the bct phase and allow for it to be fully characterized. Finally, very short polymers (4.5 kDa) favor the formation of a simple cubic lattice. This is quite surprising, as the nanoparticle surface only maintains anisotropy for a quite short brush height (~3 nm).

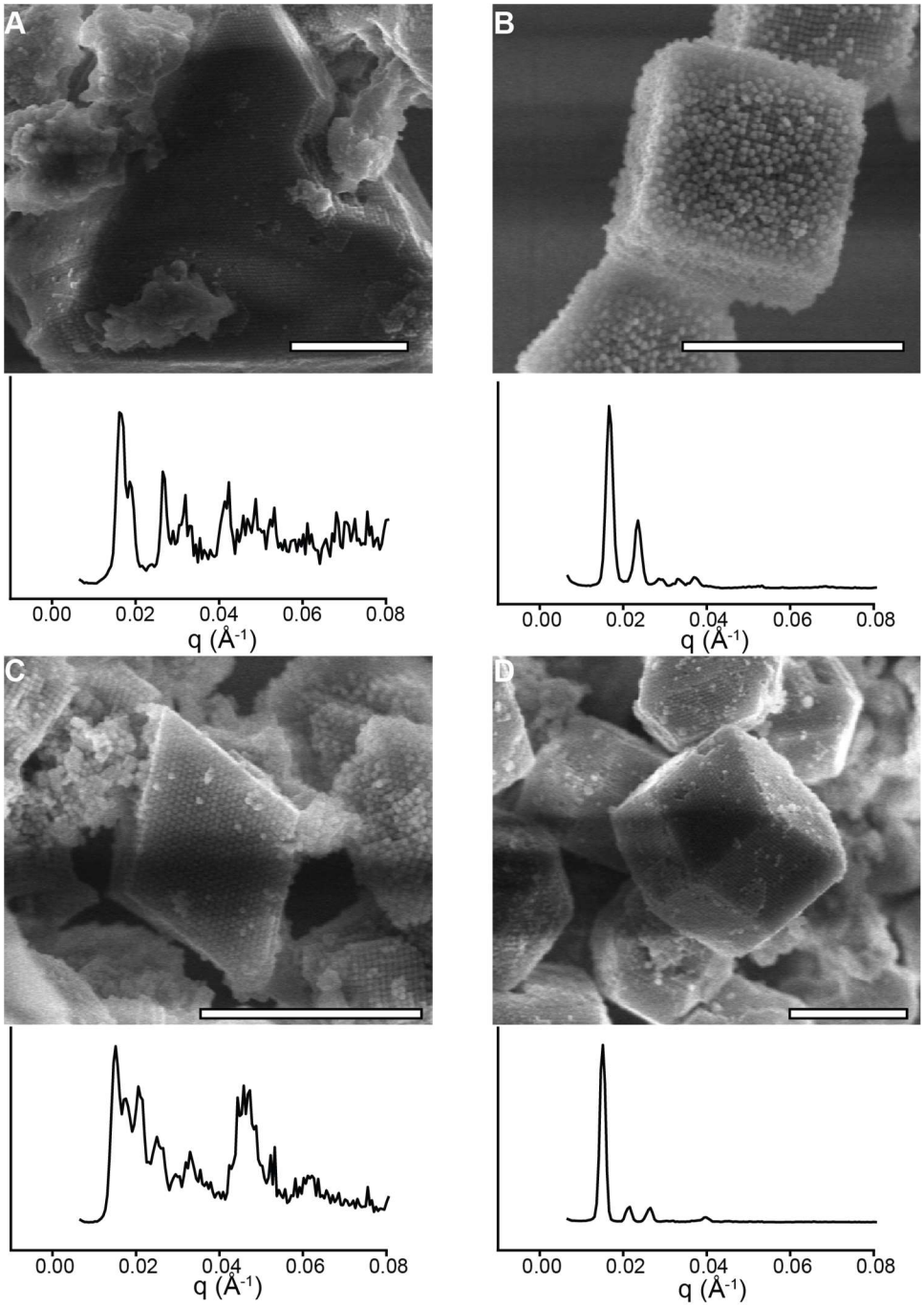

Figure 7-3. Assembly of 25 nm cubic FeO NCTs into multiple different crystal lattices. (A) SEM and SAXS of unary 8 kDa Thy NCTs forming an fcc lattice. (B) 4.5 kDa binary (DAP and Thy) NCTs form a simple cubic lattice. (C) 8 kDa binary NCTs form a mixture of phases, believed to be a mixture of bcc and bct (body centered tetragonal). (D) 13 kDa binary NCTs form a bcc lattice. Scale bars are all 1 micron.

Future work first involves creating a phase diagram of nanoparticle size and polymer length for cubic NCTs. A full range of particle sizes, and more polymer molecular weights should be studied. Focus should be placed on studying the relationship between brush height, nanoparticle size, and lattice parameter. Simple cubic and bcc phase NCTs will likely have a different dependence of brush height on polymer molecular weight, as less polymer deformation needs to occur for simple cubic lattices to form. Furthermore, the strategic addition of a non-solvent, such as decane, may allow for different phases to appear as a result of polymer brush flexibility.

Beyond the FeO cubes, different core compositions and shapes should be explored. First, cubic gold nanoparticle should be synthesized, and their behavior compared to equivalent iron oxide nanoparticles so as to determine the extent of the effects of the magnetic dipole interactions of the FeO cubes. Follow up work should involve the preparation of other nanoparticle shapes, such as rods and plates, and the coassembly of these systems with spheres and cubes to prepare a larger library of NCT phases.

7.3 NCTs with Perovskite Nanoparticle Cores

Perovskite nanoparticles are a promising nanoparticle core well-suited to the NCT system. Perovskite nanoparticles are a novel and quite interesting material because of their interesting optical properties, such as their efficient photoluminescence. However, as synthesized the perovskites are easily degraded by water, heat, and UV light, and furthermore they are chemically incompatible with other perovskites of different chemical composition. Some promising work has gone into stabilizing these perovskites with polymer shells, but the NCT system may be able to combine the extra protection of a polymer brush with the ability to self-assemble into well-defined superlattices.

Preliminary results suggest that it is possible to synthesize NCTs with perovskite nanoparticle cores, and create ordered crystals from them. A sample of $CsPbBr_3$ cubic nanoparticles was functionalized with both 10 kDa and 13 kDa Thymine terminated polystyrene with a phosphonate anchor (**Figure 7-4**). The nanoparticles are stable and maintain their photoluminescence for days in several solvents the as-prepared particles are incompatible with, such as acetone, toluene, and THF. Furthermore, these NCTs can be combined with with DAP functionalized gold nanoparticles, and self-assemble. DAP polymers appear to be incompatible with the perovskites, likely due to

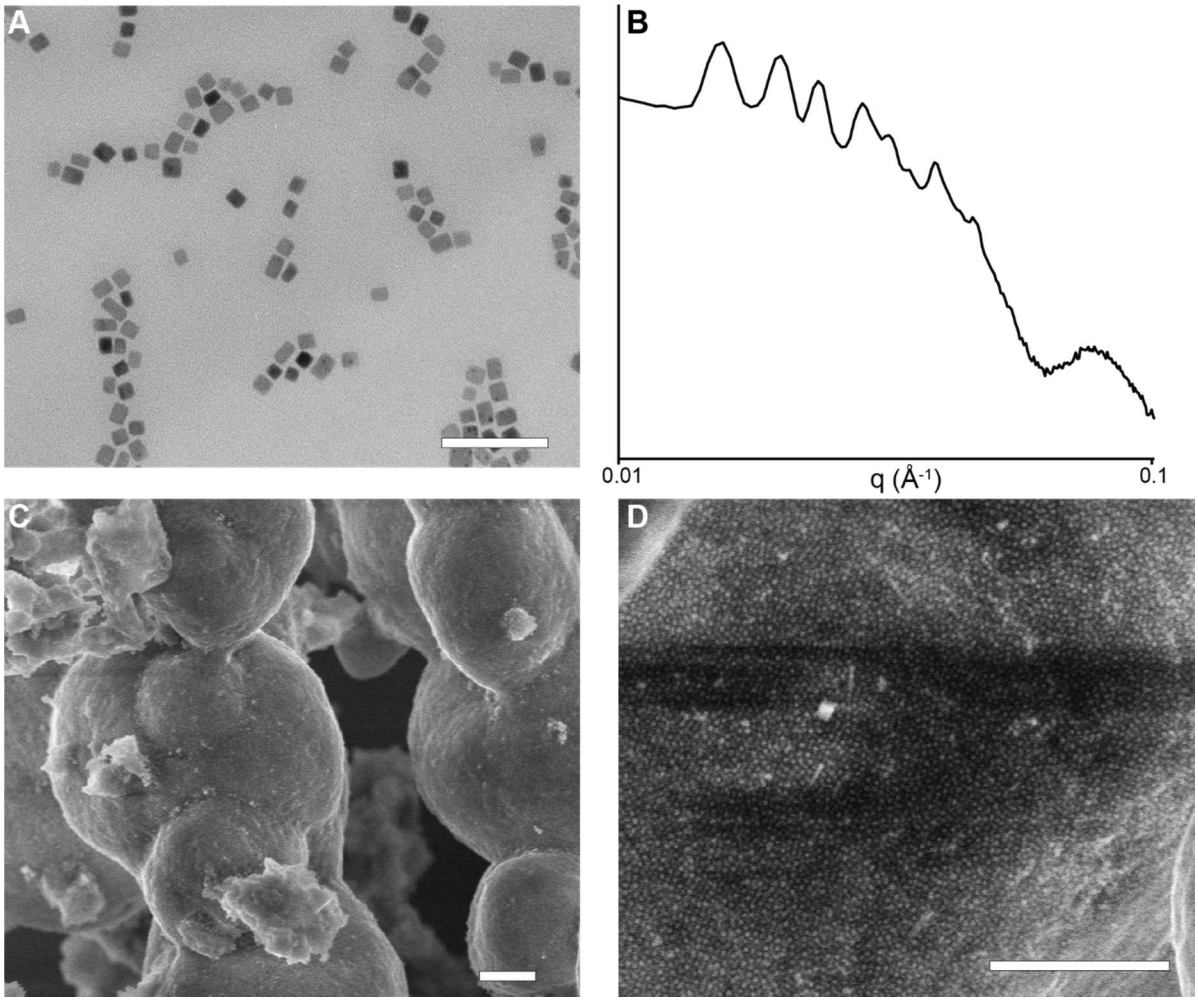

Figure 7-4. NCTs made with perovskite nanoparticle cores. (A) TEM of perovskite nanoparticles coated with 13 kDa Thy polymer. Scale bar is 100 nm (B) SAXS of 14 kDa DAP, 15 nm Au-NCTs combined with the perovskites and annealed. A highly crystalline structure is formed, but the phase is still unknown. It may be related to the Th_3P_4 lattice. (C) and (D) SEM images of the crystals formed with the gold nanoparticles and perovskites. The spherical structure may indicate the stoichiometry was mismatched, but they appear to be ordered. Scale bar is 500 nm.

residual copper from the synthesis. Future work will attempt to understand the effect of DAP polymers on the perovskites, and find a method for functionalizing them. The gold-perovskite mixed assemblies were annealed, and yielded a highly crystalline structure. The SAXS pattern does not appear to match any previously reported lattices, but may be related to the Th_3P_4 crystal structure due to the position of its peaks, though the intensity of the peaks do not match precisely.

Additional data and an SEM cross section would be able to confirm that structure, or suggest an alternative one. SEM images of the exterior of the crystallites indicate the stoichiometry was likely off during synthesis, as evidenced by their spherical shape. However, they do appear crystalline. Interestingly, the assemblies of gold and perovskite NCTs do not appear to photoluminesce, which may be a result of the gold nanoparticle quenching the perovskite. After optimizing the synthesis of perovskite NCTs and understanding their crystallization behavior, it will be possible to perform several interesting experiments to study the optical properties of NCTs, such as monitoring energy transfer between perovskite nanoparticles adjacent to gold, or other perovskite nanoparticles.

7.4 The Effect of Magnetic Fields on NCT Assembly

The ability to synthesize NCTs with magnetically responsive nanoparticle cores opens up new routes for manipulating their assembly process. Magnetic fields are a convenient method for manipulating nanoscale materials because they can be applied macroscopically without any specialized equipment, their strength can be easily modulated by manipulating the distance of the magnets to the sample, and magnetic forces will only affect certain types of materials and so they will not interfere with the solvent or the vessel used to hold the sample.

These advantages have led to the application of magnetic nanoparticles for medicine. In one therapy, particles are delivered to a cancer cell, and heated in an oscillating magnetic field. This magnetic hyperthermia causes cell death, but in the limited area of the cancer cells.[60] This technique may be particularly interesting for NCTs because of their temperature-dependent assembly, and their ability to crystallize after annealing. Furthermore, assemblies of nanoparticles respond differently to alternating magnetic fields,[313,314] and so it may be possible to selectively anneal NCTs of certain crystallite sizes. Ideally, smaller aggregates could be destroyed by the magnetic heating, therefore causing larger ones to grow.

Additionally, assembling NCTs in the presence of a magnetic field may dramatically affect their microstructure, as applying a magnetic field orients the dipoles in magnetic nanoparticles, which will then attract one another. Consequently, NCTs that formerly attracted each other through a mostly isotropic interaction now would experience symmetry breaking. Indeed, preliminary results (**Figure 7-5**) show that FeO cubes assemble into long, noodle-like structures when annealed in the presence of a magnet. Interestingly, these NCTs are still able to retain their ordering, which SAXS

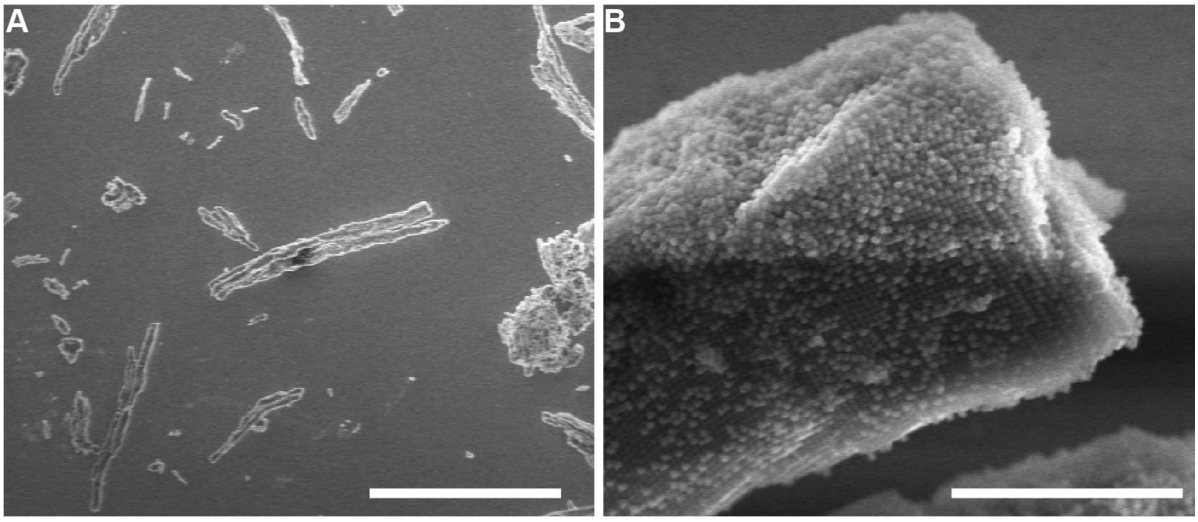

Figure 7-5. NCTs synthesized with FeO cube cores, assembled in the presence of a magnetic field. (A) The NCTs make long, noodle-like structures. Scale bar is 20 microns. (B) However, the NCTs keep their ordering, in this case a bcc crystal. Scale bar is 1 micron.

confirms to be identical (either bcc or fcc) to how they would assemble without the additional stimulus.

Some work has been done with the PAE system that shows similar behavior with magnetic field directed assembly, including some modeling that suggests that the PAEs may assemble into larger clusters first before being driven to make the elongated structures by the magnetic field.[315]

Further work with the NCT system should focus first on better understanding the mechanism of elongated structure formation. A range of particle sizes, polymer lengths, and magnetic field strengths should be applied to identify trends in how the binding energy between particles competes with magnetic dipole coupling. Additionally, this work should be combined with efforts to grow NCT crystallites off of surfaces. Ideally, the alignment of the substrate should allow for NCTs to be grown oriented parallel or perpendicular to the magnetic field.

7.5 The Effects of NCT Assembly on Magnetic Behavior

NCTs may make uniquely functional composites because they can control the nanoscale structure of the particles within the nanocomposite. This may be of particular use for magnetic nanocomposites, because the interactions between magnetic nanoparticles are strongly distance and orientation dependent.

The first key set of experiments that must be performed is to determine at what interparticle distances NCTs show detectible differences in magnetic behavior. NCTs with multiple different magnetic nanoparticle core compositions should be synthesized, and assembled with different lengths of polymer. There exists a large number of magnetic nanoparticle core types, including other transition metal oxides and rare earth elements, which all have unique magnetic responses. It may be desirable to pursue magnetic materials that can more strongly be polarized so has to maximize the chance that their dipole coupling between particles will yield significant results.

These samples can be characterized with field cooling / zero field cooling measurements to determine their blocking temperature, which should begin to rise when the particles are sufficiently close. More complex alternating field measurements and advanced AFM and EM techniques can also be performed to understand how the magnetic dipoles orient within an NCT crystalline lattice.

When the extent of NCT dipole coupling is fully understood, there are several properties worth trying to measure. First, it would be a significant achievement to measure dipolar ferromagnetism or antiferromagnetism in an NCT crystal. Because magnetic nanoparticles are small, they cannot stabilize a magnetic domain, and as a result thermal energy is sufficient to cause their magnetic dipole to realign, making the particles superparamagnetic. However, compelling theoretical and some experimental evidence suggests that arranging the magnetic nanoparticles in a lattice with particular symmetries may allow adjacent particles to stabilize one another's dipoles, creating a lattice that is either ferromagnetic or antiferromagnetic.[46,47,316] Lattices with bcc or fcc symmetry are predicted to be ferromagnetic while simple cubic lattices are predicted to be antiferromagnetic, all of which are phases that NCTs are capable of making.

Additionally, NCTs can use their ability to program the relative position of different nanoparticle compositions to create materials with novel magnetic properties. For instance, there is typically a tradeoff between the magnitude of the magnetic moment of a material and the amount of energy it takes to flip its spin. Or in other words, magnetic hysteresis loops tend to either be "tall" or "wide". However, with NCTs it would be possible to position adjacent particles with high coercivity and high saturation magnetization next to one another, to create a "dipolar exchange spring". Consequently, NCT-based magnetic composites may be very useful because they could allow for the programming of magnetic behavior and create materials with novel magnetic properties.

7.6 Mechanical Properties of NCTs

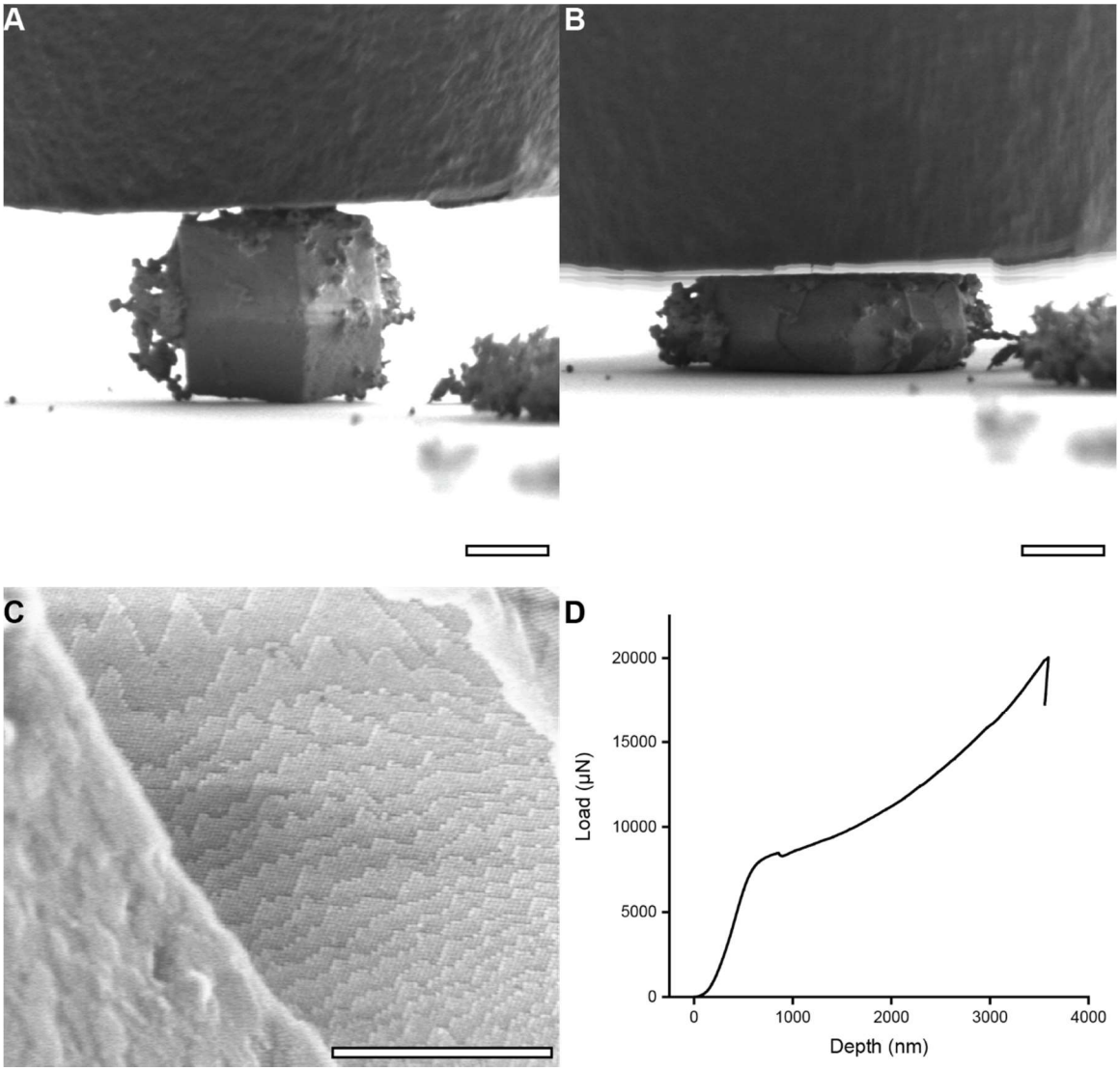

Figure 7-6. Mechanical testing of NCT crystals. 15 nm Au NCTs with 14 kDa polymer brushes were assembled into bcc crystals, and their resulting Wulff polyhedra. (A) SEM image before deforming with an in-situ picoindenter. (B) SEM image after deformation. The scale bar for (A) and (B) is 5 microns. (C) Post-mortem SEM imaging inside a crack that formed during indentation, scale bar 1 micron (D) Load-displacement curve of the experiment.

The NCT system is capable of creating solid composite materials with precisely controlled nanoscale structure, and therefore they may have unique mechanical properties. Furthermore, because they are crystalline, the NCT system can be treated as an analogue to atomic materials with each NCT representing an atom, but the NCTs can be easily visualized in an SEM and so

phenomena in metals and ceramics such as crack propagation and dislocation motion can be studied.

Initial experiments suggest that studying the mechanical properties of NCTs will be possible, and may reveal interesting results (**Figure 7-6**). Au-NCTs were crystallized to form large Wulff polyhedra, and cast onto a silicon substrate after undergoing the standard polymer brush collapse procedure. The sample was then loaded into an SEM with an in-situ picoindenter, and crushed with a punch. After being pressed, crack plane surface was imaged, demonstrating it is possible to gain information about how the nanoparticles respond to strain.

There are numerous experiments that could be performed to understand the mechanical properties of NCTs. It will first be necessary to determine the effect of nanoscale ordering on mechanical response. Single crystals of NCTs, amorphous samples, and blended composites of nanoparticles and polystyrene should all be compared to determine if positioning the nanoparticles in an ordered array changes their mechanical strength. Furthermore, single crystalline samples should be compared with polycrystalline ones, including the bulk, sintered polycrystalline NCT solids. Additionally, single crystalline samples should be indented at multiple different angles to determine if the NCTs exhibit anisotropy. It will also be interesting to study NCTs that assemble into different crystallographic phases and compare their relative properties with atomic materials, for instance if fcc crystals slip more easily than bcc, or if there is an effect of crystallite size due to the changing surface to volume ratio. Focus should be placed on understanding the deformation mechanisms in NCTs, identifying preferred slip planes, how dislocations or cracks nucleate and propagate, and how the NCTs recover after deformation. Consequently, the ability to easily tune the NCT design variables will make it possible to develop a set of rules for engineering the strongest and toughest composites.

However, several experimental modifications can be made that would improve the measurements. First, the Wulff polyhedra were not strongly affixed to the substrate, and so could be easily moved with the punch, or would detach from the surface due to static electricity. Furthermore, this would complicate efforts to understand the effects of crystallite anisotropy on mechanical strength, as it would be impossible to control which plane was being indented. An additional challenge was that the NCTs undergo significant charging, which makes it difficult to obtain the necessary resolution to observe individual particles during deformation. Many of these barriers could be ameliorated by synthesizing Winterbottom constructions on the substrate (see section 7.1). As it would be

possible to control if a facet or a corner was normal to the surface, experiments could be performed to test how different slip planes respond to deformation in the NCT system. Moreover, these crystallites would be bound to the substrate, and so would remain stationary during measurement, and may charge less in the electron beam. Changing the NCT design to use larger nanoparticles, and applying a thin coating of gold may further improve the ability to observe individual nanoparticles during deformation.

7.7 Understanding the Post-Crystallization Processing of NCTs

The recent discovery of sintering in NCTs merits further study to determine what comparisons can be made with more traditional atomic materials. Current NCT solids that are gently pressed so as to maintain crystalline ordering tend to be quite brittle, but materials that are pressed with a significant amount of force (5,000 kg) appear to be more robust, but lose their crystallinity. This may be a result of incomplete sintering, where small voids in the solid serve as sites for crack nucleation. Developing a more thorough understanding of NCT sintering may allow for an optimal process to be developed that results in fully compact materials that maintain their crystallinity.

During sintering in atomic materials, several processes occur. First, particles deform under added stress or temperature, and void space is filled by the flowing material. Then, grain boundaries will diffuse as grain growth occurs.[317] The first stage does appear to happen in NCTs, as FIB cross sections reveal deformed grains and regions of necking. However, grain boundary diffusion was limited, potentially due to the slower kinetics of large NCTs as compared with smaller atoms. The key experiment to perform here will be sintering together NCT crystallites of different compositions, such as gold and iron oxide, so that any grain boundary diffusion would be easy to identify under SEM. A number of variables such as centrifugation time, speed, and the temperature of the solution can all be explored to determine the optimal processing conditions for the NCT solids. Furthermore, direct measurement of grain boundary motion is a challenge in traditional materials, and so the orthogonality of the NCT nanoparticle cores to their overall size and chemical behavior can be taken advantage of. Potentially, a process could be designed to yield very large crystalline grains, perhaps 100 microns in diameter.

7.8 Preparing NCTs with Novel Properties

Along with developing a more complete understanding of NCT self-assembly, future research should focus on creating new devices and materials with properties that can only be produced with the NCT design concept.

An exciting avenue that could be pursued involves barium titanate ($BaTiO_3$) particles. Phosphonate anchors have been previously shown to bind to these types of nanoparticles, and so the same polymers used for functionalizing iron oxide NCTs could be applied here.[79] Barium titanate is a particularly interesting material because of its piezoelectricity; applying a voltage can cause the atomic crystal lattice to strain. In the NCT system, this could be exploited by assembling the particles into a lattice, thereby giving them an additional degree of anisotropy.

A further direction worthy of exploration involves creating novel optical and plasmonic materials. The close interparticle spacing of NCTs in the collapsed state should allow for coupling between adjacent gold nanoparticle cores, and this hypothesis is supported by the gold coloration of large crystallites viewed optically. The most exciting set of experiments revolve around the delocalization of energy due to the periodic lattice of the NCTs, which could result in significant shifts in the optical constants of the material. The optical properties of NCTs could be further manipulated by inserting polymers or small molecules with high refractive indices or strong light absorbance into the polymer brush. Furthermore, unique properties could be added to the NCT system by tweaking the microstructure of the material. Some preliminary work has shown that it is possible to synthesize core-shell structures where NCTs of two different compositions assemble into a Wulff polyhedra and then an outer shell. This could be used to create novel optical responses in the same fashion as core-shell nanoparticles. Moreover, the collapsing of the polymer brush could be used to generate a system where the two nanoparticles are size-matched in solution, but upon drying they are significantly different sizes and detach from each other. These complex architectures would be difficult to fabricate using any method other than the NCTs. Additionally, macroscopic processing could be used to create multilayer materials where different compositions of NCTs are stacked on top of one another and pressed to form a single solid.

Finally, it will be critical to examine the entire range of compositions for NCTs. One of the greatest advantages of NCTs is their ability to orthogonally change the nanoparticle core, the polymer shell,

and the supramolecular binding group. This broad design space is an exciting opportunity for producing the next generation of advanced composite materials.

Appendix 1. Supplementary Information for Self-Assembling Nanocomposite Tectons

A1.1 Materials and Characterization Methods

2,6-Diaminopyridine, thymine, acetyl chloride, 11-bromoundecan-1-ol, 2-Bromoisobutyryl bromide, styrene, N,N,N',N",N'"-Pentamethyldiethylenetriamine (PMDETA), Tris[2-(dimethylamino)ethyl]amine (Me_6TREN), and basic alumina were purchased from Fisher Scientific. Copper bromide was purchased from Sigma Aldrich. Aminoethanethiol was purchased from TCI America. General solvents were purchased from Fisher Scientific. Aqueous gold nanoparticle dispersions are purchased from Ted Pella Inc. All chemicals, including solvents, were used without further purification, except styrene, which was passed through a short column of basic alumina to remove inhibitor prior to polymerization. Note that some solvents were purchased as anhydrous grade, as noted in the experimental details. Centrifugation was performed with an Eppendorf 5424 centrifuge. ^{1}H NMR spectra were obtained on a Varian 300 MHz instrument. Gel permeation chromatography (GPC) characterizations were performed on an Agilent Technologies GPC system, with THF as the eluent at 1.0 mL/min, and monodisperse polystyrene as the standard. UV-vis spectra and measurements were obtained on a Cary-500 or Cary-50 Bio spectrometer. TGA measurements were taken on a TGA Q50 V6.7 Build 203 instrument. Small angle X-ray scattering (SAXS) measurements were performed on a SAXSLAB instrument with a Pilatus3R 300K detector and an X-ray wavelength of 1.54Å. Transmission electron microscopy (TEM) was performed with a JEOL 2010 Advanced High Performance transmission electron microscope.

A1.2 Synthesis

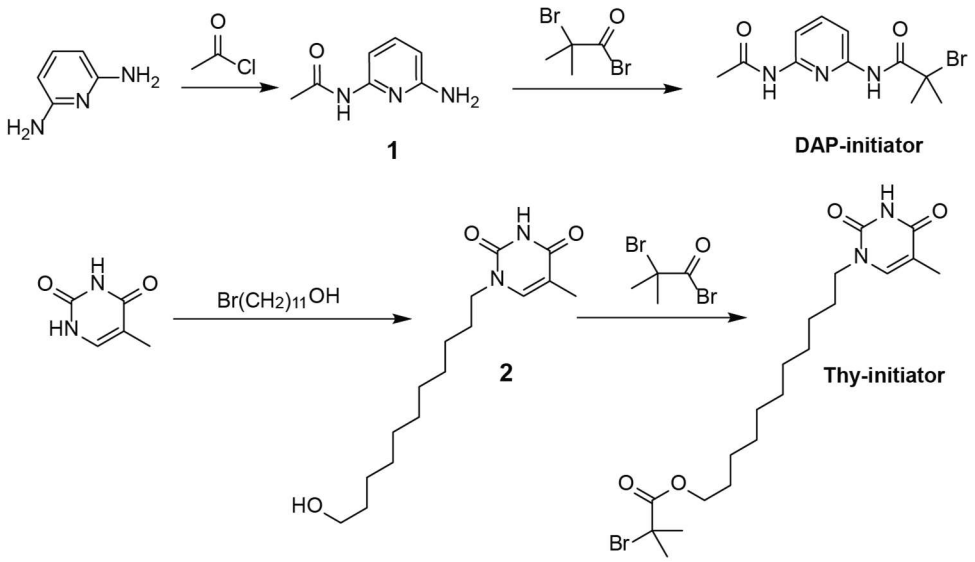

Scheme S1-1. Synthetic route to the DAP-derivative and Thy-derivative as ATRP initiators

A1.2.1 DAP-initiator

5.5 g 2,6-diaminopyridine (50 mmol) was dissolved in 40 mL dry THF in a 3-necked round bottom flask. At 0 ^{0}C, the solution of 1.96 g (25 mmol) acetyl chloride in 15 mL dry THF was added dropwise under a nitrogen atmosphere. The reaction mixture was allowed to warm to room temperature and stirred for 12 hours. The insoluble content was filtered off, and the solvent was removed under reduced pressure. The resulting solid was recrystallized in a mixture of ethanol and toluene, to afford 1 as a white solid (52%). ^{1}H NMR ($CDCl_3$, δ ppm): 7.55-7.65 (broad, s, 1H), 7.49-7.54 (broad, d, 1H), 7.45 (t, 1H), 6.25, (d, 1H), 4.32, (s, 2H), 2.16 (s, 3H).

1.9 g 1 (12.6 mmol) was dissolved in 80 mL dichloromethane, and then 3.5 mL trimethylamine (25 mmol) was added. The mixture was cooled to 0 ^{0}C, and a solution of 3.22g 2-Bromoisobutyryl bromide (17.6 mmol) in dichloromethane (~10 mL) was added dropwise under a nitrogen atmosphere. The reaction mixture was allowed to warm to room temperature and stirred for 12 hours. The insoluble content was filtered off, and the filtrate was washed with a sodium carbonate solution (x1) and saline (x3). The organic phase was dried over sodium sulfate, the solvent was removed under reduced pressure, and the product was then purified by flash chromatography ($CHCl_2$/EtOAc 4:1). The product was further purified by recrystallization in

$CHCl_2$/EtOAc/hexanes to afford the DAP-initiator (79%). ^{1}H NMR ($CDCl_3$, δ ppm): 8.74 (s, 1H), 7.90-7.96 (d, 1H), 7.83-7.89 (dd, 1H), 7.70-7.76 (t, 1H), 7.68-7.82 (broad, s, 1H), 2.21 (s, 3H), 2.04 (s, 6H).

A1.2.2 Synthesis of Thy-initiator

5.0 g thymine (40 mmol), 1.0 g 11-bromo-1-undecanol (4 mmol), 1.1 g potassium carbonate (8 mmol) and 200 mL DMSO were added to a 500 mL round bottom flask. The mixture was stirred and bubbled with nitrogen for 2 minutes, and then sealed with a septum and stirred for 48 hours. The resulting mixture was poured into water and chloroform for extraction, and the organic phase was collected and washed 3 more times with brine, followed by drying over sodium sulfate and removal of solvent. The resulting white solid was recrystallized in EtOAc/hexanes to afford compound 2 (84%). ^{1}H NMR ($CDCl_3$, δ ppm): 8.18 (s, 1H), 6.97 (d, 1H), 3.66-3.71 (t, 2H), 3.60-3.66 (t, 2H), 1.92 (d, 3H), 1.22-1.75 (m, 18 H).

With the help of very gentle heat, 592 mg 2 (2 mmol) was dissolved in 150 mL dichloromethane, and 0.39 mL trimethylamine (2.8 mmol) was added to the solution. The mixture was cooled to 0 ^{0}C, and a solution of 552 mg 2-bromoisobutyryl bromide (2.4 mmol) in dichloromethane (~ 10 mL) was added dropwise under a nitrogen atmosphere. The reaction mixture was allowed to warm to room temperature and stirred for 14 hours, and then washed with sodium carbonate (x2) and brine (x2). The organic phase was dried with sodium sulfate, and the solvent was removed under reduced pressure. The resulting mixture was purified by flash chromatography ($CHCl_2$/EtOAc 8:3), to afford the product (Rf = 0.4) Thy-initiator as an off-white solid. ^{1}H NMR ($CDCl_3$, δ ppm): 9.86 (s, 1H), 6.96 (d, 1H), 4.08-4.15 (t, 2H), 3.60-3.68 (t, 2H), 1.88 (s, 6H), 1.87 (d, 3H), 1.55-1.70 (m, 4H), 1.15-1.38 (m 14H).

A.1.2.3 Synthesis of DAP-PS polymers

In a typical polymerization process, DAP-initiator (1.0 eq), Me_6TREN (1.2 eq), styrene (100-200 eq depending on target molecular weight), and anhydrous DMF (1:1 v/v to styrene) were added to an oven-dried and nitrogen filled Schlenk flask. The reaction flask was then sealed with a rubber septum and the mixture was taken through 3 freeze-pump-thaw cycles and refilled with nitrogen. Once the mixture returned to room temperature, the septum was removed, CuBr (1.2 eq) was quickly added against a positive nitrogen flow, and the flask was immediately resealed. The mixture was stirred at 110 ^{0}C under a nitrogen atmosphere, and quenched at different time points

to give polystyrene of different molecular weights. The typical reaction time was 1-4 hours. To quench the reaction, the reaction mixture was poured into cold methanol, and the precipitated polymer was collected, redissolved in dichloromethane, and precipitated in methanol again to afford the polymer with a chain-end bromine.

Purified polystyrene obtained from DAP initiator was then dissolved in DMF (~ 10 mg/mL) with a small amount of trimethylamine (40 eq), and the solution was bubbled with nitrogen for 5 minutes, followed by the addition of 2-aminoethanethiol (15 eq). The reaction flask was capped, and the solution was stirred for 60 hours, then poured into a mixture of dichloromethane and brine. The organic phase was washed with brine repeatedly (x3), concentrated, and precipitated in methanol (redissolve-precipitate x4). The resulting white powder was dried under vacuum to give the DAP-PS polymer.

A1.2.4 Synthesis of Thy-PS

In a typical polymerization process, Thy-initiator (1 eq), PMDETA (1 eq), styrene (200 eq), and anhydrous anisole (30 v% to styrene) were added to an oven-dried and nitrogen filled Schlenk flask. The reaction flask was then sealed with a rubber septum and the mixture was taken through 3 freeze-pump-thaw cycles and refilled with nitrogen. Once the mixture returned to room temperature, the septum was removed, CuBr (1 eq) was quickly added against a positive nitrogen flow, and the flask was immediately resealed. The mixture was stirred at 110 ^{0}C under a nitrogen atmosphere, and quenched at different time points to give polystyrene of different molecular weights. Typical reaction time was 1-3 hours. To quench the reaction, the reaction mixture was poured into cold methanol, and the precipitated polymer was collected, redissolved in dichloromethane, and precipitated in methanol again to afford the polymer with a chain-end bromine.

The polymer was subsequently dissolved in DMF (~ 10 mg/mL) with small amount of trimethylamine (40 eq), and the solution was bubbled with nitrogen for 5 minutes, followed by the addition of 2-aminoethanethiol (15 eq). The reaction flask was capped, and the solution was stirred for 60 hours, then poured into a mixture of dichloromethane and brine. The organic phase was washed with brine repeatedly (x3), concentrated, and precipitated in methanol (redissolve-precipitate x4). The resulting white powder was dried under vacuum to give the Thy-PS polymer.

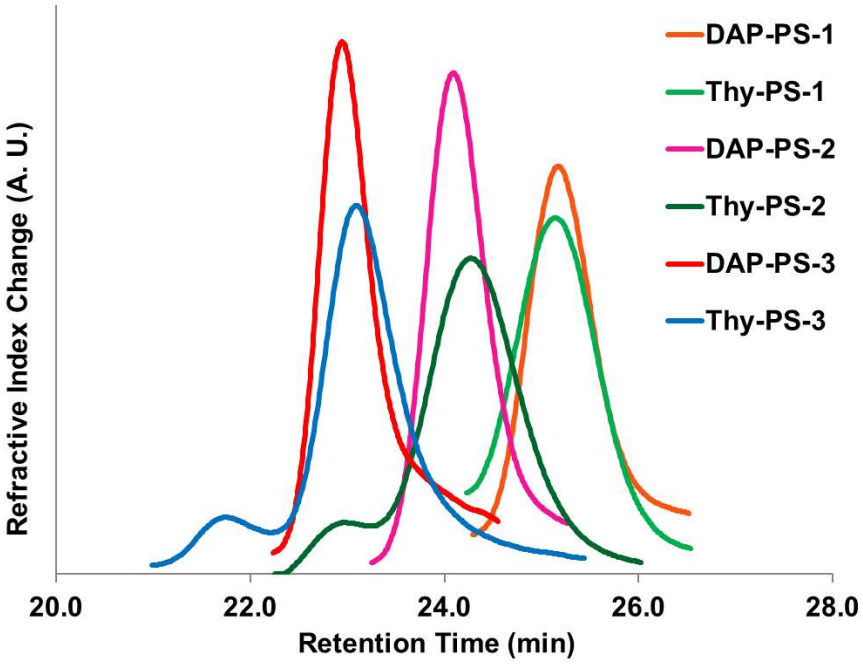

Figure S1-1. GPC traces of the DAP-PS and Thy-PS polymers used in this work. Eluent: THF, 1 mL/min.

	DAP-1	Thy-1	DAP-2	Thy-2	DAP-3	Thy-3
Mn	3800	3900	5900	5500	11600	11200
PDI	1.07	1.07	1.04	1.10	1.06	1.11

Table S1-1. Molecular weight and polydispersity index of the DAP-PS and Thy-PS polymers.

A1.2.5 Synthesis of NCTs

In a typical synthetic process, an appropriate amount of DAP-PS or Thy-PS polymers was dissolved in 5.0 mL of acetone in a glass vial to yield a 1.3 * 10^{-4} M solution. The solution was vigorously stirred while 5.0 mL of gold nanoparticle (AuNP) solution was quickly poured into the vial, and the resulting suspension was allowed to stir for 1 hour. After the formation of dark red precipitate on the wall and at the bottom of the vial, the colorless supernatant was removed by direct decantation or with the aid of light centrifugation. DMF (5-6 mL) was added to the vial to redisperse the precipitate, and the resulting dispersion was distributed in centrifuge tubes and purified for 3 centrifuge cycles. The centrifuge protocols (table S2) were mainly determined by

the particle size, while the polymer length had very limited influence. The solvents used to redisperse the AuNPs precipitate at the end of each cycle were DMF, toluene, and toluene, respectively, and the final toluene dispersions were used for the self-assembly experiments.

Particle Size (nm)	Protocol
10	13,000 RPM, 60 min
15	7,000 RPM, 50 min
20	7,000 RPM, 30 min
40	2,500 RPM, 25 min

Table S1-2. Centrifuge protocol for different AuNP sizes.

A1.3 Characterization of NCTs

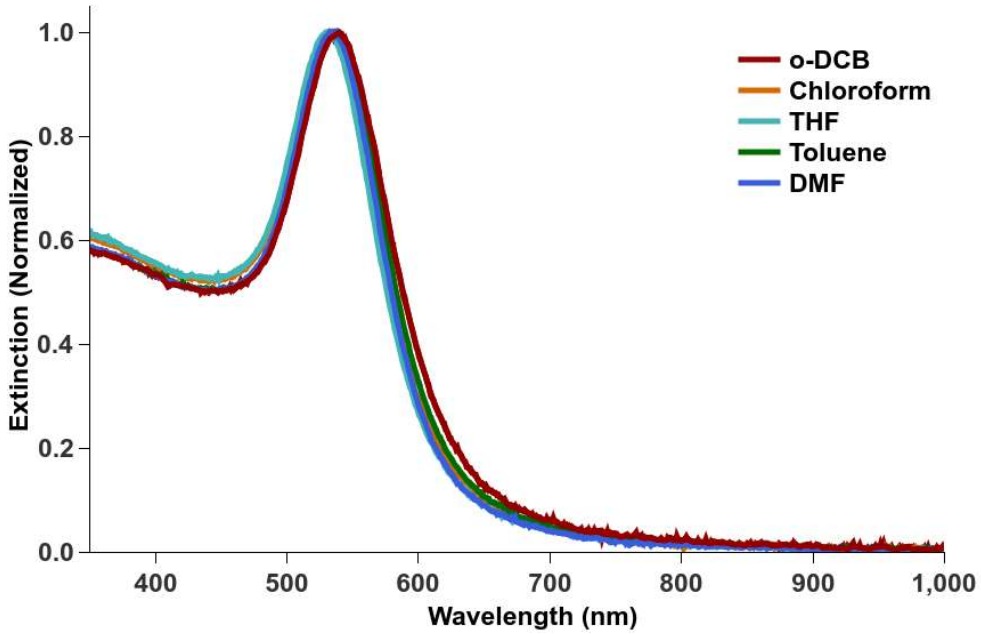

Figure S1-2. Representative UV-vis-NIR spectra of NCTs (DAP-PS-3, 20 nm AuNP) in organic solvents.

UV-vis-NIR spectroscopy of NCTs: The NCTs made from different polymers (DAP-PS and Thy-PS, of varied molecular weight) and AuNPs in the targeted size range (10-40 nm) formed stable dispersions in common organic solvents, with a plasmonic extinction peak between 530-540 nm, with a slight variation for different solvents due to differences in solvent refractive index. As a

representative example, the UV-vis-NIR spectra of NCTs from DAP-PS-3 and 20 nm AuNP in o-dichlorobenzene (o-DCB), chloroform, tetrahydrofuran (THF), toluene and N,N'-dimethylformamide (DMF) are displayed in **Figure S1-2**.

Thermal gravimetric analysis (TGA): An NCT solution in dichloromethane was drop cast on a platinum TGA pan, and allowed to fully evaporate before loading into the instrument. The sample was then ramped at 15 °C per minute up to 600 °C. The starting mass was taken to be the mass at 200 °C, and the final mass taken to be after the mass loss event. Grafting density in chains/nm^2 was then calculated by:

$$\sigma = \frac{m_{Polymer} * N_A * \rho_{Au}}{m_{NP} * MW_{Polymer} * D_{NP} * (6 \cdot 10^{21})}$$

where $m_{polymer}$ is the mass fraction of the polymer by TGA, N_A is Avogadro's number, ρ_{Au} is the density of gold, m_{NP} is the nanoparticle mass fraction, $MW_{Polymer}$ is the polymer's number-averaged molecular weight, D_{NP} is the nanoparticle diameter, and $6 \cdot 10^{21}$ contains geometric constants and an appropriate scaling factor. The grafting density values are shown in **Figure S1-3**. The grafting density of the 10 and 20 nm AuNPs is approximately 0.7 chains/nm^2. The larger 40

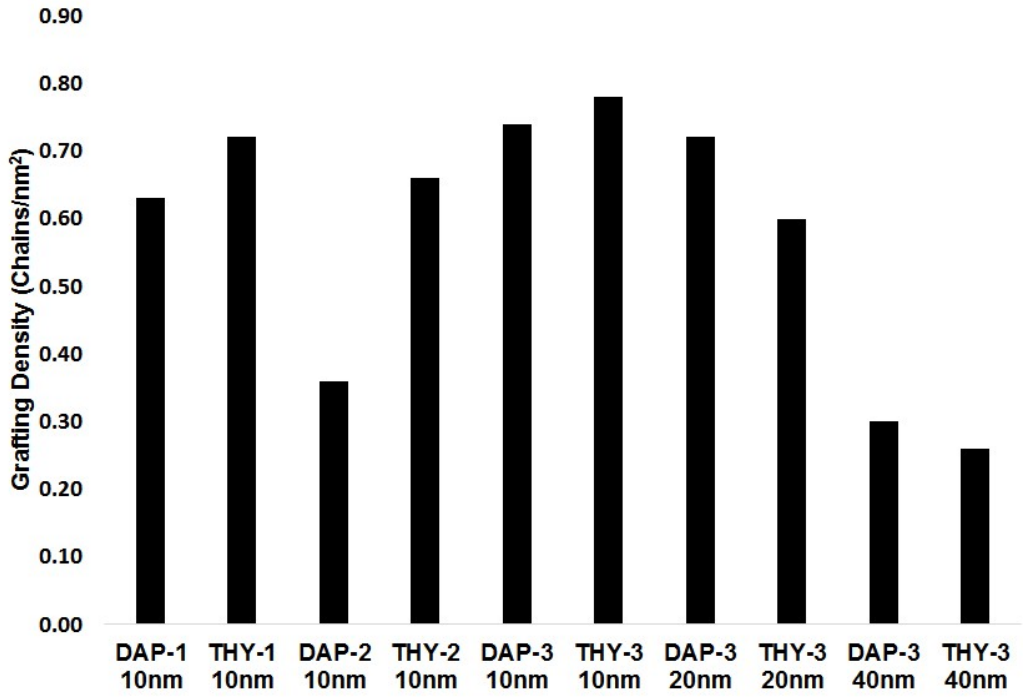

Figure S1-3. Loading density of different NCTs based on TGA data.

nm particles have a lower grafting density of approximately 0.3 chains/nm^2, which could be due to the lower curvature of the particles. For 10-20 nm NCTs, there is no clear trend in grafting density regarding polymer ligand length.

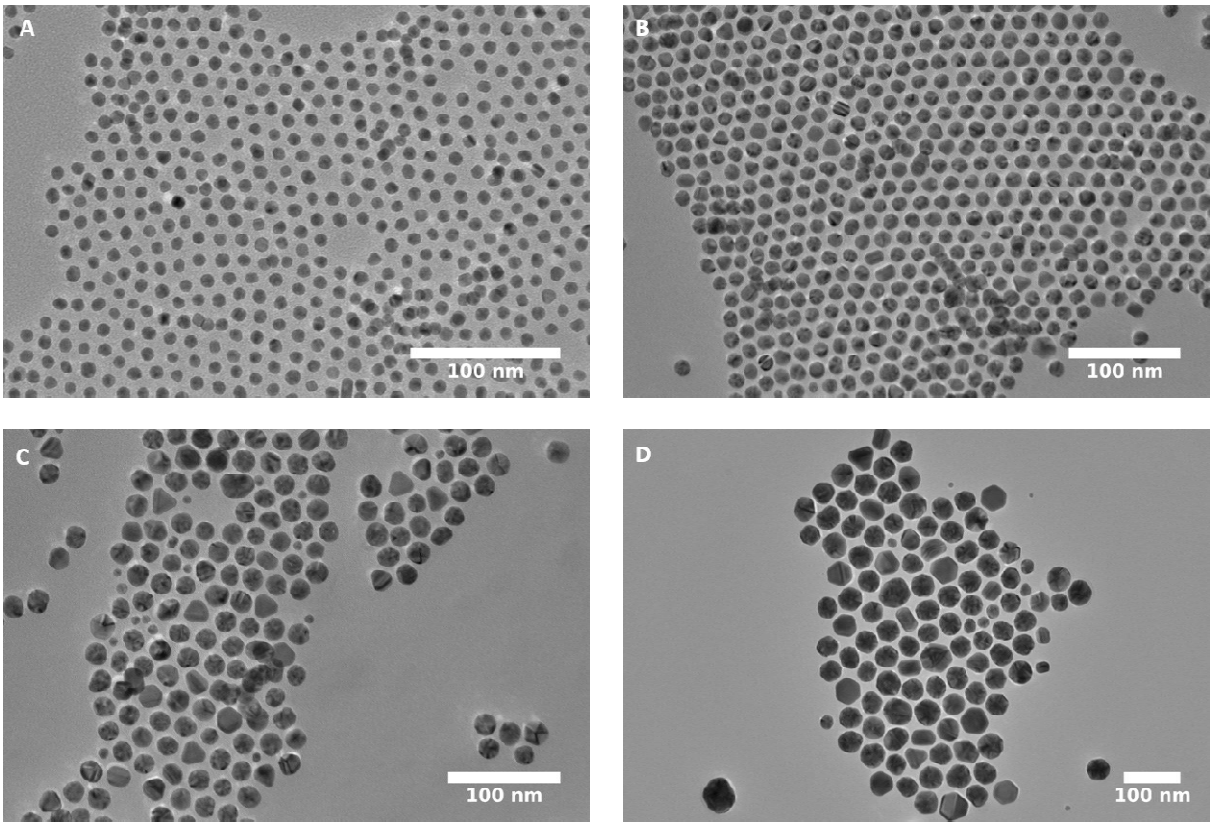

Figure S1-4. TEM micrographs of unassembled, polymer-grafted particles with nominal diameters of (A) 10 nm (B) 15 nm (C) 20 nm (D) 40 nm. Scale bars are 100 nm. Particles were functionalized with polystyrene using the same protocol used for synthesizing NCTs and drop cast from DCM onto formavar coated TEM grids

Sample Name	Measured Diameter	Dispersity
Ted Pella 10 nm	8.7 nm	14 %
Ted Pella 15 nm	13.4 nm	16 %
Ted Pella 20 nm	17.6 nm	12 %
Ted Pella 40 nm	37.3 nm	14 %

Table S1-3. Measured diameter and dispersity of gold nanoparticles purchased from Ted Pella, using the images in **Figure S1-4**. Analysis was performed in ImageJ.

A1.4 Study of the self-assembly behavior of NCTs

A1.4.1 Thermal Analysis of NCT Assembly

Melt analysis was performed on a Cary-500 UV-Vis Spectrophotometer with a thermal multicell accessory. Before the experiment, a clean quartz cuvette was treated with hexamethyldisilazane (HMDS) by solvent annealing in a 1:1 HMDS:n-hexane solution in a sealed chamber at room temperature for 20 hours. Then, in a typical experiment, equal volumes of DAP and Thy NCTs in toluene at the same optical density were mixed in the treated quartz cuvette and allowed to completely assemble. The cuvette was then placed in the thermal multicell accessory, and heated at a rate of 0.25°C/minute. The extinction was monitored at 520 nm to generate the melt profiles, and normalized to generate **Figure 2-3**.

A1.4.2. Heat-cool cycles of NCT assembly

To analyze the reversibility of NCT assemblies (**Figure 2-2C**), equal volumes of complementary (DAP-PS and Thy-PS functionalized) NCTs in toluene at the same optical density with 20 nm cores and 11.0 kDa polymers were mixed in an Eppendorf microcentrifuge tube. The sample was subjected to through multiple heat-cool cycles between 55 °C and 20 °C (room temperature). At each temperature, an aliquot was taken and its UV-vis spectrum was recorded in a multicell accessory preset at the same temperature. **Figure 2-2C** was generated with the extinction difference between 520 nm and 600 nm to reflect the spectral change.

A1.4.3 Crystallization of NCT assemblies

The NCT assemblies were formed by mixing NCTs with complementary supramolecular bonding groups in toluene. After the assembly was completed, the samples were annealed in solvent at a temperature just below the melting temperature for 3 hours. The specific annealing temperatures were 37 °C for NCTs made from 20 nm AuNPs and 11.0 kDA PS, at 32 °C for NCTs made from 10 nm AuNPs with 6.0 kDA PS, and 20 °C for NCTs made from 10 nm AuNPs and 11.0 kDA PS. Small angle X-ray scattering (SAXS) experiments: SAXS was performed at the Massachusetts Institute of Technology (MIT) Center for Materials Science and Engineering (CMSE) X-ray Diffraction Shared Experimental Facility on a SAXSLAB system. The Rigaku 002 microfocus X-ray source produced Cu $K_{\alpha 1}$ x-rays of wavelength 1.5409 Å; Osmic staggered parabolic multilayer optics focused the beam crossover at the second pinhole. Two sets of JJ X-ray jaw collimation slits

set at 0.45mm and 0.2mm, respectively, were used to define the beam. The system was calibrated using silver behenate as a standard.

Each sample was added to a short section of 1.5mm diameter Polyimide Tubing (Cole-Parmer) and sealed at both ends with epoxy. The tubes were placed horizontally in the sample chamber and pumped down to 0.08 mbar. Each crystalline sample was exposed for 20 min; form factor was collected via ~8 hour exposure of unassembled NCTs. The scattered radiation was detected with a Dectris Pilatus 300K detector set at a distance of 1400 mm. 1-dimensional SAXS data was obtained via radial averaging of the 2-dimensional scattering pattern. These data were then transformed into profiles of scattering intensity as a function of scattering vector q. Form factor of free NCTs was divided out from the crystalline samples to determine peak positions and relative intensities.

Body-centered cubic (bcc) ordering was confirmed with comparison to modeled bcc X-ray diffraction spectra from PowderCell with Lorentzian peaks (**Figure 2-4** and **Figure S1-6**). The relevant crystalline parameters were then calculated as follows:

$$\text{Interparticle Distance} = d = \frac{\sqrt{6}\pi}{q_0}$$

$$\text{Lattice Parameter} = a = \frac{2d}{\sqrt{3}}$$

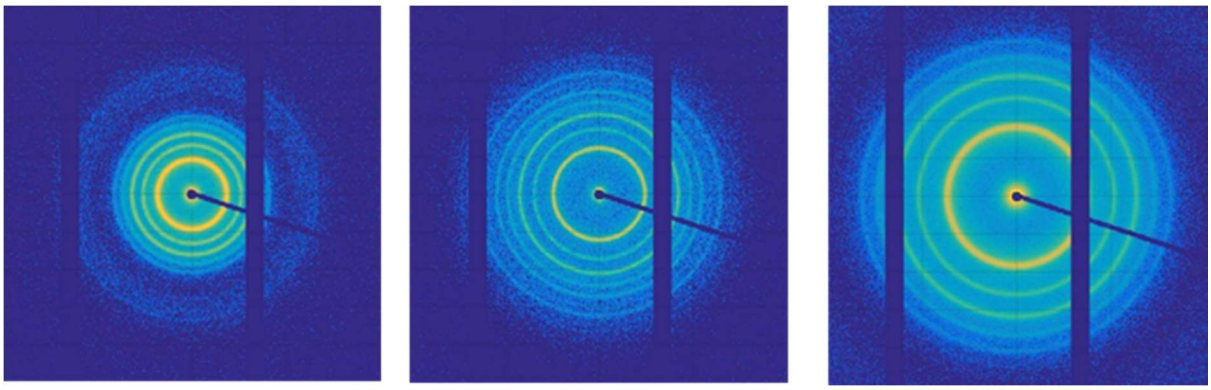

Figure S1-5. 2D SAXS images: (left) 20 nm AuNPs and 11.0 kDa PS; (center) 10nm AuNPs and 11.0 kDa PS; (right) 10 nm AuNPs and 6.0 kDa PS

NCT Design	Packing Order	q_0 Peak Position	Interparticle Distance (nm)	Lattice Parameter (nm)
20 nm AuNPs and 11.0 kDa PS	bcc	0.0184	41.8	48.3
10 nm AuNPs and 11.0 kDa PS	bcc	0.0244	31.5	36.4
10 nm AuNPs and 6.0 kDa PS	bcc	0.0366	21.0	24.2

Table S1-4. Structural parameters derived from SAXS

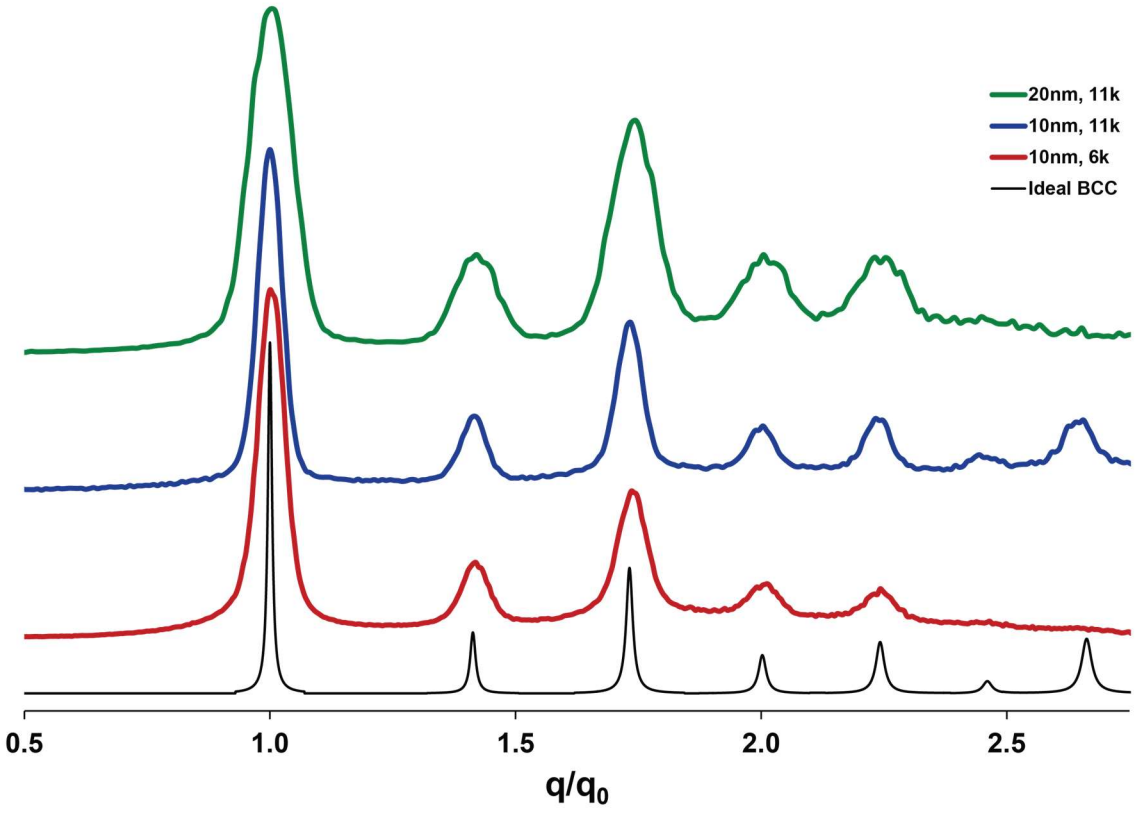

Figure S1-6. SAXS data from **Figure 2-4**, normalized as a function of their respective q_0 scattering vectors: (green trace) 20 nm AuNPs and 11.0 kDa PS; (blue trace) 10 nm AuNPs and 11.0 kDa PS; (red trace) 10 nm AuNPs and 6.0 kDa PS; (black trace) predicted SAXS pattern for a perfect bcc lattice.

Sample	(110)	(200)	(211)	(220)	(310)	(222)	(321)
10 nm AuNPs, 6.0 kDa PS	1.00	1.42	1.73	2.01	2.24		
10 nm AuNPs, 11.0 kDa PS	1.00	1.42	1.73	2.00	2.23	2.44	2.66
20 nm AuNPs, 11.0 kDa PS	1.00	1.42	1.75	2.01	2.23		
Ideal bcc	1.00	1.41	1.73	2.00	2.24	2.45	2.65

Table S1-5. Normalized peak positions of NCT assemblies compared to the peak positions of an ideal bcc lattice.

A1.4.4 Transmission electron microscopy (TEM)

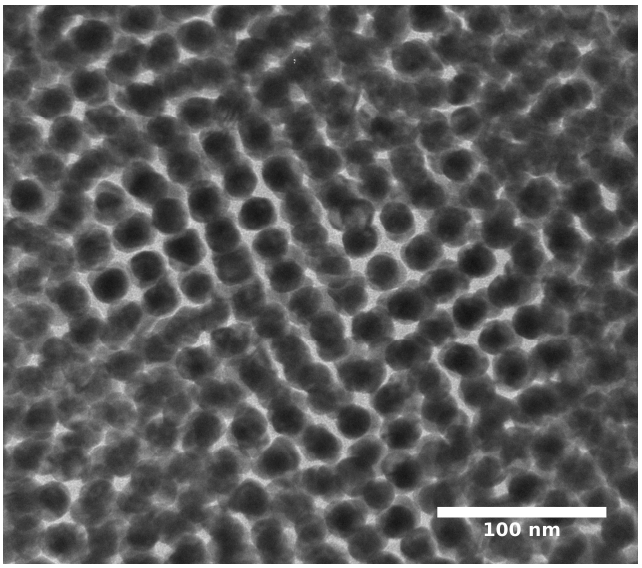

Figure S1-7. TEM micrograph of 20 nm AuNPs and 11.0 kDa PS NCTs assembled and then dried.

NCT samples in toluene that had been used to generate ordered SAXS patterns were drop cast onto a formavar stabilized with carbon 200 mesh copper TEM grid. As can be seen in the representative image of a dried film of annealed NCT assemblies made from 20 nm AuNPs and complementary 11.0 kDA PS (**Figure S1-7**), dried samples do not exhibit the same degree of ordering that is observed in solution with SAXS. Additionally, the interparticle distance has shrunk from the 41.8 nm recorded by SAXS to ~25 nm. These data indicate that without solvent present, the polymer chains condense and the structure collapses. However, the dried film still retains some cubic ordering instead of the hexagonal close packing typical of dried nanoparticle films, which supports the conclusion that bcc ordering is present in solution.

Appendix 2. Supplementary Information for Dictating Nanoparticle Assembly via Systems-Level Control of Molecular Multivalency

A2.1 Materials and Characterization Methods

2,6-Diaminopyridine, thymine, acetyl chloride, 11-bromoundecan-1-ol, 1-bromoundecane, 2-Bromoisobutyryl bromide, styrene, N,N,N',N",N'"-Pentamethyldiethylenetriamine (PMDETA), trisodium citrate dihydrate, Tris[2-(dimethylamino)ethyl]amine (Me_6TREN), iodine, and basic alumina were purchased from Fisher Scientific. Copper bromide, gold (III) chloride trihydrate, 2,2 dimethylbutanoyl chloride, and methyl-α-bromo isobutyrate was purchased from Sigma Aldrich. Aminoethanethiol was purchased from TCI America. General solvents were purchased from Fisher Scientific. All chemicals, including solvents, were used without further purification, except styrene, which was passed through a short column of basic alumina to remove inhibitor prior to polymerization. Note that some solvents were purchased as anhydrous grade, as noted in the experimental details.

Centrifugation was performed with an Eppendorf 5424 centrifuge. ^{1}H NMR spectra were obtained on a Varian Mercury 300 MHz instrument or on a Varian Inova 500 MHz instrument with variable temperature control. ^{13}C NMR spectra were obtained with a collection frequency of 101 MHz. Mass spectra were collected on a JEOL AccuTOF – DART spectrometer. Gel permeation chromatography (GPC) characterizations were performed on an Agilent Technologies GPC system, with THF as the eluent at 1.0 mL/min, and monodisperse polystyrene as the standard. UV-vis spectra and measurements were obtained on a Cary-5000 spectrometer. TGA measurements were taken on a TGA Q50 V6.7 Build 203 instrument. Small angle X-ray scattering (SAXS) measurements were performed on a SAXSLAB instrument with a Pilatus3R 300K detector and an X-ray wavelength of 1.54Å. Transmission electron microscopy (TEM) was performed with a JEOL 2010 Advanced High Performance transmission electron microscope. Dynamic light scattering experiments (DLS) were performed at the Massachusetts Institute of Technology (MIT) BioInstrumentation Facility (BIF) on a Wyatt DynaPro NanoStar instrument with a laser wavelength of 658nm. Samples dispersed in toluene and TCE were loaded into PMMA cuvettes and exposed to 10, 5 second exposures which were then averaged. DLS analysis was performed on Dynamics 7.1.4.3 software.

A2.2 Synthesis

We have previously reported the synthesis of the supramolecular polymer initiators, the polymers themselves, and NCTs.[222] Below, that information is briefly summarized in addition to the new syntheses in this work. Full NMR spectra are attached at the end of the supporting information.

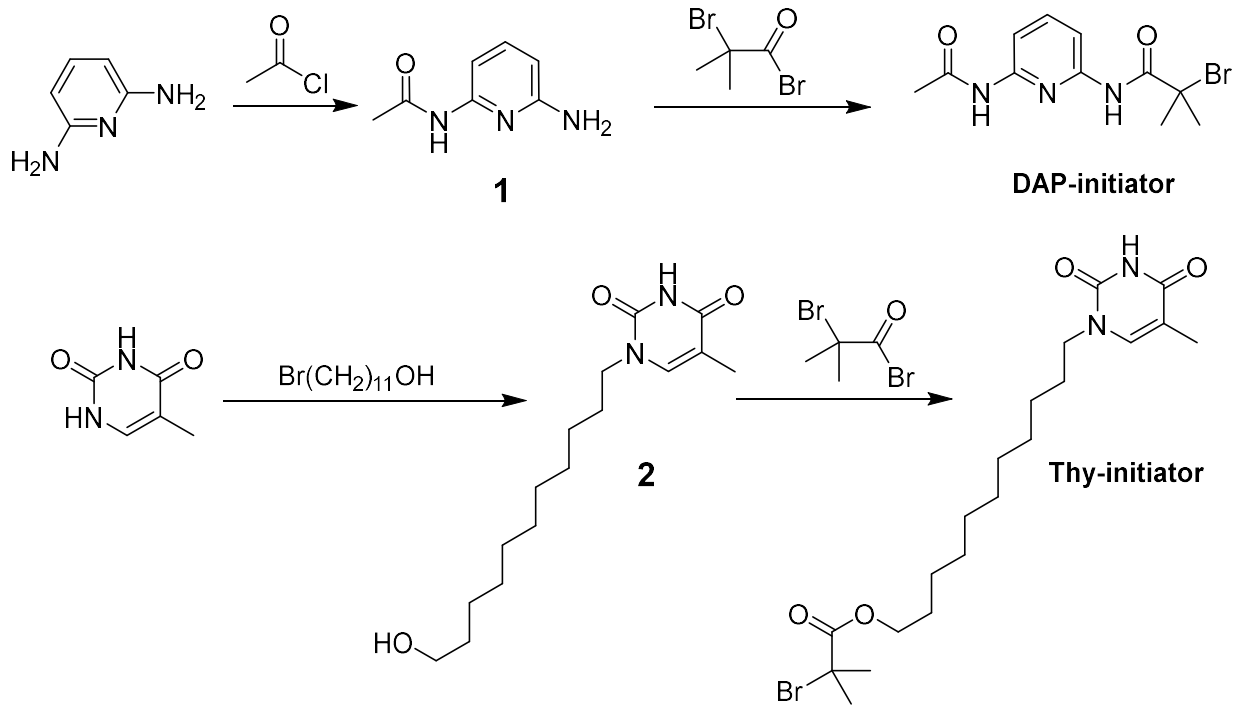

Scheme S2-1. Synthetic scheme for DAP and Thy initiators

A2.2.1 DAP-Initiator

5.5 g 2,6-diaminopyridine (50 mmol) was dissolved in 40 mL dry THF in a 3-necked round bottom flask. At 0 ºC, the solution of 1.96 g (25 mmol) acetyl chloride in 15 mL dry THF was added dropwise under a nitrogen atmosphere. The reaction mixture was allowed to warm to room temperature and stirred for 12 hours. The insoluble content was filtered off, and the solvent was removed under reduced pressure. The resulting solid was recrystallized in a mixture of ethanol and toluene, to afford **1** as a white solid (52%). ^{1}H NMR ($CDCl_3$, δ ppm): 7.55-7.65 (broad, s, 1H), 7.49-7.54 (broad, d, 1H), 7.45 (t, 1H), 6.25, (d, 1H), 4.32, (s, 2H), 2.16 (s, 3H). 1.9 g **1** (12.6 mmol) was dissolved in 80 mL dichloromethane, and then 3.5 mL triethylamine (25 mmol) was added to this solution. The mixture was cooled to 0 ºC, and a solution of 3.22g 2-bromoisobutyryl bromide (17.6 mmol) in dichloromethane (~10 mL) was added dropwise under a nitrogen atmosphere. The

reaction mixture was allowed to warm to room temperature and stirred for 12 hours. The insoluble content was filtered off, and the filtrate was washed with a sodium carbonate solution (x1) and brine (x3). The organic phase was dried over sodium sulfate, the solvent was removed under reduced pressure, and the product was then purified by flash chromatography (CH_2Cl_2/EtOAc 4:1). The product was further purified by recrystallization in CH_2Cl_2/EtOAc/hexanes to afford N-(6-acetamidopyridin-2-yl)-2-bromo-2-methylpropanamide (DAP-Initiator) (79%). ^{1}H NMR ($CDCl_3$, δ ppm): 8.74 (s, 1H), 7.90-7.96 (d, 1H), 7.83-7.89 (dd, 1H), 7.70-7.76 (t, 1H), 7.68-7.82 (broad, s, 1H), 2.21 (s, 3H), 2.04 (s, 6H) ^{13}C NMR ($CDCl_3$, δ ppm): 170.36, 168.59, 149.66, 149.10, 141.08, 110.09, 109.25, 61.85, 32.38, 24.93. MS: $[BrC_{11}H_{15}N_3O_2]^+$ Calculated 300.03480, Found 300.0350

A2.2.2 Thy-Initiator

5.0 g thymine (40 mmol), 1.0 g 11-bromo-1-undecanol (4 mmol), 1.1 g potassium carbonate (8 mmol) and 200 mL DMSO were added to a 500 mL round bottom flask. The mixture was stirred and bubbled with nitrogen for 2 minutes, and then sealed with a septum and stirred for 48 hours. The resulting mixture was poured into water and chloroform for extraction, and the organic phase was collected and washed 3 more times with brine, followed by drying over sodium sulfate and

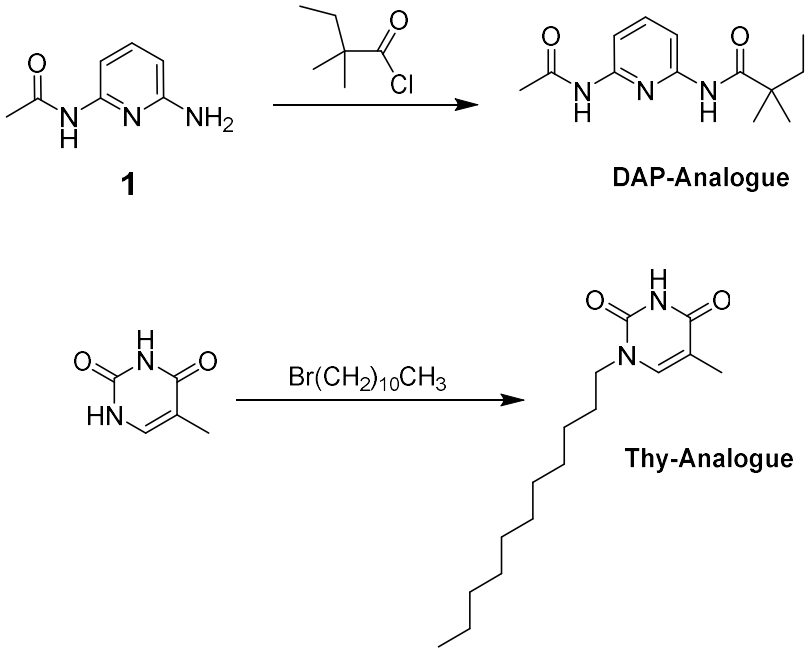

Scheme S2-2. Synthesis of the DAP and Thy Analogues

removal of solvent. The resulting white solid was recrystallized in EtOAc/hexanes to afford compound 2 (84%). 1H NMR (CDCl3, δ ppm): 8.18 (s, 1H), 6.97 (m, 1H), 3.66-3.71 (t, 2H), 3.60-3.66 (t, 2H), 1.92 (d, 3H), 1.22-1.75 (m, 18 H). With the help of very gentle heat, 592 mg **2** (2 mmol) was dissolved in 150 mL dichloromethane, and 0.39 mL triethylamine (2.8 mmol) was added to the solution. The mixture was cooled to 0 ºC, and a solution of 552 mg 2-bromoisobutyryl bromide (2.4 mmol) in dichloromethane (~ 10 mL) was added dropwise under a nitrogen atmosphere. The reaction mixture was allowed to warm to room temperature and stirred for 14 hours, and then washed with sodium carbonate (x2) and brine (x2). The organic phase was dried with sodium sulfate, and the solvent was removed under reduced pressure. The resulting mixture was purified by flash chromatography (CH_2Cl_2/EtOAc 8:3), to afford the 11-(5-methyl- 2,4-dioxo-3,4-dihydropyrimidin -1(2H)-yl)undecyl 2-bromo-2-methylpropanoate (Thy-Initiator) (Rf = 0.4) as an off-white solid. ^{1}H NMR ($CDCl_3$, δ ppm): 9.86 (s, 1H), 6.96 (d, 1H), 4.08-4.15 (t, 2H), 3.60-3.68 (t, 2H), 1.88 (s, 6H), 1.87 (d, 3H), 1.55-1.70 (m, 4H), 1.15-1.38 (m 14H). ^{13}C NMR ($CDCl_3$, δ ppm): 171.89, 164.08, 150.78, 140.53, 110.63, 66.28, 56.18, 48.71, 30.94, 29.53, 29.31, 29.26, 28.48, 26.58, 25.90, 12.49. MS: $[BrC_{20}H_{34}N_2O_4]^+$ Calculated 445.17023, Found 445.1711

A2.2.3 Synthesis of Small Molecule DAP Analogue

0.9 g **1** (5.96 mmol) was dissolved in 20 mL dry tetrahydrofuran, and then 1.7 mL triethylamine (12 mmol) was added. The mixture was cooled to 0 ºC, and a solution of 1 g 2,2 dimethylbutanoyl chloride (7.74 mmol) in tetrahydrofuran (~10 mL) was added dropwise under a nitrogen atmosphere. The reaction mixture was allowed to warm to room temperature and stirred for 12 hours. The insoluble content was filtered off, and the filtrate was washed with a sodium carbonate solution (x1) and brine (x3). The organic phase was dried over sodium sulfate, the solvent was removed under reduced pressure, and the product was then purified by flash chromatography (CH_2Cl_2/EtOAc 4:1). The product was further purified by recrystallization in CH_2Cl_2/EtOAc/hexanes to afford N-(6-acetamidopyridin-2-yl)-2,2-dimethylbutanamide (DAP-Analogue) (54%). ^{1}H NMR ($CDCl_3$, δ ppm): 7.45-8.0 (broad, m, 5H), 2.16 (s, 3H), 1.59-1.69 (q, 2H), 1.27 (s, 6H), 0.88-0.94 (t, 3H). ^{13}C NMR ($CDCl_3$ δ ppm): 176.39, 168.48, 149.72, 149.43, 141.00, 109.58, 109.42, 43.66, 34.05, 25.01, 24.90, 9.33. MS: $[C_{13}H_{20}N_3O_2]^+$ Calculated 250.1550, Found 250.1552

A2.2.4 Synthesis of Small Molecule Thy Analogue

8.0 g thymine (63 mmol), 1.41 mL 1-bromoundecane (6.3 mmol), 1.7 g potassium carbonate (12.6 mmol) and 200 mL DMSO were added to a 500 mL round bottom flask. The mixture was stirred and bubbled with nitrogen for 2 minutes, and then sealed with a septum and stirred for 48 hours. The resulting mixture was poured into water and chloroform for extraction, and the organic phase was collected and washed 3 more times with brine, followed by drying over sodium sulfate and removal of solvent. The product was purified by flash chromatography (CH2Cl2/EtOAc 4:1), and then was further purified by precipitation in hexanes to afford 5-methyl-1-undecylpyrimidine-2,4(1H,3H)-dione (Thy-Analogue) (57%). ^{1}H NMR (CDCl3, δ ppm): 8.06 (s, 1H), 6.97 (m, 1H), 3.64-3.71 (t, 2H), 1.92 (d, 3H), 1.16-1.75 (m, 18 H), 0.82-0.94 (t, 3H). ^{13}C NMR ($CDCl_3$ δ ppm): 164.10, 150.79, 140.54, 110.61, 48.73, 32.03, 29.70, 29.67, 29.59, 29.44, 29.34, 29.25, 26.59, 22.82, 14.26, 12.48. MS: $[C_{16}H_{29}N_2O_2]^+$ Calculated 281.2223, Found 281.2227

A2.2.5 DAP-PS Polymers

In a typical polymerization process, DAP-initiator (1.0 eq), Me6TREN (1.2 eq), styrene (100-200 eq depending on target molecular weight), and anhydrous DMF (1:1 v/v to styrene) were added to an oven-dried and nitrogen filled Schlenk flask. The reaction flask was then sealed with a rubber septum and the mixture was taken through 3 freeze-pump-thaw cycles and refilled with nitrogen. Once the mixture returned to room temperature, the septum was removed, CuBr (1.2 eq) was quickly added against a positive nitrogen flow, and the flask was immediately resealed. The mixture was stirred at 110 ºC under a nitrogen atmosphere, and quenched at different time points to give polystyrene of different molecular weights. The typical reaction time was 1-4 hours. To quench the reaction, the reaction mixture was poured into cold methanol, and the precipitated polymer was collected, redissolved in dichloromethane, and precipitated in methanol again to afford the polymer with a chain-end bromine.

Purified polystyrene obtained from DAP initiator was then dissolved in DMF (~ 10 mg/mL) with a small amount of triethylamine (40 eq), and the solution was bubbled with nitrogen for 5 minutes, followed by the addition of 2-aminoethanethiol (15 eq). The reaction flask was capped, and the solution was stirred for 60 hours, then poured into a mixture of dichloromethane and brine. The organic phase was washed with brine repeatedly (x3), concentrated, and precipitated in methanol

(redissolve-precipitate x4). The resulting white powder was dried under vacuum to give the DAP-PS polymer.

A2.2.6 Thy-PS Polymers

In a typical polymerization process, Thy-initiator (1 eq), PMDETA (1.0 eq), styrene (200 eq), and anhydrous anisole (30 vol% in styrene) were added to an oven-dried and nitrogen filled Schlenk flask. The reaction flask was then sealed with a rubber septum and the mixture was taken through 3 freeze-pump-thaw cycles and refilled with nitrogen. Once the mixture returned to room temperature, the septum was removed, CuBr (1.0 eq) was quickly added against a positive nitrogen flow, and the flask was immediately resealed. The mixture was stirred at 110 ºC under a nitrogen atmosphere, and quenched at different time points to give polystyrene of different molecular weights. Typical reaction time was 1-3 hours. To quench the reaction, the reaction mixture was poured into cold methanol, and the precipitated polymer was collected, redissolved in dichloromethane, and precipitated in methanol again to afford the polymer with a chain-end bromine.

The polymer was subsequently dissolved in DMF (~ 10 mg/mL) with small amount of triethylamine (40 eq), and the solution was bubbled with nitrogen for 5 minutes, followed by the addition of 2-aminoethanethiol (15 eq). The reaction flask was capped, and the solution was stirred for 60 hours, then poured into a mixture of dichloromethane and brine. The organic phase was washed with brine repeatedly (x3), concentrated, and precipitated in methanol (redissolve-precipitate x4). The resulting white powder was dried under vacuum to give the Thy-PS polymer.

A2.2.7 Blank Polymer

In a typical polymerization process, methyl-α-bromo isobutyrate initiator (1.0 eq), PMDETA (0.3 eq), and styrene (130 eq) were added to an oven-dried and nitrogen filled Schlenk flask. The reaction flask was then sealed with a rubber septum and the mixture was taken through 3 freeze-pump-thaw cycles and refilled with nitrogen. Once the mixture returned to room temperature, the septum was removed, CuBr (0.3 eq) was quickly added against a positive nitrogen flow, and the flask was immediately resealed. The mixture was stirred at 90 ºC under a nitrogen atmosphere, and quenched at different time points to give polystyrene of different molecular weights. To

quench the reaction, the reaction mixture was poured into cold methanol, and the precipitated polymer was collected, redissolved in dichloromethane, and precipitated in methanol again to afford the polymer with a chain-end bromine.

The polymer was subsequently dissolved in DMF (~ 10 mg/mL) with small amount of triethylamine (40 eq), and the solution was bubbled with nitrogen for 5 minutes, followed by the addition of 2-aminoethanethiol (15 eq). The reaction flask was capped, and the solution was stirred for 60 hours, then poured into a mixture of dichloromethane and brine. The organic phase was washed with brine repeatedly (x3), concentrated, and precipitated in methanol (redissolve-precipitate x4). The resulting white powder was dried under vacuum to give the Blank-PS polymer. Thiol conversion was monitored by ^{1}H NMR (**Figure S2-1**), observing the substitution of the bromine end group by noting the disappearance of its germinal protons' peak, with a conversion ≥ 95%.[318] Presence of thiols is further confirmed by the functionalization of gold nanoparticles (see **Figure S2-4** for TGA data), which does not occur with bromine terminated polymers.

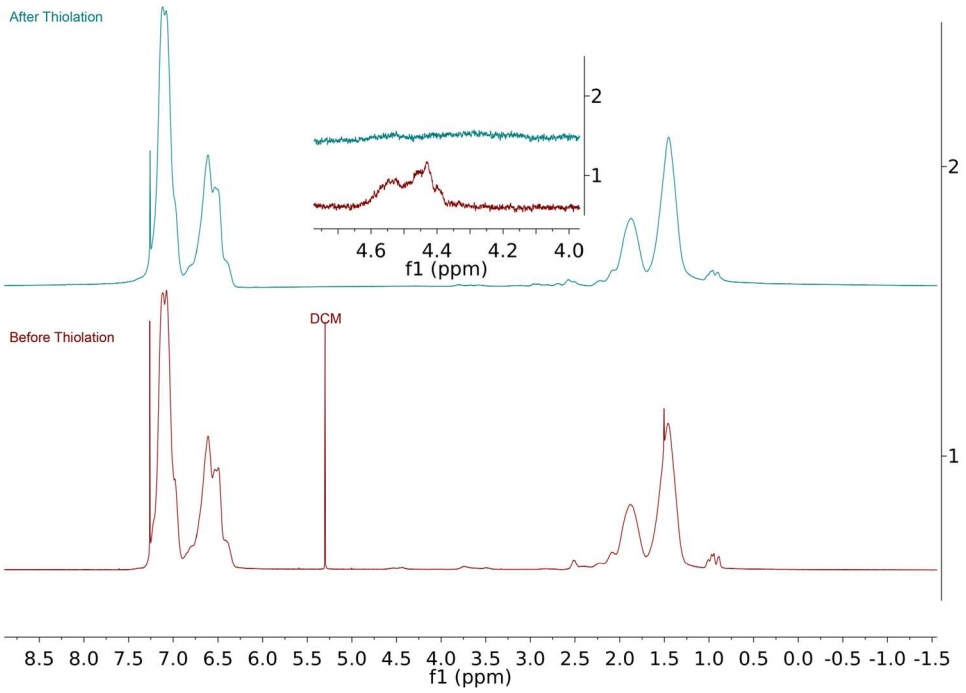

Figure S2-1. ^{1}H NMR spectra before and after the reaction of bromine terminated polystyrene with aminoethanethiol.

A2.2.8 Polymer Characterization

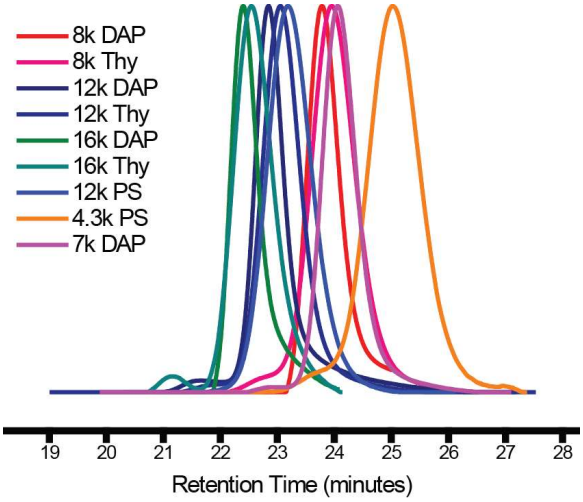

Figure S2-2. Normalized GPC traces for the polymers used in this work. See **Table S2-1** for more information.

Sample Name	Mn (kDa)	Dispersity
8k DAP	7.9	1.06
8k Thy	7.6	1.07
12k DAP	13.0	1.11
12k Thy	12.1	1.06
16k DAP	17.5	1.03
16k THY	16.1	1.05
12k PS	11.4	1.05
4.3k PS	4.3	1.09
7k DAP	7.1	1.05

Table S2-1. Molecular weight and dispersities of the polymers used in this work.

Polymer molecular weight and dispersity were determined by GPC against polystyrene standards. As the DAP and Thy polymers used separate initiators, each polymerization was done as an individual batch. Therefore, the molecular weights for a family of polymers (e.g. 8k DAP and 8k

Thy) exhibit some variation in length, within 10% of their target value. The measured values are provided in **Table S2-1**.

A2.2.9 Nanoparticle Synthesis

Gold nanoparticles were synthesized from an established seeded growth protocol.[29] Briefly, a 500 mL solution of 2.2 mM trisodium citrate dihydrate was brought to a boil. To synthesize 12 nm nanoparticles, 2 mL of 25 mM $HAuCl_4{:}3H_2O$ was rapidly injected to the solution under vigorous stirring. Within one minute the solution began to darken, and after 15 minutes it stabilized as a deep red color. To synthesize larger nanoparticles, the same procedure was used as the starting point of a seeded growth method. After the initial injection to synthesize the seeds, the solution temperature was lowered to 90°C, and given 30 minutes to equilibrate. Then, another injection of 2 mL of 25 mM $HAuCl_4{:}3H_2O$ was performed, the solution given 30 minutes to equilibrate, followed by a final injection of another 2 mL of 25 mM $HAuCl_4{:}3H_2O$. After the third addition of the precursor gold salt, half of the solution (250 mL) was removed from the flask and stored in the dark at room temperature. The volume of the reaction solution was brought back to 500 mL by adding 250 mL 2.2 mM sodium citrate, and allowed to equilibrate at 90°C for 30 minutes. Three more injection and equilibration steps were performed, and the final solution was again split in half and the reaction mixture similarly diluted. The entire process was repeated until five different generations were obtained (the seeds and four grown particles).

The nanoparticles were characterized by casting onto formvar coated TEM grids, and images of at least 100 nanoparticles used to calculate the size distribution. Analysis was performed with ImageJ.

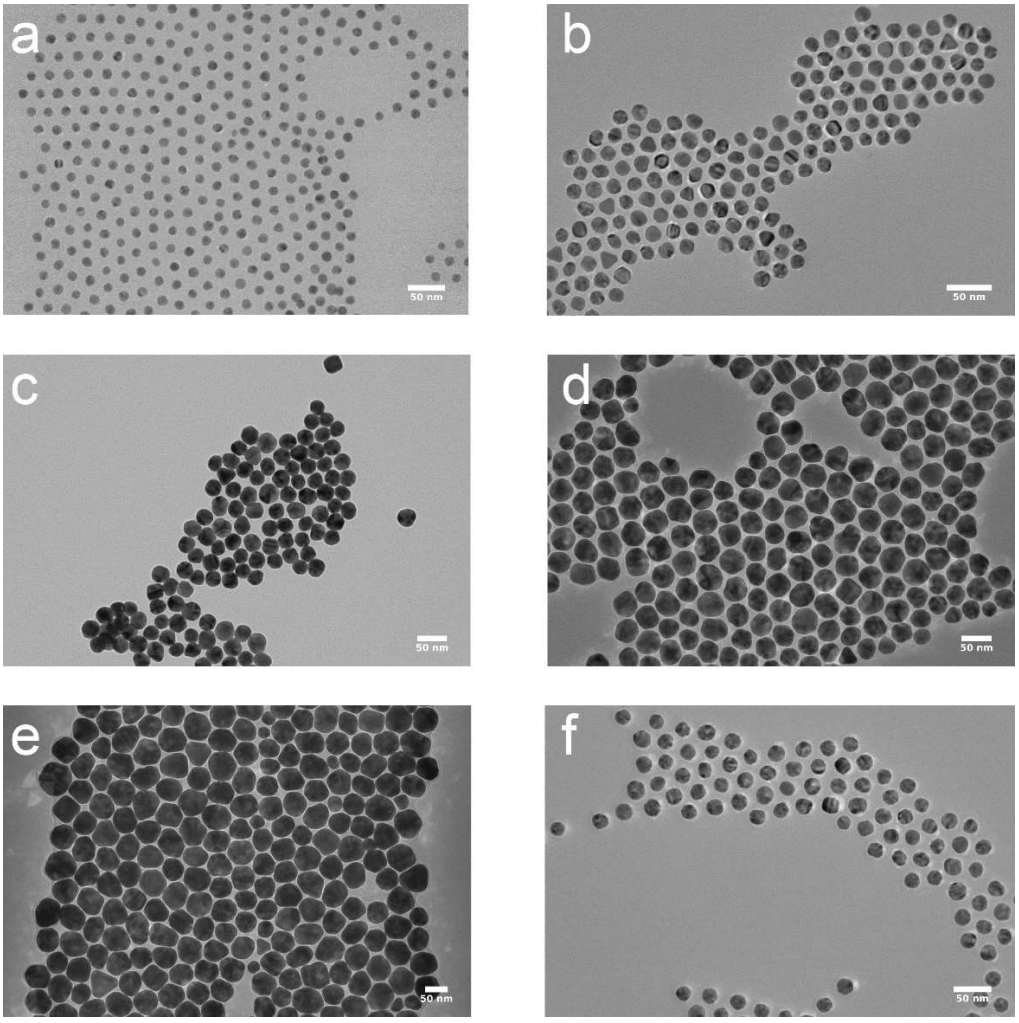

Figure S2-3. Nanoparticles synthesized for this work: (a) seeds (b) first generation (c) second generation (d) third generation (e) fourth generation (f) a second synthesis of the first generation particles used for making the Th_3P_4 superlattice. The scale bar is 50 nm for each image.

Sample	Diameter (nm)	Relative standard deviation
Seeds	12.46	5.4%
First generation	16.48	8.2%
Second generation	26.01	7.3%
Third generation	36.55	11.3%
Fourth generation	49.96	14.3%
Repeat first generation	19.95	7.5%

Table S2-2. Size and dispersity information for the nanoparticles used in this work.

A2.2.10 Synthesis of NCTs

NCTs were synthesized from the AuNP and polymer components as was previously reported.[203,222] In a typical synthesis, an appropriate mass of DAP-PS or Thy-PS polymer (thiol terminated) was dissolved in 5.0 mL of acetone in a glass vial to yield a 0.2 mM solution. The solution was vigorously stirred while 5.0 mL of gold nanoparticle (AuNP) solution was quickly poured into the vial, and the resulting suspension was allowed to stir for 1 hour. After the formation of dark red precipitate on the wall and at the bottom of the vial, the colorless supernatant was removed by direct decantation or with the aid of light centrifugation. 5-6 mL of solvent was added to the vial to redisperse the precipitate, and the resulting dispersion was distributed in centrifuge tubes and purified for 3 centrifuge cycles. The centrifuge protocols (**Table S2-3**) were identical for all particles of a given core diameter, regardless of polymer length. The solvents used to redisperse the AuNP precipitate at the end of each cycle were DMF, toluene, and toluene, respectively, and the final toluene dispersions were used for the self-assembly experiments.

Particle Size (nm)	Protocol
12	8,476 RCF, 50 min
16	4602 RCF, 50 min
26	2,348 RCF, 40 min
36	962 RCF, 40 min
50	376 RCF, 25 minutes

Table S2-3. Centrifuge protocol for different AuNP sizes

A2.3 NCT Characterization

A2.3.1 Thermal Gravimetric Analysis (TGA)

An NCT solution in dichloromethane was drop cast on a platinum TGA pan, and allowed to fully evaporate before loading into the instrument. The sample was heated to 200°C, held for 10 minutes, then ramped at 15 °C per minute up to 600 °C. All samples showed a characteristic step function at approximately 400 ºC, interpreted to be mass loss from the polymer, $m_{Polymer}$. The remaining mass was assumed to be from the gold nanoparticle, m_{NP}. Grafting density in chains/nm^2 was then calculated by:

$$\sigma = \frac{m_{Polymer} * N_A * \rho_{Au}}{m_{NP} * MW_{Polymer} * D_{NP} * (6 \cdot 10^{21})} \quad \text{(Equation S2-1)}$$

where N_A is Avogadro's number, ρ_{Au} is the density of gold, $MW_{Polymer}$ is the polymer's number-averaged molecular weight determined by GPC, D_{NP} is the nanoparticle diameter determined by TEM, and $6 \cdot 10^{21}$ contains geometric constants and an appropriate scaling factor to provide data in units of chains/nm^2. A representative TGA curve and the grafting density values for all NCT systems are shown in **Figure S2-4**. Grafting density varies only slightly with alterations to NCT design within the size regimes studied in this work, representing non-statistically significant changes in density as a function of polymer length or NP diameter.

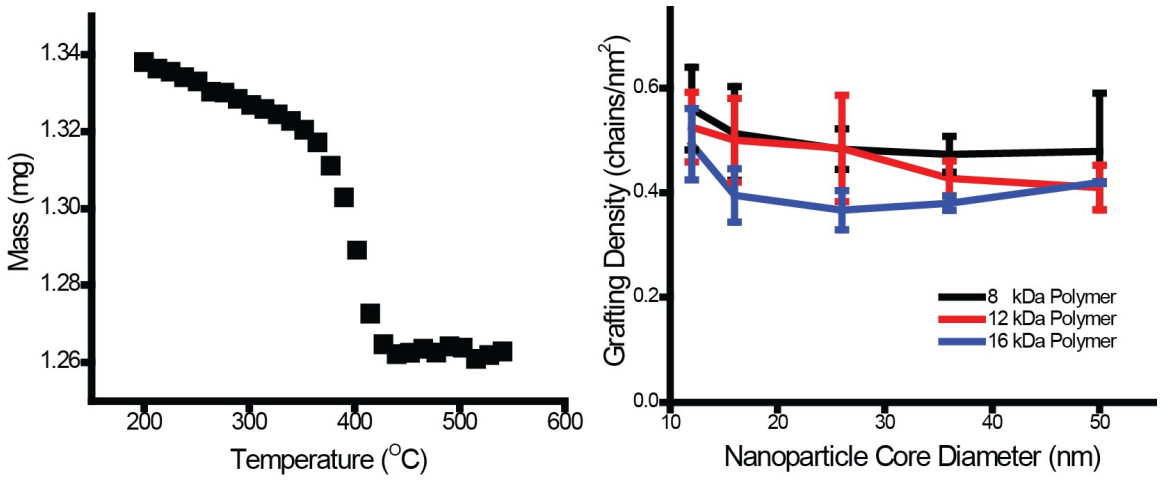

Figure S2-4. (Left) Sample TGA data collected for NCTs synthesized with 12 kDa DAP polymer and 50 nm AuNPs. The polymer fraction was calculated as the mass loss during the step function (sample mass at 350°C minus mass at 450°C). (Right) Calculated grafting densities from the nanoparticle/polymer pairs used in this study. Error bars are standard deviations, N=2

A2.3.2 Dynamic Light Scattering

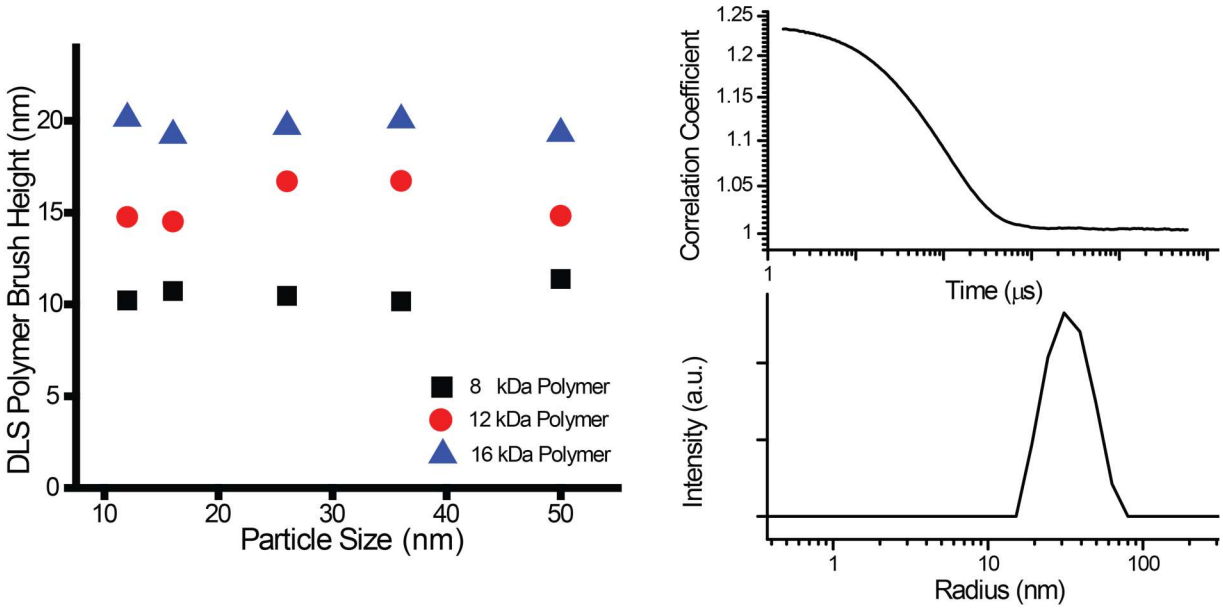

Figure S2-5. (Left) Length of polymers as determined by dynamic light scattering (DLS) on the different nanoparticle cores studied in this work. Data was taken in toluene, and is the average of 10 scans with the radius of the nanoparticle core subtracted. (Right) Representative correlation coefficient and size distribution for the 12 kDa, 26nm sample, this sample showed a PDI of 13.3%, and a radius of 29.7 nm. This corresponds to a brush height of 16.7 nm.

Dynamic light scattering was used to determine the hydrodynamic radius of the NCTs, and the core radius measured by TEM was subtracted from that value to determine polymer length. The data indicate no significant change in polymer length as a function of nanoparticle core diameter.

A2.4 Assembly Experiments

A2.4.1 Derivation of Equilibrium Relationships

NCT melting thermodynamic parameters were analyzed according to the methodology of Jin et al.[158] In a typical melt experiment, a quartz cuvette was treated with a hexamethyldisilazane (HMDS) vapor by placing the cuvette in a sealed container with an open vial of a solution of equal volumes HMDS and hexanes for at least 12 hours. Freshly synthesized DAP and Thy functionalized NCTs were brought to equal concentrations in toluene, as determined by measuring their absorbance, and then combined in a polypropylene centrifuge tube. After the NCTs had assembled, they were briefly sonicated, transferred to the treated quartz cuvette equipped with a

stir bar, and diluted so that the absorbance of the solution in its melted state would be approximately 1. The cuvette was then placed in a Cary 5000 spectrophotometer with a temperature controller accessory, and allowed to equilibrate at 15°C, while stirring, for 1 hour. When the equilibration was completed, the temperature was ramped at 0.25°C per minute, with a measurement of the absorbance at 520 nm taken every minute to approximate the fraction of non-bonded, dispersed NCTs as a function of temperature (f, **Figure S2-6-7**). The data were then normalized such that the lowest absorption value (the fully assembled state) had a value of 0, and the fully melted state had a value of 1. The measured quantity, f, corresponds to the relative change in absorption at 520 nm, and correlates to the fraction of the nanoparticles in the melt state:

$$f = \frac{M}{M+A} \qquad \text{(Equation S2-2)}$$

where M is the fraction of melted nanoparticles and A is the fraction of nanoparticles in aggregates. Based on equation S2-2, K_d is the collective equilibrium constant for release of an NCT from the aggregate state into the melt state. Thus:

$$K_d = \frac{M}{A} \qquad \text{(Equation S2-3)}$$

$$f = \frac{M}{M+\frac{M}{K_d}} = \frac{1}{1+\frac{1}{K_d}} \qquad \text{(Equation S2-4)}$$

Crucially, the numerous supramolecular binding groups on each NCT are engaging in a complex, multivalent reaction during the melt process, and multiple supramolecular bonds must be broken to release an NCT from an aggregate. K_d describes this collective reaction, as the nanoparticle substrate is able to separate from the aggregate only when all supramolecular linkages are broken. The melting of an NCT can therefore be mathematically analyzed as a stepwise process without any cooperativity between steps, where K_d is a sum of multiple reactions—breaking the *nth* DAP-Thy bond, the *n – 1th* bond, etc., until it breaks the final bond. This collective reaction is expressed as:

$$A + P_N \rightarrow A + P_{N-1} + D + T$$
$$A + P_{N-1} \rightarrow A + P_{N-2} + D + T$$
$$\ldots$$
$$A + P_1 \rightarrow A + M + D + T$$

where D is an unbound DAP supramolecular group, T is an unbound Thy supramolecular group, A is the aggregate and P_N is a particle bound by N constructively interacting DAP-Thy

supramolecular bonds. Note that P_0 is a particle without any connections to the aggregate, i.e. a melted particle (M). The key assumptions for this model of NCT melting are that the NCTs dissociate in a stepwise manner (e.g. diffusing from the surface one at a time) and that the aggregates are large enough that they do not dramatically change upon the departure of a single NCT. It can therefore be hypothesized that because (as discussed in the main text) the supramolecular groups bundle together, N will be the number of supramolecular bonds in the largest bundle. When P_N reaches P_0, the particle separates from the aggregate and the overall reaction occurs:

$$A \rightarrow M$$

K_d is the sum of all of the stepwise reactions taking place, each with a respective equilibrium constant:

$$K_1 = \frac{[D][T][P_0]}{[P_1]} \qquad \text{(Equation S2-5)}$$

$$K_2 = \frac{[D][T]\,[P_1]}{[P_2]}$$

$$\dots$$

$$K_N = \frac{[D][T]\,[P_{N-1}]}{[P_N]}$$

From these, K_d can be expressed as the constant for all of these reactions happening:

$$K_d = \prod_{i=1}^{N} K_i \qquad \text{(Equation S2-6)}$$

Additionally, each equilibrium constant can be written in terms of an enthalpy at a melting temperature using the Van't Hoff equation (approximating a zero heat capacity for the interaction, see **Figure S2-6**), which is accurate close to T_m:

$$K_i = e^{\frac{-\Delta H_i}{R}\left(\frac{1}{T} - \frac{1}{T_{m,i}}\right)} \qquad \text{(Equation S2-7)}$$

Where T_m is a temperature where $K_i = 1$. This results in K_d being equal to:

$$K_d = e^{\frac{-N*\Delta H_i}{R}\left(\frac{1}{T} - \frac{1}{T_m}\right)} \qquad \text{(Equation S2-8)}$$

And this can be substituted into (2-3):

$$f = \frac{1}{1+e^{\frac{\Delta H_m}{R}*\left(\frac{1}{T} - \frac{1}{T_m}\right)}} \qquad \text{(Equation S2-9)}$$

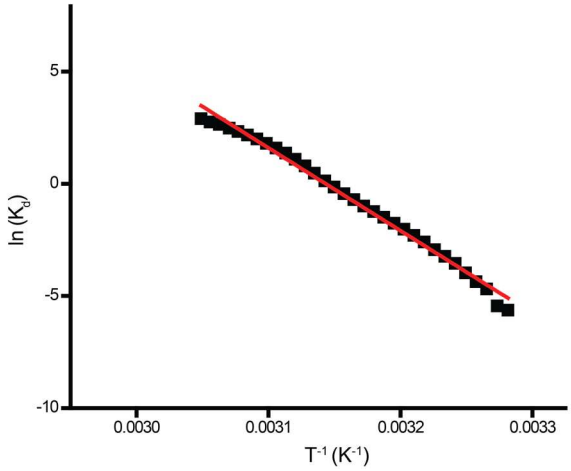

Figure S2-6. van't Hoff plot of representative melt data over the transition window. The linear relationship (r^2 = 0.991) indicates that there is a minimal dependence of enthalpy on temperature, validating the use of the van't Hoff equation.

A2.4.2 Assembly at Different Concentrations of NCTs

Supramolecular chemistry with discrete molecular species often shows a concentration dependence, but this is not predicted in the mathematical model for NCT melting. To confirm this, NCT melts were performed at varying concentrations (**Figure S2-7**). When *f* is calculated there is not significant difference in the melt curve, supporting the accuracy of the model.

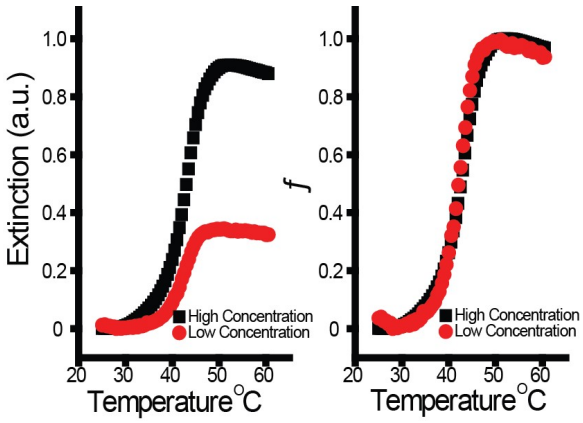

Figure S2-7. Comparison of NCT melt experiments performed at varying concentration (different measured extinction values on the left) and the resulting calculation for *f* (right).

A2.5 Coloading Experiments and Bundle Bonds

Because NCTs all possess a large number of grafted polymer chains, this affords the possibility of grafting multiple different types of polymer to a single NCT. This coloading procedure can be performed with either polymer chains that are all of the same length, or polymers of two different lengths; coloading can be done on the Thy NCTs, the DAP NCTs, or both simultaneously. Each of these conditions requires slightly different analysis procedures and each results in different thermodynamics of the assembly behavior.

A2.5.1 Determination of Number of Active Polymer Chains on Coloaded NCTs

Coloading NCTs with both active polymer chains that contain a supramolecular group and shorter polymer chains lacking this functionality complicates the calculation of NCT polymer grafting density process, as the lower steric bulk of the shorter polymer chains allows them to load onto the particle at a faster rate. As a result, the feed ratio of the two polymer types added to solution during particle functionalization does not necessarily coordinate to the final ratio of polymers on the NCT. To address this, two techniques were performed to quantify the coloading distribution, specifically GPC analysis of the grafted polymer chains and TGA of the coloaded particles. First, a solution of functionalized and purified NCTs was mixed with iodine to digest the gold nanoparticles, resulting in the formation of a black precipitate. After stirring overnight, the supernatant was recovered by centrifugation (2,348 RCF, 10 minutes), then allowed to evaporate to yield a yellow solid. This solid was dissolved in DCM and precipitated in methanol, then centrifuged (2,348 RCF, 10 minutes) to yield a white polystyrene powder. The polymer was then characterized by GPC in the same manner as described above. According to a previously reported analysis,[319] the two distinct peaks that arise due to the difference in polymer molecular weight can be fit to Gaussian peaks, integrated, divided by their molecular weight, and compared to give a ratio of the relative number of long and short polymers in the sample. As an important note, this analysis was only performed with the Thy-based polymers because DAP-based polymers showed an increase in molecular weight by ~ 3 kDa after the iodine treatment, presumably because the DAP moiety is able to coordinate with some metal ion species, resulting in a change in its elution behavior.

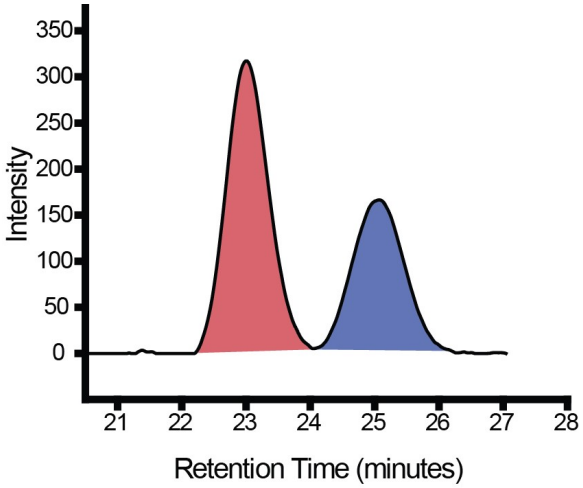

Figure S2-8. Sample GPC analysis of a sample with a feed ratio of 80% Thy polymer. The long polymer (red) and short polymer (blue) are distinct enough that they can be separated in a single pass through a GPC column.

Feed Thy	**A_1**	**A_2**	**N_1**	**N_2**	**F_{Thy}**	**σ**	**σ_{Thy}**	**r_{Thy}**
90	740.80	243.79	0.06	0.06	0.52	0.62	0.33	0.68
80	249.25	162.31	0.02	0.04	0.36	0.70	0.25	0.52
70	318.54	244.65	0.03	0.06	0.32	0.70	0.23	0.47
60	232.88	215.60	0.02	0.05	0.28	0.76	0.21	0.44
50	129.63	371.75	0.01	0.08	0.11	0.91	0.10	0.21

Table S2-4. Summary of coloading analysis for NCTs with two different polymer chain lengths. *Feed Thy* is the percentage of Thy polymer in the feed (with the rest being blank 4.4 kDa PS), A_1 is the integral of the first peak (larger polymer), and A_2 is the integral of the second peak. N_1 and N_2 are those areas divided by their respective molecular weights. F_{Thy} is the fraction of the longer, active polymer containing a Thy group. σ is the grafting density from TGA, σ_{Thy} is the grafting density of Thy polymers. r_{Thy} is the relative amount of Thy polymer to equivalent NCTs without the coloaded shorter polymer.

After finding the ratio between short and long polymers, TGA experiments were performed to determine the grafting density of polymer to the surface, with the linear combination of molecular weights used as the $MW_{Polymer}$ term in equation S2-1. Together, TGA and GPC analyses afforded the actual grafting density ratio of the short and long polymer chains.

A2.5.2 Effects of Coloading with Shorter Polymer Chains on NCT Binding Strength

Coloading NCTs with an active longer polymer and an inactive shorter polymer (**Figure S2-9**) has several notable effects on the assembly process that differ both from NCTs that are not coloaded and from coloaded NCTs where the active and inactive polymer chains are of equivalent length. The latter two cases are discussed in the main text; here were summarize the behavior arising from NCTs containing short inactive polymers.

First, while the relationship between T_m and coloading is linear (just as with the systems with longer inactive polymers), the change in T_m is less pronounced. This reduced effect on T_m can be explained by the fact that when NCTs bind and the active polymer chain ends are bundled together,

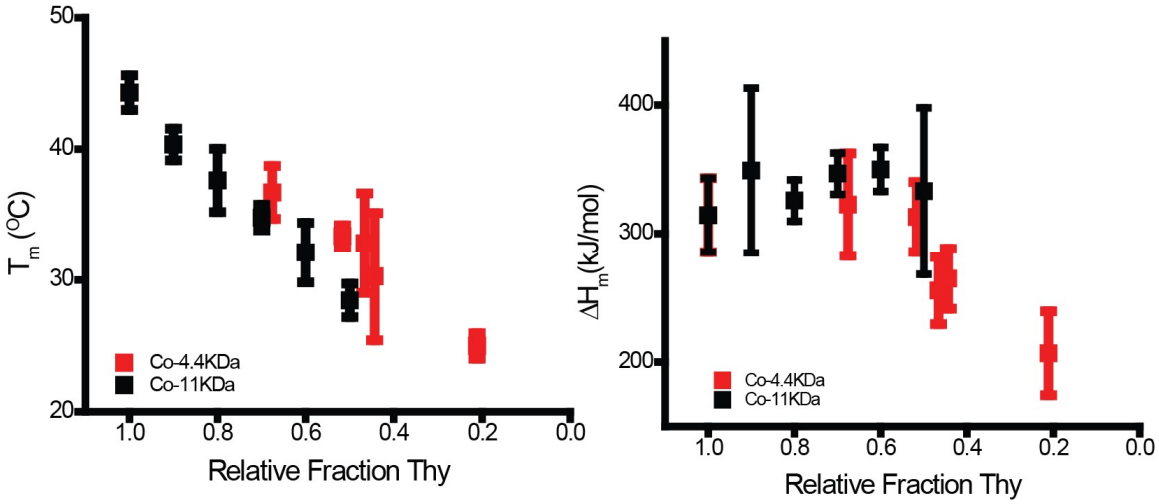

Figure S2-9. Melting temperature and enthalpy data for NCTs with coloaded Thy particles containing both the 11kDa PS and the 4.4 kDa PS.

the shorter inactive polymers provide a lower amount of steric hindrance and thus lower entropy penalty. Importantly, this difference enables assembly of NCTs with much lower fractions of active polymer than when coloading with two polymer chains of equal length. As noted in the main text, NCT binding enthalpy is the same for all coloaded systems up to ~50% of the maximum active polymer loading; samples with less active polymer had T_m values too low to properly analyze. In the samples with shorter inactive polymers, the same plateau in binding enthalpy is observed for loading fractions of 100%-50% active polymer. However, because lower fractions of active polymers are accessible for this system, it can be observed that at about 40% of the maximum active polymer loading, the binding enthalpy deviates from its plateau. A more rigorous

exploration of this phenomenon will be pursued in future work, but a preliminary hypothesis is that below the critical coloading ratio, the number of active polymers in each bundle bond begins to decrease.

It is also possible to perform symmetric coloading experiments with the inactive polymer on both the DAP and Thy NCTs (**Figure S2-10**). Similar trends to the asymmetric case can be observed, specifically, a fairly linear decrease in T_m and a plateau in ΔH_m. However, fewer samples were able to be analyzed due to the faster decrease in T_m, and the results were subject to much higher experimental error.

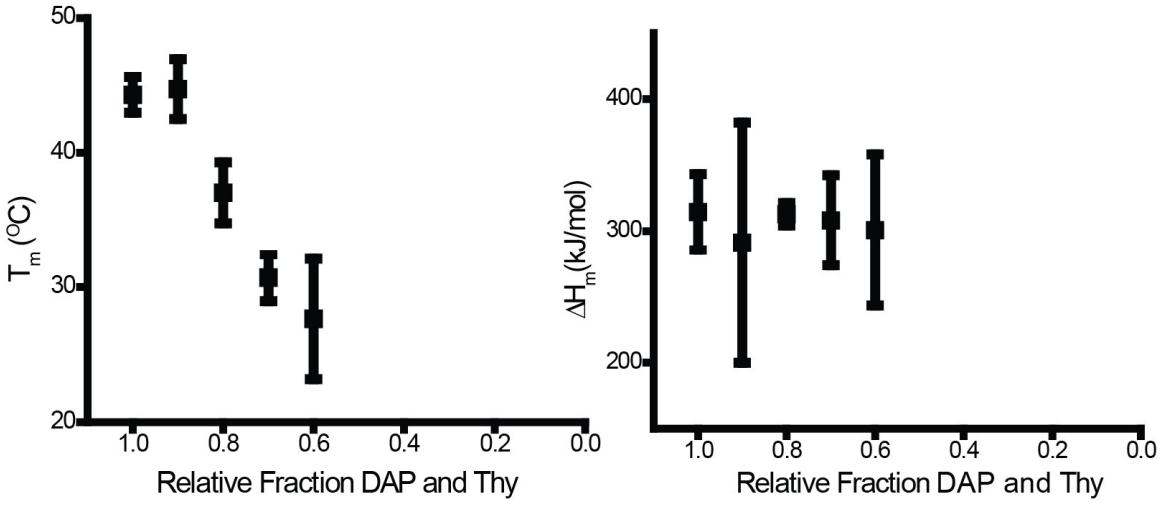

Figure S2-10. Melting temperature and enthalpy data for NCTs coloaded for both DAP and Thy components.

A2.5.3 DLS Analysis of Polymers

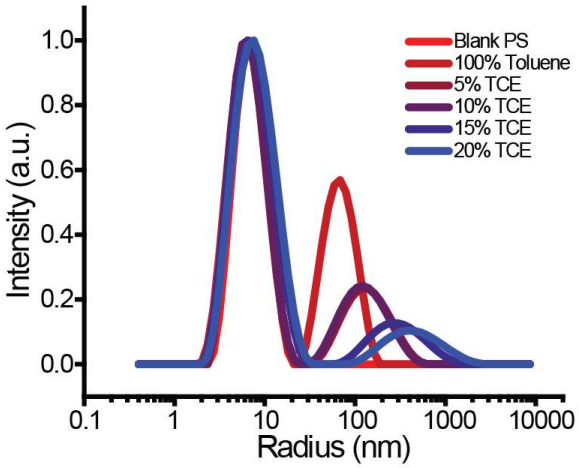

Figure S2-11. DLS measurements of polymer chains in toluene at 5 mg/ mL concentration. The Blank PS curve refers to the 12k polystyrene sample without any supramolecular functional group (overlaps with the sample containing supramolecular groups in 100% toluene). The other measurements are of mixtures of the 12k DAP and 12k Thy polymers in varying solvent compositions. Each curve was normalized to the small radius peak.

Polystyrene polymers terminated in a polar functional group are known to phase segregate in toluene,[230] resulting in the formation of reverse micelles. This behavior was confirmed in the system examined here by using dynamic light scattering (DLS) to measure the hydrodynamic radius of free polymer chains both with and without terminal supramolecular groups. While polystyrene chains without any supramolecular groups do not show any larger features, the addition of a binding group results in the presence of large aggregates (**Figure S2-11**). Adding polar TCE increases the size of these aggregates, but also decreases the relative amount in solution; these are consistent with both the analysis of the bundle bonds in the main text and prior results on reverse micelle formation.[320] It should be noted that the concentration in the DLS experiments is significantly lower than the local concentration present on the surface of NCTs, which is higher than is experimentally accessible.

A2.6 Simulations of NCT Assembly

Coarse-grained molecular dynamics simulations[321] of NCTs in an explicit solvent condition were performed to study the binding interface between NCTs, specifically the formation of the "bundle" bonds. Each NCT is modeled by a spherical nanoparticle densely grafted with spring-bead chains[322] with number of monomers $N = 16$ (see **Figure S2-12a**). The polar groups at the chain ends are represented by assigning the last monomer in the polymer chains to be a new type of bead. The nanoparticle is made of a shell-like shaped assembly of beads in a hexagonal closed-packed (HCP) lattice with an outside radius of 10.0 σ and inside radius of 8.0 σ. To provide enough grafting points and smooth the surface, the density of the HCP lattice is set to 10.0 σ^{-3}. In total, 1216 polymer chains are grafted roughly uniformly on the surface with a grafting density of 0.968 σ^{-2}. Solvents are represented by single coarse-grained beads.

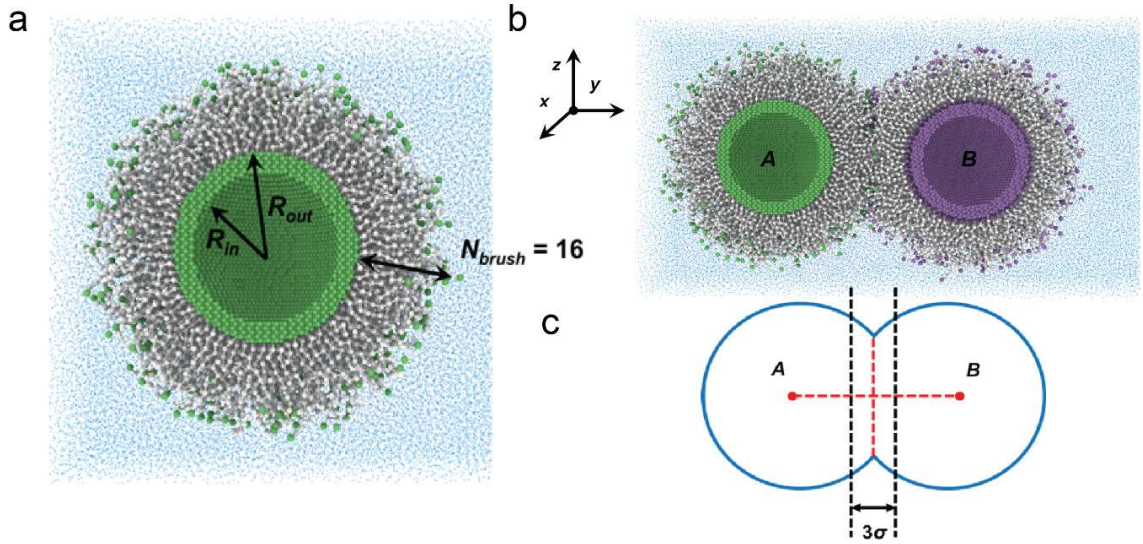

Figure S2-12. (a) Simulation snapshot of a cross section view of a NCT. (b) Simulation snapshot of a cross section view of a NCT. (c) Schematic representation of two NCTs in contact. Interface is defined as the layer with thickness of 3σ at the contact. See Table S5 for the interaction potentials.

The interactions between all beads in a system are modeled by the truncated-shifted Lennard-Jones (LJ) potential:

$$U_{\mathrm{LJ}}(r_{\mathrm{ij}}) = \begin{cases} 4\varepsilon_{\mathrm{LJ}}\left[\left(\frac{\sigma}{r_{\mathrm{ij}}}\right)^{12} - \left(\frac{\sigma}{r_{\mathrm{ij}}}\right)^{6} - \left(\frac{\sigma}{r_{\mathrm{cut}}}\right)^{12} + \left(\frac{\sigma}{r_{\mathrm{cut}}}\right)^{6}\right] & r_{\mathrm{ij}} \le r_{\mathrm{cut}} \\ 0 & r_{\mathrm{ij}} > r_{\mathrm{cut}} \end{cases} \qquad \text{(Equation S2-10)}$$

where r_{ij} is the distance between the ith and jth beads and σ is the bead diameter. The cutoff distance r_{cut} is 2.5 σ. All values of the Lennard-Jones interaction parameter $\varepsilon_{\mathrm{LJ}}$ are summarized in **Table S2-5**.

$\varepsilon_{\mathrm{LJ}}$ / $k_{\mathrm{B}}T$	NP	PS	DAP (A)	THY (B)	Toluene	TCE
NP	1.0	1.0	1.0	1.0	1.0	1.0
PS		1.0	0.5	0.5	1.0	1.0
DAP (A)			1.0	3.0	0.5	1.0
THY (B)				1.0	0.5	1.0
Toluene					1.0	1.0
TCE						1.0

Table S2-5. Lennard-Jones Interaction Parameters

Strong bonds (the connections between beads in the polymer chains and the bonds grafting the polymers to the nanoparticle) are modeled by the finite extension nonlinear elastic (FENE) potential:

$$U_{\mathrm{FENE}}(r) = -\frac{1}{2}k_{\mathrm{spring}}R_{\mathrm{max}}^2 \ln\left(1 - \frac{r^2}{R_{\mathrm{max}}^2}\right) \qquad \text{(Equation S2-11)}$$

with the spring constant $k_{\mathrm{spring}} = 30k_{\mathrm{B}}T/\sigma^2$ and the maximum bond length $R_{\mathrm{max}} = 1.5\sigma$. The repulsive part of the bond potential was modeled by the LJ-potential with $r_{\mathrm{cut}} = 2^{1/6}\sigma$ and $\varepsilon_{\mathrm{LJ}} = 1.0k_{\mathrm{B}}T$ (k_B is the Boltzmann constant and T is the absolute temperature). Simulations were carried out in the canonical (NVT) ensemble. The constant temperature is maintained by coupling the system (excluding beads on nanoparticle, treated as a rigid body) to a Langevin thermostat. In this case, the equation of motion of the ith bead is

$$m\frac{\mathrm{d}\vec{v}_i(t)}{\mathrm{d}t} = \vec{\mathrm{F}}_i(t) - \xi\vec{v}_i(t) + \vec{\mathrm{F}}_i^{\mathrm{R}}(t) \qquad \text{(Equation S2-12)}$$

where m is the bead mass set to unity for all particles in a system, $\vec{v}_i(t)$ is the bead velocity, and $\vec{F}_i(t)$ denotes the net deterministic force acting on the ith bead. The stochastic force $\vec{F}_i^R(t)$ has a zero average value and δ-functional correlations $< \vec{F}_i^R(t)\ \vec{F}_j^R(t') > = 6k_BT\xi\delta_{ij}\delta(t-t')$. The friction coefficient ξ is set to $\xi = 0.143\ m/\tau_{LJ}$, where τ_{LJ} is the standard LJ-time $\tau_{LJ} = \sigma(m/\varepsilon_{LJ})^{1/2}$. The velocity-Verlet algorithm with a time step $\Delta t = 0.01\ \tau_{LJ}$ is used for integration of the equation of motion. The system is periodic in all directions. All simulations are performed using LAMMPS.[323]

A2.6.1 Preparation of NCTs

The nanoparticle is made of a shell-like shaped assembly of beads in a hexagonal closed-packed (HCP) lattice with an outside radius of 10.0 σ and inside radius of 8.0 σ. To provide enough grafting points and smooth the surface, the density of the HCP lattice is set to 10.0 σ^{-3}. A Fibonacci sphere is generated to make the 1216 grafting points roughly uniformly distributed on the surface of the nanoparticle. Each grafting point is tethered with a spring-bead chain in an ideal configuration with number of monomers $N = 16$. To equilibrate the NCT, non-bonded interactions between polymer chains are slowly turned on from zero to the desired value.

A2.6.2 Simulation Procedures

The simulation starts with placing two NCTs in a box with dimension of $50.0\sigma \times 95\sigma \times 50\sigma$ (see Figure S13). The remaining volume is filled with coarse-grained beads with density of 1.0 σ^3 as explicit solvents. The system is equilibrated for $2\times10^3\ \tau_{LJ}$ to reach equilibrium configuration. The position of the nanoparticle of NCT A is frozen at its initial location as a reference point. To make two NCTs in contact, a harmonic spring with the spring constant $K_{sp} = 200k_BT/\sigma^2$ is tethered to the center of mass of NCT B to push towards NCT A for 200 τ_{LJ}. Upon contact, the spring is removed and the system was equilibrated for $10^4\tau_{LJ}$. The equilibrium NCTs contact (see **Figure S2-12b**) is obtained from simulation runs lasting additional $10^4\tau_{LJ}$. Number of polar groups is counted at the contact of two NCTs defined as a slab at the interface with a thickness of 3.0σ (see **Figure S2-14**). A comparison of geometry between simulation and its corresponding mapped experiment is listed in **Table S2-6**.

	Experiment	Simulation
R_{NP}	13.0 nm	10.0 σ
Molecular Weight	12 kDa	15 bead
End Group	DAP or THY	1 bead
ρ_{brush}	0.5 nm^{-2}	0.968 σ^{-2}
Total Number of Brushes	1061	1216
Thickness of Brush Layer	15.5 nm	12.0 σ
H_{brush} / R_{NP}	1.19	1.2
Inter NCTs distance	46.18 nm	32.00 - 35.00 σ
D_{NCTs} / R_{NCT}	1.62	1.45~1.59

Table S2-6. Comparison of Geometry between Experiment and Coarse-grained Simulations

To study the effect of co-loading on number of active groups and bundling at the contact interface, the fraction of active groups at the chain end in the coarse-grained simulations was varied, and results are summarized in **Table S2-7**. To quantify the bundle size of aggregated active groups between NCTs, Silhouette analysis[324] was performed on k-means clustering[325] using the coordinates of active groups at the contact interface. A range of centroids was looped while running k-means clustering analysis, where the number of bundles was labelled at the highest Silhouette score. Dependence of number of active groups and bundle size on fraction of active polymers is plotted in **Figure S2-13**. Typical configurations of bundling of active groups at NCT-NCT interfaces are shown in **Figure S2-14** and **Figure S2-15**. To investigate the effect of the polar solvent TCE on the interfaces of NCTs through coarse-grained MD simulations, we varied a fraction (from 5% to 100%) of the solvent beads from toluene into a different type with a stronger affinity to DAP and Thy (see **Table S2-5** for detailed interaction parameters). The system was re-equilibrated before a production run of $10^4\tau_{LJ}$. The radial distribution functions (RDF) of toluene and TCE were calculated to validate the preferential solvation effect around NCTs (**Figure S2-16-17**). Only the non-contact hemisphere was considered in the calculations. To compare the relative strength of inhomogeneity across different TCE fractions, density distribution curves were normalized by their far field values respectively. Below a radius of approximately 20σ there is a sharp rise in solvent density, which is due to the decreasing density of the polymer brush further from the nanoparticle core. At low TCE concentrations, the density of TCE is greater at the NCT

periphery than it is in the bulk. This can be explained by a preferential solvation effect, where the polar TCE solvent is attracted to the polar supramolecular groups. At higher TCE concentrations, the effect becomes less pronounced, due to the large amount of available TCE. In order to quantify the dynamics of the polar groups at the interface, mean square displacement (MSD) was calculated during the entire production run for different TCE volume fractions (**Figure S2-17**). $MSD(\Delta t) = \frac{1}{N_0}\sum_{i=1}^{N_0}\left(x_i(t) - x_i(t+\Delta t)\right)^2$ where N_0 is the total number of polar groups at the interface of the initial configuration, and $x_i(t)$ is the position of bead i at time t. Increasing TCE results in a larger value of MSD, which signifies a higher mobility of the supramolecular binding groups.

f_A	f_B	N_A	N_B	N_{Total}	D_{Inter}
1.00	1.00	150.812	152.475	303.287	34.05
0.90	1.00	139.257	143.366	282.623	34.792
0.80	1.00	160.406	174.356	334.762	31.038
0.70	1.00	137.663	167.089	304.752	31.422
0.60	1.00	96.99	130.04	227.03	34.142
0.50	1.00	86.158	133.891	220.049	33.418
0.25	1.00	47.97	134.356	182.326	30.939
0.90	0.90	171.455	163.574	335.029	30.69
0.80	0.80	141.97	133.525	275.495	32.539
0.70	0.70	116.614	110.535	227.149	32.599
0.60	0.60	84.812	80.277	165.089	33.571
0.50	0.50	67.168	66.752	133.92	33.372
0.25	0.25	28.95	33.337	62.287	31.908

Table S2-7. Simulation Results of Number of Polar Groups at the Interface

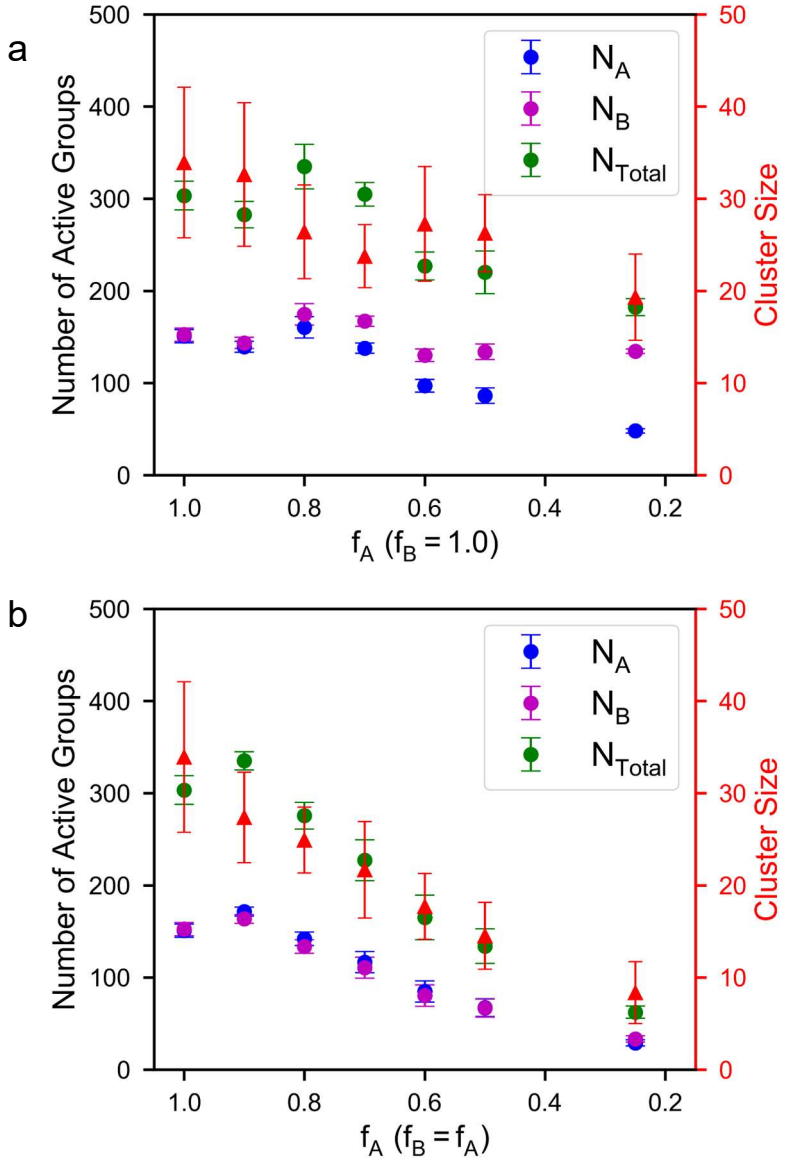

Figure S2-13. Dependence of number of active groups (left Y-axis) and cluster size (right Y-axis) on fraction of active polymer for co-loading of one side (a) and two sides symmetrically (b).

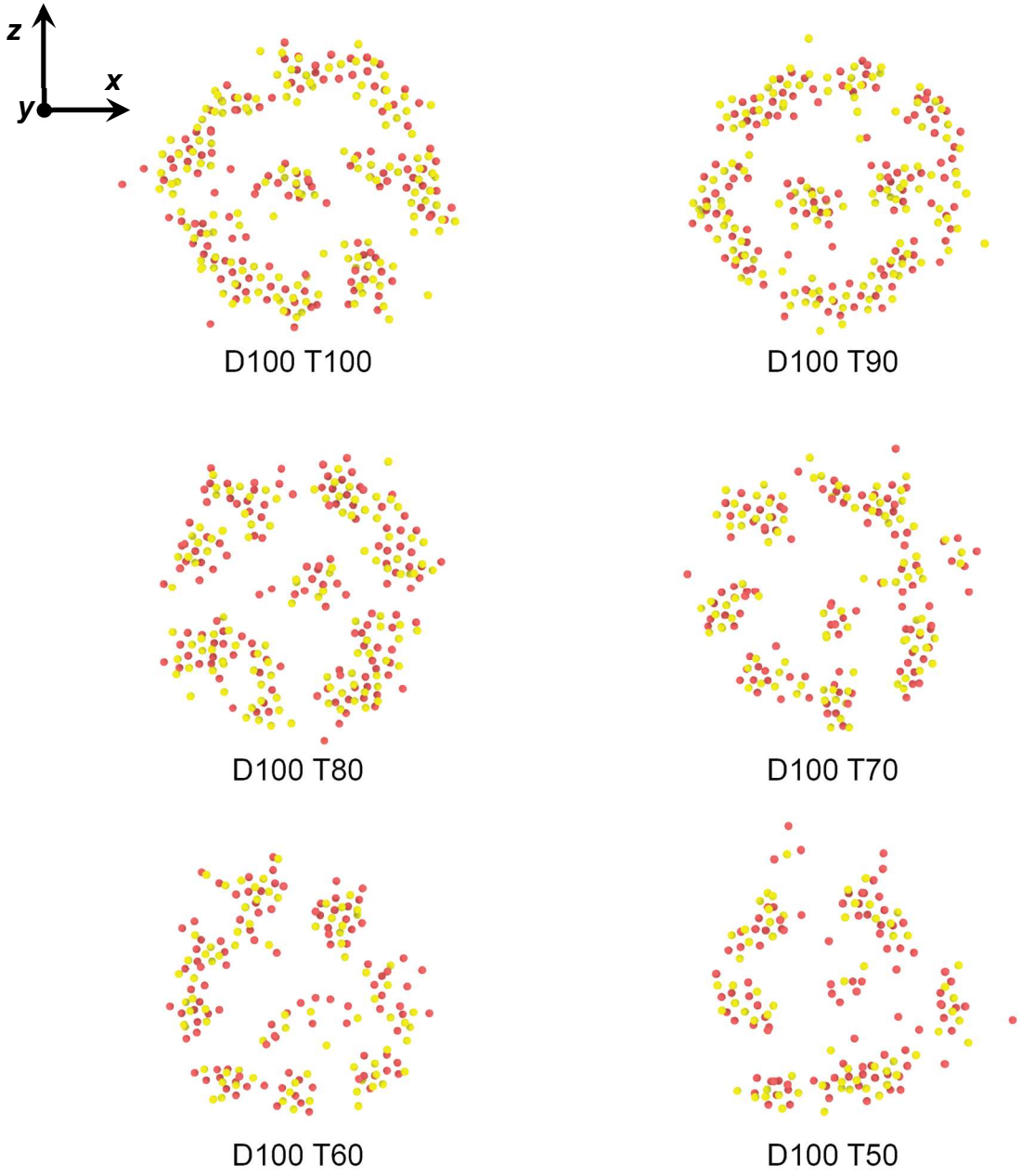

Figure S2-14. Snapshots of the NCT-NCT interface for asymmetrically coloaded NCTs as calculated by molecular dynamics simulations.

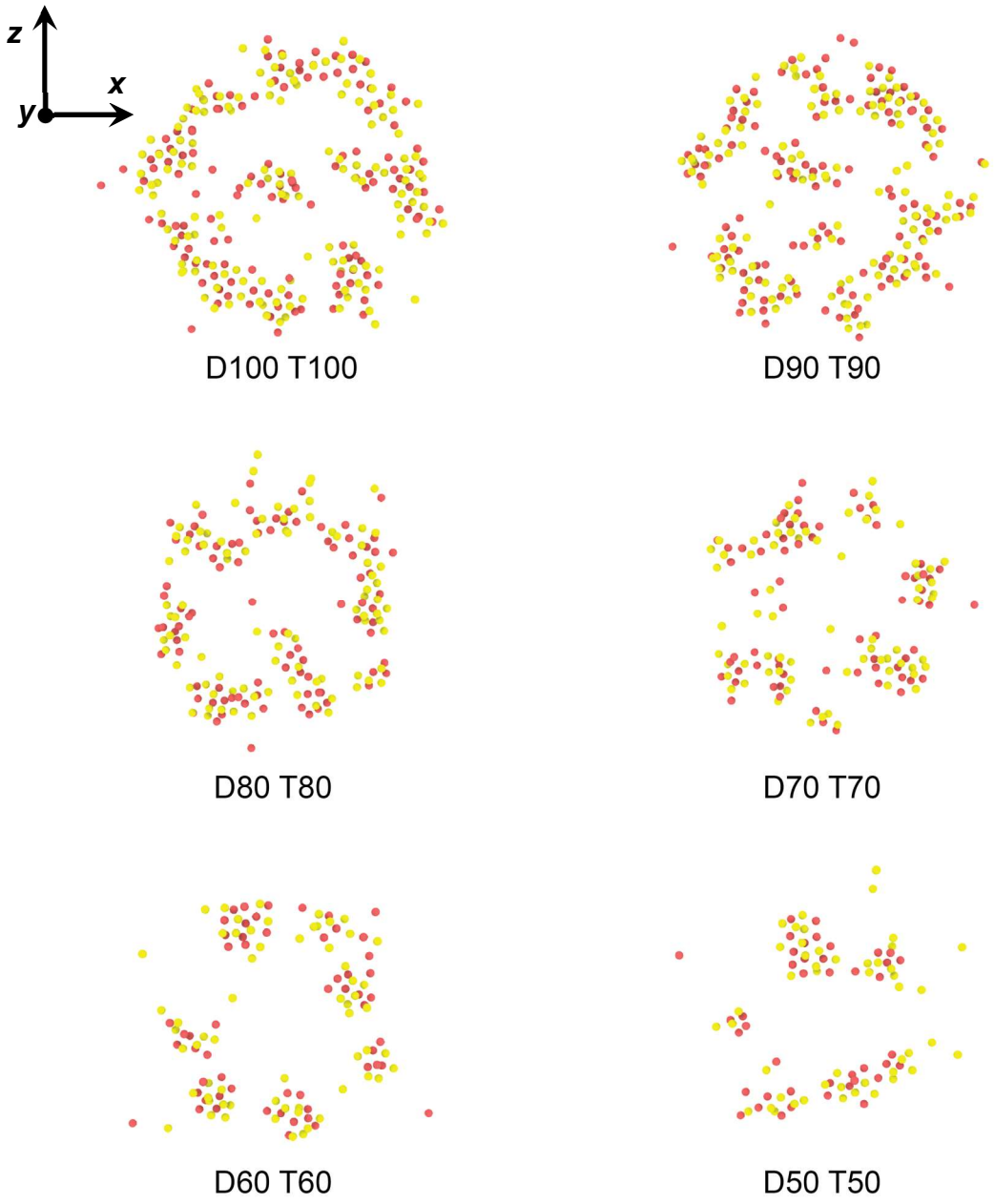

Figure S2-15. Snapshots of the NCT-NCT interface for symmetrically coloaded NCTs as calculated by molecular dynamics simulations.

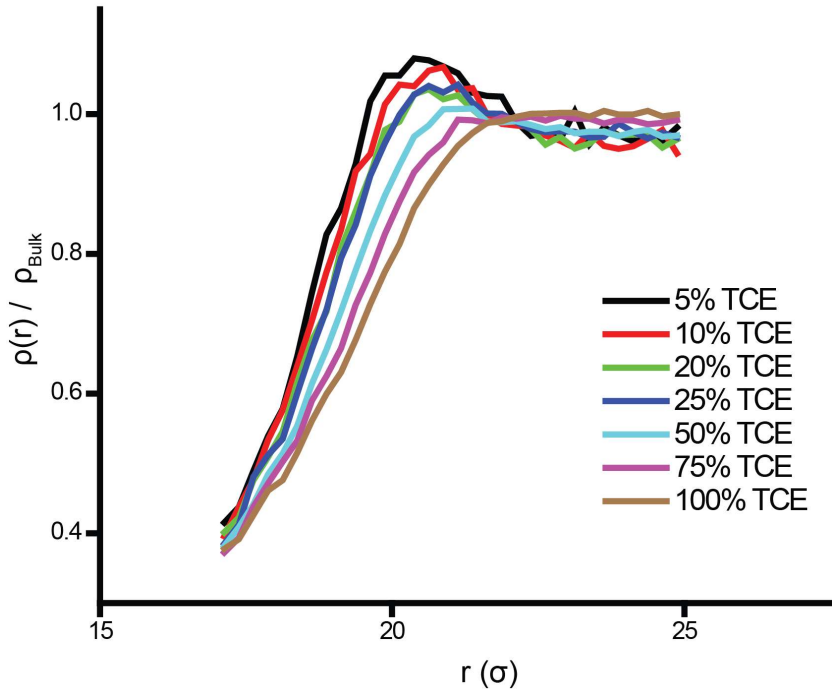

Figure S2-16. Normalized radial distribution functions of TCE.

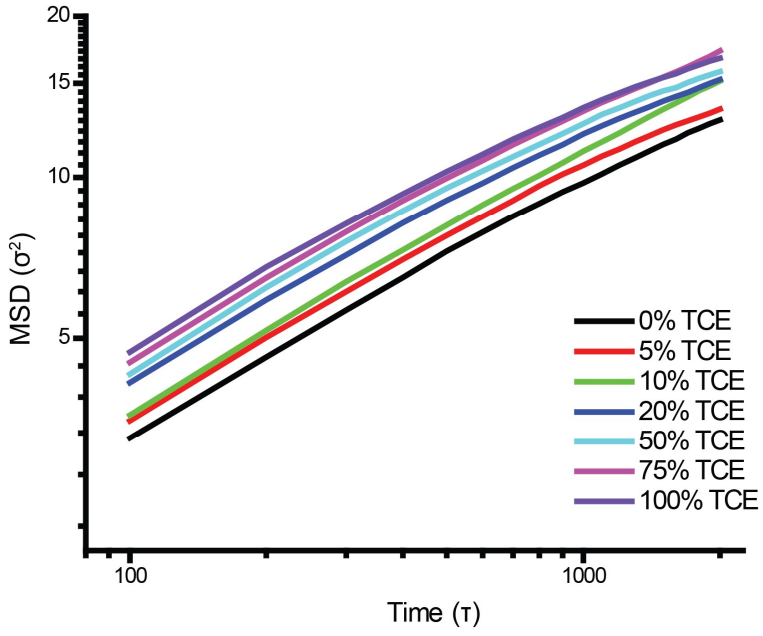

Figure S2-17. Mean square displacement of polar groups at contact interface.

A2.7 Variable Temperature ^{1}HNMR Titrations of Small Molecule Analogues

Thermodynamic parameters (enthalpy, entropy) for the binding of the small molecule DAP and Thy analogues were determined using variable temperature NMR by measuring the shift of the ^{1}HNMR peak for the thymine imide proton. The isotherms were calculated by using the BindFit online tool,[326] and an Arrhenius plot generated from the resulting association constants. The enthalpies were used in this work, though the binding entropy was not considered because they are expected to substantially increase when the supramolecular binding groups are tethered to polymers, and additionally entropy values calculated from ^{1}HNMR titrations are highly susceptible to small errors in the fitting and so should be regarded with caution. The energy of even a single hydrogen bond pair is quite high, and so can be reasonably approximated as the sole enthalpic contributor to NCT assembly. A minimal contribution is expected from the polymer chains, as toluene and TCE are both good solvents for polystyrene, and other van der Waals forces can be safely neglected.

Sample	**ΔH (kJ/mol)**
100% Toluene	31.93
5 % TCE	23.50
10% TCE	18.83
15% TCE	17.58
20% TCE	16.57
100% TCE	16.05

Table S2-8. Summary of variable temperature ^{1}HNMR Titrations

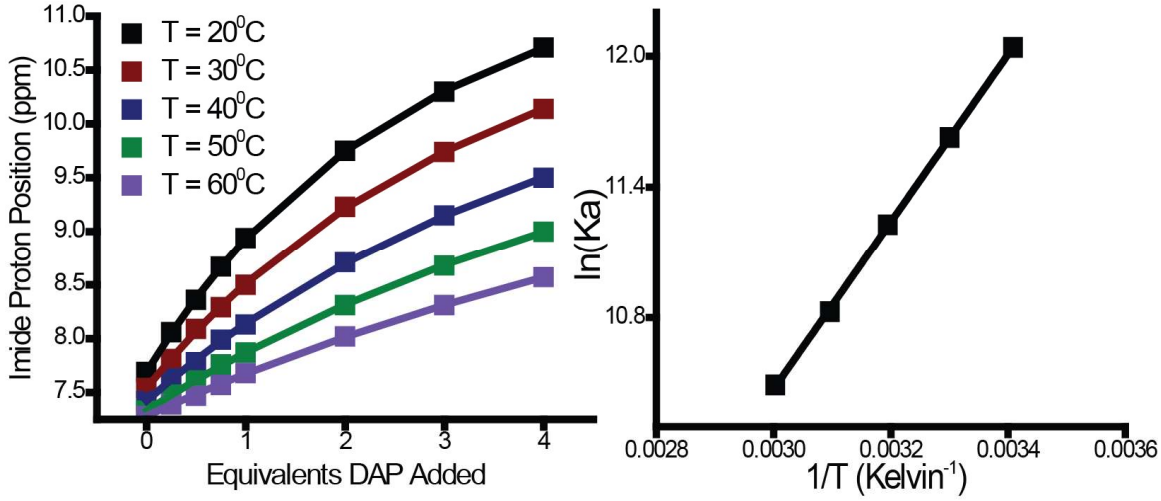

Figure S2-18. Variable temperature ^{1}HNMR titration of DAP and Thy small molecule analogues in toluene

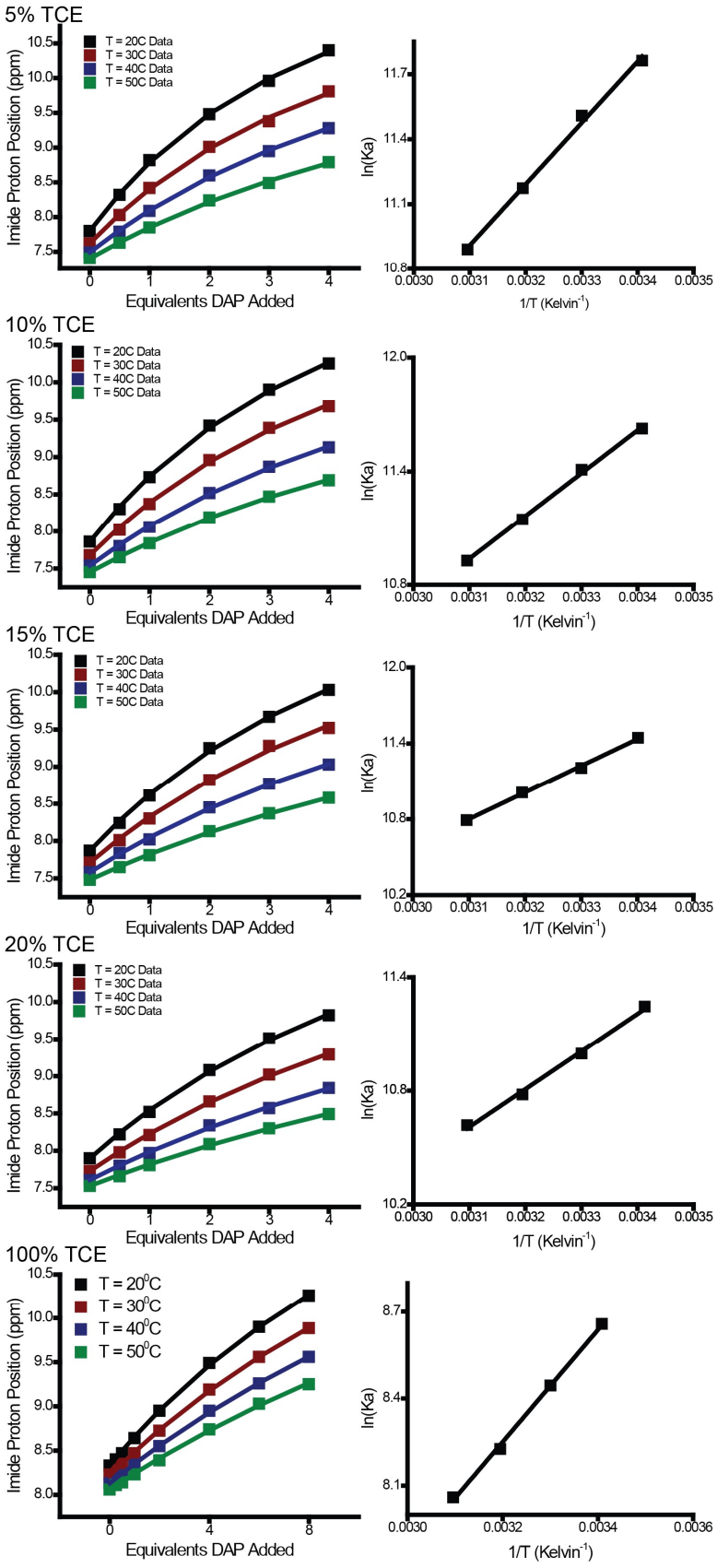

Figure S2-19. Variable temperature ^{1}HNMR titrations to determine the enthalpy for DAP-Thy in varying volume fractions of TCE.

A2.8 SAXS of Amorphous NCT Aggregates

SAXS experiments on amorphous NCT aggregates were used to corroborate the molecular dynamics model by matching the interparticle spacings of the model to the interparticle spacings measured experimentally for the exact NCT system modeled (46.2 nm). Here, the interparticle distance was calculated as $= \frac{2\pi}{q_0}$.

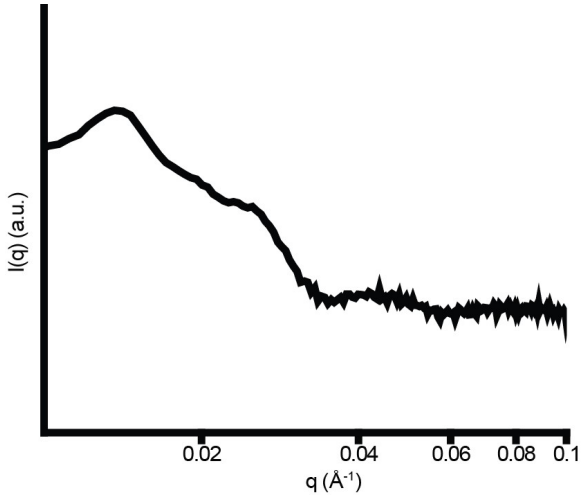

Figure S2-20. SAXS of an amorphous NCT aggregate made from 12 kDa DAP and Thy polymers and 26 nm AuNPs, the system that the coloading experiments were performed on, and was simulated in the model. The interparticle distance is comparable to the result of the simulation.

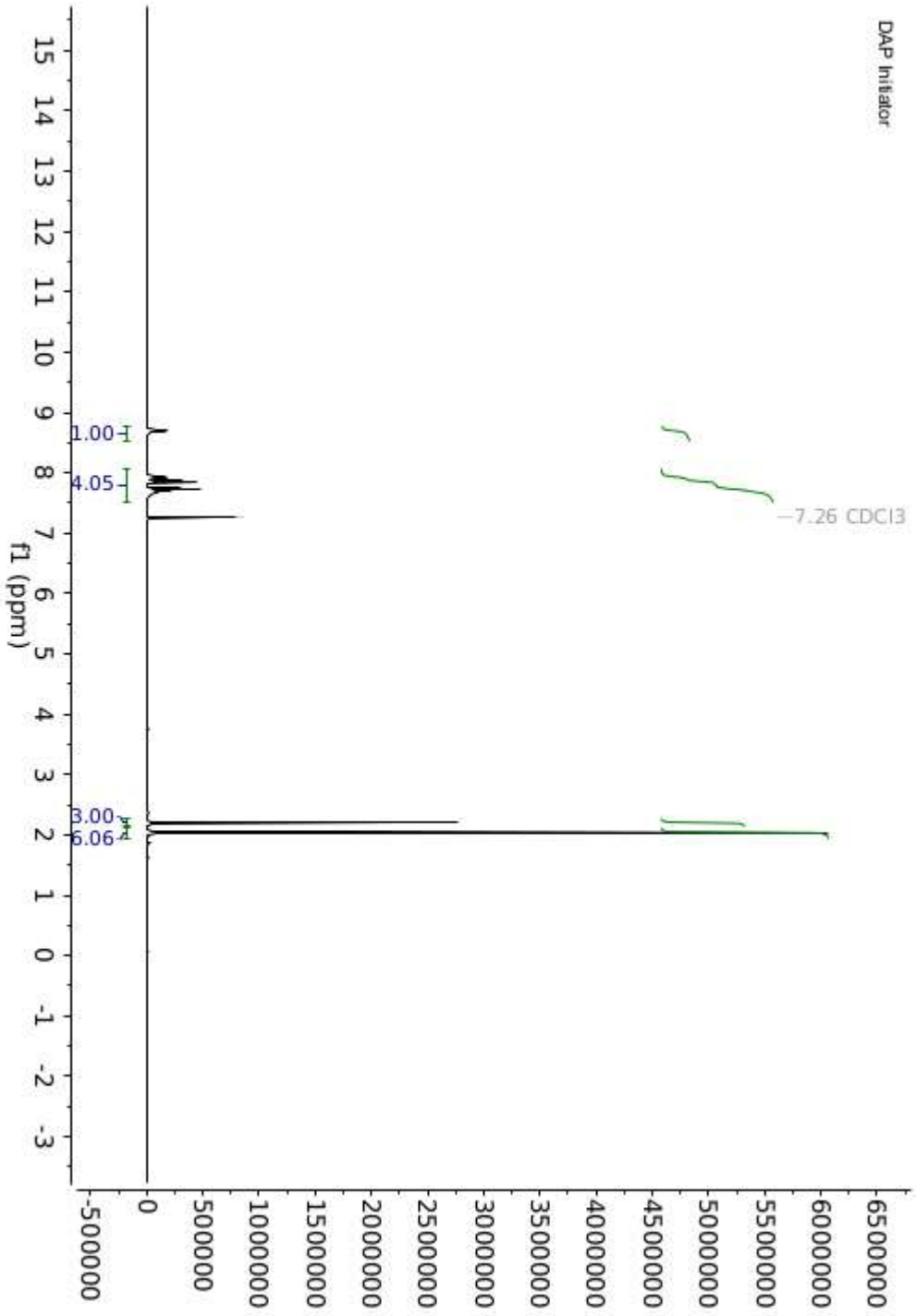
DAP Initiator
7.26 CDCl3
1.00
4.05
3.00
6.06
f1 (ppm)

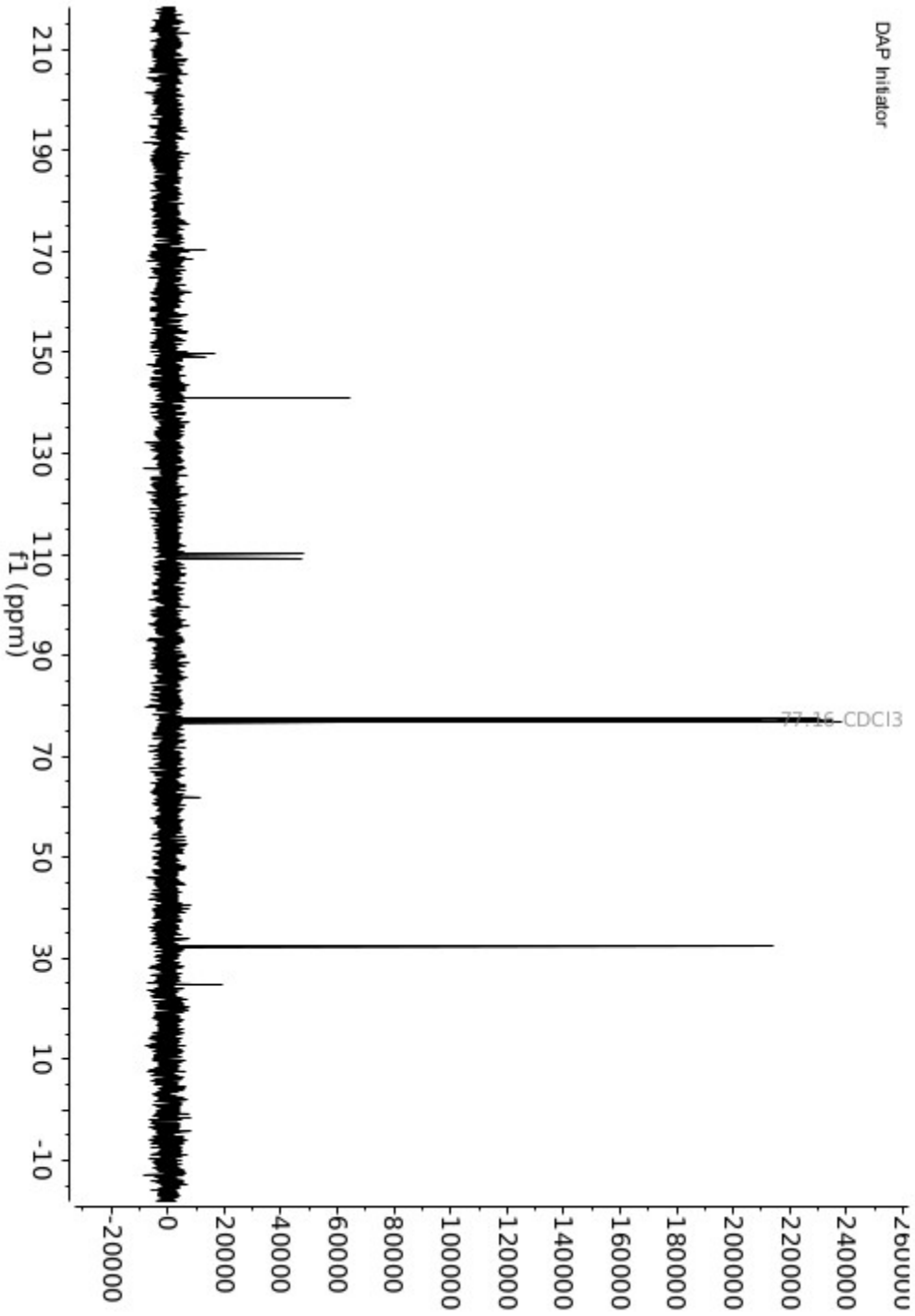
DAP Initiator
77.16 CDCl3
f1 (ppm)
210
190
170
150
130
110
90
70
50
30
10
-10
-20000
0
20000
40000
60000
80000
100000
120000
140000
160000
180000
200000
220000
240000

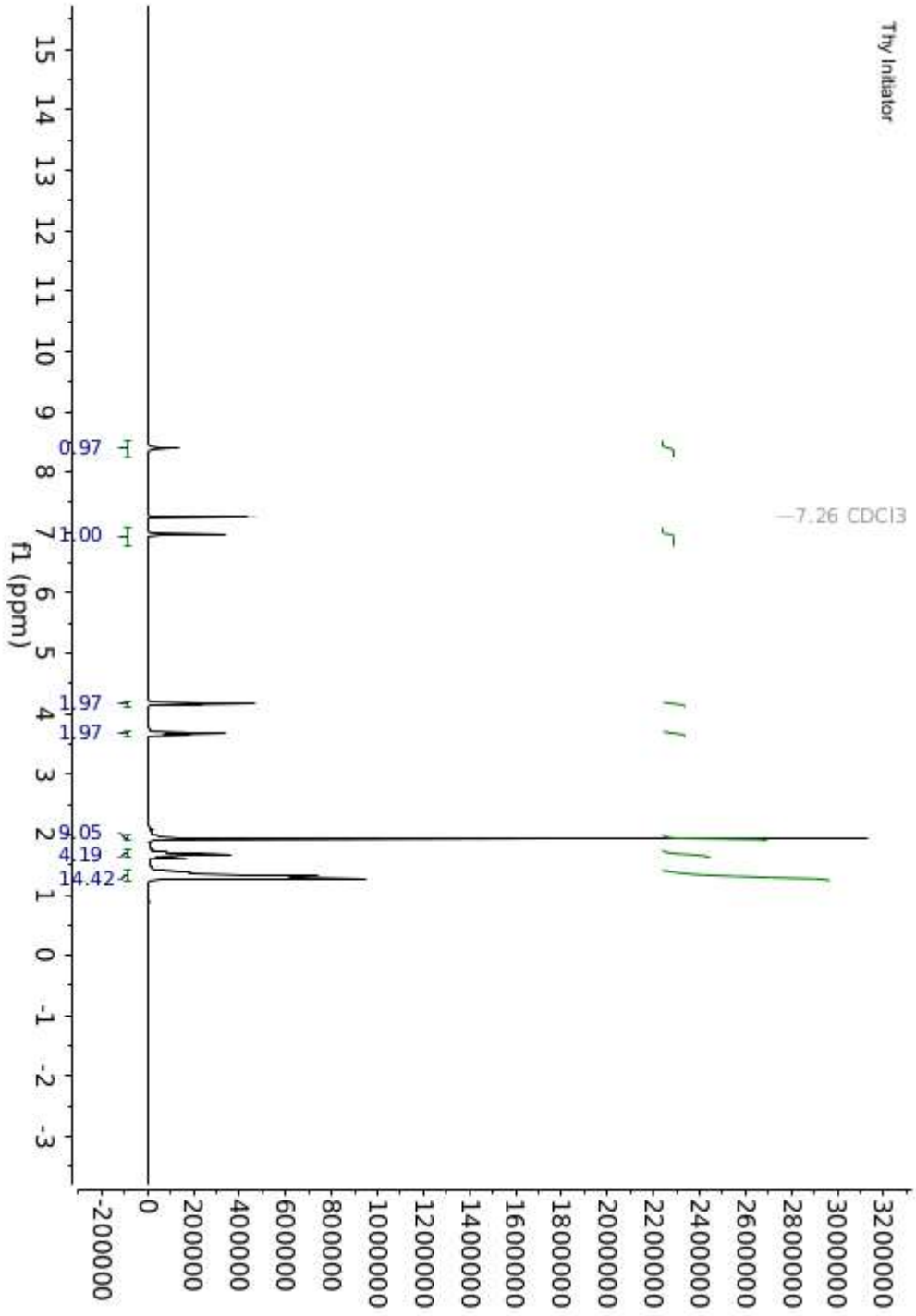
Thy Initiator
7.26 CDCl3
0.97
1.00
1.97
1.97
9.05
4.19
14.42
f1 (ppm)

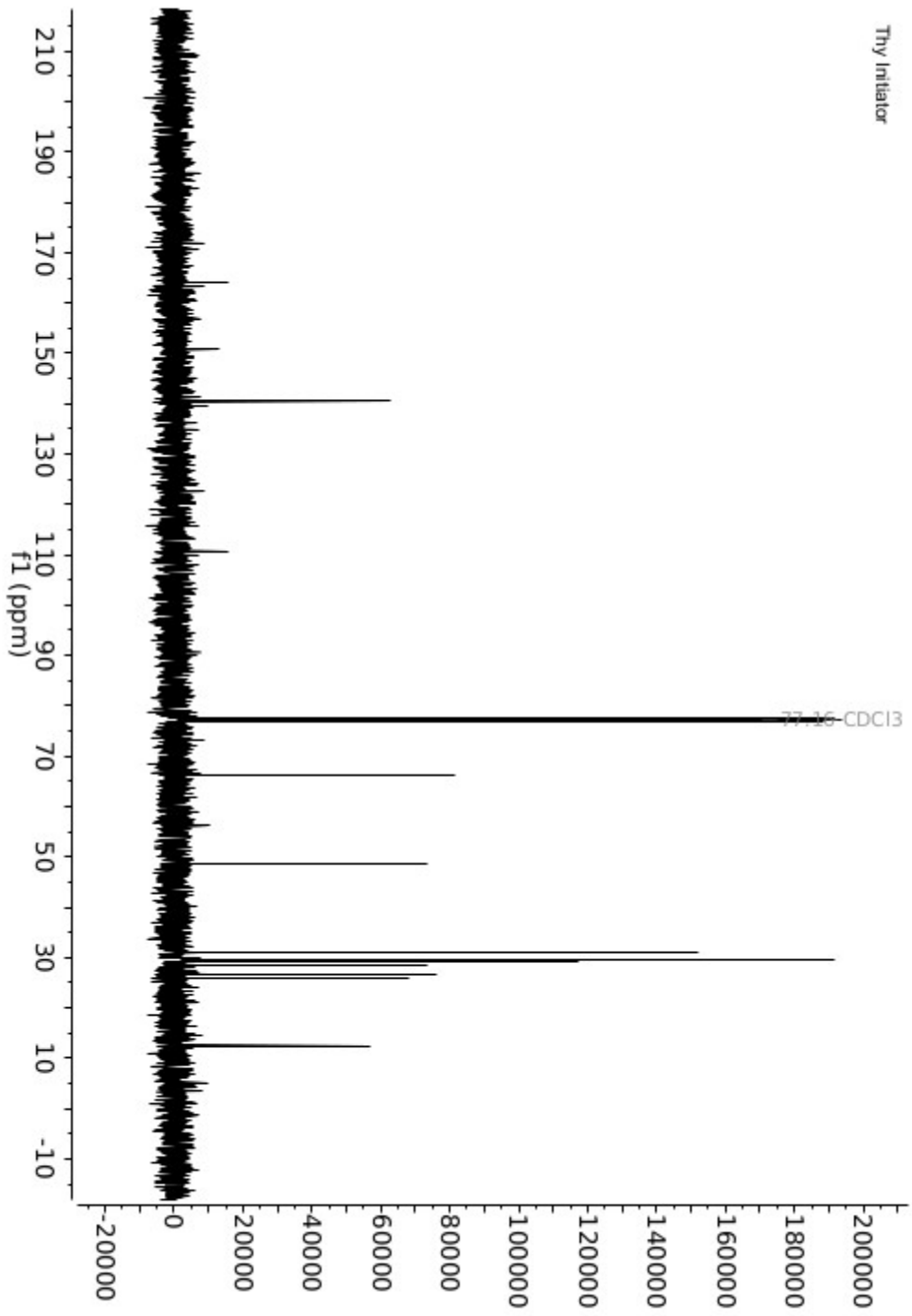
Thy Initiator
77.16-CDCl3
f1 (ppm)
210
190
170
150
130
110
90
70
50
30
10
-10
-20000
0
20000
40000
60000
80000
100000
120000
140000
160000
180000
200000

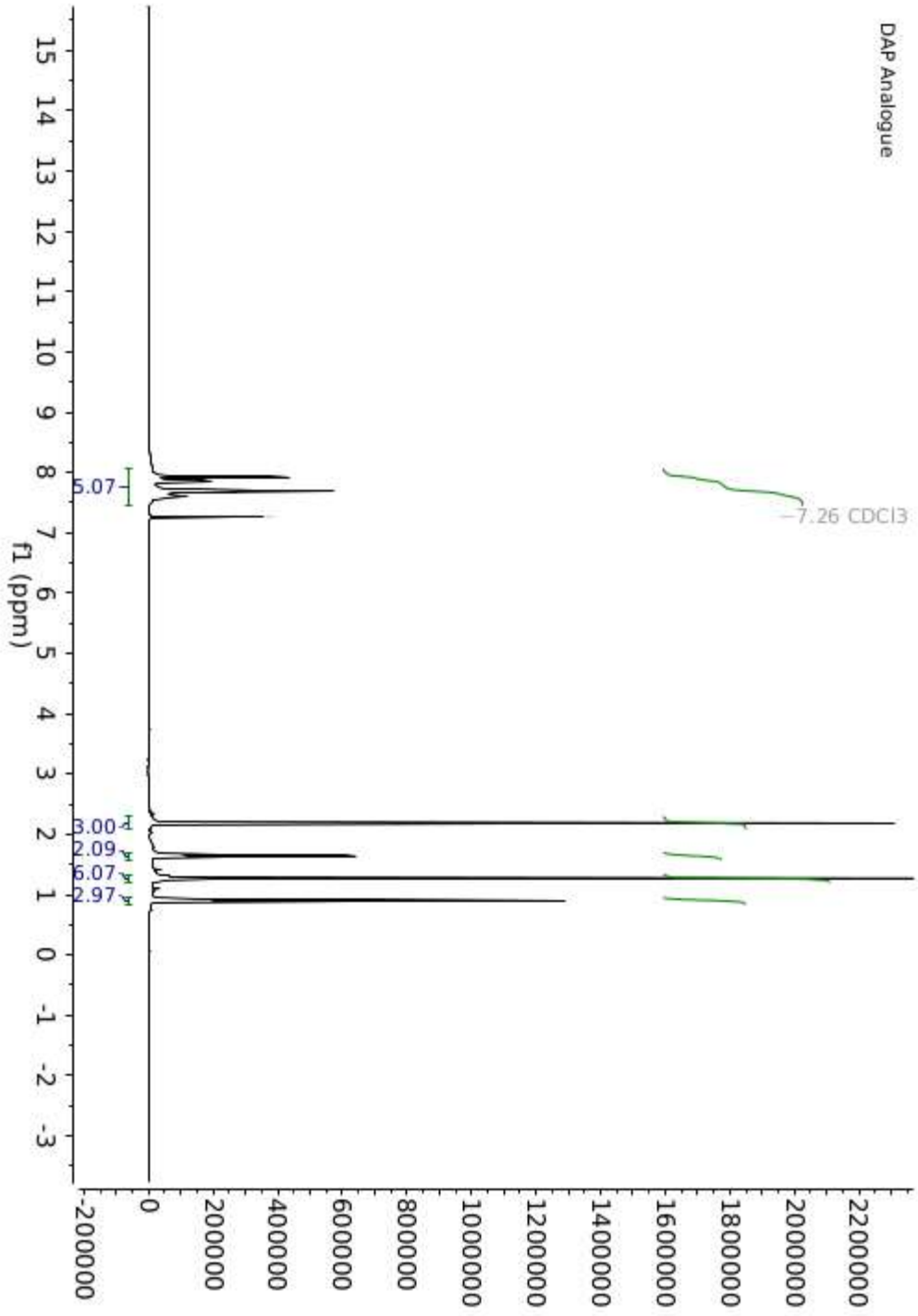
DAP Analogue
7.26 CDCl3
6.07
3.00
2.09
6.07
2.97
f1 (ppm)

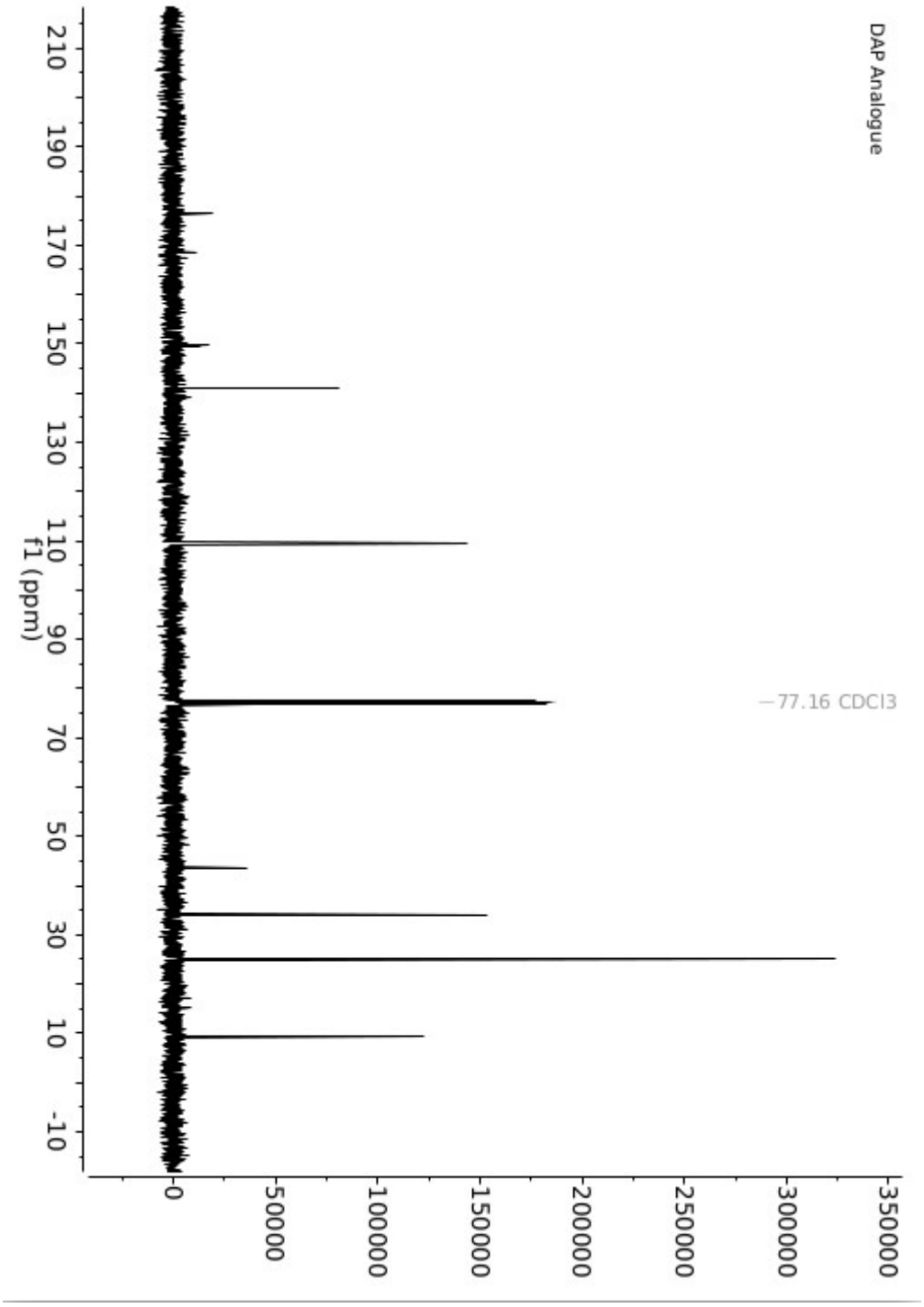
DAP Analogue
77.16 CDCl3
f1 (ppm)
210
190
170
150
130
110
90
70
50
30
10
-10
0
50000
100000
150000
200000
250000
300000
350000

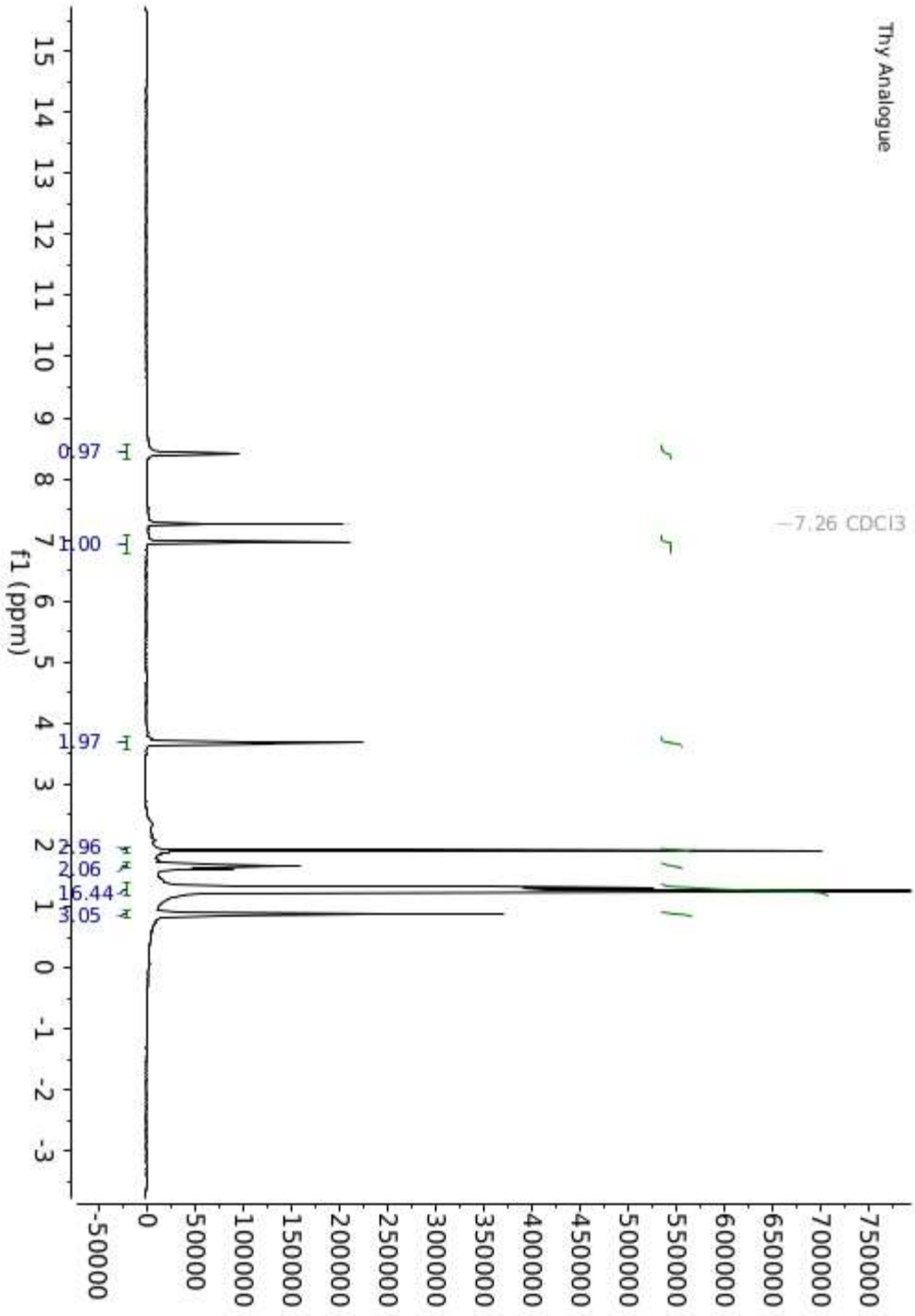
Thy Analogue
7.26 CDCl3
0.97
1.00
1.97
2.96
2.06
16.44
3.05
f1 (ppm)

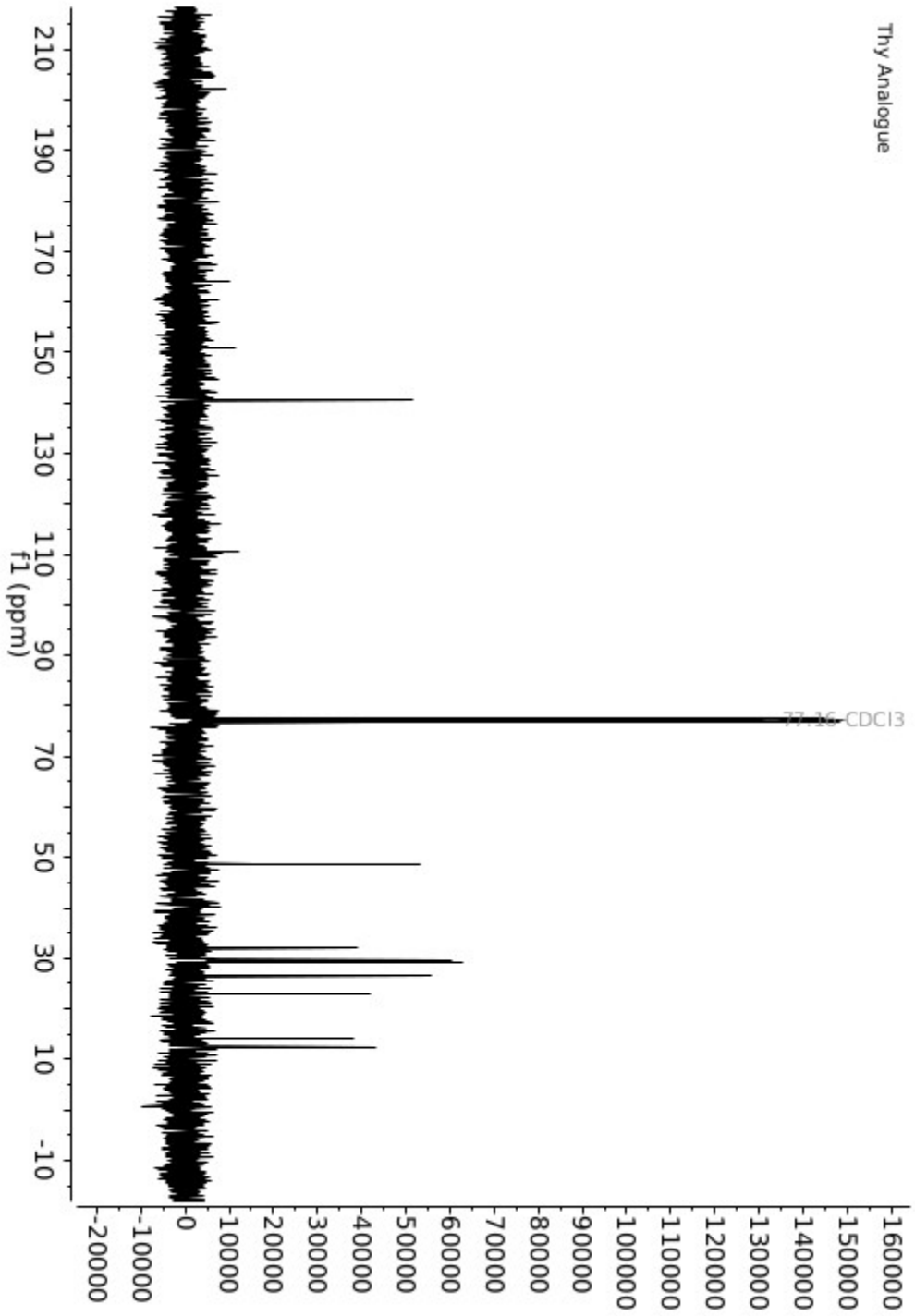
Thy Analogue
77.16-CDCl3
f1 (ppm)
210
190
170
150
130
110
90
70
50
30
10
-10
-20000
-10000
0
10000
20000
30000
40000
50000
60000
70000
80000
90000
100000
110000
120000
130000
140000
150000
160000

Appendix 3. Assembling Ordered Crystals with Disperse Building Blocks

A3.1 Materials and Characterization Methods

2,6-Diaminopyridine, thymine, acetyl chloride, 11-bromoundecan-1-ol, 2-Bromoisobutyryl bromide, styrene, N,N,N',N",N'"-Pentamethyldiethylenetriamine (PMDETA), trisodium citrate dihydrate, Tris[2-(dimethylamino)ethyl]amine (Me_6TREN), tin(II) 2-ethylhexanoate, and basic alumina were purchased from Fisher Scientific. Copper (I) bromide, copper (II) bromide, and gold (III) chloride trihydrate were purchased from Sigma Aldrich. Aminoethanethiol was purchased from TCI America. General solvents were purchased from Fisher Scientific. All chemicals, including solvents, were used without further purification, except styrene, which was passed through a short column of basic alumina to remove inhibitor prior to polymerization. Note that some solvents were purchased as anhydrous grade, as noted in the experimental details.

Centrifugation was performed with an Eppendorf 5424 centrifuge. ^{1}H NMR spectra were obtained on a Varian Mercury 300 MHz instrument or on a Varian Inova 500 MHz instrument. ^{13}C NMR spectra were obtained with a collection frequency of 101 MHz. Mass spectra were collected on a JEOL AccuTOF – DART spectrometer. Gel permeation chromatography (GPC) characterizations were performed on an Agilent Technologies GPC system, with THF as the eluent at 1.0 mL/min, and monodisperse polystyrene as the standard. UV-vis spectra and measurements were obtained on a Cary-5000 spectrometer. In-situ small angle x-ray scattering (SAXS) measurements were performed at the 12ID-B station at the Advanced Photon Source (APS) at Argonne National Laboratory. The samples were probed using 14 keV (0.8856 Å) X-rays, and the sample-to-detector distance was calibrated with a silver behenate standard. The beam was collimated using two sets of slits, and a pinhole was used. Scattered radiation was detected using a Pilatus 2 M detector. Other SAXS measurements were performed on a SAXSLAB instrument with a Pilatus3R 300K detector and an X-ray wavelength of 1.54Å. Transmission electron microscopy (TEM) was performed with a JEOL 2010 Advanced High Performance transmission electron microscope.

A3.2 Synthesis

We have previously reported the synthesis of the supramolecular polymer initiators, the polymers themselves, and NCTs.[222] Below, that information is briefly summarized:

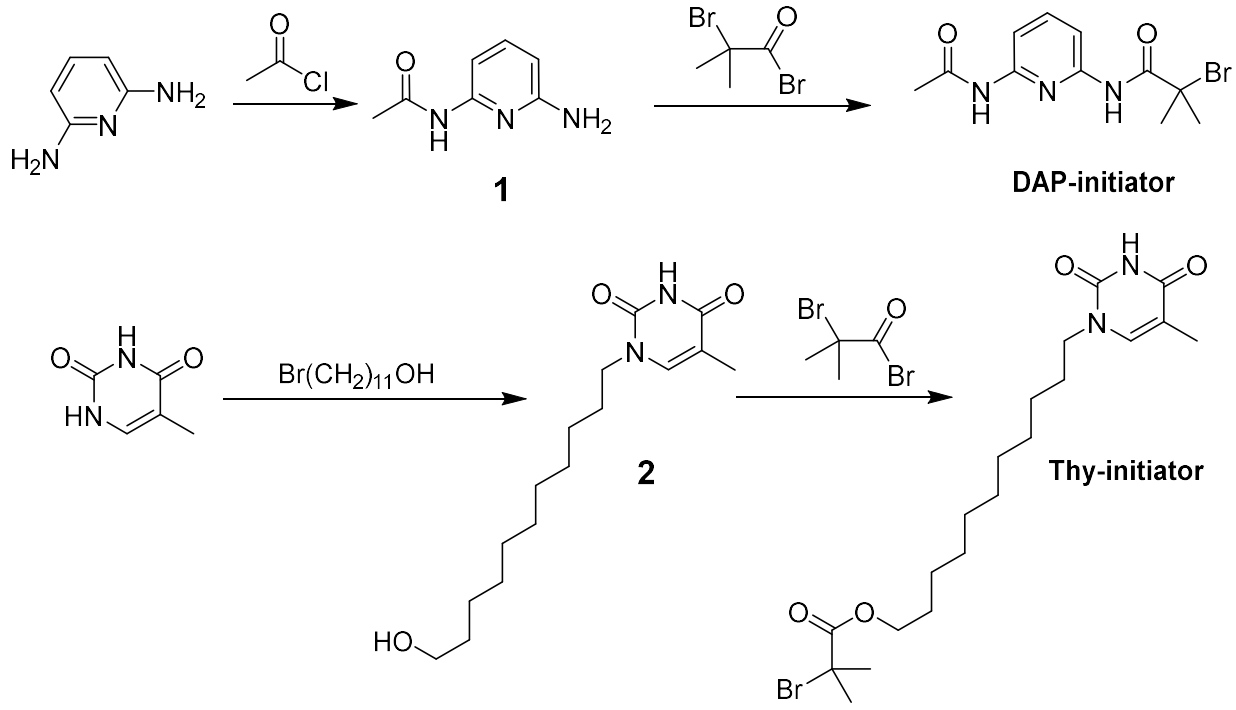

Scheme S3-1. Synthetic scheme for DAP and Thy initiators

A3.2.1 DAP-Initiator

5.5 g 2,6-diaminopyridine (50 mmol) was dissolved in 40 mL dry THF in a 3-necked round bottom flask. At 0 ºC, the solution of 1.96 g (25 mmol) acetyl chloride in 15 mL dry THF was added dropwise under a nitrogen atmosphere. The reaction mixture was allowed to warm to room temperature and stirred for 12 hours. The insoluble content was filtered off, and the solvent was removed under reduced pressure. The resulting solid was recrystallized in a mixture of ethanol and toluene, to afford **1** as a white solid (52%). ^{1}H NMR ($CDCl_3$, δ ppm): 7.55-7.65 (broad, s, 1H), 7.49-7.54 (broad, d, 1H), 7.45 (t, 1H), 6.25, (d, 1H), 4.32, (s, 2H), 2.16 (s, 3H). 1.9 g **1** (12.6 mmol) was dissolved in 80 mL dichloromethane, and then 3.5 mL triethylamine (25 mmol) was added to this solution. The mixture was cooled to 0 ºC, and a solution of 3.22g 2-bromoisobutyryl bromide (17.6 mmol) in dichloromethane (~10 mL) was added dropwise under a nitrogen atmosphere. The

reaction mixture was allowed to warm to room temperature and stirred for 12 hours. The insoluble content was filtered off, and the filtrate was washed with a sodium carbonate solution (x1) and brine (x3). The organic phase was dried over sodium sulfate, the solvent was removed under reduced pressure, and the product was then purified by flash chromatography (CH_2Cl_2/EtOAc 4:1). The product was further purified by recrystallization in CH_2Cl_2/EtOAc/hexanes to afford N-(6-acetamidopyridin-2-yl)-2-bromo-2-methylpropanamide (DAP-Initiator) (79%). ^{1}H NMR ($CDCl_3$, δ ppm): 8.74 (s, 1H), 7.90-7.96 (d, 1H), 7.83-7.89 (dd, 1H), 7.70-7.76 (t, 1H), 7.68-7.82 (broad, s, 1H), 2.21 (s, 3H), 2.04 (s, 6H) ^{13}C NMR ($CDCl_3$, δ ppm): 170.36, 168.59, 149.66, 149.10, 141.08, 110.09, 109.25, 61.85, 32.38, 24.93. MS: $[BrC_{11}H_{15}N_3O_2]^+$ Calculated 300.03480, Found 300.0350

A3.2.2 Thy-Initiator

5.0 g thymine (40 mmol), 1.0 g 11-bromo-1-undecanol (4 mmol), 1.1 g potassium carbonate (8 mmol) and 200 mL DMSO were added to a 500 mL round bottom flask. The mixture was stirred and bubbled with nitrogen for 2 minutes, and then sealed with a septum and stirred for 48 hours. The resulting mixture was poured into water and chloroform for extraction, and the organic phase was collected and washed 3 more times with brine, followed by drying over sodium sulfate and removal of solvent. The resulting white solid was recrystallized in EtOAc/hexanes to afford compound 2 (84%). 1H NMR (CDCl3, δ ppm): 8.18 (s, 1H), 6.97 (m, 1H), 3.66-3.71 (t, 2H), 3.60-3.66 (t, 2H), 1.92 (d, 3H), 1.22-1.75 (m, 18 H). With the help of very gentle heat, 592 mg **2** (2 mmol) was dissolved in 150 mL dichloromethane, and 0.39 mL triethylamine (2.8 mmol) was added to the solution. The mixture was cooled to 0 ºC, and a solution of 552 mg 2-bromoisobutyryl bromide (2.4 mmol) in dichloromethane (~ 10 mL) was added dropwise under a nitrogen atmosphere. The reaction mixture was allowed to warm to room temperature and stirred for 14 hours, and then washed with sodium carbonate (x2) and brine (x2). The organic phase was dried with sodium sulfate, and the solvent was removed under reduced pressure. The resulting mixture was purified by flash chromatography (CH_2Cl_2/EtOAc 8:3), to afford the 11-(5-methyl- 2,4-dioxo-3,4-dihydropyrimidin -1(2H)-yl)undecyl 2-bromo-2-methylpropanoate (Thy-Initiator) (Rf = 0.4) as an off-white solid. ^{1}H NMR ($CDCl_3$, δ ppm): 9.86 (s, 1H), 6.96 (d, 1H), 4.08-4.15 (t, 2H), 3.60-3.68 (t, 2H), 1.88 (s, 6H), 1.87 (d, 3H), 1.55-1.70 (m, 4H), 1.15-1.38 (m 14H). ^{13}C NMR ($CDCl_3$,

δ ppm): 171.89, 164.08, 150.78, 140.53, 110.63, 66.28, 56.18, 48.71, 30.94, 29.53, 29.31, 29.26, 28.48, 26.58, 25.90, 12.49. MS: $[BrC_{20}H_{34}N_2O_4]^+$ Calculated 445.17023, Found 445.1711

A3.2.3 DAP-PS Polymers

In a typical polymerization process, DAP-initiator (1.0 eq), Me6TREN (0.83 eq), styrene (200-300 eq depending on target molecular weight), copper (II) bromide (0.1 eq), and anisole (0.8:1 v/v to styrene) were added to an oven-dried and nitrogen filled Schlenk flask. The reaction flask was then sealed with a rubber septum and the mixture was taken through 3 freeze-pump-thaw cycles and refilled with nitrogen. Simultaneously, tin(II) 2-ethylhexanoate (0.15 eq) and anisole (0.2:1 v/v to styrene) were combined in a vial and bubbled with N_2. After the reaction flask finished returning to room temperature, the tin(II) 2-ethylhexanoate mixture was injected and the flask immersed in an oil bath at 105ºC. The mixture was stirred at 105ºC under a nitrogen atmosphere, and quenched at different time points to give polystyrene of different molecular weights. The typical reaction time was 1-4 hours. To quench the reaction, the reaction mixture was poured into cold methanol, and the precipitated polymer was collected, redissolved in dichloromethane, and precipitated in methanol again to afford the polymer with a chain-end bromine.

Purified polystyrene obtained from DAP initiator was then dissolved in DMF (~ 10 mg/mL) with a small amount of triethylamine (40 eq), and the solution was bubbled with nitrogen for 5 minutes, followed by the addition of 2-aminoethanethiol (15 eq). The reaction flask was capped, and the solution was stirred for 60 hours, then poured into a mixture of dichloromethane and brine. The organic phase was washed with brine repeatedly (x3), concentrated, and precipitated in methanol (redissolve-precipitate x4). The resulting white powder was dried under vacuum to give the DAP-PS polymer.

A3.2.4 Thy-PS Polymers

In a typical polymerization process, Thy-initiator (1 eq), PMDETA (1.0 eq), styrene (200 eq), and anhydrous anisole (30 vol% in styrene) were added to an oven-dried and nitrogen filled Schlenk flask. The reaction flask was then sealed with a rubber septum and the mixture was taken through 3 freeze-pump-thaw cycles and refilled with nitrogen. Once the mixture returned to room temperature, the septum was removed, CuBr (1.0 eq) was quickly added against a positive nitrogen

flow, and the flask was immediately resealed. The mixture was stirred at 110 ºC under a nitrogen atmosphere, and quenched at different time points to give polystyrene of different molecular weights. Typical reaction time was 1-3 hours. To quench the reaction, the reaction mixture was poured into cold methanol, and the precipitated polymer was collected, redissolved in dichloromethane, and precipitated in methanol again to afford the polymer with a chain-end bromine.

The polymer was subsequently dissolved in DMF (~ 10 mg/mL) with small amount of triethylamine (40 eq), and the solution was bubbled with nitrogen for 5 minutes, followed by the addition of 2-aminoethanethiol (15 eq). The reaction flask was capped, and the solution was stirred for 60 hours, then poured into a mixture of dichloromethane and brine. The organic phase was washed with brine repeatedly (x3), concentrated, and precipitated in methanol (redissolve-precipitate x4). The resulting white powder was dried under vacuum to give the Thy-PS polymer.

A3.2.5 Nanoparticle Synthesis

Gold nanoparticles were synthesized from an established seeded growth protocol.[29] Briefly, a 500 mL solution of 2.2 mM trisodium citrate dihydrate was brought to a boil. To synthesize 12 nm nanoparticles, 2 mL of 25 mM $HAuCl_4{:}3H_2O$ was rapidly injected to the solution under vigorous stirring. Within one minute the solution began to darken, and after 15 minutes it stabilized as a deep red color. To synthesize larger nanoparticles, the same procedure was used as the starting point of a seeded growth method. After the initial injection to synthesize the seeds, the solution temperature was lowered to 90°C, and given 30 minutes to equilibrate. Then, another injection of 2 mL of 25 mM $HAuCl_4{:}3H_2O$ was performed, the solution given 30 minutes to equilibrate, followed by a final injection of another 2 mL of 25 mM $HAuCl_4{:}3H_2O$. After the third addition of the precursor gold salt, half of the solution (250 mL) was removed from the flask and stored in the dark at room temperature. The volume of the reaction solution was brought back to 500 mL by adding 250 mL 2.2 mM sodium citrate, and allowed to equilibrate at 90°C for 30 minutes. The resulting average nanoparticle diameter size could be reliably controlled by modifying the number of injections of gold precursor.

A3.2.6 Synthesis of NCTs

NCTs were synthesized from the AuNP and polymer components as was previously reported.[203,222] In a typical synthesis, an appropriate mass of DAP-PS or Thy-PS polymer (thiol terminated) was dissolved in 5.0 mL of acetone in a glass vial to yield a 0.2 mM solution. The solution was vigorously stirred while 5.0 mL of gold nanoparticle (AuNP) solution was quickly poured into the vial, and the resulting suspension was allowed to stir for 1 hour. After the formation of dark red precipitate on the wall and at the bottom of the vial, the colorless supernatant was removed by direct decantation or with the aid of light centrifugation. 5-6 mL of solvent was added to the vial to redisperse the precipitate, and the resulting dispersion was distributed in centrifuge tubes and purified for 3 centrifuge cycles, 40 minutes at 2,348 RCF. The solvents used to redisperse the AuNP precipitate at the end of each cycle were DMF, toluene, and toluene, respectively, and the final toluene dispersions were used for the self-assembly experiments.

A3.2.6 Polymer Characterization

Polymer molecular weight and dispersity were determined by GPC against polystyrene standards (traces, **Figure S3-1**). For ease of understanding, each batch of polymer was then given a name corresponding to the molecular weight rounded to the nearest kilodalton (kDa), summarized in **Table S3-1**.

Sample Name	Mn (kDa)	Dispersity
DAP 10K	9.644	1.048
DAP 11K	10.820	1.062
DAP 12K	12.420	1.052
Thy 12K	12.220	1.061
DAP 13K	12.920	1.053
DAP 14K	13.850	1.038
DAP 16K	16.030	1.044

Table S3-1. Molecular weight and dispersities of the polymers used in this work.

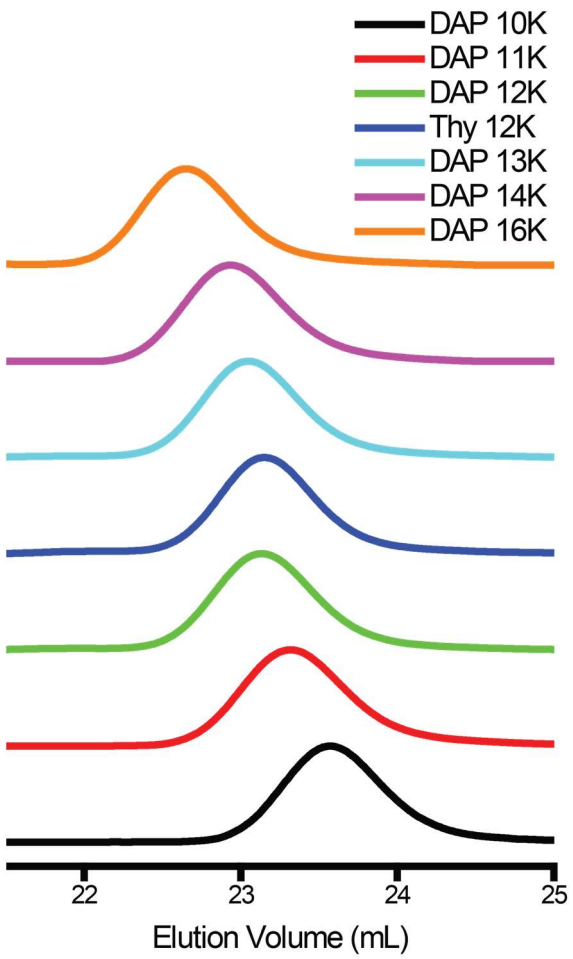

Figure S3-1. Normalized GPC traces for the polymers used in this work. See **Table S3-1**for more information.

To synthesize NCTs with polymer brushes of varying dispersity, 0.2 mM stock solutions of each DAP polymer molecular weight were prepared, and combined in an appropriate ratio to yield an average molecular weight of 12 kDa (equal amounts added for all samples, except for the 10K + 16K). These samples were then characterized by GPC to determine a dispersity ratio. The traces are presented in the main text (**Figure 4-3**) and the results summarized in **Table S3-2**. The disperse DAP samples were assembled with 12 kDa Thy polymer – a single Thy molecular weight was used to minimize error from combining two sets of varying molecular weight polymer.

Sample Name	Dispersity
12	1.052
11-12-13	1.184
11-13	1.207
10-12-14	1.28
10-14	1.292
10-16	1.44

Table S3-2. Dispersity of polymer mixtures used in Figure 4-3. Labels refer to the mixtures of polymers used.

To confirm the polymers were grafted to the nanoparticles in a similar ratio as the feed solution, a series of decomposition experiments were performed. A large batch of NCTs (20 mL) would be prepared, reserving a small fraction of the polymer solution used to functionalize the nanoparticles for determining the distribution of polymers in the feedstock. After the solution of NCTs was

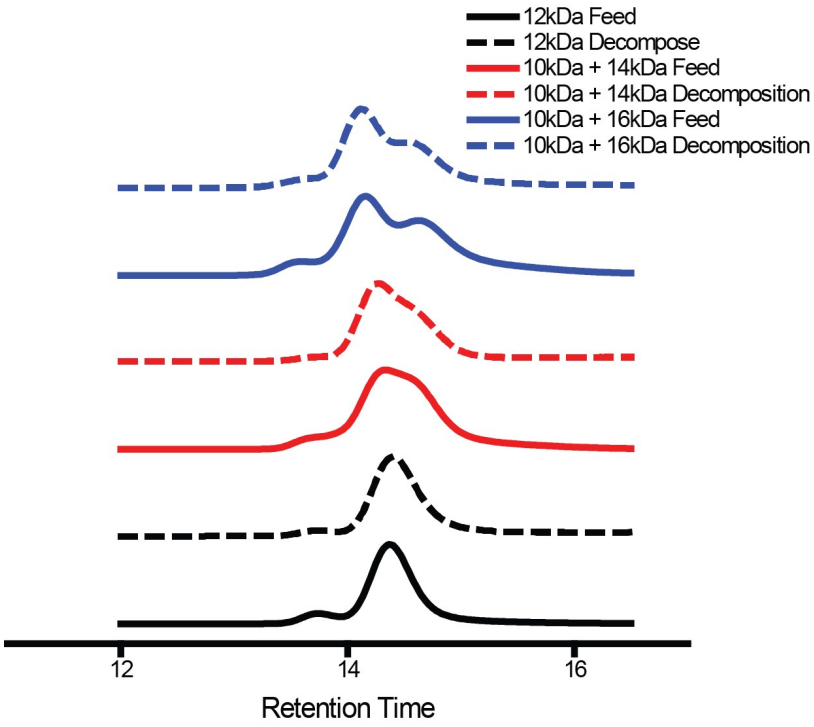

Figure S3-2. GPC traces of polymer mixtures before being grafted to gold nanoparticles (solid lines), and after the nanoparticles were decomposed (dashed lines).

prepared, they were concentrated, and redispersed in 1 mL of an iodine solution, 5 mg/mL, in dichloromethane. This solution was stirred overnight to ensure the complete decomposition of the nanoparticles. The solution was centrifuged, the supernatant recovered, and allowed to evaporate until only ~0.1 mL remained. Then, 1 mL of methanol was added to precipitate the polymer, which was recovered by centrifugation. Due to the small amount of polymer, a higher quality Agilent 1260 Infinity 2 GPC instrument with a ResiPore column and a UV detector set to 254 nm was used to measure the polymer distribution (**Figure S3-2**). The recovered polymers from the decomposed nanoparticles are very similar to the feed polymers, suggesting the feed dispersity accurately reflects the dispersity of polymers on the NCTs.

A3.2.7 Nanoparticle Characterization

AuNPs were cast onto TEM grids, and their diameters determined by image analysis using ImageJ (over 100 particles were used for each sample). Images of the nanoparticles are present in the main text in **Figure 4-5**, a summary of their size and relative standard deviation (RSD) are presented in **Table S3-3**.

Sample Name	Diameter (nm)	Relative Standard Deviation (RSD, %)
AuNP-19	19.00	11.5
AuNP-24	24.05	8.82
AuNP-28	28.48	9.16

Table S3-3. Diameter and relative standard deviation of the gold nanoparticles used in this work.

To prepare NCTs with disperse nanoparticle cores, the concentrations of AuNP-19, AuNP-24, and AuNP-28 solutions were determined by UV-Vis, and mixtures of the three solutions were prepared with 100%, 80%, 60%, 40%, 20% and 0% AuNP-24. The particle distributions of the original AuNP-19, AuNP-24, and AuNP-28 solutions were modeled as Gaussians, and then linearly combined to estimate the size and standard deviation of the particle solutions. The values are presented in **Table S3-4**, and the calculated distributions depicted in **Figure S3-3**.

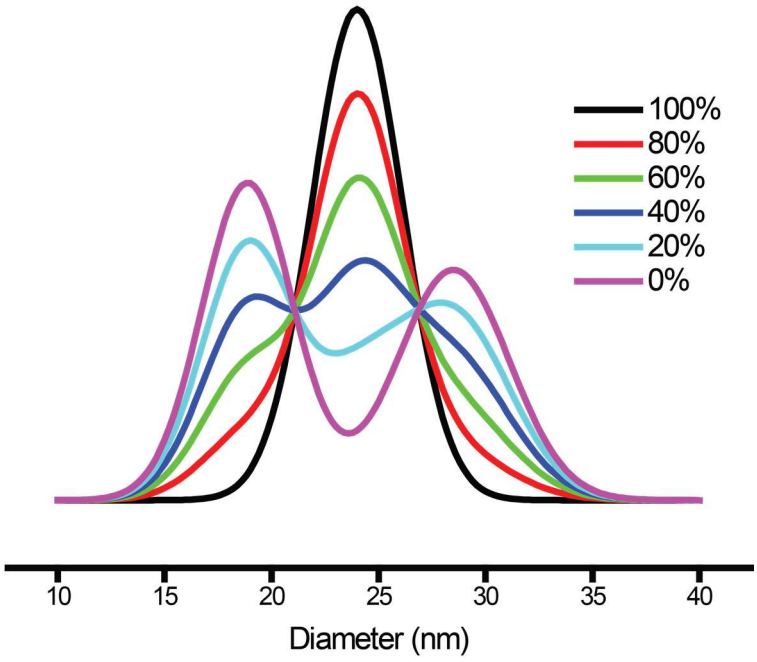

Figure S3-3. Calculated size distributions of nanoparticle cores used for particle dispersity experiments. The percentage refers to the fraction of 24 nm nanoparticles in the mixture, with the balance an equal mixture of 19 and 28 nm particles.

% AuNP-24	Diameter (nm)	Relative Standard Deviation (RSD, %)
100	24.05	8.82
80	23.87	13.41
60	23.74	16.50
40	23.61	19.05
20	23.51	21.06
0	23.40	22.81

Table S3-4. Calculated relative standard deviation of gold nanoparticle mixtures used for studying the effect of particle core dispersity on NCT assembly. The % AuNP-24 refers to the fraction of 24 nm nanoparticles in the feed mixture, with the balance being an equal contribution of 19 nm and 28 nm particles. The RSD and diameter are calculated from the initial nanoparticle data in **Table S3-3**.

Solutions of nanoparticles with different radii will show markedly different form factors in SAXS, as larger diameter nanoparticles will have their first oscillation appear at lower q values than smaller nanoparticles. When combinations of nanoparticles are made, as is done so in **Figure 4-5** in the main text, the addition of the form factors will dampen the intensity of the oscillations. To demonstrate this, SAXS patterns were modeled using SASview (http://www.sasview.org/) for nanoparticles with equal size and dispersity as the nanoparticles used in the experiments, and at equal concentrations (**Figure S3-4**). Combining these form factors creates a similar flattening of the form factor in the high q region as is shown in the experiments in **Figure 4-5**, further indicating that a broad distribution of nanoparticle diameters has been incorporated into the superlattices.

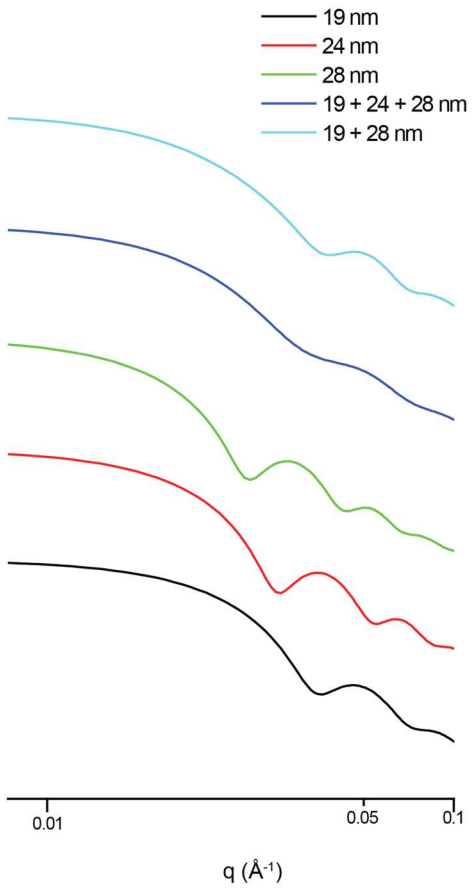

Figure S3-4. Calculated SAXS form factors for the three nanoparticle sizes used in these experiments and sums of mixtures of those nanoparticles in equal combinations. When nanoparticles of different diameter are combined, the oscillations in the form factor flatten out, as is seen in **Figure 4-5** in the main text.

A3.3 NCT Assembly Characterization

Melting temperatures were determined on a Cary-5000 UV-Vis Spectrophotometer with a thermal multicell accessory. Before the experiment, a clean quartz cuvette was treated with hexamethyldisilazane (HMDS) by solvent annealing in a 1:1 HMDS:n-hexane solution in a sealed chamber at room temperature for 20 hours. Then, in a typical experiment, equal volumes of DAP and Thy NCTs in toluene at the same optical density were mixed in the treated quartz cuvette and allowed to completely assemble. The cuvette was then placed in the thermal multicell accessory, and heated at a rate of 0.25°C/minute. The extinction was monitored at 520 nm to generate the melt profiles, and the melting temperature determined as the inflection point of the curve.

There exists a strong relationship between polymer molecular weight and the melting temperature of NCT assemblies, therefore making it a good metric for understanding which molecular weight of polymer dominates the NCT binding behavior (see **Figure S3-6**).

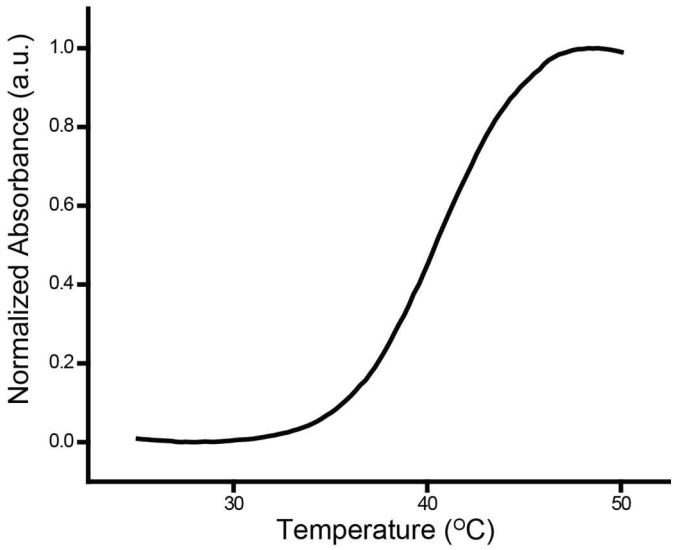

Figure S3-5. Representative melt curve for NCTs synthesized with 24 nm AuNPs and 12 kDa DAP and Thy polymers. The inflection point of the curve corresponds to the melting temperature of the NCT assembly.

Domain sizes of NCT superlattices were calculated from the SAXS data using the Scherrer equation.[327] First, the q_0 peak was identified and fit with a Voigt function,[328] integrated, and divided by its peak height to calculate its integral breadth. Then, the Scherrer equation was used to calculate the domain size:

$$D = \frac{2\pi K}{\Delta q}$$

Where D is the domain size, K is a constant taken to be 0.9, and Δq is the integral breadth of the q_0 peak. The Scherrer equation is known to only give an estimate for domain size with some error, but because the same analysis is used for samples it can provide a consistent method for comparison.

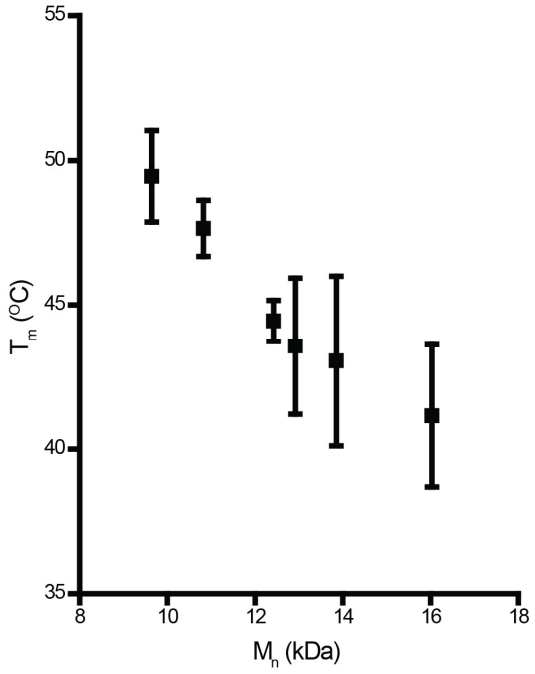

Figure S3-6. Polymer molecular weight has a strong influence on NCT melting temperature. Error bars are standard deviations, n = 3.

During the slow cooling method, NCT crystals rapidly form, but do not dramatically change in size. Using a faster cooling rate results in slightly lower quality crystals as determined by their domain sizes, but the change is not statistically significant below 8 °C/min. A key limiting factor is hypothesized to be the sedimentation rate, which would explain the practical maximum.

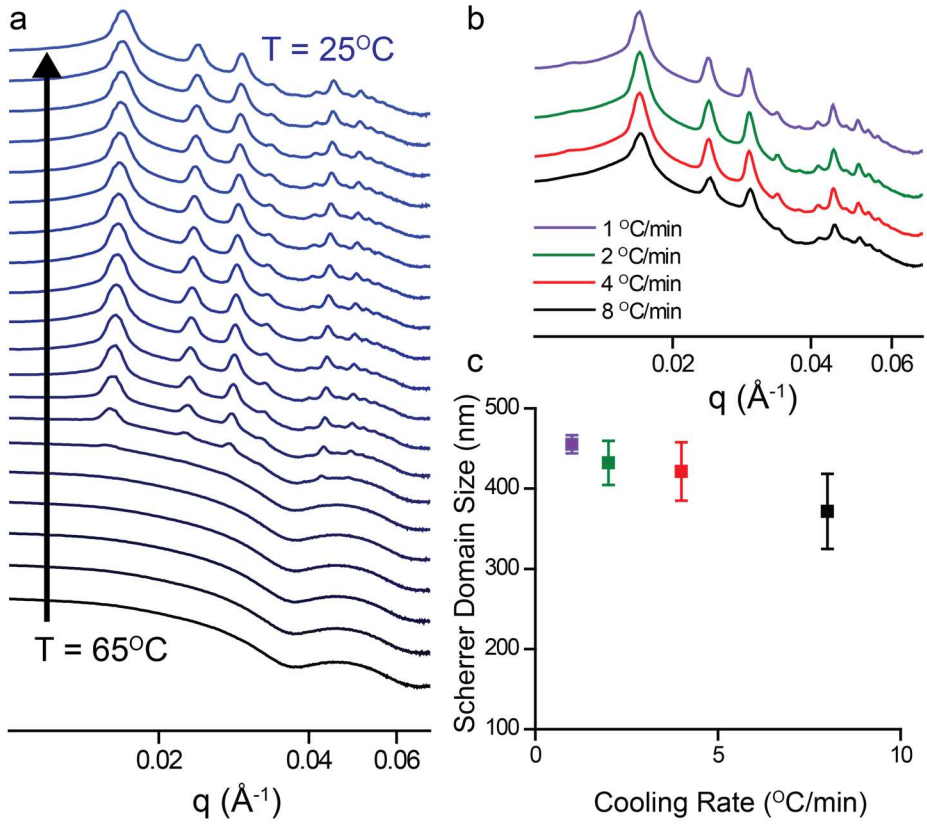

Figure S3-7. a. In-situ SAXS of NCTs cooling at 4 °C/min. After the transition, there is minimal change in crystal quality b. SAXS of NCT crystals after cooling at different rates c. The effect of cooling rate on domain size. Faster rates do lead to smaller domains, but insignificantly so below 8 °C/min. Error bars are standard deviations, n = 5.

Appendix 4. Supplementary Information for Reinforcing Supramolecular Bonding with Magnetic Dipole Interactions to Assemble Dynamic Nanoparticle Superlattices

A4.1 Materials and Methods

2,6-Diaminopyridine, thymine, acetyl chloride, 11-bromoundecan-1-ol, sodium azide, ethylenediaminetetraacetic acid sodium salt, 2-Bromoisobutyryl bromide, styrene, N,N,N',N",N'"-Pentamethyldiethylenetriamine (PMDETA), propargyl alcohol, and citric acid monohydrate were purchased from Acros. Trisodium citrate dihydrate, hexamethyldisilazane, Tris[2-(dimethylamino)ethyl]amine (Me_6TREN), and tin(II) 2-ethylhexanoate were purchased from Alfa Aesar. Docosane, phosphorous acid, cyclohexamine, iodine, ferric chloride hexahydrate, oleic acid, copper (I) bromide, hydrochloric acid, and copper (II) bromide were purchased from Sigma Aldrich. 1-octadecene and gold (III) chloride trihydrate were purchased from Beantown Chemical. Aminoethanethiol and sodium oleate were purchased from TCI America. Basic Alumina and general solvents were purchased from Fisher Scientific. All chemicals, including solvents, were used without further purification, except styrene, which was passed through a short column of basic alumina to remove inhibitor prior to polymerization. Note that some solvents were purchased as anhydrous grade, as noted in the experimental details.

Centrifugation was performed with an Eppendorf 5424 centrifuge. Gel permeation chromatography (GPC) characterizations were performed on an Agilent Technologies Infintiy 1260 GPC system with triple detection (refractive index, 90º light scattering, and viscometry), with Resipore columns, and with THF as the eluent at 1.0 mL/min. UV-vis spectra and measurements were obtained on a Cary-5000 spectrometer. Small angle x-ray scattering (SAXS) measurements were performed at the 12ID-B station at the Advanced Photon Source (APS) at Argonne National Laboratory. The samples were probed using 14 keV (0.8856 Å) X-rays, and the sample-to-detector distance was calibrated with a silver behenate standard. The beam was collimated using two sets of slits, and a pinhole was used. Scattered radiation was detected using a Pilatus 2 M detector. Transmission electron microscopy (TEM) was performed with a JEOL 2010 Advanced High Performance transmission electron microscope. Magnetic measurements were performed on a Quantum Design Inc. Magnetic Property Measurement System. Thermogravimetric analysis (TGA) was performed on a TA Instruments Discover TGA with high temperature platinum pans.

X-ray diffraction was performed on a Bruker D8 Discover with a General Area Detector Diffraction System (GADDS) Vantec-2000 2D detector and a cobalt anode (1.790 Å).

A4.2 Synthesis

We have previously reported the synthesis of the DAP and Thy initiators for atom transfer radical polymerization (ATRP), the procedures are briefly summarized below.[222]

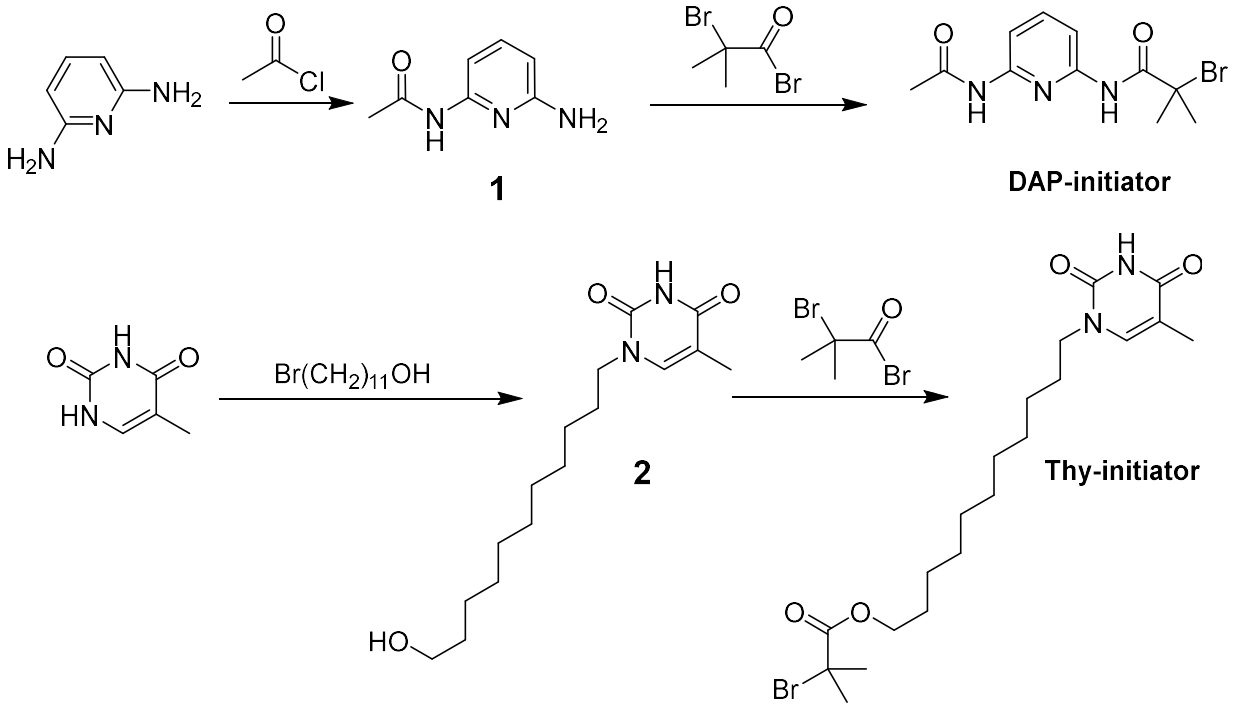

Scheme S4-1. Synthetic scheme for DAP and Thy initiators

A4.2.1 DAP Initiator

5.5 g 2,6-diaminopyridine (50 mmol) was dissolved in 40 mL dry THF in a 3-necked round bottom flask. At 0 ºC, the solution of 1.96 g (25 mmol) acetyl chloride in 15 mL dry THF was added dropwise under a nitrogen atmosphere. The reaction mixture was allowed to warm to room temperature and stirred for 12 hours. The insoluble content was filtered off, and the solvent was removed under reduced pressure. The resulting solid was recrystallized in a mixture of ethanol and toluene, to afford **1** as a white solid. 1.9 g **1** (12.6 mmol) was dissolved in 80 mL dichloromethane, and then 3.5 mL triethylamine (25 mmol) was added to this solution. The mixture was cooled to 0 ºC, and a solution of 3.22g 2-bromoisobutyryl bromide (17.6 mmol) in dichloromethane (~10 mL) was added dropwise under a nitrogen atmosphere. The reaction mixture was allowed to warm to room temperature and stirred for 12 hours. The insoluble content was filtered off, and the filtrate

was washed with a sodium carbonate solution (x1) and brine (x3). The organic phase was dried over sodium sulfate, the solvent was removed under reduced pressure, and the product was then purified by flash chromatography (CH_2Cl_2/EtOAc 4:1). The product was further purified by recrystallization in CH_2Cl_2/EtOAc/hexanes to afford N-(6-acetamidopyridin-2-yl)-2-bromo-2-methylpropanamide (DAP-Initiator). All characterization matches previous literature reports.

A4.2.2 Thy Initiator

5.0 g thymine (40 mmol), 1.0 g 11-bromo-1-undecanol (4 mmol), 1.1 g potassium carbonate (8 mmol) and 200 mL DMSO were added to a 500 mL round bottom flask. The mixture was stirred and bubbled with nitrogen for 2 minutes, and then sealed with a septum and stirred for 48 hours. The resulting mixture was poured into water and chloroform for extraction, and the organic phase was collected and washed 3 more times with brine, followed by drying over sodium sulfate and removal of solvent. The resulting white solid was recrystallized in EtOAc/hexanes to afford compound 2. With the help of very gentle heat, 592 mg **2** (2 mmol) was dissolved in 150 mL dichloromethane, and 0.39 mL triethylamine (2.8 mmol) was added to the solution. The mixture was cooled to 0 ºC, and a solution of 552 mg 2-bromoisobutyryl bromide (2.4 mmol) in dichloromethane (~ 10 mL) was added dropwise under a nitrogen atmosphere. The reaction mixture was allowed to warm to room temperature and stirred for 14 hours, and then washed with sodium carbonate (x2) and brine (x2). The organic phase was dried with sodium sulfate, and the solvent was removed under reduced pressure. The resulting mixture was purified by flash chromatography (CH_2Cl_2/EtOAc 8:3), to afford the 11-(5-methyl- 2,4-dioxo-3,4-dihydropyrimidin -1(2H)-yl)undecyl 2-bromo-2-methylpropanoate (Thy-Initiator) as an off-white solid. All characterization matches prior literature reports.

A4.2.3 Propargyl Phosphonate Anchor

The phosphonate group to anchor DAP and Thy polymers onto iron oxide nanoparticles was synthesized according to a literature procedure.[329] Briefly, phosphorous acid (0.41 g, 5 mmol, 1 eq), propargyl alcohol (10 mL, 142 mmol, 34.4 eq), and trimethylamine (2.5 mL, 18 mmol, 3.6 eq) were combined in a 100 mL round bottom flask. Iodine (1.9 g, 7.5 mmol, 1.5 eq) was slowly added with a spatula over several minutes. After reacting for 30 minutes, the mixture was precipitated in 200 ml acetone with 5 mL cyclohexamine and allowed to rest for 2 hours without stirring. The fine powder was recovered through filtration, dissolved in 30 mL hot ethanol, with

500 μL cyclohexamine and recrystallized overnight to yield the propargyl phosphate cyclohexamine salt as a white powder. Characterization was consistent with prior literature reports.

A4.2.4 Gold Nanoparticle Synthesis

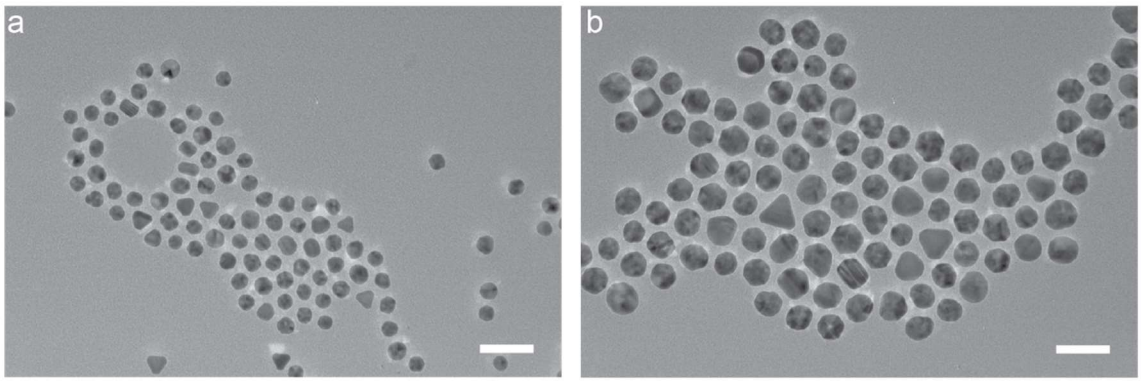

Figure S4-1. Representative TEM images of gold nanoparticles (AuNPs) used in this work. (a) AuNps with an average diameter of 15.3 nm (b) AuNPs with an average diameter of 23.7 nm. All scale bars are 50 nm. See **Table S4-1** for particles' relative standard deviations.

Gold nanoparticles (AuNPs) were synthesized according to a modified literature procedure.[26,29,287] All glassware was cleaned with aqua regia. To synthesize 15 nm AuNPs, an 800 mL buffer of trisodium citrate (2.06 mM) and citric acid monohydrate (0.688 mM) in Milli-Q purified water (resistivity of 18.2 MΩ•cm) was brought to a boil and 6.4 mg ethylenediaminetetraacetic acid sodium salt (0.02 mmol) was added. A separate solution of 104 mg $HAuCl_4{:}3H_2O$ in 6 mL Milli-Q water was prepared, and 3 mL of that solution rapidly injected into the boiling solution while being stirred at 800 RPM. The solution underwent a series of color changes and finally became a deep red color. After reacting for 30 minutes, the solution temperature was lowered to 90°C, and given 30 minutes to equilibrate. The other 3 mL of the gold precursor solution was injected, reacted for 30 minutes, and cooled to room temperature.

To synthesize 24 nm AuNPs, identical conditions were used to prepare the buffer as described above. A solution of 314.4 mg $HAuCl_4{:}3H_2O$ in 18 mL Milli-Q water was prepared, and 3 mL injected into the boiling citrate buffer. After reacting for 30 minutes, the solution temperature was cooled to 90°C, and given 30 minutes to equilibrate. A second injection of 3 mL of the gold precursor was performed, and allowed to equilibrate for 30 minutes. Then a third injection was performed, and allowed 30 minutes to equilibrate. After the third addition of precursor, 400 mL of the reaction mixture was removed, and an additional 400 mL citrate buffer added to the solution,

and given 30 minutes to return to 90°C. Three more injection and equilibration steps were performed, and the final solution allowed to cool back to room temperature.

Nanoparticles were characterized by TEM and analyzed using ImageJ (**Figure S4-1**, **Figure S4-2**. **Table S4-1**).

A4.2.5 Iron Oxide Nanoparticles

Iron oxide nanoparticles were synthesized through the thermal decomposition of an iron oleate precursor.[54]

First, the iron oleate precursor was prepared by combining ferric chloride hexahydrate (10.8g, 40 mmol, 1 eq) and sodium oleate (36.5 g, 120 mmol, 3 eq) in a mixture of water (60 mL), ethanol (80 mL), and hexanes (140 mL). The reaction was heated to reflux for 4 hours, and the organic layer extracted 3 times with water. The hexanes were removed on a rotary evaporator, and dried under vacuum while gradually heating to 120°C to form a thick orange oil. Care must be taken to avoid excessive foaming during drying.

To synthesize nanoparticles, iron oleate precursor (6.4 g), oleic acid, and solvent were combined in a 250 mL three-necked flask equipped with a reflux condenser and temperature probe. The flask was heated to 120°C, evacuated and refilled with nitrogen three times, and then heated to reflux at a controlled rate of 3°C/min. After refluxing for one hour, the reaction mixture was transferred to a storage container, and stored as a solid in the refrigerator. The size of the nanoparticles could be controlled by varying the solvent and amount of oleic acid. 9 nm particles were synthesized in 100 mL 1-octadecene and 1.5 g oleic acid, 14 nm particles were synthesized in 100 mL 1-octadecene and 2 g oleic acid, 16 nm particles were synthesized in 25 mL docosane and 2 g oleic acid, and 23 nm particles were synthesized in 25 mL docosane and 2.5 g oleic acid.

The nanoparticles were characterized by TEM, and analyzed in ImageJ.

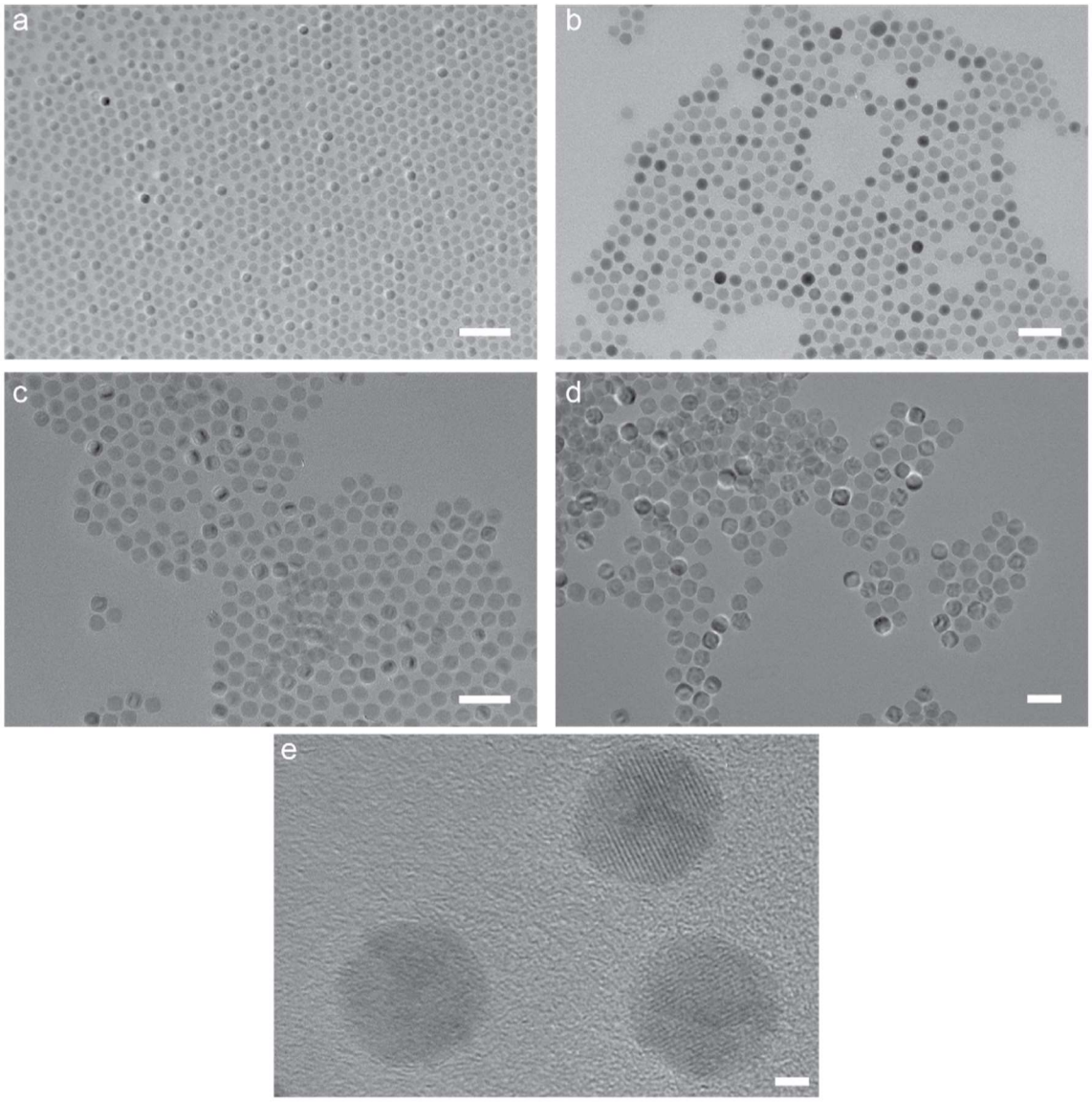

Figure S4-2. Representative TEM images of iron oxide nanoparticles (IONPs) used in this work. (a) IONPs with an average diameter of 9.2 nm (b) IONPs with an average diameter of 13.7 nm (c) IONPs with an average diameter of 15.9 nm (d) IONPs with an average diameter of 22.7 nm. All scale bars are 50 nm. e) High resolution TEM image of 15.9 nm IONPs, showing they are single crystalline. Scale bar is 5 nm. See **Table S4-1** for the particles' relative standard deviations.

Sample Name	Diameter (nm)	Relative Standard Deviation (RSD, %)
IONP-9	9.2	8.4
IONP-14	13.7	9.5
AuNP-15	15.3	9.4
IONP-16	15.9	6.1
IONP-23	22.7	9.8
AuNP-24	23.7	11.4

Table S4-1. Nanoparticle sizes and relative standard deviations (RSD) used in these experiments. Diameters and RSDs are calculated from at least 100 particles imaged by TEM.

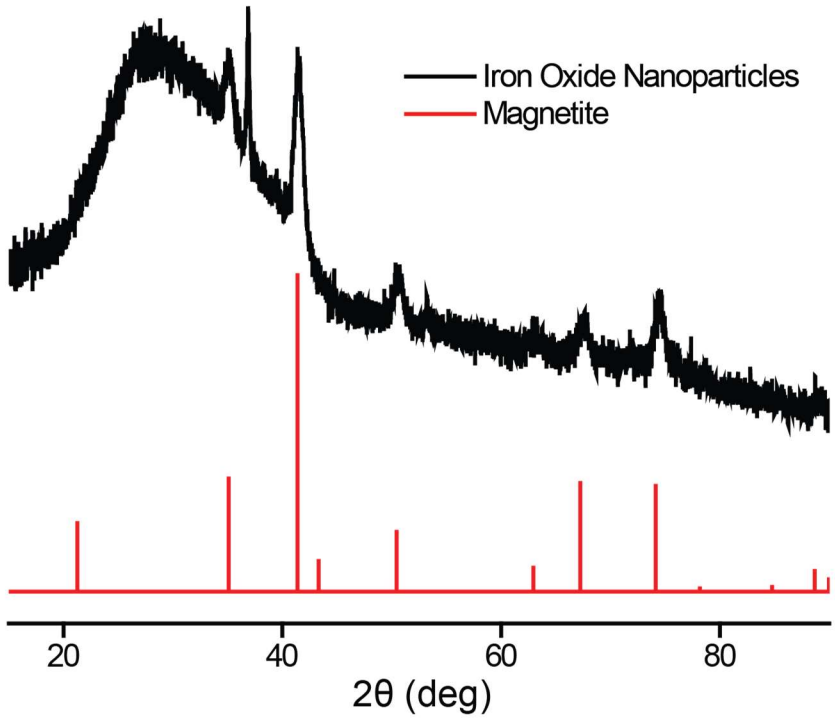

Figure S4-3. X-ray diffraction of 16 nm iron oxide nanoparticles (black trace) and the peak positions corresponding to magnetite (red trace).

A4.2.6 DAP Polymers

In a typical polymerization process, DAP-initiator (1.0 eq), Me6TREN (0.83 eq), styrene (200-300 eq depending on target molecular weight), copper (II) bromide (0.1 eq), and anisole (0.8:1 v/v to styrene) were added to an oven-dried and nitrogen filled Schlenk flask. The reaction flask was then sealed with a rubber septum and the mixture was taken through 3 freeze-pump-thaw cycles

and refilled with nitrogen. Simultaneously, tin(II) 2-ethylhexanoate (0.15 eq) and anisole (0.2:1 v/v to styrene) were combined in a vial and bubbled with N_2. After the reaction flask finished returning to room temperature, the tin(II) 2-ethylhexanoate mixture was injected and the flask immersed in an oil bath at 105ºC. The mixture was stirred at 105ºC under a nitrogen atmosphere, and quenched at different time points to give polystyrene of different molecular weights. The typical reaction time was 1-4 hours. To quench the reaction, the reaction mixture was poured into cold methanol, and the precipitated polymer was collected, redissolved in dichloromethane, and precipitated in methanol again to afford the polymer with a chain-end bromine.

A4.2.7 Thy Polymers

In a typical polymerization process, Thy-initiator (1 eq), PMDETA (1 eq), styrene (200 eq), and anhydrous anisole (30 vol% in styrene) were added to an oven-dried and nitrogen filled Schlenk flask. The reaction flask was then sealed with a rubber septum and the mixture was taken through 3 freeze-pump-thaw cycles and refilled with nitrogen. Once the mixture returned to room temperature, the septum was removed, CuBr (1.0 eq) was quickly added against a positive nitrogen flow, and the flask was immediately resealed. The mixture was stirred at 110 ºC under a nitrogen atmosphere, and quenched at different time points to give polystyrene of different molecular weights. Typical reaction time was 1-3 hours. To quench the reaction, the reaction mixture was poured into cold methanol, and the precipitated polymer was collected, redissolved in dichloromethane, and precipitated in methanol again to afford the polymer with a chain-end bromine.

To cap the polymer with a thiol for functionalizing AuNPs, the polymer was subsequently dissolved in DMF (~ 10 mg/mL) with small amount of triethylamine (40 eq), and the solution was bubbled with nitrogen for 5 minutes, followed by the addition of 2-aminoethanethiol (15 eq). The reaction flask was capped, and the solution was stirred for 60 hours, then precipitated in methanol (redissolve-precipitate x4). The resulting white powder was dried under vacuum to give the sulfur terminated PS polymer.

Sample Name	M_p (kDa)	M_n (kDa)	Dispersity (Đ)
8 kDa DAP IO-NCTs	7.92	7.09	1.03
8 kDa Thy IO-NCTs	7.77	7.50	1.05
9 kDa DAP Au-NCTs	9.54	9.12	1.03
9 kDa Thy Au-NCTs	9.12	8.78	1.03
13 kDa DAP IO-NCTs	13.84	13.09	1.03
13 kDa Thy IO-NCTs	12.58	12.17	1.02
14 kDa DAP Au-NCTs	14.41	13.82	1.03
14 kDa Thy Au-NCTs	14.06	13.70	1.06

Table S4-2. Summary of GPC results including the peak molecular weight (M_p), the number average molecular weight (M_n), and the dispersity of the polymers.

To cap the polymer with a phosphonate to functionalize IONPs, the bromine terminated polymer would be stirred with 4 equivalents sodium azide in DMF overnight. The azide terminated polymer would be recovered by precipitating in methanol, and purified by repeatedly dissolving the polymer in dichloromethane and precipitating in methanol (3x) before drying under vacuum.

The alkyl functionalized phosphonate was added to the polymer through an azide-alkyne cycloaddition. The polymer (1 eq) was dissolved in DMF with the propargyl phosphate (3 eq) and PMDETA (1 eq). The solution underwent three freeze-pump-thaw cycles, and upon the third freeze the flask was opened under a strong nitrogen flow, and copper (I) bromide (1 eq) was added. The flask was evacuated and refilled with nitrogen twice, evacuated, thawed, and finally refilled with nitrogen. It was then reacted at 30°C for 48 hours. The polymer was then precipitated in methanol with 1% HCl, filtered, and redissolved in DCM and precipitated in methanol two more times before drying under vacuum.

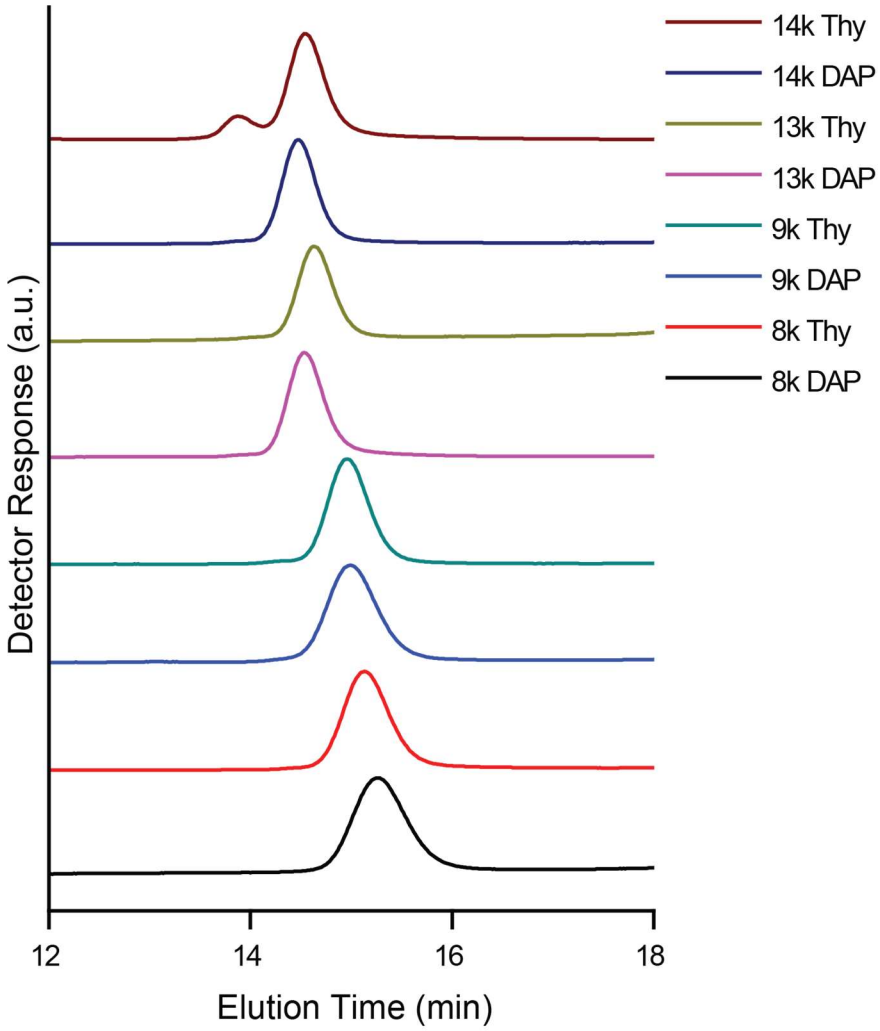

Figure S4-4. GPC traces of the refractive index detector for the polymers used in this work. Values for the polymers' molecular weights and dispersities are reported in **Table S4-2**. Note, the additional small peak in the 14 kDa Thy trace is due to dithiol formation.

GPC results are presented in **Figure S4-4** and **Table S4-2**. Each DAP polymer was matched with a corresponding Thy polymer possessing a molecular weight within 10%, as the molecular weights cannot match exactly due to batch to batch variation. The nominal molecular weight was derived from M_p, the peak of the GPC trace because some of the longer and shorter chains arise from the elimination of the terminal bromine or chain-chain termination, and each scenario will prevent the addition of the anchor component and therefore will not be able to functionalize nanoparticles.

A4.2.7 Au-NCTs

The synthesis of NCTs with gold nanoparticle cores has been previously described.[222] In a representative synthesis, a 6 mL solution of thiol terminated 14 kDa polymer (1 mg/mL) in acetone was prepared. Citrate capped 15 nm AuNPs (6 mL, as synthesized) were poured into the polymer solution and stirred for thirty minutes. The functionalized nanoparticles were recovered by a brief (2 minute) centrifugation, and redispersed in 6 mL DMF. The NCTs were purified and concentrated by three cycles of centrifugation, redispersing in 1 mL DMF, 1 mL toluene, and 1 mL toluene after each respective centrifugation.

A4.2.8 IO-NCTs

In a representative synthesis, 200 mg 16 nm IONP reaction mixture in docosane (stored in a refrigerator, a solid) was dissolved in a solution of 2 mL THF and 2 mL acetone. The nanoparticles were centrifuged and redispersed in THF 3 times to remove residual docosane and reaction byproducts, and concentrated to 2 mL THF. The nanoparticle solution was then split into 2 fractions, 1 mL nanoparticles added to 50 mg DAP or Thy phosphonate terminated polymer each. The solutions were briefly sonicated, and then shaken at room temperature overnight. The DAP and Thy functionalized NCTs were diluted by 4 mL THF each (8 mL total), and then underwent three cycles of centrifugation and redispersion in THF, toluene, and toluene, and were concentrated to 1 mL for both the DAP and Thy NCTs.

A4.2.9 Grafting Density of NCTs

The grafting densities of NCTs were determined through thermogravimetric analysis (TGA). An NCT solution in dichloromethane was drop cast on a platinum TGA pan, and evaporated before loading into the instrument. The sample was heated to 150 °C, held for 5 minutes, then ramped at 20 °C per minute up to 600 °C. All samples showed a characteristic step function at approximately 400 ºC, interpreted to be mass loss from the polymer, $m_{Polymer}$. The remaining mass was assumed to be from the inorganic nanoparticle, m_{NP}. Grafting density in chains/nm^2 was then calculated by:

$$\sigma = \frac{m_{Polymer} * N_A * \rho_{NP}}{m_{NP} * MW_{Polymer} * D_{NP} * (6 \cdot 10^{21})}$$

where N_A is Avogadro's number, ρ_{AP} is the density of gold or iron oxide, $MW_{Polymer}$ is the polymer's number-averaged molecular weight determined by GPC, D_{NP} is the nanoparticle diameter determined by TEM, and $6 \cdot 10^{21}$ contains geometric constants and an appropriate scaling factor to

provide data in units of chains/nm^2. A representative TGA curve is shown in **Figure S4-5**, and the grafting densities presented in **Table S4-3**. The grafting densities do not appear to strongly depend on any of the design parameters used in this work, with similar values obtained for different polymer molecular weights, functionalities, and core compositions.

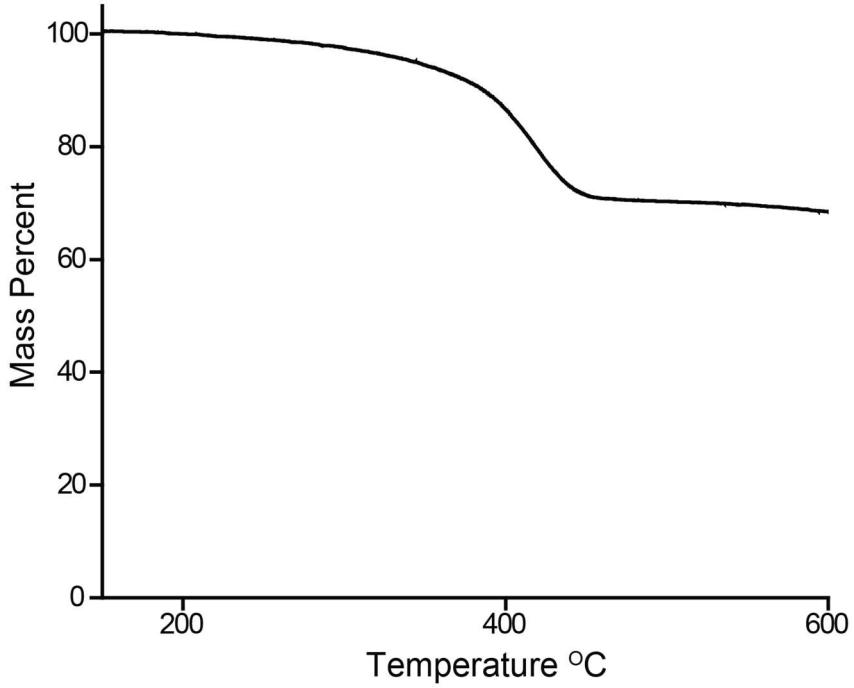

Figure S4-5. Representative TGA data for a 16 nm iron oxide NCT with an 8 kDa DAP polymer shell.

Sample Name	Grafting Density (chains/nm^2)
8 kDa DAP IO-NCTs	0.45
8 kDa Thy IO-NCTs	0.57
9 kDa DAP Au-NCTs	0.52
9 kDa Thy Au-NCTs	0.61
13 kDa DAP IO-NCTs	0.35
13 kDa Thy IO-NCTs	0.38
14 kDa DAP Au-NCTs	0.50
14 kDa Thy Au-NCTs	0.46

Table S4-3. Summary of TGA results for the NCTs presented in the main text.

A4.3 Assembly Experiments

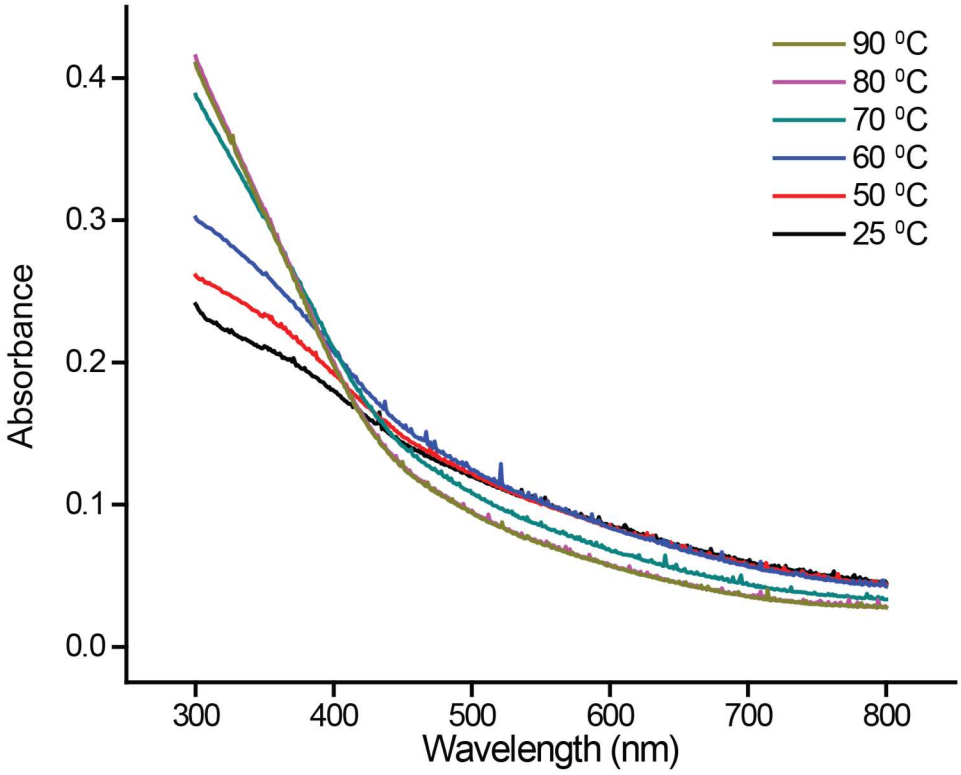

Figure S4-6. UV-Vis measurements of 16 nm, 8 kDa IO-NCTs at varying temperatures.

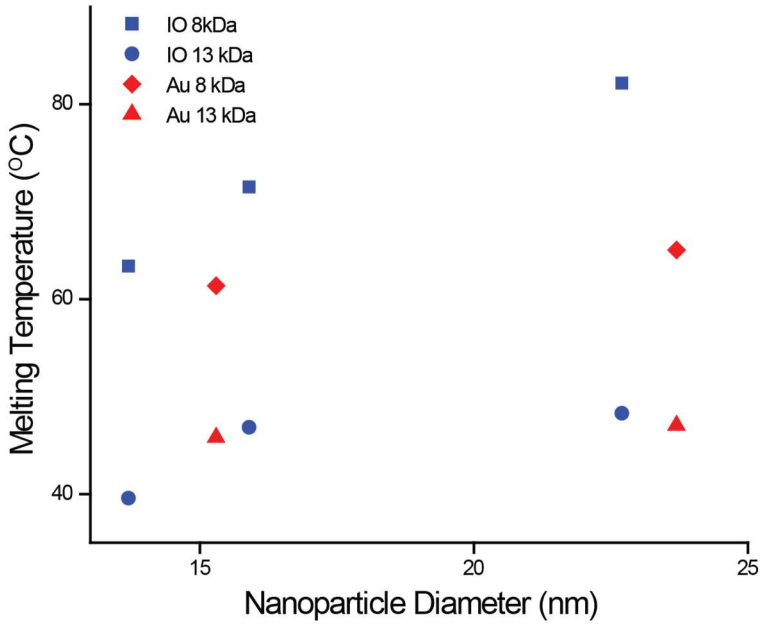

Figure S4-7. Plot of melting temperatures used in this work. IO-NCTs with short polymer exhibit a stronger enhancement of melting temperature with respect to particle size.

To perform thermal melt experiments, purified NCTs were combined in a quartz cuvette that was pretreated for 12 hours with hexamethyldisilazane vapors. The NCTs were diluted so that their absorbance would be between 0.5 and 1 in their melted state. The sample would be slowly ramped at 0.25 ºC/min using the thermal cell of the instrument, and the absorbance of the sample measured. Au-NCTs were monitored at 520 nm, the plasmon resonance of the gold nanoparticles. As is shown in **Figure S4-7**, IO-NCTs showed a substantial change in absorbance at low wavelengths, and so were monitored at 325 nm. The T_m of the NCTs was taken to be the inflection point of the melt curves.

To assemble NCTs into ordered body centered cubic (bcc) lattices, complementary solutions of NCTs were combined in a polypropylene centrifuge tube. The solution was then heated above the T_m of the NCTs in a heat block, and then allowed to cool to room temperature while sitting in the heat block with the power turned off. The resulting black aggregates were loaded into kapton capillary tubing, sealed with 5-minute epoxy, and analyzed by SAXS. The structure factor, S(q), was calculated by dividing the intensity measurement, I(q), by the form factor of the nanoparticles, which was determined by SAXS measurements of the unassembled DAP functionalized NCTs. For the face centered cubic (fcc) lattices in **Figure 5-4** of the main text, the 16 nm IO-NCTs with 8 kDa Thy polymer would spontaneously aggregate after the solvent was exchanged to toluene. Ordered lattices were formed by heating the sample to 60 ºC and cooling to room temperature. Interparticle distances were calculated from the q_0 peak[162]:

$$d_{bcc} = \frac{\pi\sqrt{6}}{q_0} \qquad d_{CsCl} = \frac{\pi\sqrt{3}}{q_0} \qquad d_{fcc} = \frac{\pi\sqrt{6}}{q_0}$$

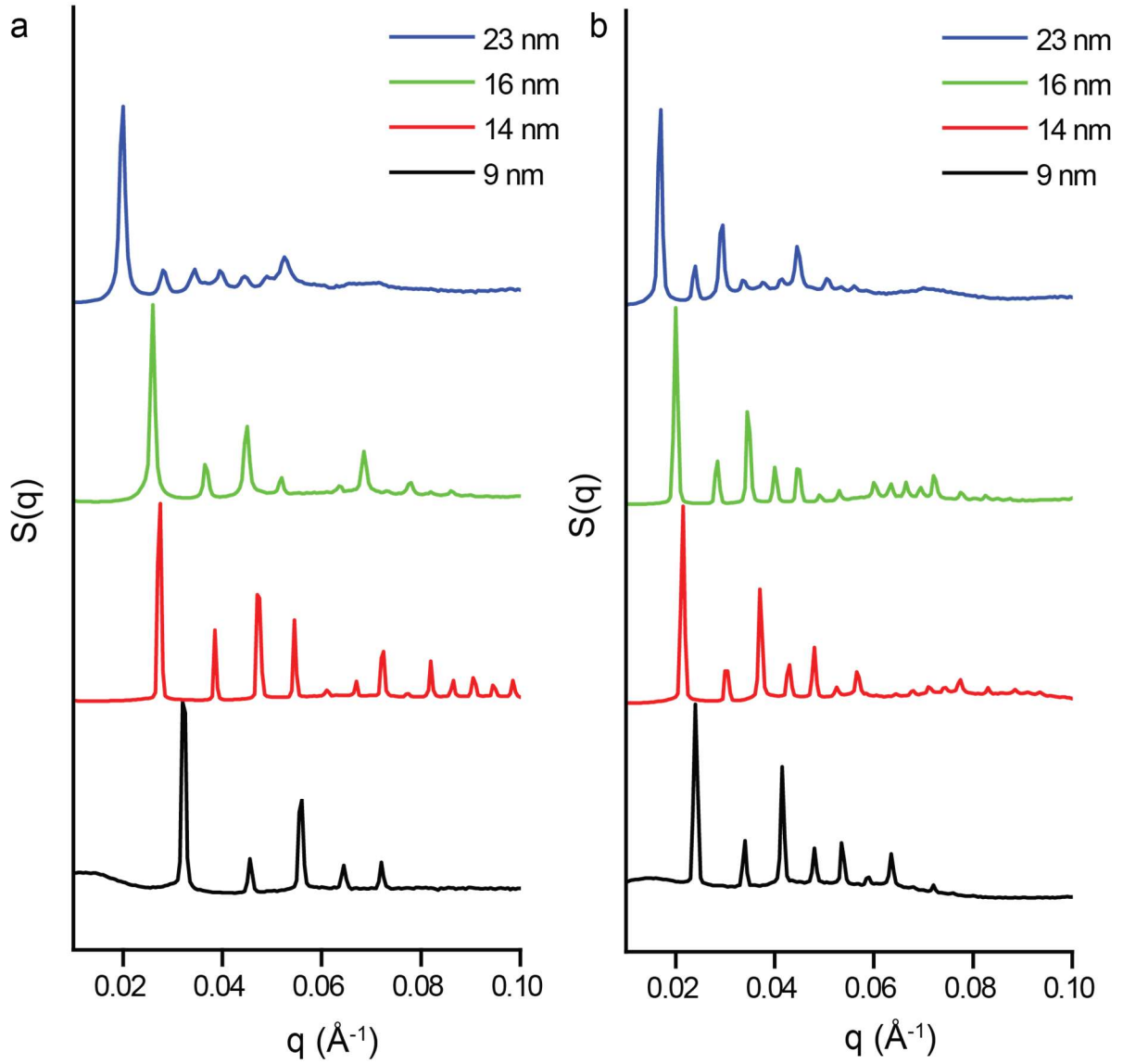

Figure S4-8. SAXS of bcc superlattices synthesized from IO-NCTs with 9, 14, 16, and 23 nm IONP cores and with (a) 8 kDa polymer brushes (b) 13 kDa polymer brushes.

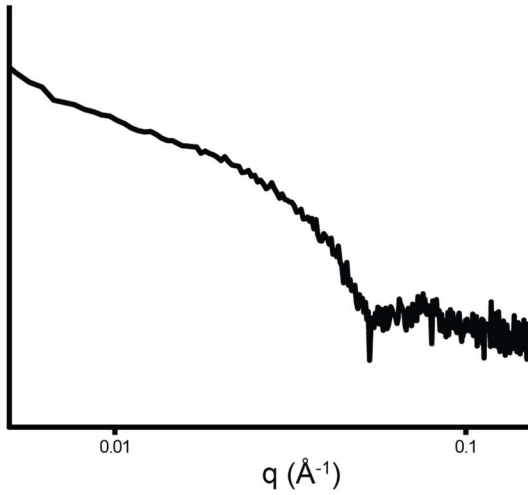

Figure S4-9. SAXS measurement of 16 nm 13 kDa Thy particles. No noticeable assembly is present.

A4.4 Magnetic Experiments

To measure the magnetic properties of the NCT assemblies, Kapton capillaries of crystallized NCTs were loaded into a straw sample holder in the Magnetic Property Measurement System. Field response at 300 K was measured by changing the applied magnetic field from -1.5 T to 1.5 T, and measuring the magnetization of the sample in DC mode. Then, to perform the zero field cooled experiment the field was set to 0 T, and the sample cooled to 10 K at 50 K per minute. A

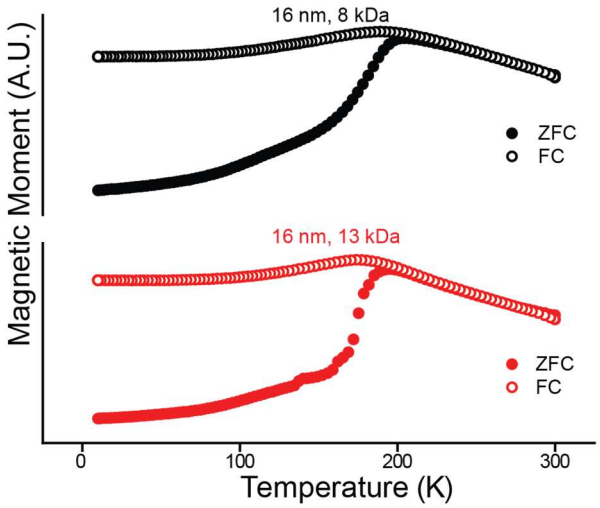

Figure S4-10. Field cooled / zero field cooled data used to calculate the curve in **Figure 5-3**.

measurement field of 200 Oe was applied, and the temperature raised at 5 K per minute to 300 K and the magnetic response of the sample measured. To perform the field cooled experiment, a measurement field of 200 Oe was applied, and the sample's magnetic response monitored while cooling to 10 K at 5 K per minute. Finally, the field response was measured by performing another loop at 10 K from -1.5 T to 1.5T.

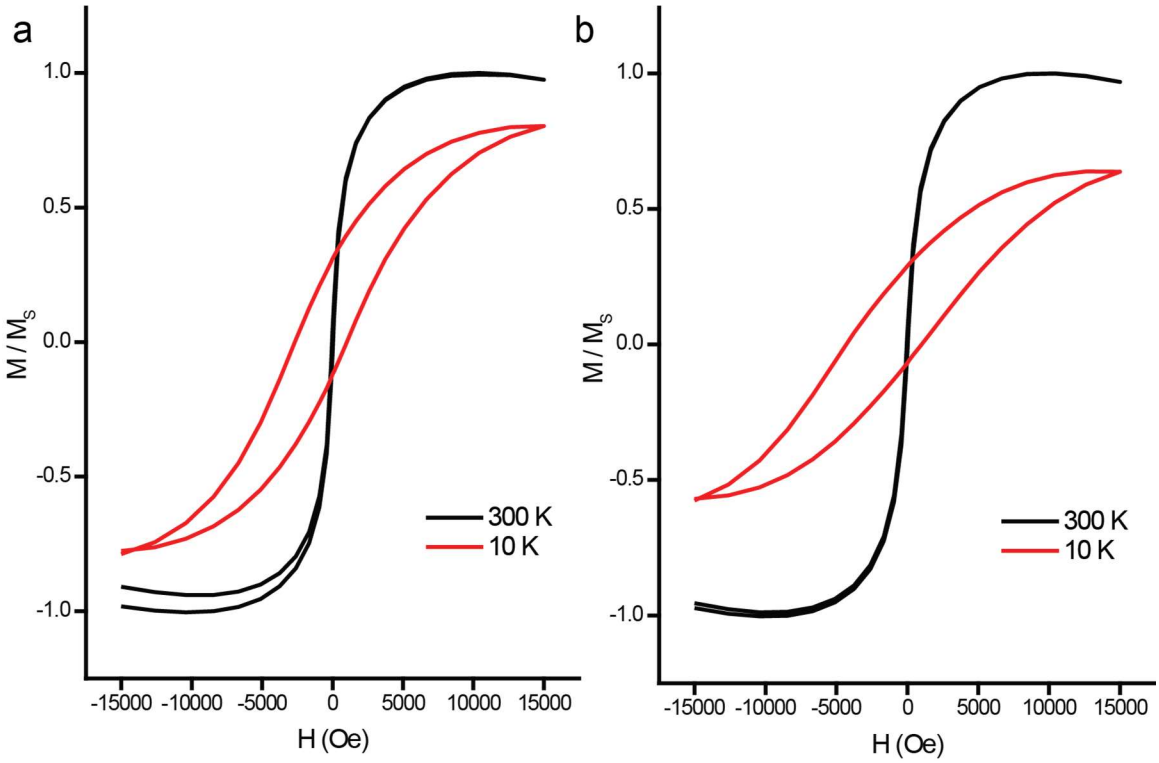

Figure S4-11. Field dependence of magnetization of crystallized (a) 16 nm IO NCTs with 8 kDa polymer and (b) 16 nm IO NCTs with 13 kDa polymer at 300 K and 10 K. Magnetization is normalized for each sample by the saturation magnetization at room temperature.

Appendix 5. Supplementary Information for Nanoparticle Composite Materials with Programmed Nanoscale, Microscale, and Macroscale Structure

A5.1 Materials and Characterization Methods

A5.1.1 Materials

2,6-Diaminopyridine, thymine, acetyl chloride, 11-bromoundecan-1-ol, sodium azide, ethylenediaminetetraacetic acid sodium salt, 2-Bromoisobutyryl bromide, styrene, N,N,N',N",N'"-Pentamethyldiethylenetriamine (PMDETA), propargyl alcohol, and citric acid monohydrate were purchased from Acros. Trisodium citrate dihydrate, hexamethyldisilazane, Tris[2-(dimethylamino)ethyl]amine (Me_6TREN), and tin(II) 2-ethylhexanoate were purchased from Alfa Aesar. Docosane, phosphorous acid, cyclohexamine, ferric chloride hexahydrate, oleic acid, copper (I) bromide, hydrochloric acid, and copper (II) bromide were purchased from Sigma Aldrich. N-hexane, N-octane, N-decane, and gold (III) chloride trihydrate were purchased from Beantown Chemical. Aminoethanethiol and sodium oleate were purchased from TCI America. Basic Alumina and general solvents were purchased from Fisher Scientific. A polyoxymethylene bar was purchased from McMaster Carr. All chemicals, including solvents, were used without further purification, except styrene, which was passed through a short column of basic alumina to remove inhibitor prior to polymerization.

A5.1.2 Instrumentation

Centrifugation was performed with an Eppendorf 5424 centrifuge. Gel permeation chromatography (GPC) characterizations were performed on an Agilent Technologies Infintiy 1260 GPC system with triple detection (refractive index, 90º light scattering, and viscometry), with Resipore columns, and with tetrahydrofuran (THF) as the eluent at 1.0 mL/min. UV-vis spectra and measurements were obtained on a Cary-5000 spectrometer. Small angle x-ray scattering (SAXS) measurements were performed at the Massachusetts Institute of Technology (MIT) Center for Materials Science and Engineering (CMSE) X-ray Diffraction Shared Experimental Facility on a SAXSLAB system. The Rigaku 002 microfocus X-ray source produced Cu Kα1 x-rays of wavelength 1.5409 Å; Osmic staggered parabolic multilayer optics focused the beam crossover at the second pinhole. Two sets of JJ X-ray jaw collimation slits set at 0.45mm and 0.2mm, respectively, were used to define the beam. The system was calibrated using silver behenate as a

standard. Solvated SAXS samples were loaded into a short section of 1.5 mm diameter Polyimide Tubing (Cole-Parmer) and sealed at both ends with epoxy. Before loading samples into the tubing, one end was sealed with epoxy and the tubing baked at 110 °C overnight. Dried SAXS samples were prepared by casting onto polyimide film, or for macroscopic samples wrapping in polyimide tape. The lowest q peak identified in SAXS (q_0) were fit using a Pseudo-Voight function, and the interparticle distance for bcc crystals was determined as:

$$d_{bcc} = \frac{\pi\sqrt{6}}{q_0} \tag{S5-1}$$

And for CsCl crystals as:

$$d_{CsCl} = \frac{\pi\sqrt{3}}{q_0} \tag{S5-2}$$

Transmission electron microscopy (TEM) was performed with a JEOL 2010 Advanced High Performance transmission electron microscope, with samples cast onto formvar coated TEM grids (Ted Pella). Top-down Scanning electron microscopy (SEM) was performed on either a Zeiss Sigma 300 VP Field Emission SEM (5kV electron beam with in-lens detector) or a Helios Nanolab 600 dual beam (86 pA and 5 kV electron beam with in-lens detector). To be imaged, samples were cast and dried onto copper tape or silicon wafers (150 mm P-Type Prime (100) wafers with polished surfaces purchased from Wafernet) which had 2 nm of chromium (Cr) and 8 nm of gold (Au) deposited (*via* AJA eBeam evaporator) to aid conduction. Cross-sectional micrographs were collected on the Helios Nanolab 600 dual beam focused ion beam milling system with a 52° relative difference between the ion and electron beam. After a layer of titanium was deposited over the area of interest, the sample was milled with a 93 pA (30 kV) ion beam. Each cross-section was imaged with an 86 pA (5 kV) electron beam using the in-lens detector on the SEM without using the software's tilt correction. SEM images were stitched together using Photoshop and had the y-axis scale adjusted for tilt angle such that it is representative of the real space length using the following equation:

$$y_{processed} = \frac{y_{raw}}{\cos(90°-52°)} = \frac{y_{raw}}{\cos(38°)} = 1.269 \times y_{raw} \tag{S5-3}$$

A5.2 Synthesis

The synthesis of the diaminopyridine (DAP) initiator, thymine (Thy) initiator, and phosphonate anchor have been previously reported.[311]

The DAP polymers were synthesized by the Activator ReGenerated by Electron Transfer Atom Transfer Radical Polymerization (ARGET-ATRP)[201] of polystyrene using the DAP initiator as previously reported.[287] The Thy polymers were synthesized by the ATRP of polystyrene using the Thy initiator as previously reported.[222] GPC traces of the polymers used in this work are featured in **Figure S5-1**, and the results summarized in **Table S5-1**.

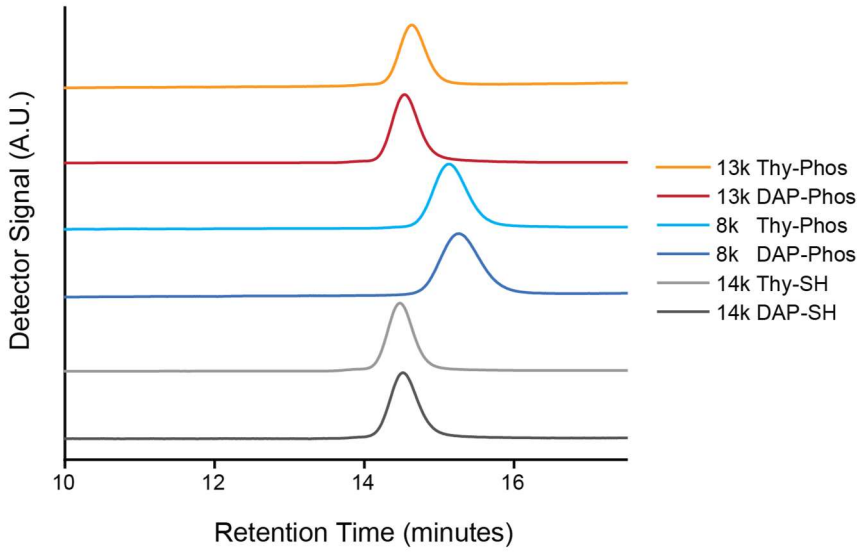

Figure S5-1. GPC traces of polymers used in this work. Data is summarized in **Table S5-1**.

	M_n (kDa)	M_w (kDa)	M_p (kDa)	Đ
DAP-SH 14 kDa	13.1	13.6	14.0	1.036
Thy-SH 14 kDa	13.8	14.2	14.4	1.028
DAP-Phos 8 kDa	7.1	7.4	7.7	1.050
Thy-Phos 8 kDa	7.5	7.7	7.9	1.033
DAP-Phos 13 kDa	13.1	13.5	13.8	1.031
Thy-Phos 13 kDa	12.2	12.4	12.6	1.019

Table S5-1. Summary of GPC results for the polymers used in this work.

After polymerization, the terminal bromine of polymers that were to functionalize gold nanoparticles was substituted with aminoethanethiol, as described previously.[222] The terminal

bromine of polymers that were to functionalize iron oxide nanoparticles was substituted with sodium azide, and a "click" reaction was performed to install the phosphanate anchor as described previously.[311]

Citrate capped gold nanoparticles were synthesized by a literature procedure[29] that was slightly modified.[285]

Iron oxide nanoparticles were synthesized according to a literature procedure from the thermal decomposition of an iron oleate precursor.[54,311] TEM micrographs of the nanoparticles used in this

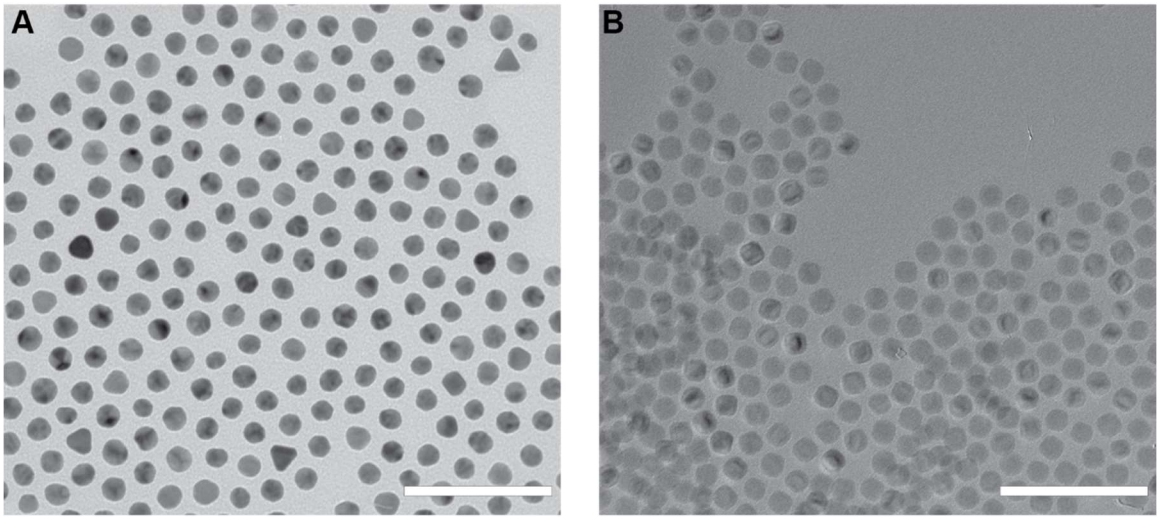

Figure S5-2. TEM Micrographs of the gold (A) and iron oxide (B) nanoparticles used in this

	Diameter (nm)	Relative Standard Deviation (%)
Gold Nanoparticles	15.4	8.5
Iron Oxide Nanoparticles	15.9	6.1

Table S5-2. Size and dispersity of the nanoparticles used in these experiments.

work are featured in **Figure S5-2**, and their sizes and distributions summarized in **Table S5-2**.

Gold Nanocomposite Tecton (Au-NCTs) synthesis was performed as previously reported.[222] Briefly, a solution of as-synthesized gold nanoparticles was added to an equal volume of 1 mg/mL thiolated DAP or Thy polystyrene, and vigorously shaken for 1 minute. The resulting pink precipitate was collected by a gentle centrifugation, and redispersed in N,N-dimethylformamide (DMF). The NCTs then underwent a series of 3 centrifuge cycles (5000 RCF, 45 minutes),

redispersing in DMF, Toluene, and Toluene. The concentration of the NCTs was measured using Beer's Law, and adjusted to match the desired concentration for the experiment.

Iron Oxide NCTs (IO-NCTs) were synthesized as previously described.[311] Briefly, iron oxide nanoparticle docosane reaction mixture (500 mg) was dissolved in 4 mL THF. Reaction byproducts were removed by centrifugation (2 x 8,500 RCF) and redispersion in THF. The nanoparticles in THF were divided in half, and added to either DAP or Thy polymer equipped with the phosphonate anchor (40 mg). The solutions were shaken overnight, and then purified by three centrifuge cycles (8,500 RCF) redispersing in THF, Toluene, and Toluene.

A5.3 NCT Crystallization

To prepare crystalline Au-NCT assemblies, equal volumes of purified DAP and Thy NCTs were combined in a PCR tube. Analysis of the melting curve (Figure S3) indicated the standard case NCTs (15 nm Au NPs with 14 kDa polymer) were totally dissociated at 55 ℃. Therefore, the annealing process was performed by slow cooling the mixed NCT solution from 55℃ to 25℃ in a Techne Prime Thermal Cycler at a desired cooling rate (if not mentioned, 0.1 ℃ / minute). IO-NCTs were crystallized by heating to 80 ℃ on a heat block, removing the sample, and allowing the NCTs to return to room temperature.

A5.4 Collapsing the Polymer Brush

NCTs cast directly from toluene do not retain their ordering upon solvent evaporation (**Figure S5-3**). As the solvent evaporates the polymer brush uncontrollably deswells, and capillary forces distort the lattice, although some local ordering is preserved.

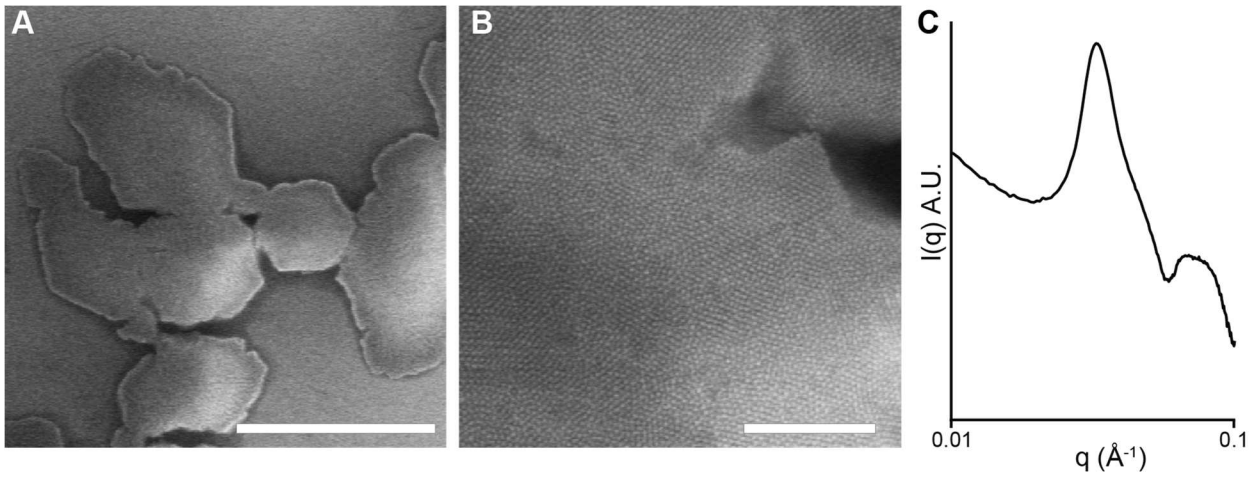

Figure S5-3. SEM (A and B) and SAXS data (C) of NCTs cast directly from toluene and dried. Scale bars are (A) 5 microns and (B) 500 nm.

Ordering can be preserved by gradually adding a poor solvent that does not disrupt the hydrogen bonding interactions of the NCTs (**Figure S5-4**). N-Decane was the preferred solvent for the experiments in the main text because its slower evaporation rate allowed for trace amounts of residual toluene to be removed before the assembly completely dried. The typical procedure was to increase the volume fraction of non-solvent by 0.2 every 30 minutes, and when the solution reached 80% non-solvent it was removed with a needle and replaced with pure alkane. The system could accommodate faster addition rates, but shaking samples to mix the solvents would frequently generate static electricity which would pull the NCTs out of solution and destroy them, making their study difficult. Therefore, a more conservative procedure that allowed ample time for solvent diffusion was preferred.

Additionally, the collapsed NCT brush can be swollen with toluene again, without any loss in ordering (**Figure S5-5**).

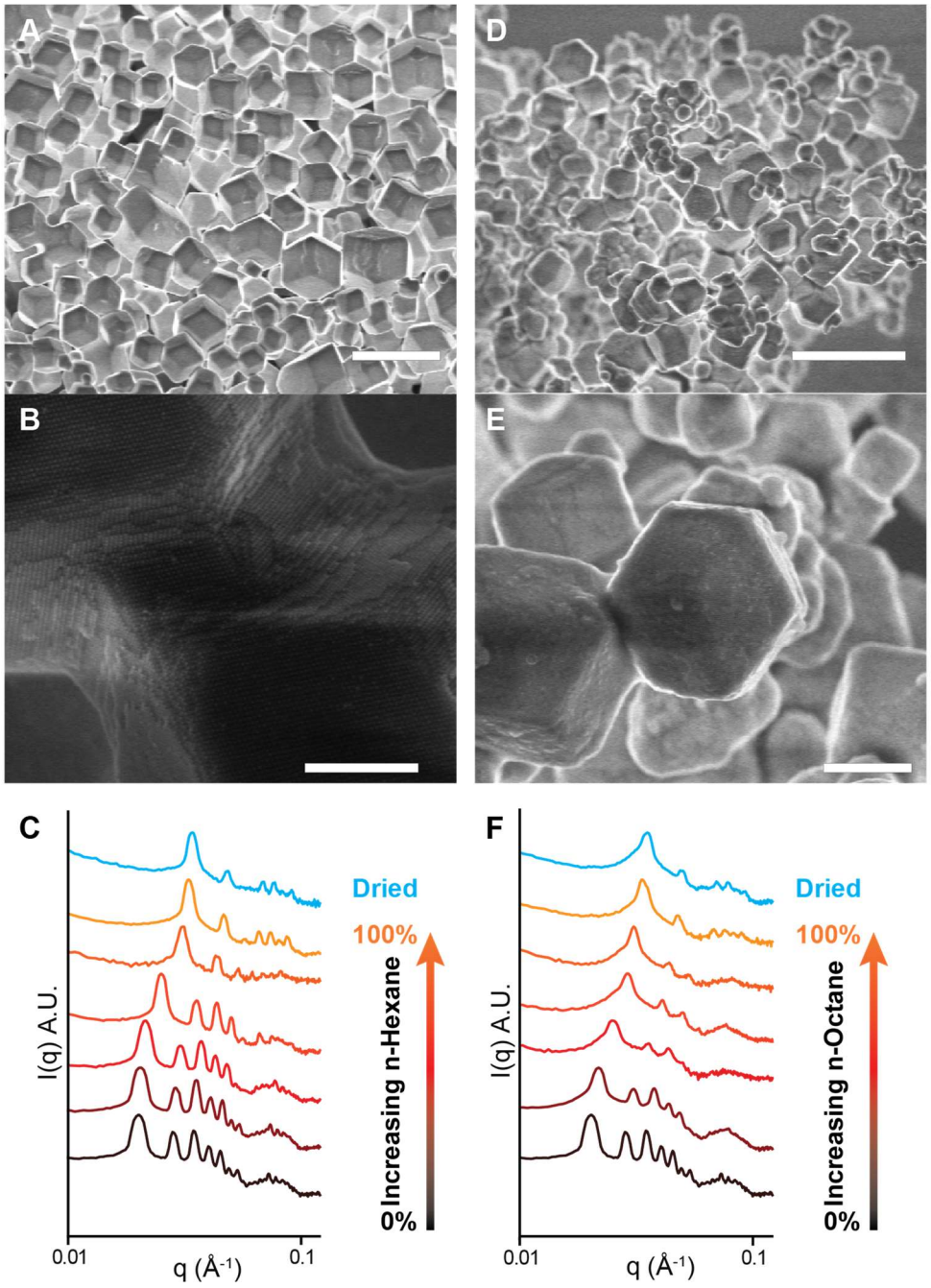

Figure S5-4. (A and B) SEM micrographs of NCTs with the brushes collapsed with n-hexane. Scale bars are 5 microns (A) and 500 nm (B). (C) SAXS of NCT crystallites in 0, 20, 40, 60, 80, and 100 volume percent n-Hexane, and of a dried sample. (D and E) SEM micrographs of NCTs with the brushes collapsed with n-Octane. Scale bars are 5 microns (D) and 1 micron (E) (C) SAXS of NCT crystallites in 0, 20, 40, 60, 80, and 100 volume percent n-Octane, and of a dried sample.

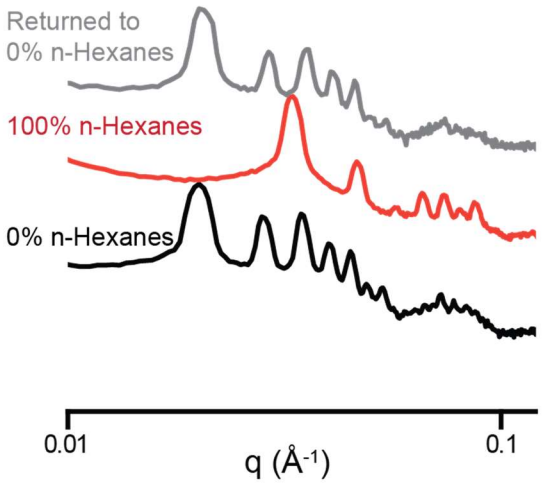

Figure S5-5. Sample of Au-NCTs that was transitioned to 100% n-Hexane, and then returned to 100% toluene.

A potential key advantage of these NCT solids with collapsed polymer brushes is the ability to assemble lattices of nanoparticles with very small interparticle distances, which could find use in plasmonic, optical, or magnetic materials.[46,330] Do demonstrate this, Au-NCTs were assembled with a 6 kDa polymer brush and collapsed, leading to well-ordered lattices with an interparticle distance of 19.5 nm, or a surface to surface distance of 4.1 nm (**Figure S5-6**).

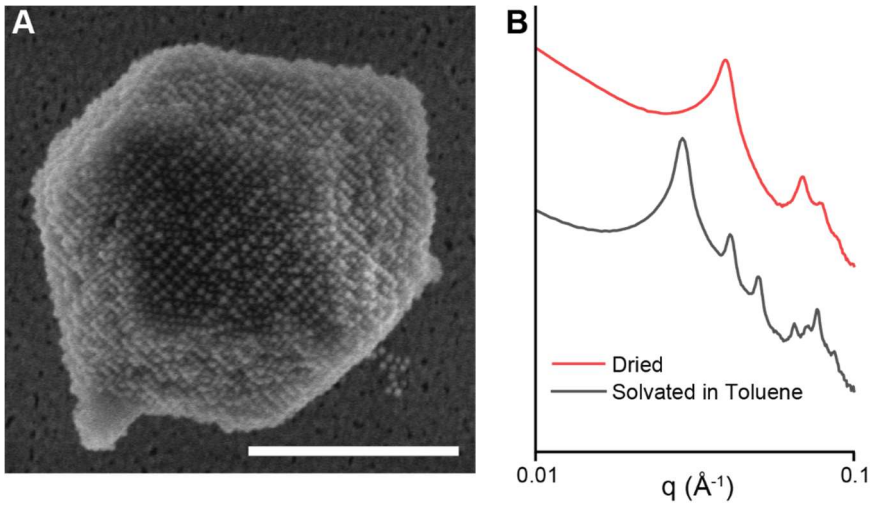

Figure S5-6. SEM (A) and SAXS (B) of Au-NCTs synthesized with a shorter, 6 kDa polymer, resulting in a very short interparticle distance (19.5 nm, 4.1 nm surface to surface). Scale bar is 500 nm.

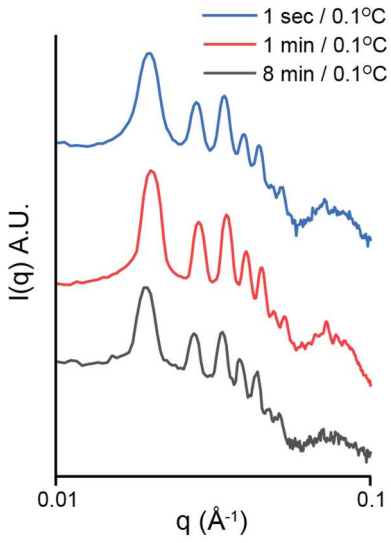

Figure S5-7. NCTs form well-ordered crystals at a variety of cooling rates. Even when cooled very rapidly at a rate of 0.1°C/s, an ordered bcc lattice is formed.

A5.5 Controlling NCT Crystallite Size with Concentration and Cooling Rate

To investigate the effects of NCT concentration and cooling rate on crystallite size, several samples were crystallized via slow cooling as described above with various cooling rates (1sec/0.1ºC to 8min/0.1ºC) and NCT concentrations (5nM to 80nM). The resulting crystallites were collected, their polymers collapsed, and drop cast onto substrates for SEM analysis. A minimum of 50 micrographs for each condition were collected where each image contains several crystallites, which tend to conglomerate together on the substrate. Three characteristic SEM micrographs of each condition are included for reference in **Figure S5-8** through **Figure S5-24**. The individual crystallites in each micrograph were measured in ImageJ by tracing the dimensions with a stylus and averaging the major and minor axis lengths to yield a characteristic length (roughly akin to a diameter). The number of crystallites (N) measured for each condition is summarized in the following table and included at minimum 200 individual crystallites. Histograms of characteristic length reveal roughly Gaussian size distributions for every condition (**Figure S5-25** and **26**) with increasing average values for slower cooling rates and higher concentrations. Descriptive statistics of each distribution is summarized in the following table.

Cooling Rate^{-1} (Time/0.1°C)	NCT Concentration (nM)	N	Mean (nm)	Standard Deviation (nm)	Minimum (nm)	1st Quartile (Q1) (nm)	Median (nm)	3rd Quartile (Q3) (nm)	Maximum (nm)
1sec	20	988	436	103	81	370	432	499	847
15sec	20	1137	1,237	218	28	1,111	1,261	1,377	2,246
30sec	20	955	1,531	316	454	1,325	1,537	1,725	2,801
1min	20	723	1,782	574	483	1,404	1,784	2,129	3,918
2min	20	501	2,046	743	539	1,576	2,006	2,510	5,526
4min	20	468	2,231	909	527	1,595	2,049	2,735	5,473
8min	20	225	3,508	1,696	631	2,185	3,214	4,594	8,438
1min	5	223	1,150	259	403	992	1,185	1,324	1,921
1min	10	288	1,699	433	607	1,429	1,697	1,947	3,547
1min	40	517	2,233	926	28	1,780	2,206	2,588	9,903
1min	80	468	2,299	908	547	1,733	2,180	2,795	9,043
2min	20	456	2,055	657	502	1,641	2,043	2,441	5,337
4min	20	291	2,339	617	709	1,936	2,281	2,735	4,369
8min	20	318	3,509	1,471	703	2,262	3,284	4,668	8,817
2min	40	719	2,313	775	499	1,786	2,332	2,762	5,461
4min	40	373	2,804	1,245	507	2,050	2,598	3,330	8,807
8min	40	539	5,054	2,587	1,276	3,153	4,371	6,438	15,777
2min	80	495	2,952	1,217	612	2,147	2,810	3,645	10,853
4min	80	1095	3,077	1,434	863	2,286	2,793	3,529	20,169
8min	80	421	6,190	4,191	1,246	3,711	4,445	7,223	26,341

Table S5-3. Summary and descriptive statistics of crystallite size for all conditions studied.

A5.5.1 Cooling Rate

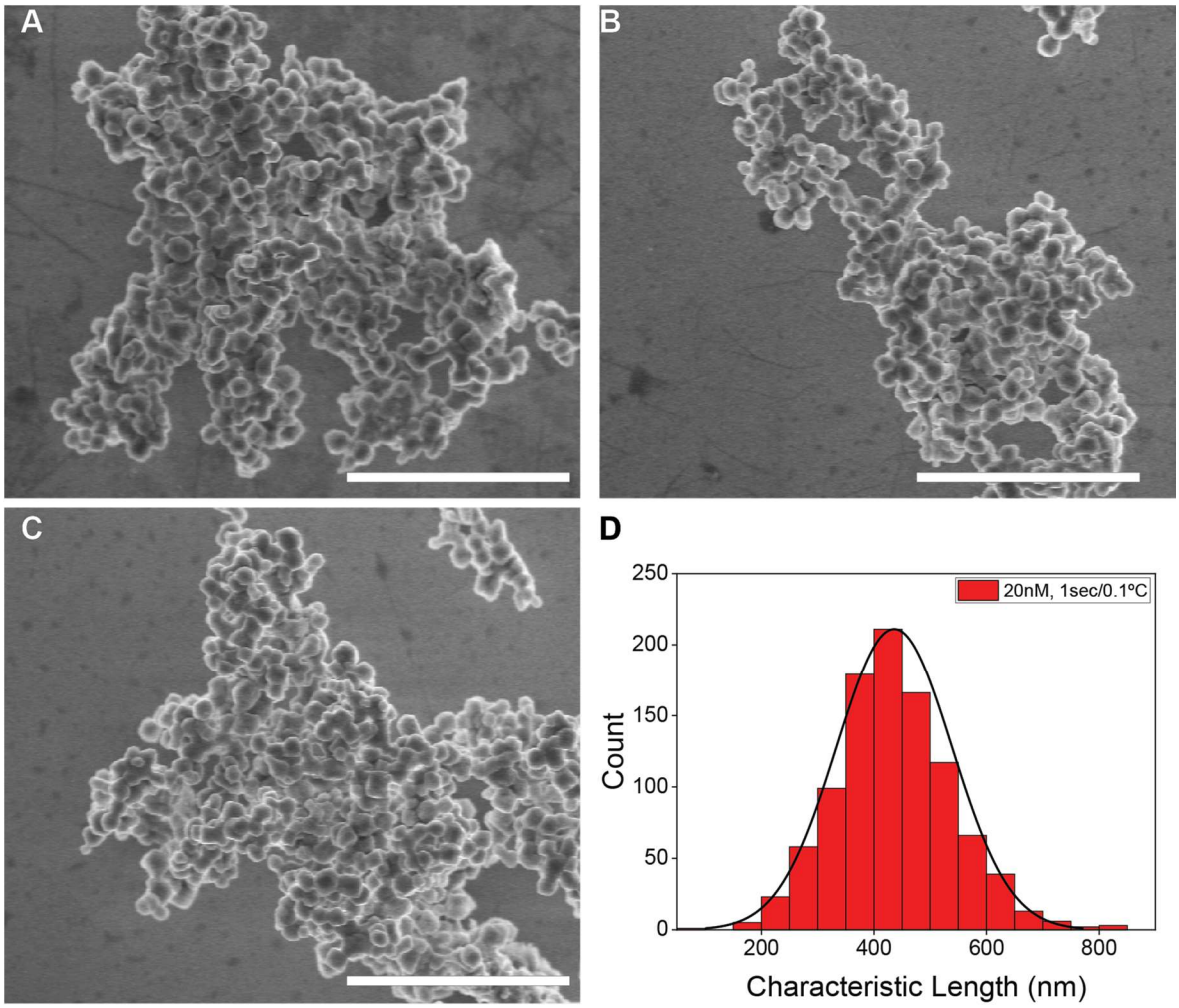

Figure S5-8. (A-C) SEM images of NCTs crystallized with a cooling rate of 1 second per 0.1 °C and a concentration of 20 nM. Scale bar is 5 microns. (D) Histogram of crystallite sizes with a Gaussian fit.

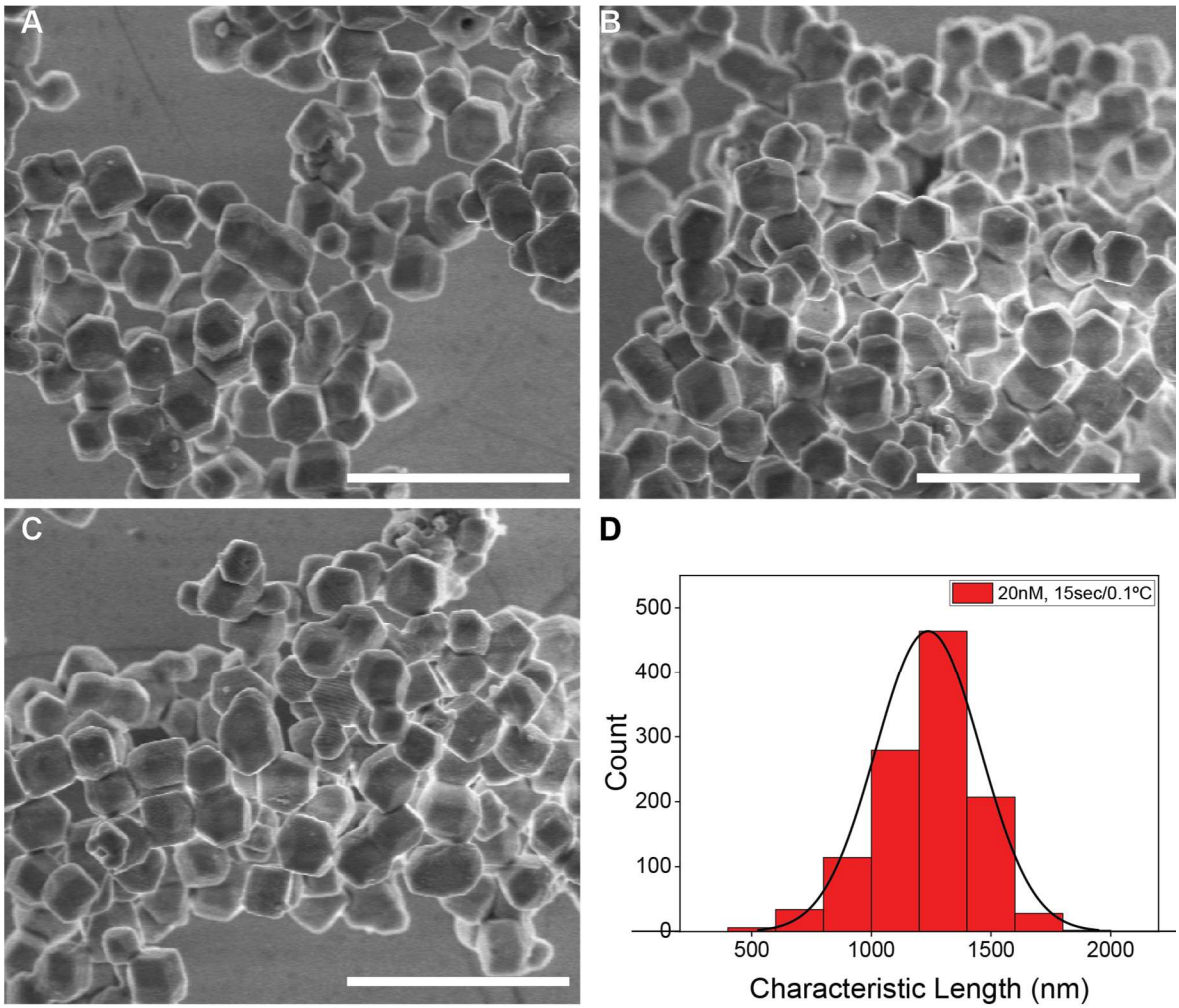

Figure S5-9. (A-C) SEM images of NCTs crystallized with a cooling rate of 15 seconds per 0.1 °C and a concentration of 20 nM. Scale bar is 5 microns. (D) Histogram of crystallite sizes with a Gaussian fit.

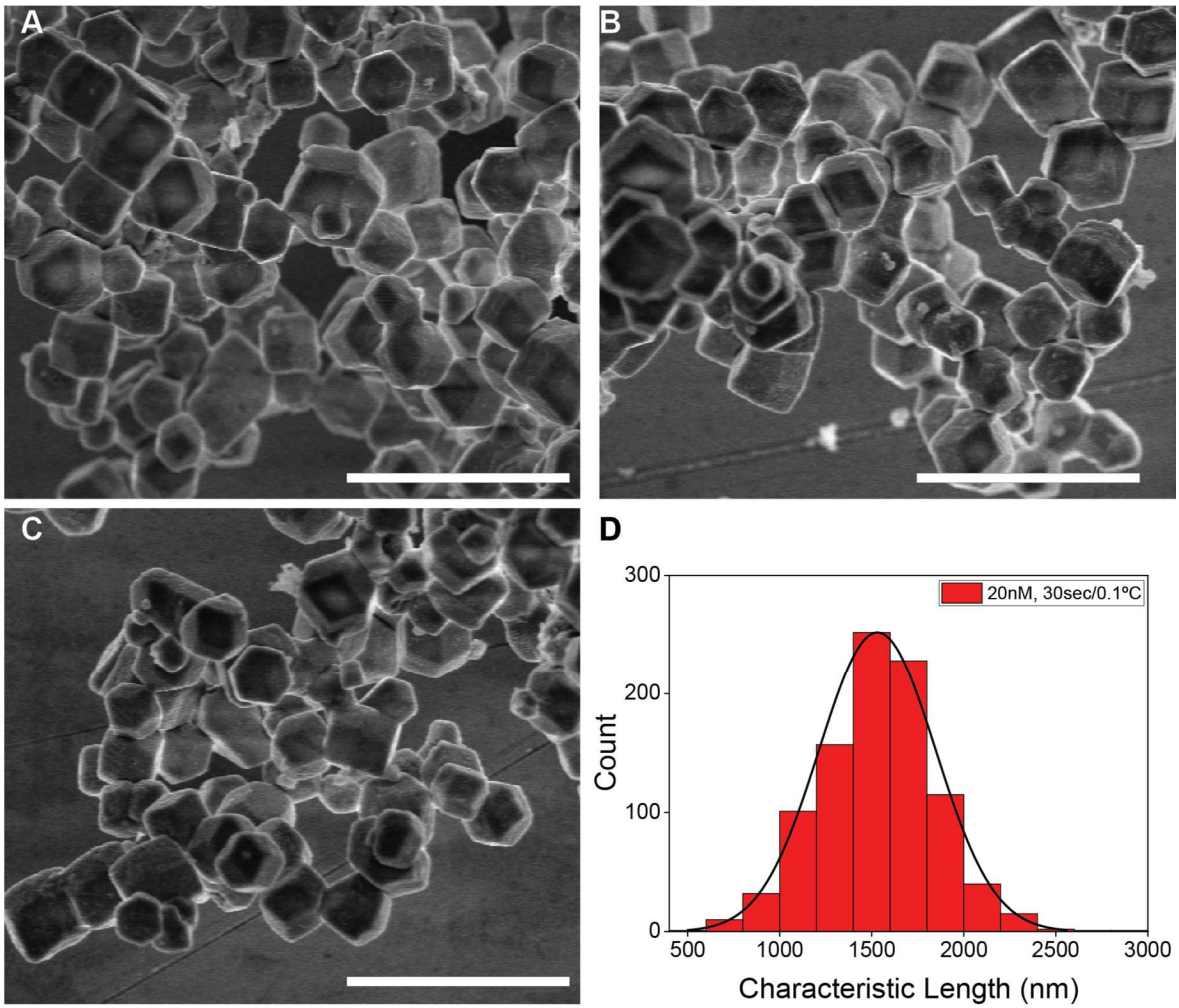

Figure S5-10. (A-C) SEM images of NCTs crystallized with a cooling rate of 30 seconds per 0.1 °C and a concentration of 20 nM. Scale bar is 5 microns. (D) Histogram of crystallite sizes with a Gaussian fit.

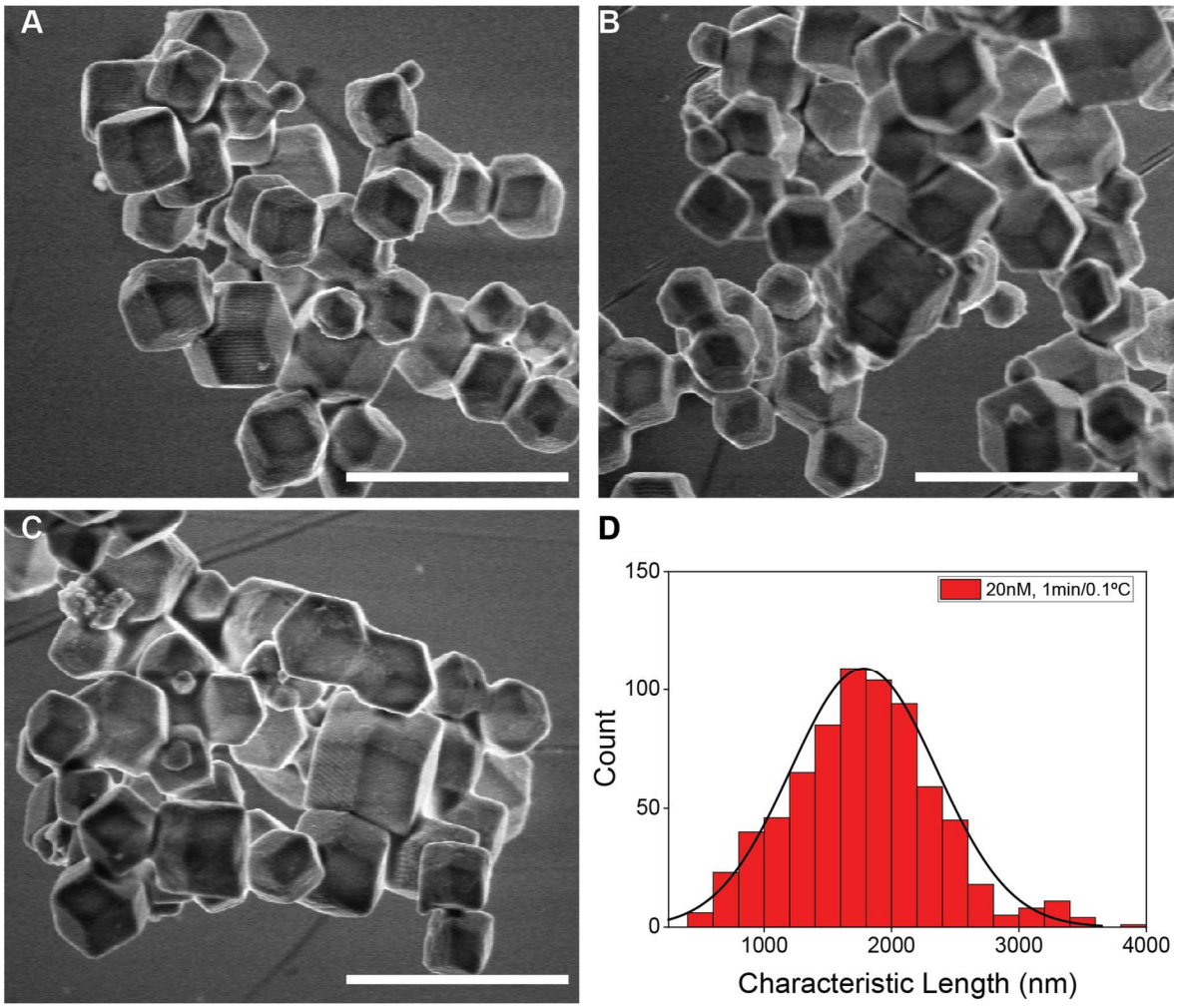

Figure S5-11. (A-C) SEM images of NCTs crystallized with a cooling rate of 1 minute per 0.1 °C and a concentration of 20 nM. Scale bar is 5 microns. (D) Histogram of crystallite sizes with a Gaussian fit.

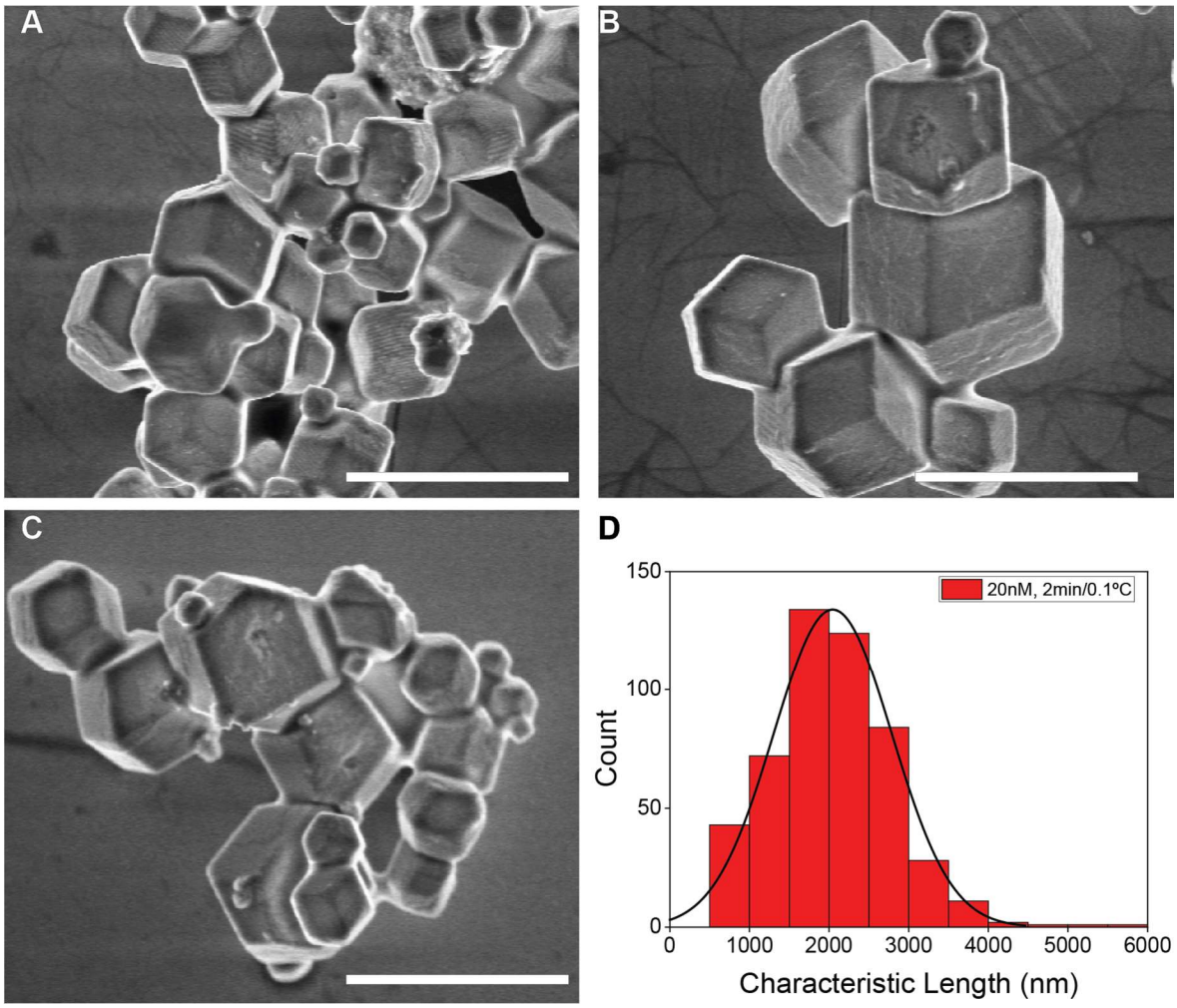

Figure S5-12. (A-C) SEM images of NCTs crystallized with a cooling rate of 2 minutes per 0.1 °C and a concentration of 20 nM. Scale bar is 5 microns. (D) Histogram of crystallite sizes with a Gaussian fit.

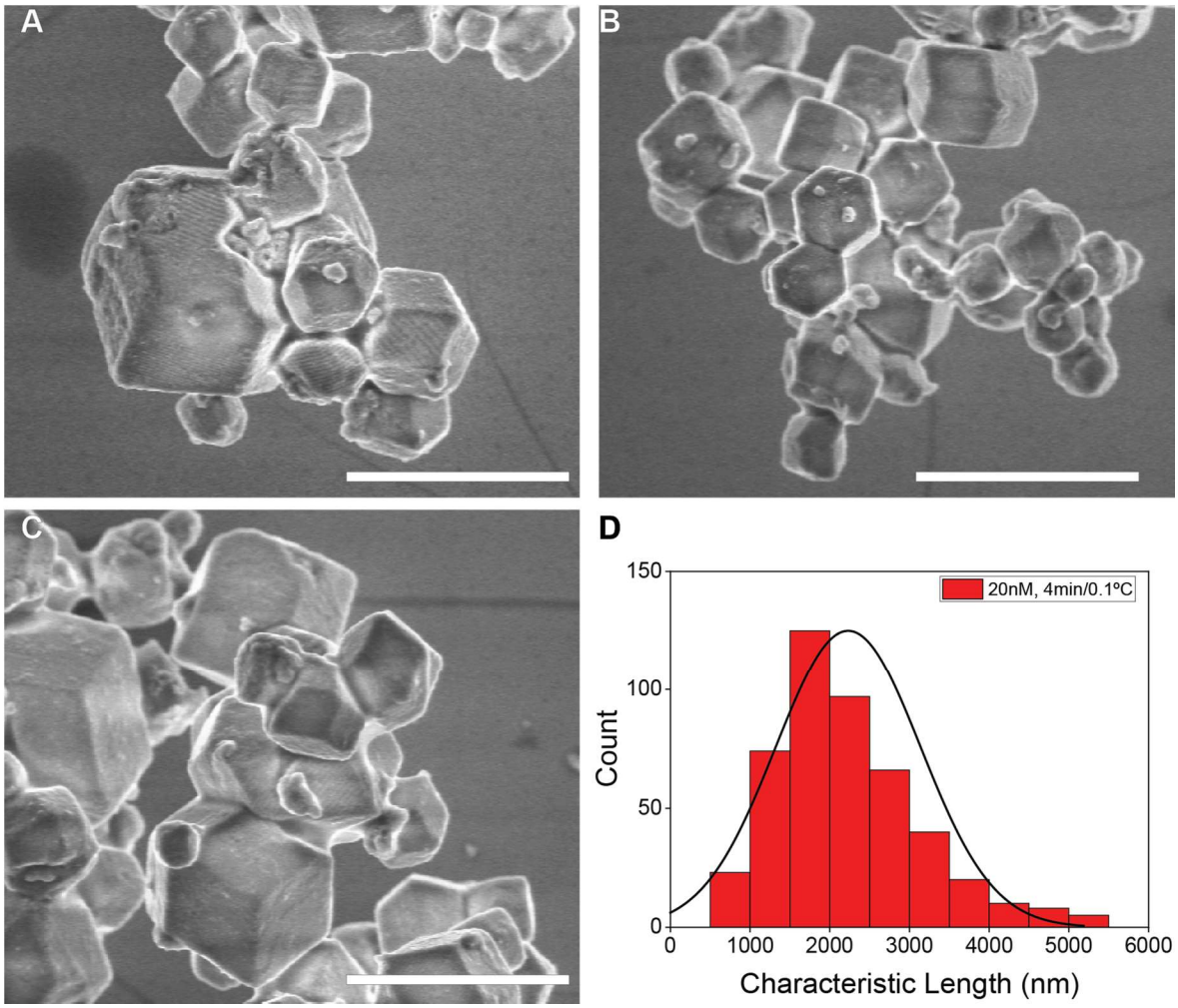

Figure S5-13. (A-C) SEM images of NCTs crystallized with a cooling rate of 4 minutes per 0.1 °C and a concentration of 20 nM. Scale bar is 5 microns. (D) Histogram of crystallite sizes with a Gaussian fit.

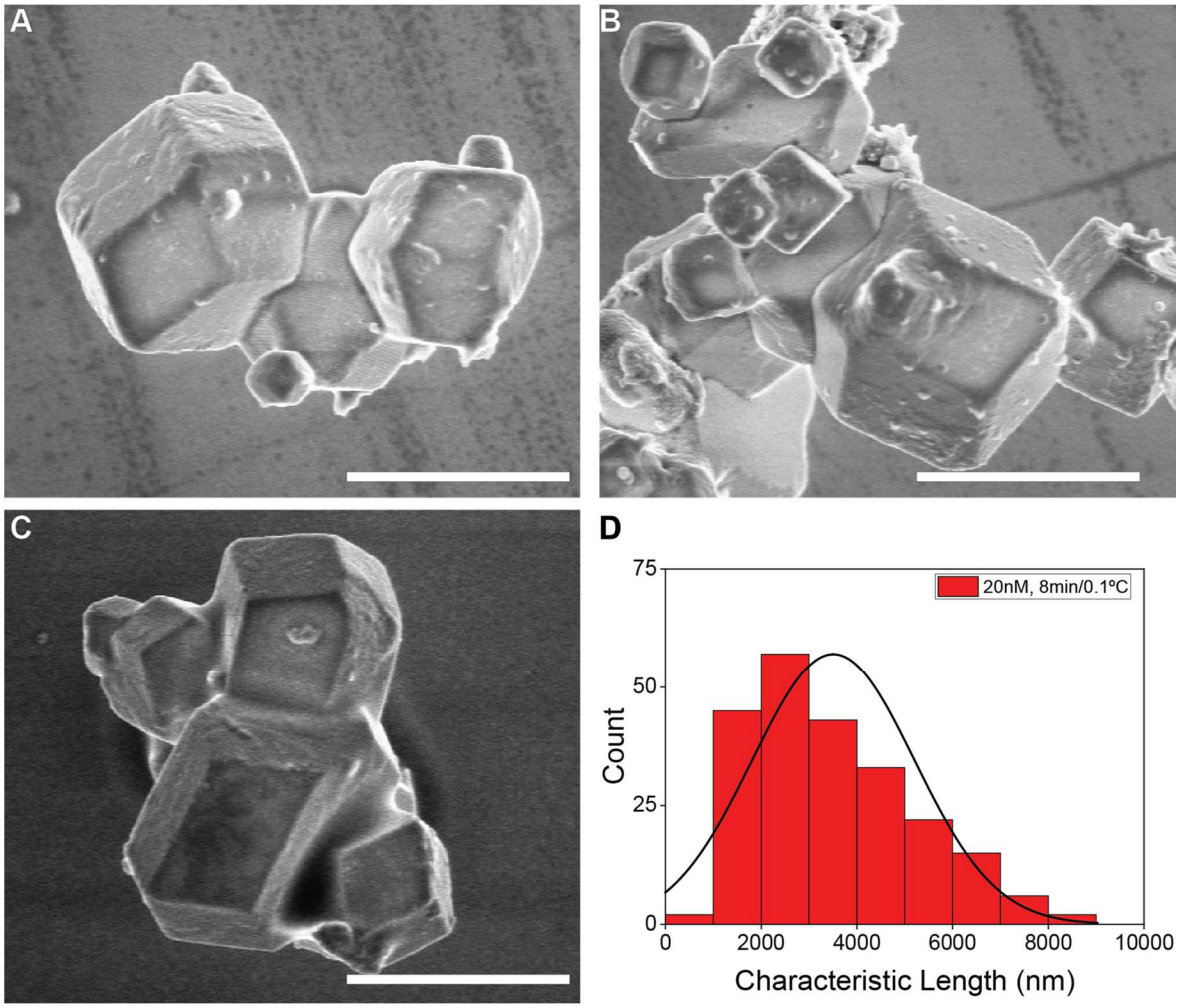

Figure S5-14. (A-C) SEM images of NCTs crystallized with a cooling rate of 8 minutes per 0.1 °C and a concentration of 20 nM. Scale bar is 5 microns. (D) Histogram of crystallite sizes with a Gaussian fit.

A5.5.2 Concentration

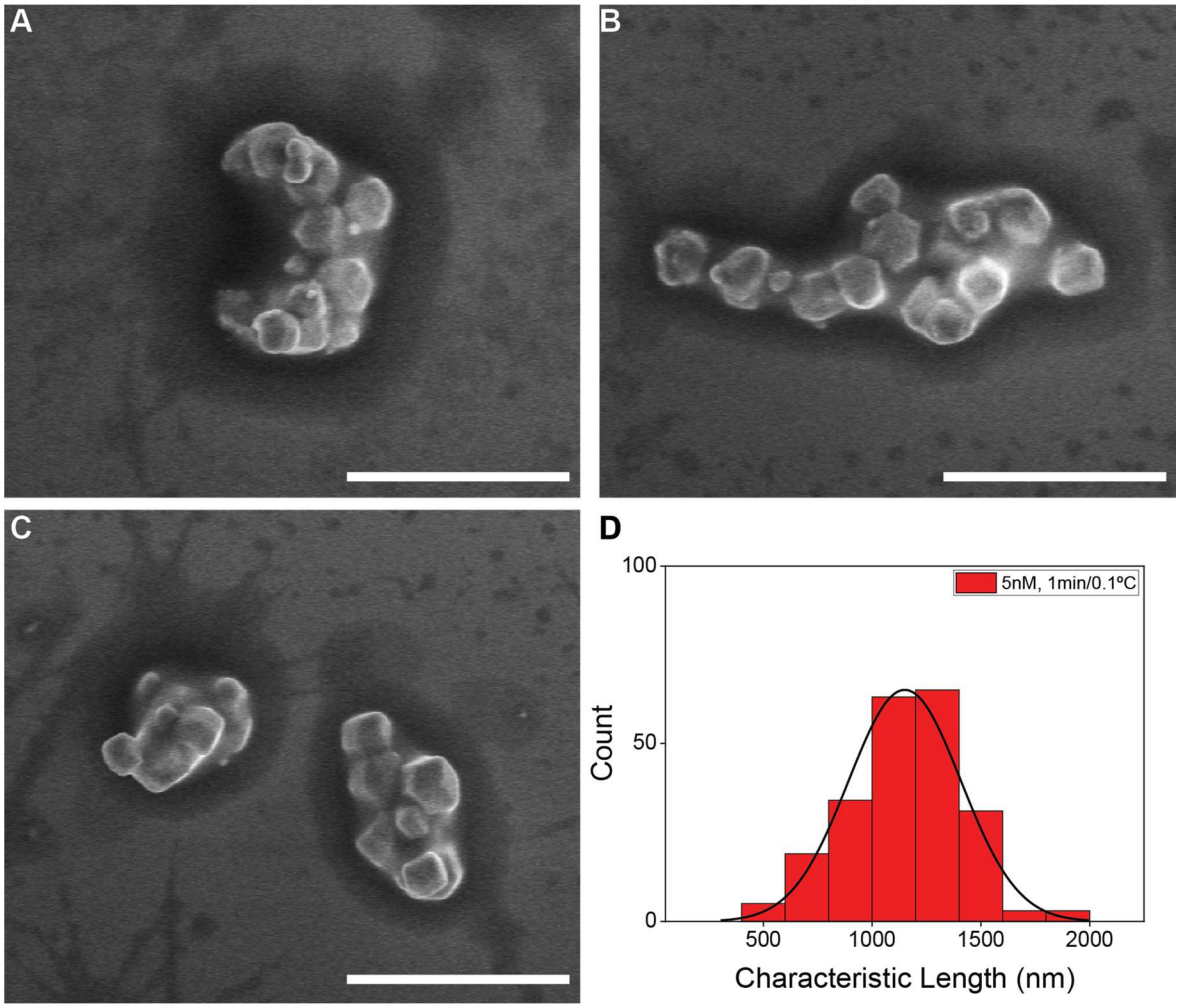

Figure S5-15. (A-C) SEM images of NCTs crystallized with a cooling rate of 1 minute per 0.1 °C and a concentration of 5 nM. Scale bar is 5 microns. (D) Histogram of crystallite sizes with a Gaussian fit.

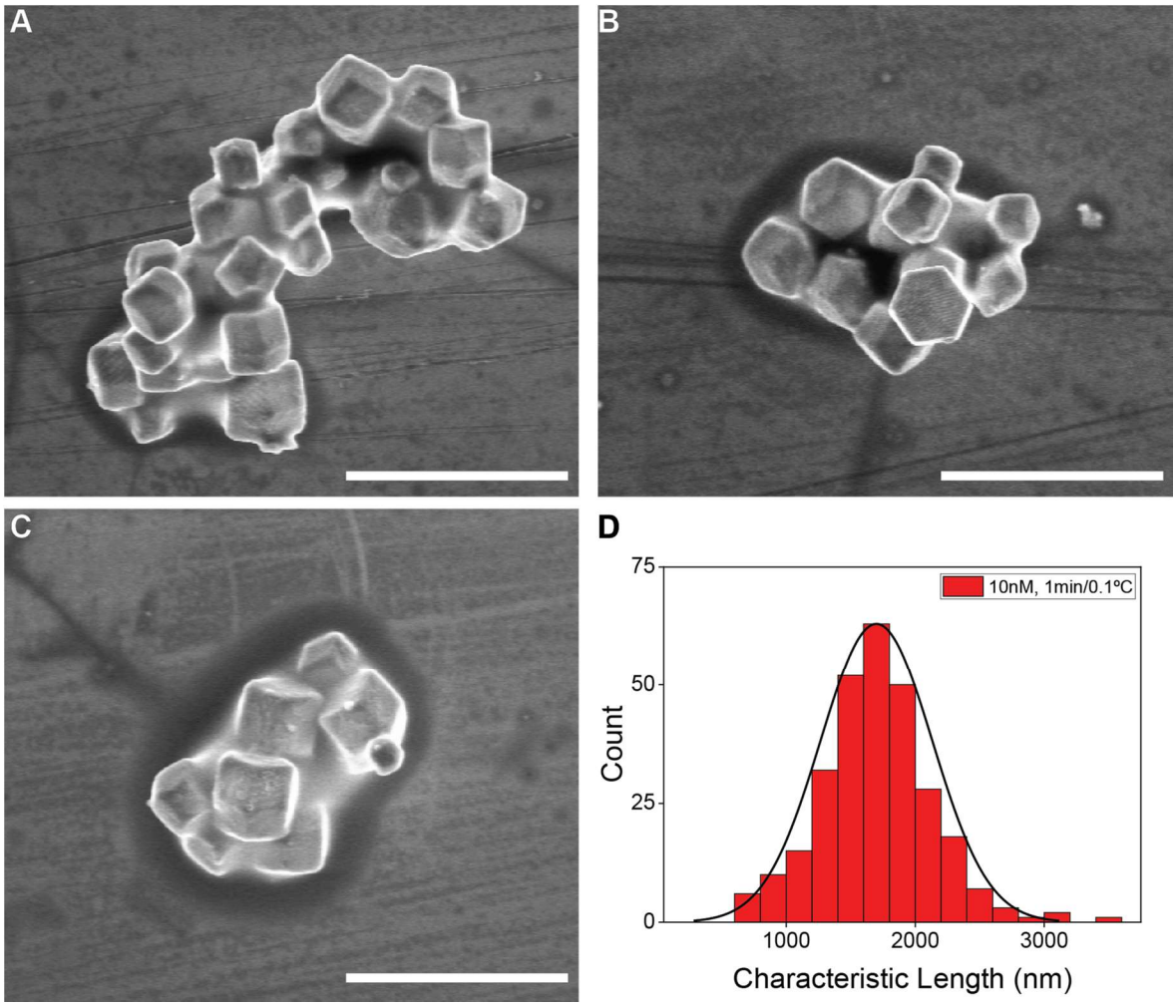

Figure S5-16. (A-C) SEM images of NCTs crystallized with a cooling rate of 1 minute per 0.1 °C and a concentration of 10 nM. Scale bar is 5 microns. (D) Histogram of crystallite sizes with a Gaussian fit.

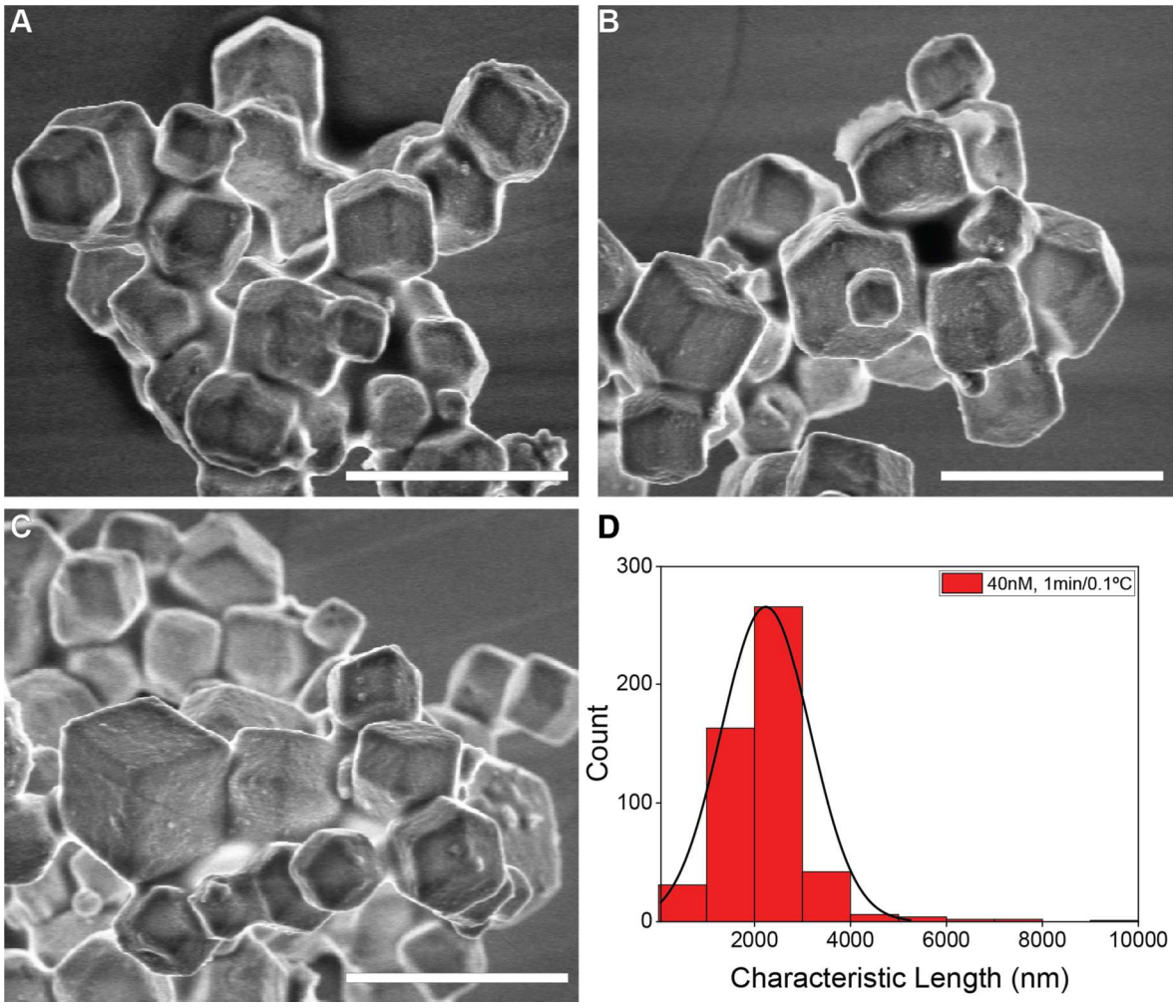

Figure S5-17. (A-C) SEM images of NCTs crystallized with a cooling rate of 1 minute per 0.1 °C and a concentration of 40 nM. Scale bar is 5 microns. (D) Histogram of crystallite sizes with a Gaussian fit.

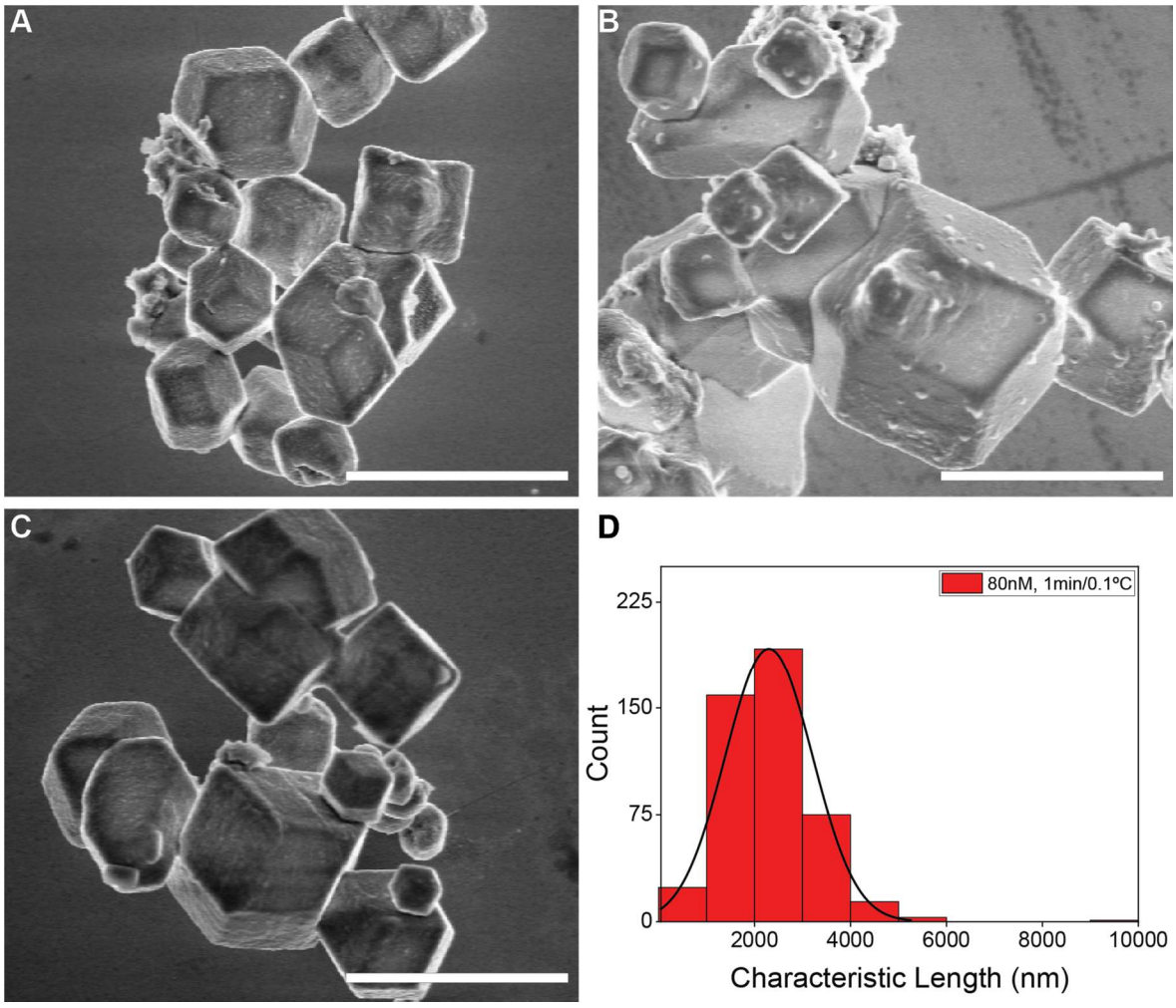

Figure S5-18. (A-C) SEM images of NCTs crystallized with a cooling rate of 1 minute per 0.1 °C and a concentration of 80 nM. Scale bar is 5 microns. (D) Histogram of crystallite sizes with a Gaussian fit.

A5.5.3 Combining Slow Cooling Rate and High Concentration

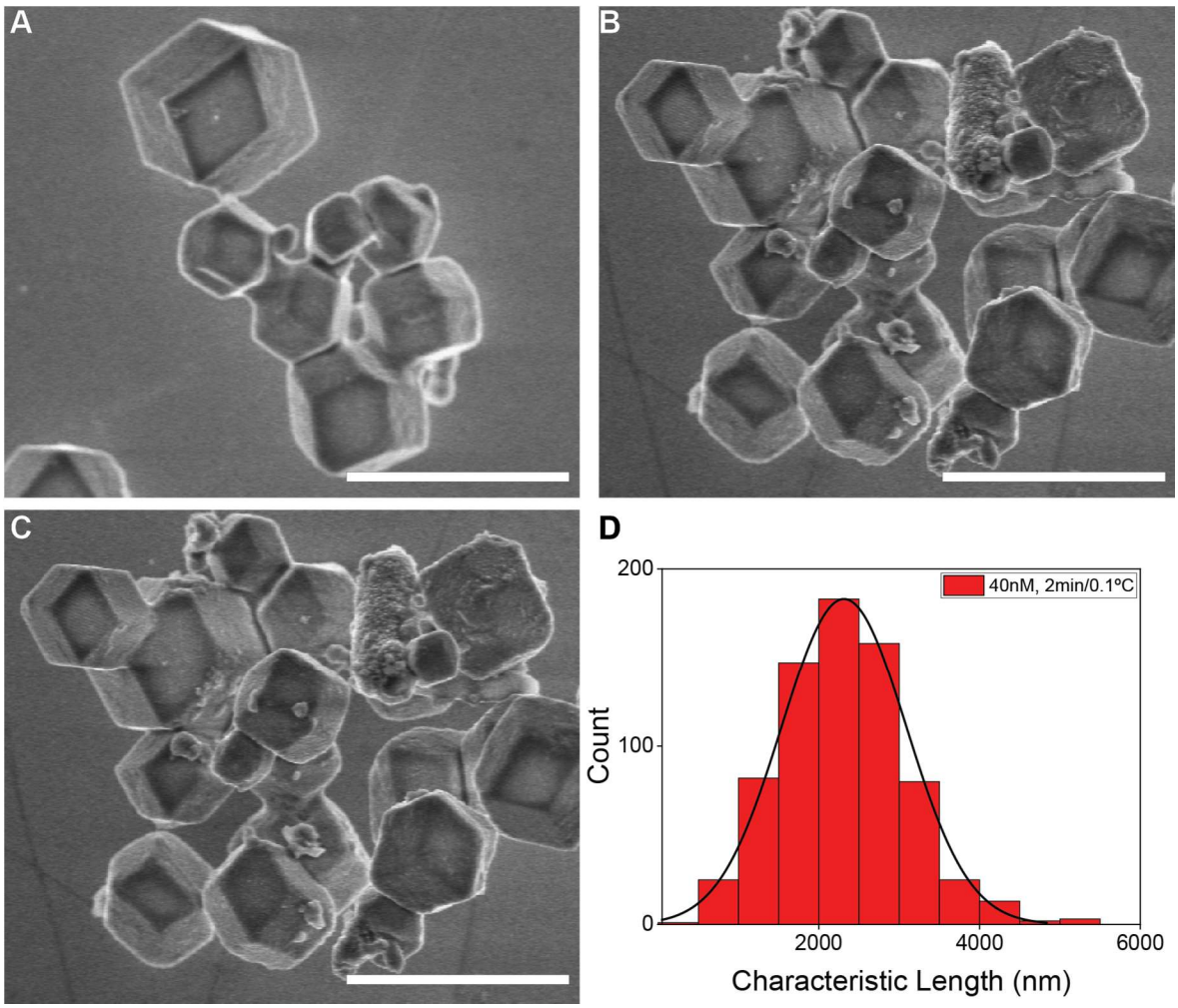

Figure S5-19. (A-C) SEM images of NCTs crystallized with a cooling rate of 2 minute per 0.1 °C and a concentration of 40 nM. Scale bar is 5 microns. (D) Histogram of crystallite sizes with a Gaussian fit.

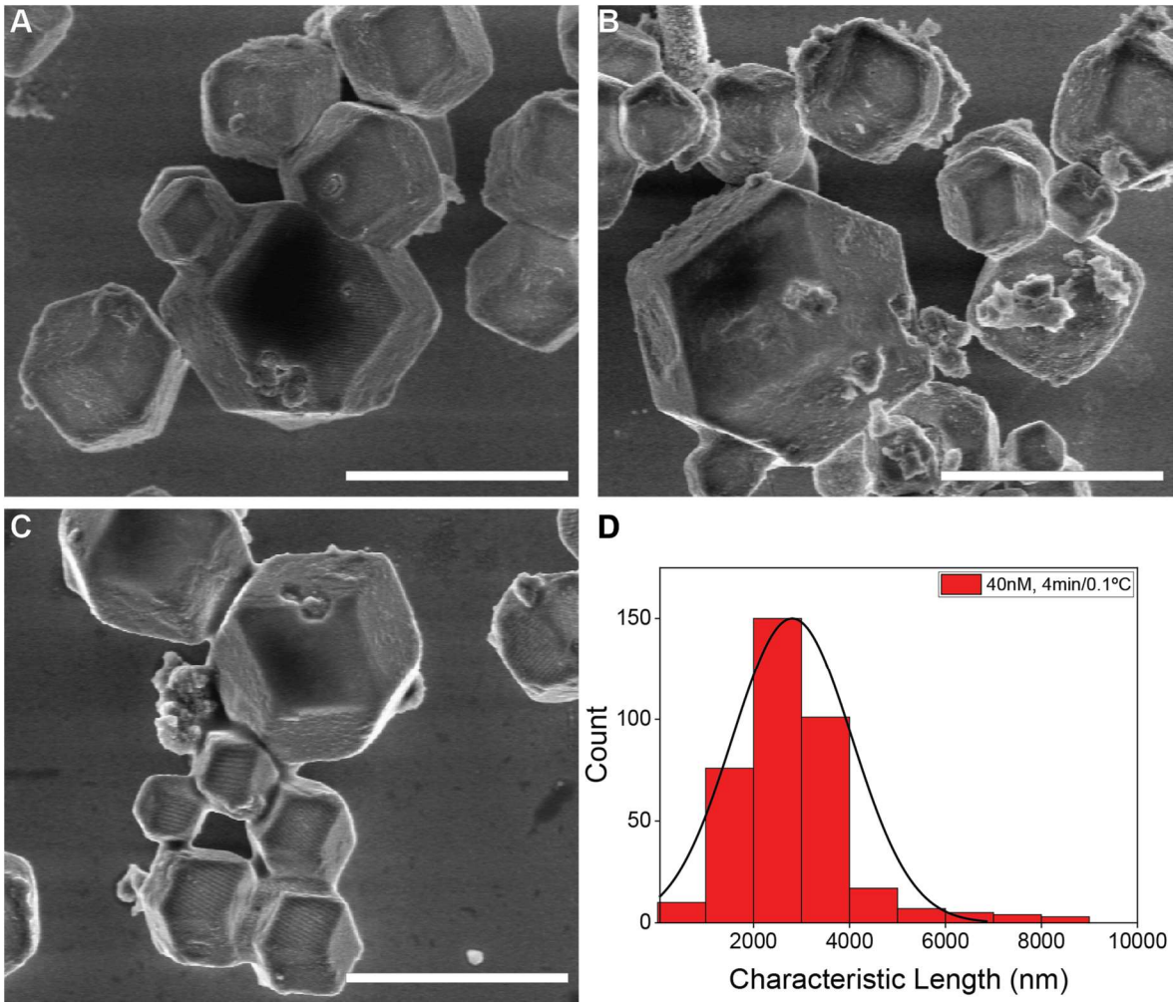

Figure S5-20. (A-C) SEM images of NCTs crystallized with a cooling rate of 4 minute per 0.1 °C and a concentration of 40 nM. Scale bar is 5 microns. (D) Histogram of crystallite sizes with a Gaussian fit.

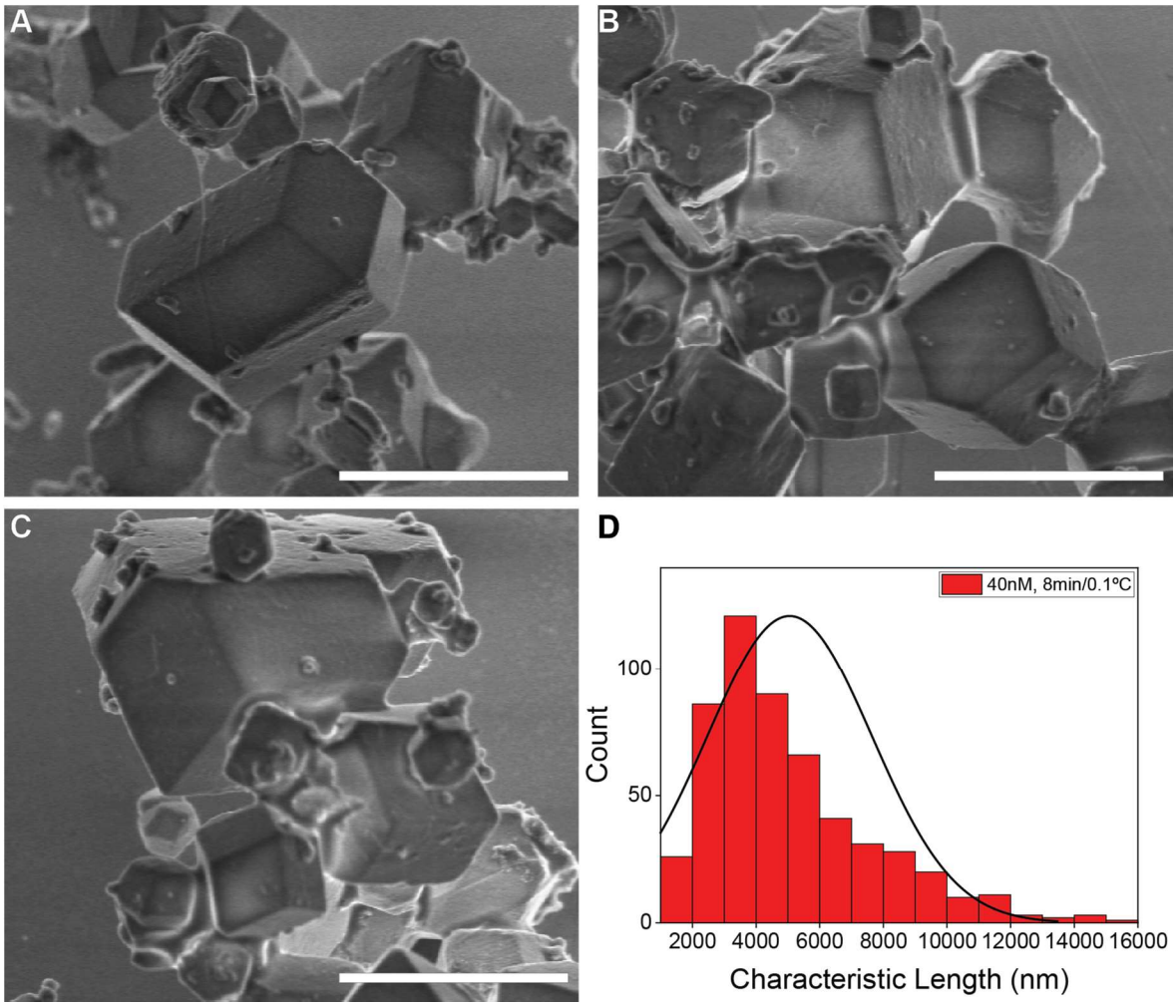

Figure S5-21. (A-C) SEM images of NCTs crystallized with a cooling rate of 8 minute per 0.1 °C and a concentration of 40 nM. Scale bar is 10 microns. (D) Histogram of crystallite sizes with a Gaussian fit.

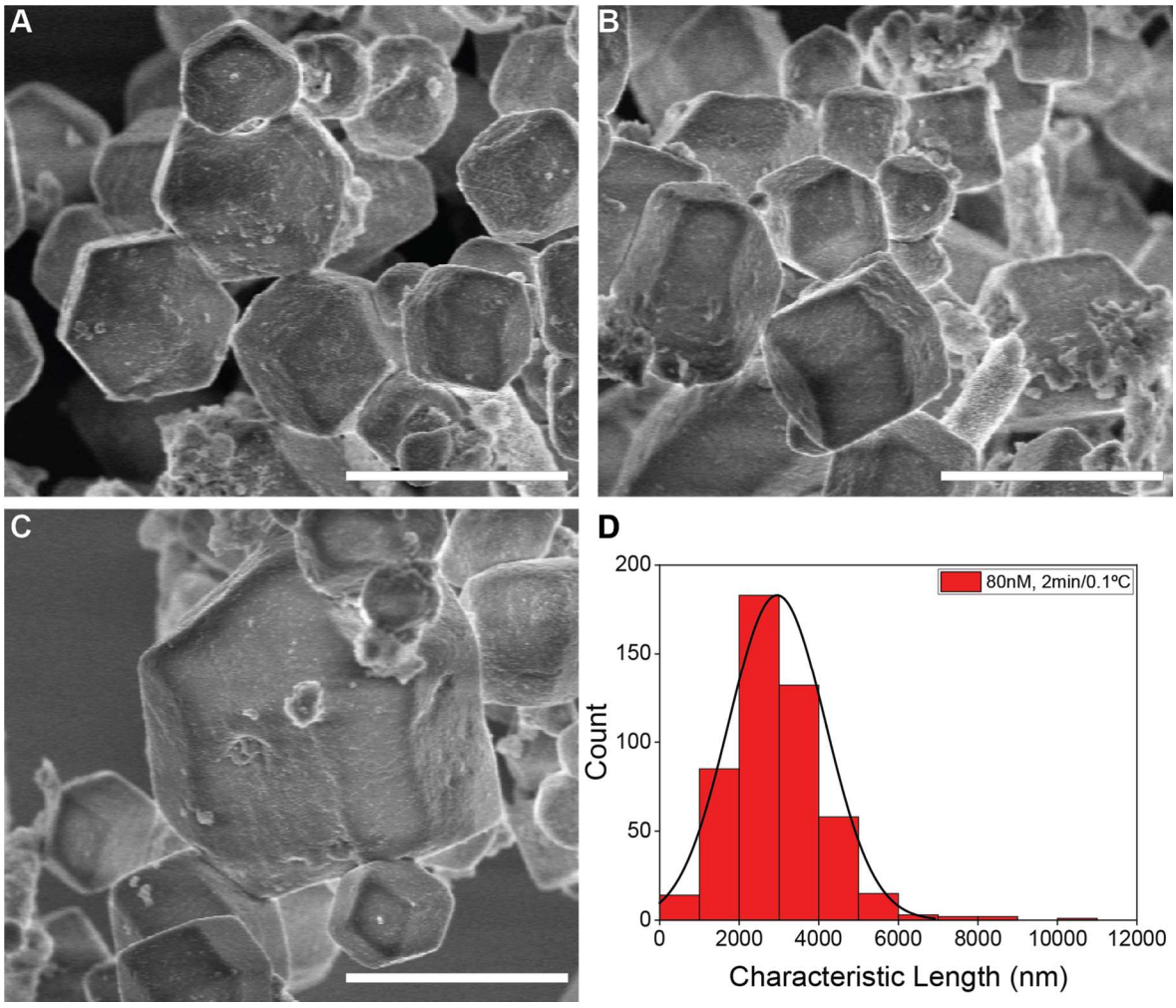

Figure S5-22. (A-C) SEM images of NCTs crystallized with a cooling rate of 2 minute per 0.1 ºC and a concentration of 80 nM. Scale bar is 5 microns. (D) Histogram of crystallite sizes with a Gaussian fit.

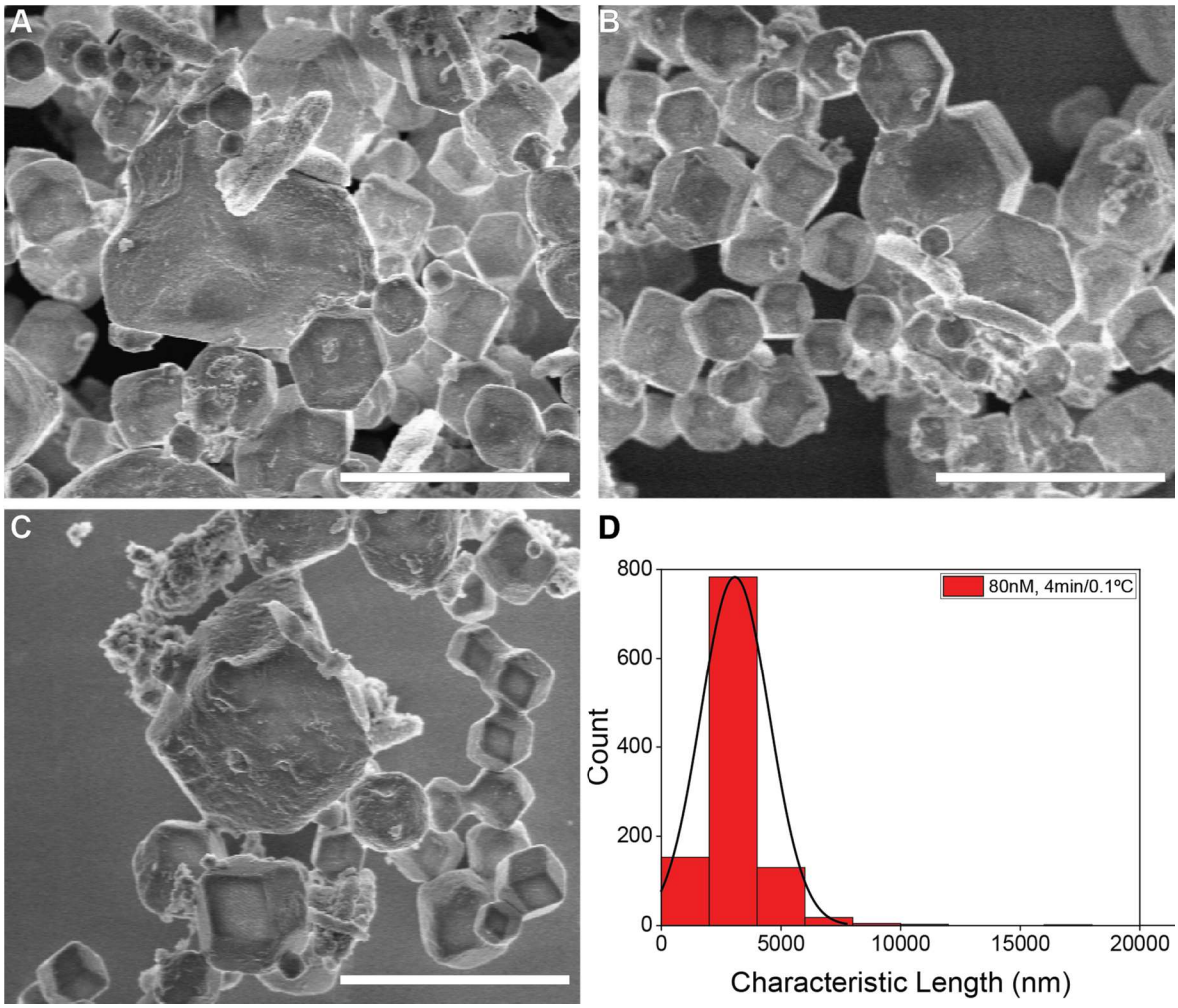

Figure S5-23. (A-C) SEM images of NCTs crystallized with a cooling rate of 4 minute per 0.1 °C and a concentration of 80 nM. Scale bar is 10 microns. (D) Histogram of crystallite sizes with a Gaussian fit.

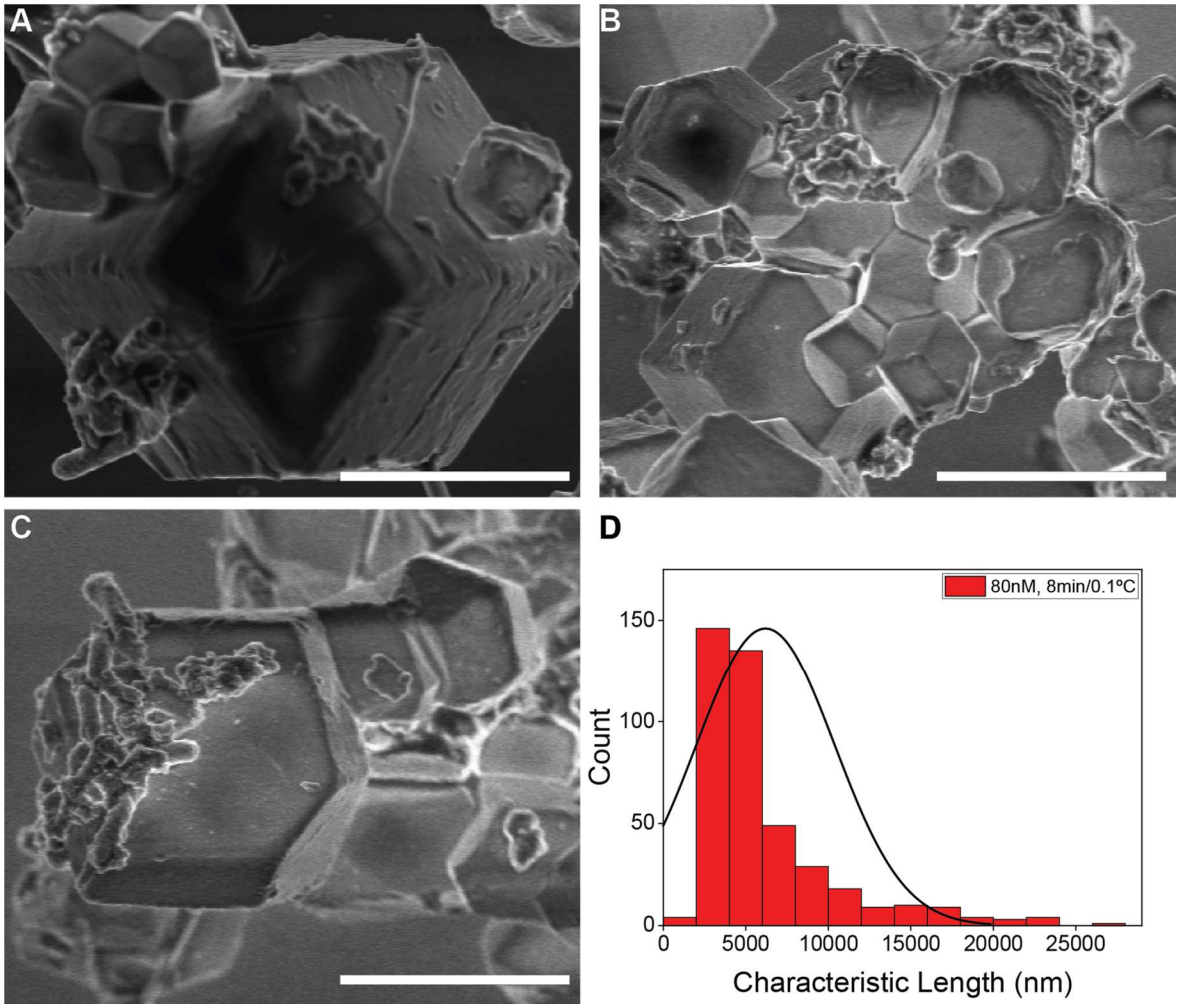

Figure S5-24. (A-C) SEM images of NCTs crystallized with a cooling rate of 8 minute per 0.1 °C and a concentration of 80 nM. Scale bar is 10 microns. (D) Histogram of crystallite sizes with a Gaussian fit.

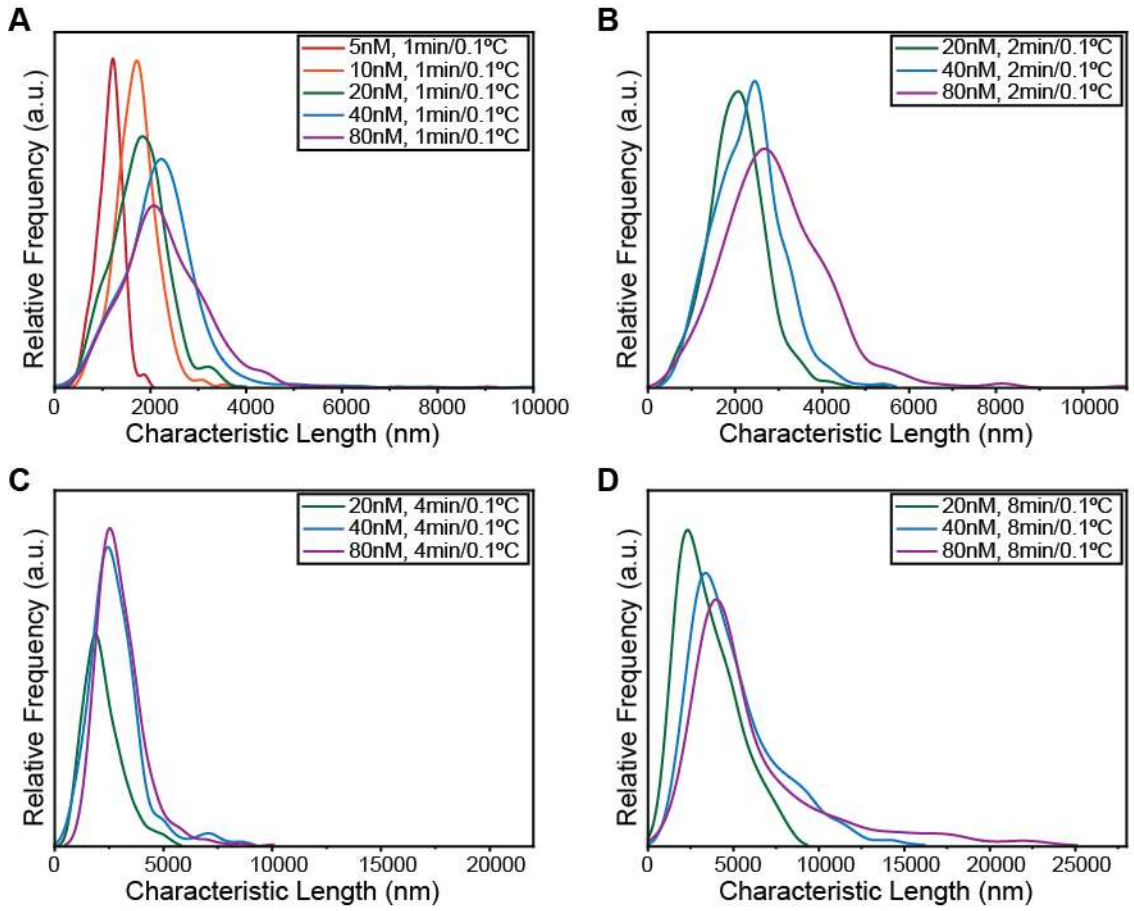

Figure S5-25. Size distribution comparisons as a function of NCT concentration for samples with cooling rate^{-1} of (A) 1min/0.1°C, (B) 2min/0.1°C, (C) 4min/0.1°C, and (D) 8min/0.1°C.

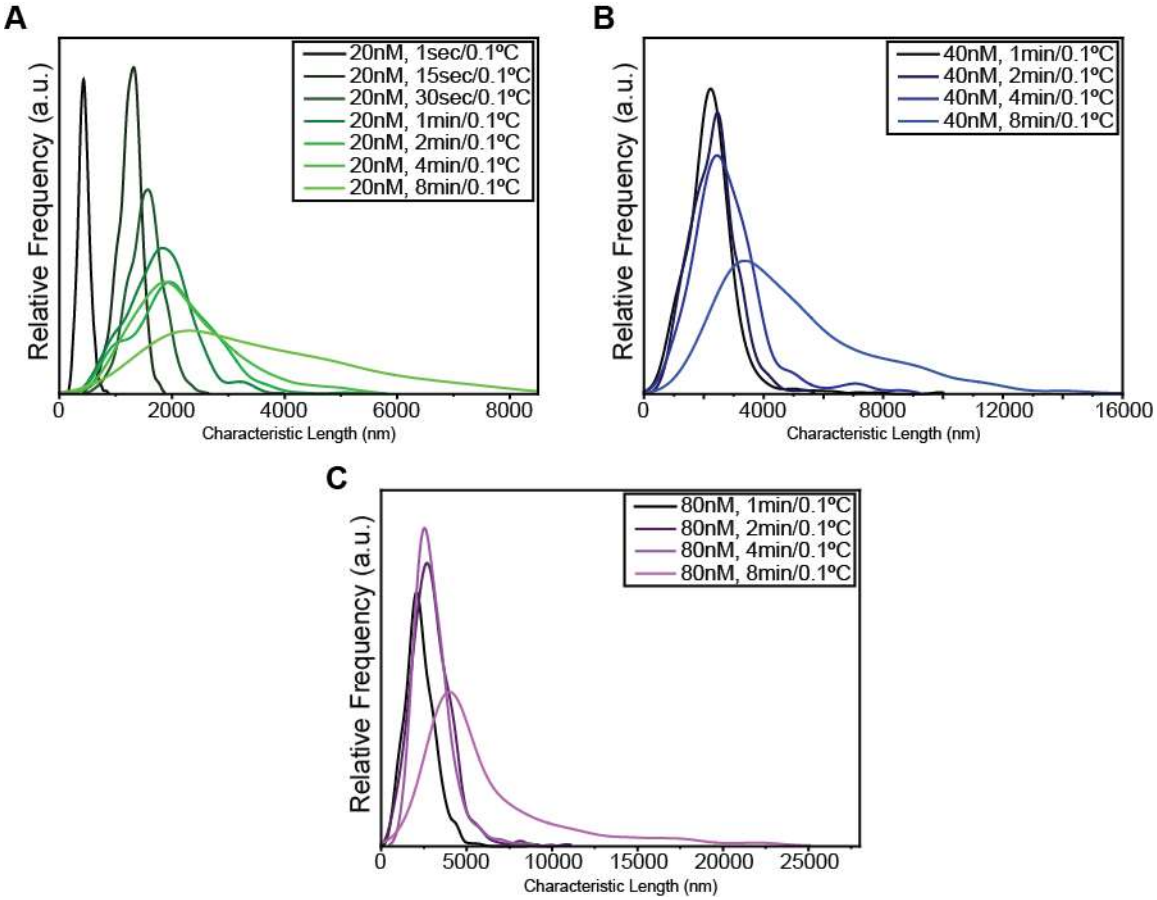

Figure S5-26. Size distribution comparisons as a function of NCT concentration for samples with cooling rate^{-1} of (A) 1min/0.1℃, (B) 2min/0.1℃, (C) 4min/0.1℃, and (D) 8min/0.1℃.

Upon determining that the 80nM, 8min/0.1ºC condition yielded the largest average size crystallites, the sample was searched for its largest crystallites. These crystallites were not included in the size analysis, which consisted of randomly selected regions to image. However, the SEM micrographs of the largest three observed crystallites are included here for reference.

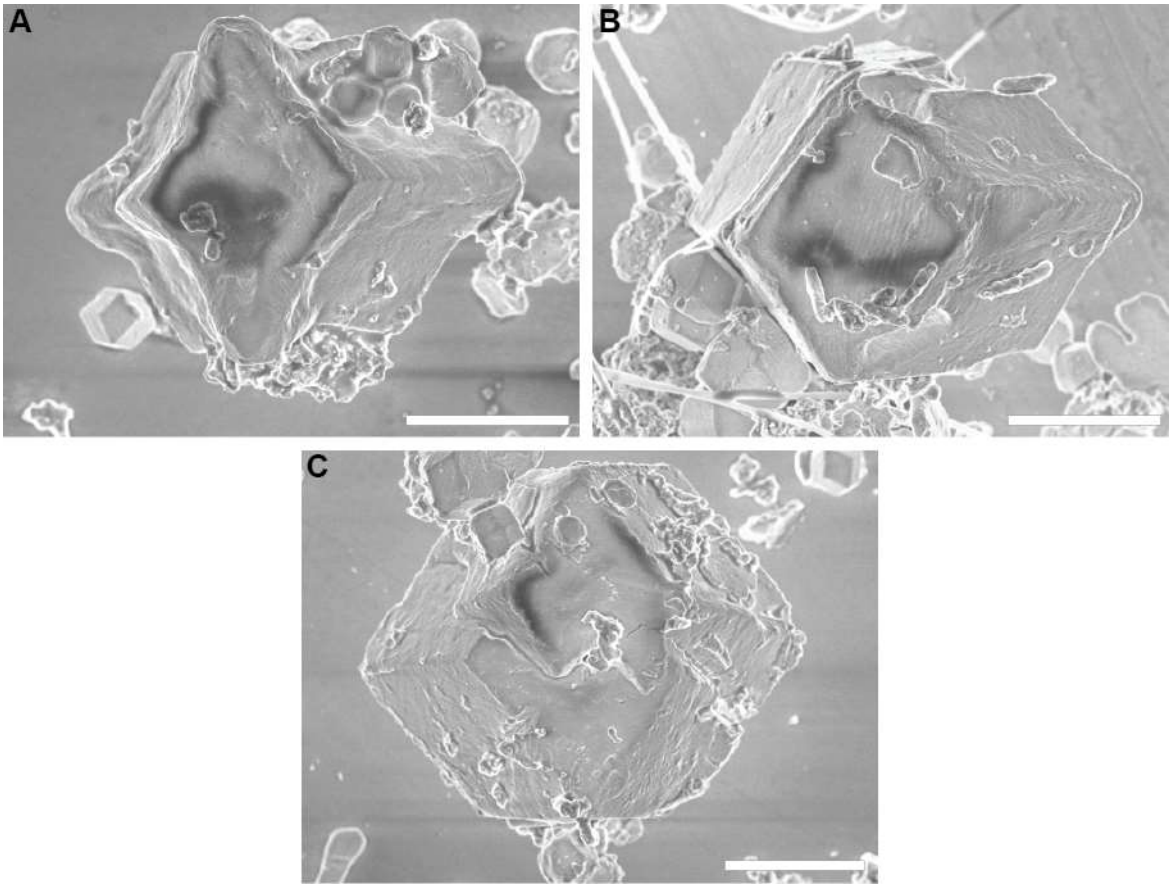

Figure S5-27. SEM micrographs of the three largest observed NCT crystallites (all from the conditions of 80nM and 8min/0.1ºC) with diameters of (A) 28 microns, (B) 29.5 microns, and (C) 31 microns. Scale bars are 10 microns.

A5.6 Model of NCT Crystallization

A5.6.1 Thermodynamics of NCT Assembly

NCTs have multiple weak supramolecular binding groups that collectively form a particle-particle bond. At low temperatures, the nanoparticles form bonds and aggregate together, forming solid-

like assembled state. At higher temperatures, the bonds between particles break, forming a solute-like state of free particles in solution. Previous work[285] has captured this behavior using a simple model that assumes that particles reach an equilibrium between the "assembled" and "free" state via a unimolecular reaction.

$$NCT_a \leftrightarrow NCT_f \tag{S5-4}$$

The quantities of assembled NCTs A and free NCTs F must preserve the total number of particles P

$$A + F = P \tag{S5-5}$$

At equilibrium, the quantities of assembled NCTs A and free NCTs F are also related by the temperature-dependent thermodynamic relation

$$\frac{A}{F} = K = K_0 e^{-\frac{\Delta H}{RT}} \tag{S5-6}$$

The quantities A and F are then given by

$$F = \frac{P}{1+K_0 e^{-\frac{\Delta H}{RT}}} \tag{S5-7}$$

$$A = \frac{P}{1+\frac{1}{K_0 e^{-\frac{\Delta H}{RT}}}} \tag{S5-8}$$

This melt may be monitored using UV-vis data at varying temperatures by assuming particles in the assembled state have an effective extinction coefficient of ϵ_a and particles in the free state have an extinction coefficient of ϵ_f, such that the sample absorptivity may be calculated using the Beer-Lambert law:

$$\alpha_{total} = \epsilon_a * A + \epsilon_f * F \tag{S5-9}$$

$$\alpha_{total} = P\frac{\epsilon_a * K_0 e^{-\frac{\Delta H}{RT}} + \epsilon_f}{1+K_0 e^{-\frac{\Delta H}{RT}}} \tag{S5-10}$$

$$\alpha_{normalize} = \frac{\alpha_{total} - \epsilon_a P}{\epsilon_f P - \epsilon_a P} = \frac{1}{1+K_0 e^{-\frac{\Delta H}{RT}}} \tag{S5-11}$$

This model allows for simple estimation of the enthalpy of the interparticle bonds while accurately capturing several key features of the NCT melt curve: not only the sigmoidal transition from assembled to free particle states, but also the proportional dependence on concentration of the total particle count, allowing for consistent normalized absorptivity curves at varying concentrations (**Figure S5-28**). This is inconsistent with conventional transitions from the solid phase to a

dissolved state; in conventional systems, a solid will dissolve up to a maximum saturation concentration regardless of the quantity of excess solid present, and additional solid material will remain in the solid form rather than dissolving. Instead, for the NCT system, increasing the amount of assembled NCTs in the system will proportionally increase the amount free NCTs in solution, and assembled NCTs added to a system at equilibrium will not remain assembled, but will partially dissociate. To account for this, we propose that NCTs in this "melting window" region behave analogously to a flocculated aggregate, with a thermodynamically determined distribution of aggregate sizes in lieu of a thermodynamically determined solubility in equilibrium with an assembled state.

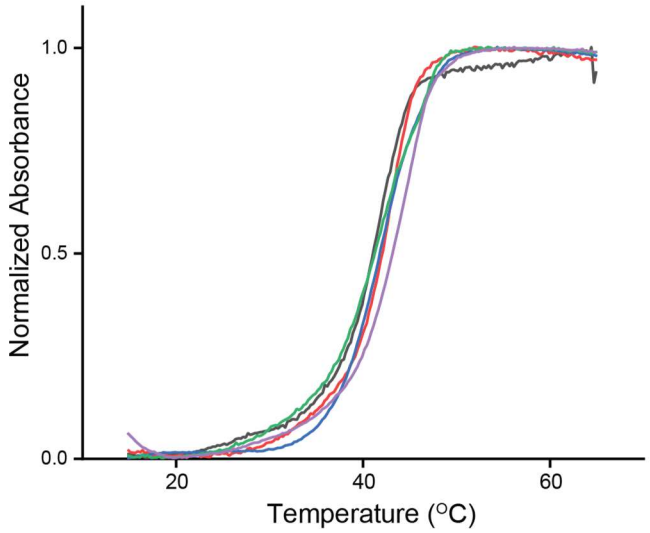

Figure S5-28. Melt curves of 5 separate batches of Au-NCTs. Each experiment was performed at a different concentration, but the curves can be normalized independent of the total particle number due to the proportionality between assembled and free species.

A5.6.2 Cluster Behavior of NCTs

In conventional crystallizing processes, components are initially fully dissolved in solution below the saturation concentration. Nucleation of crystals is initiated when the system transitions from an unsaturated state (in which all components are dissolved) into a supersaturated state, such as by evaporating solvent (which increases the solute concentration in the remaining solvent) or cooling

the system (which lowers the saturation concentration). These nucleated crystals are all approximately the same size: specifically, the minimum size at which the enthalpy of crystallization is sufficient to offset the surface energy penalty. After nucleation, the small crystals continue to grow in the supersatured solution, until the solvent is no longer supersaturated. The number of nucleation events increases with the amount of supersaturation, so increasing the initial concentration will increase the number of crystallites formed, rather than increase the final crystallite size. In fact, the increased nucleation will often decrease the final crystallite size, since nucleation rate typically scales nonlinearly with degree of supersaturation.

Since the NCT system does not exhibit saturation behavior, we must instead develop a mechanism for crystal nucleation and growth that accounts for the NCT's clustering behavior. The thermodynamic distribution of NCT clusters may be approximated by replacing the single unimolecular reaction in Eq. S4 into a series of unimolecular reactions between clusters of increasing size:

$$NCT_1 \leftrightarrow NCT_2 \leftrightarrow \cdots \leftrightarrow NCT_n \leftrightarrow NCT_{n+1} \ldots$$

We may approximate the equilibrium constant between clusters as equivalent, since each reaction corresponds to the addition of an identical nanoparticle subunit. This allows us to express P_n, the quantity of nanoparticles in clusters of size n, by the expression:

$$\frac{P_{n+1}}{P_n} = K \rightarrow \frac{P_n}{P_1} = K^{n-1} \tag{S5-12}$$

Where P_1 corresponds to the quantity of nanoparticles in clusters of size 1 (i.e. isolated nanoparticles), and K is the equilibrium constant between cluster reactions.

For K<1 (conditions that favor dissociation), this value may be normalized with a sum over all cluster sizes

$$P_n = \frac{K^{n-1}}{\sum_{m=1}^{\infty} K^{m-1}} = K^{n-1}(1-K) \tag{S5-13}$$

As expected, larger cluster sizes are favored as K approaches 1, causing the distribution to broaden outwards (**Figure S5-29**, blue curves). However, for K>1, the distribution inverts as larger clusters become thermodynamically preferred, and the distribution is no longer normalizeable (**Figure S5-29**, red curves). This distribution is also nonphysical, as it predicts infinite particles in clusters of infinite size. However, if we truncate the distribution to a maximum cluster size N, such as the total number of particles in the system, the model remains both physical and renormalizeable.

$$P_n = \frac{K^{n-1}}{\sum_{m=1}^{m=N} K^{m-1}} = K^{n-1}\frac{1-K}{1-K^N} \tag{S5-14}$$

For K<1, this system reduces to the unbound distribution as $N \to \infty$. For K>1, the cluster population rapidly collapses to the upper bound cluster size. For example, a system with maximum cluster size of 1000 is shown to be highly sensitive to population inversion, with dramatic shift towards clustered state upon equilibrium constant K shifting from 0.99 to 1.01.

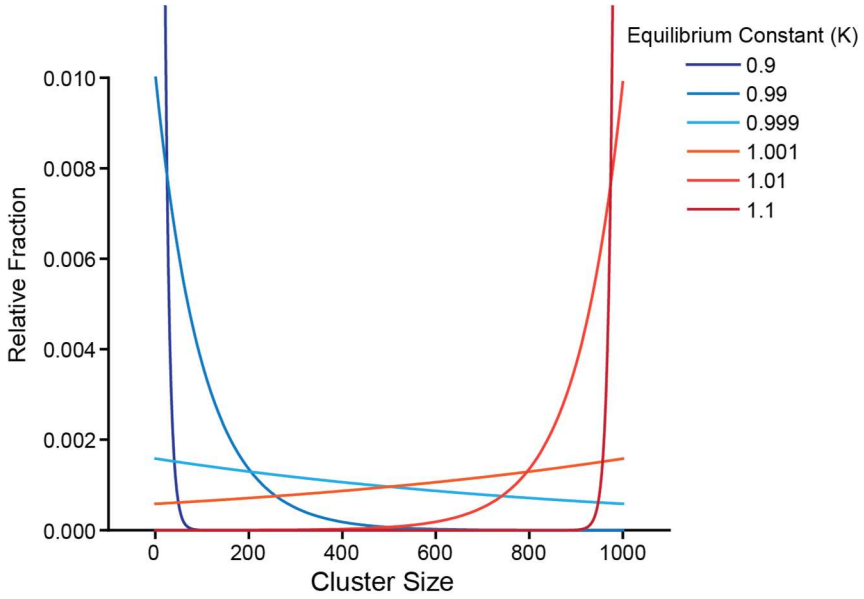

Figure S5-29. Effect of the NCT equilibrium constant (K) on cluster size. For values of K below 1 (blue curves), the system strongly tends toward smaller clusters, or entirely free particles. Conversely, for values of K above 1 (red curves), the distribution rapidly inverts to favor larger aggregates.

This suggests that, in contrast to classical nucleation, there is no metastable barrier to nanoparticle aggregation. When decreasing temperature causes K to increase above 1, the particles are free to smoothly invert their cluster size distribution, and ultimately collapse into the maximum cluster size.

To confirm consistency with the observed melt curves, we may estimate the absorptivity of these clusters. The quantity of we may consider the quantity of clusters of size n

$$C_n = \frac{P_n}{n} \tag{S5-15}$$

We may approximate the absorptivity of each cluster size by scaling with the cross-sectional area of the cluster,

$$\epsilon_n \sim \epsilon_1 n^{\frac{2}{3}} \quad \text{(S5-16)}$$

Then the measured absorptivity α_{total} would be given by the sum of contributions of each cluster size

$$\alpha_{Total} = \sum_{n=1}^{\infty} C_n \epsilon_n = \epsilon_1 P \sum_{n=1}^{N} K^{n-1} \left(\frac{1-K}{1-K^N}\right) n^{-\frac{1}{3}} \quad \text{(S5-17)}$$

We may compare the normalized absorptivity generated by the cluster kinetic model and the existing coarse model, to real NCT melt data, and find that the general shape is in good agreement (**Figure S5-30**).

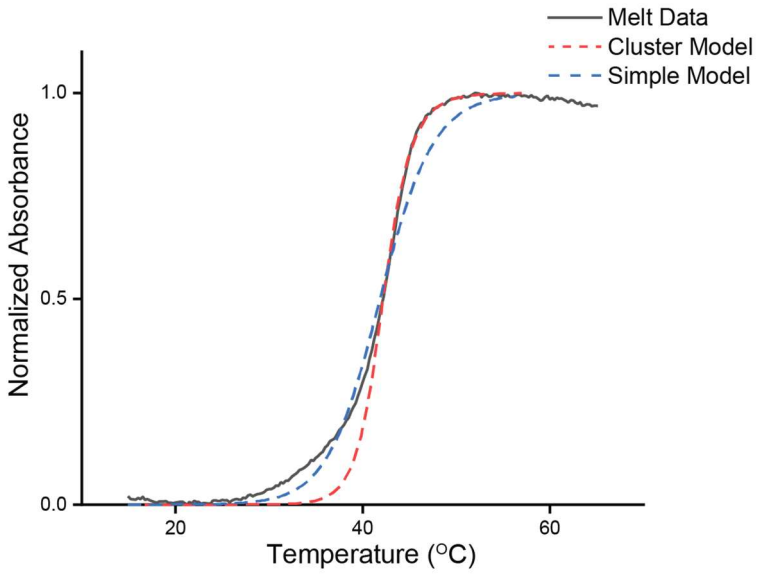

Figure S5-30. The cluster model matches the general lineshape of the real melt data. The representative graphs were manually generated using nonphysical values.

A5.6.3 Diffusion in NCT Crystallization

For the system at thermodynamic minimum, the maximum cluster size would correspond to the total number of particles present in the system. However, it is not kinetically feasible for the particles to all assemble into a single aggregate. Instead, we limit the maximum number of particles per cluster by the ability of nanoparticles to diffuse between clusters, resulting in an "interaction volume" that collapses when K>1 rather than the full volume of the system. This interaction volume may be estimated by calculating the characteristic diffusion length of a nanoparticle, given by:

$$l = \sqrt{Dt} \quad \text{(S5-18)}$$

Where D is the diffusivity of the particle and t is the characteristic diffusion time of the system. If the particle clusters "collapse" during a finite window of temperature with range W, while cooling at a reciprocal rate of τ, then the characteristic time may be approximated as:

$$t \approx W\tau \tag{S5-19}$$

The interaction volume V may then be calculated by the sphere with radius equal to the characteristic diffusion length, corresponding to the ability for other particles to diffuse towards each other from opposite ends of the sphere

$$V = \frac{4}{3}\pi l^3 = \frac{4}{3}\pi = \frac{4}{3}\pi D^{\frac{3}{2}} W^{\frac{3}{2}} \tau^{\frac{3}{2}} \tag{S5-20}$$

The cluster size N is then given by the collapse of all particles in an interaction volume

$$N = cV = \frac{4}{3}\pi W^{\frac{3}{2}} * c\tau^{\frac{3}{2}} \tag{S5-21}$$

Where c is the total concentration of particles in solution.

5.6.4 Prediction of Trends

Given that the crystallite volume scales with the number of particles in the crystallite, the 1D characteristic crystal size L then scales with

$$L \sim N^{\frac{1}{3}} \sim c^{\frac{1}{3}} \tau^{\frac{1}{2}} \tag{S5-22}$$

This is consistent with the observed data for concentration and reciprocal rate (**Figure S5-31**). This model also predicts relationships between other parameters which may be used to alter crystal size, such as the breadth of the melting window (which may be controlled by binding group loading) or particle diffusivity (which may be controlled by particle size). However, these parameters are correlated to other factors in the system, such as melting temperature, and so were beyond the scope of this current work.

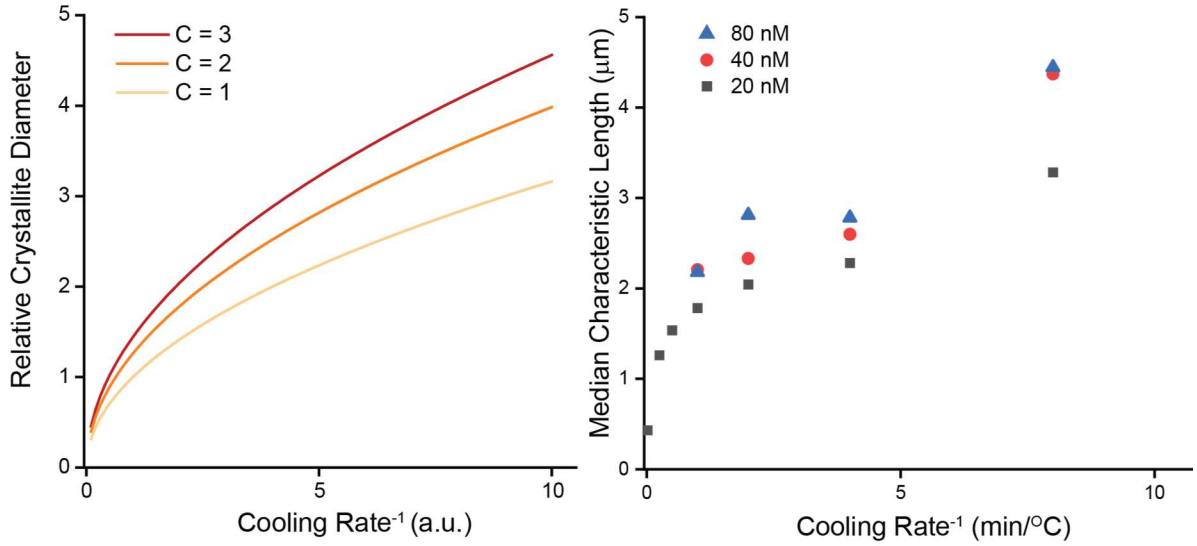

Figure S5-31. Comparison of trends between the NCT crystallization model using non-physical values for concentration, rate, and diameter (left), and the data reported in this manuscript (right, adopted from Fig. 2 in the main text). The trends in the model are consistent with the experimental data.

A5.7 Sintering NCTs

To sinter NCT crystallites into macroscopic solids, they were loaded into a microcentrifuge tube, and centrifuged for 10 minutes at 20,000 RCF. Other speeds were also effective, but gave a less dense microstructure. Moreover, the sintering process was only effective while the brush was in toluene, likely because in the collapsed state new hydrogen bonds were slower to form (**Figure S5-32**). After centrifuging the sample underwent the standard polymer brush collapse, and were allowed to dry.

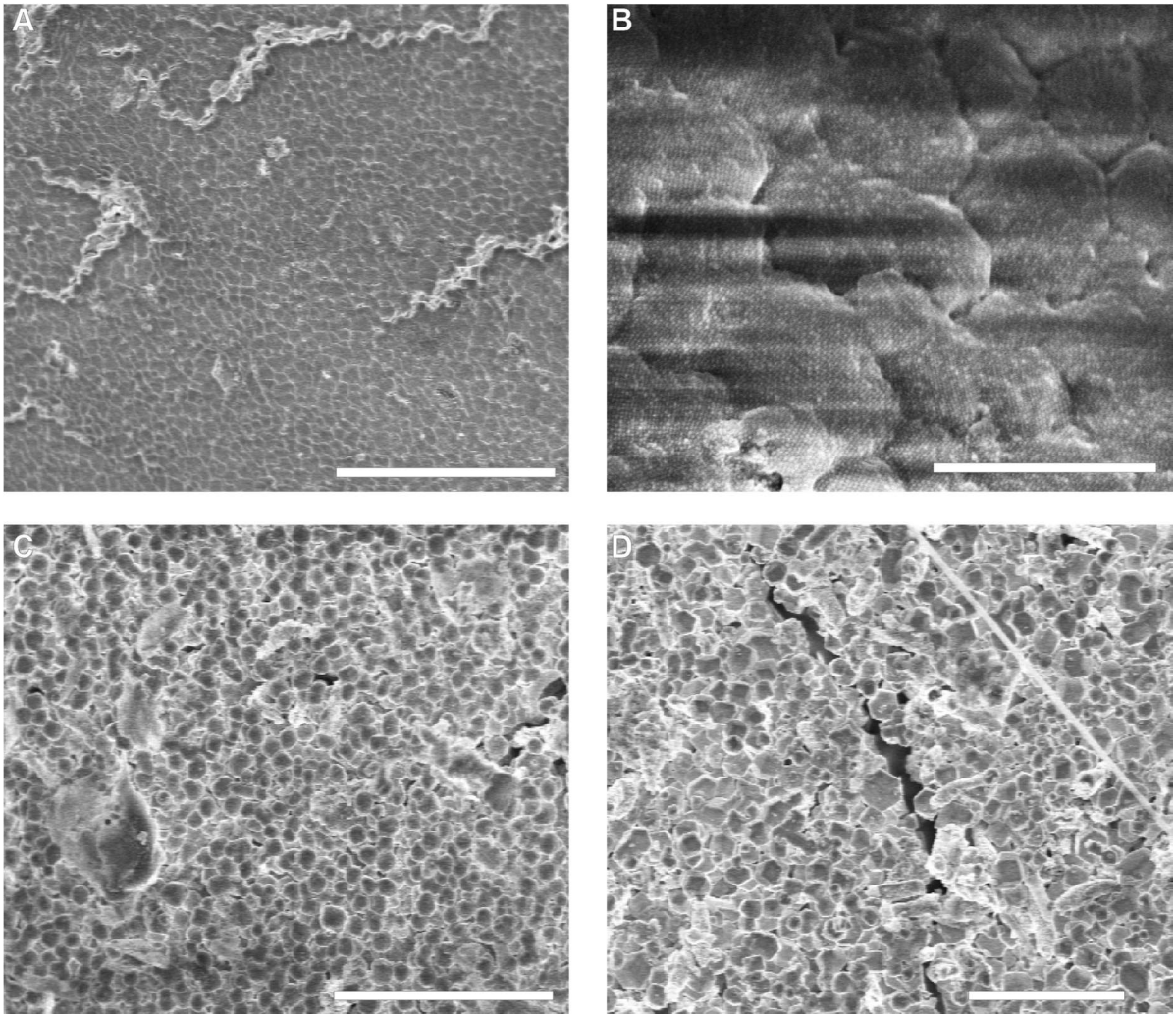

Figure S5-32. Effect of sintering conditions on NCT microstructure. (A) NCTs centrifuged at 20,000 RCF in toluene. (B) Closer image of the sintered solid in A. (C) NCTs centrifuged at 10,000 RCF in toluene. The sintered solid appeared to be continuous and could be manipulated by hand, but the microstructure is less compact. (D) NCTs centrifuged at 20,000 RCF in n-Decane. The material prepared from n-Decane was significantly less compact. It was not powder like, and did not separate upon being exposed to air flow, but it could not withstand physical contact. The scale bars of A, C, and D are 10 microns, the scale bar of B is 1 micron.

The mixes between Au and IO-NCTs were prepared in the same fashion, with the IO-NCTs added to the Au-NCTs before sintering, and mixed with a pipette. Note, the concentration of IO-NCTs is significantly higher than that of Au-NCTs. Consequently, CsCl lattices formed slightly rounded shapes instead of polyhedral, and the sintered solids were predominantly IO-NCTs. For the CsCl

NCTs, the excess IO-NCTs were removed with a syringe before any further processing. SAXS and SEM imaging of the crystallites used to make the sintered solids in the main text are presented in **Figure S5-40** and **Figure S5-39**. Optical images of the solids are presented in **Figure S5-42**.

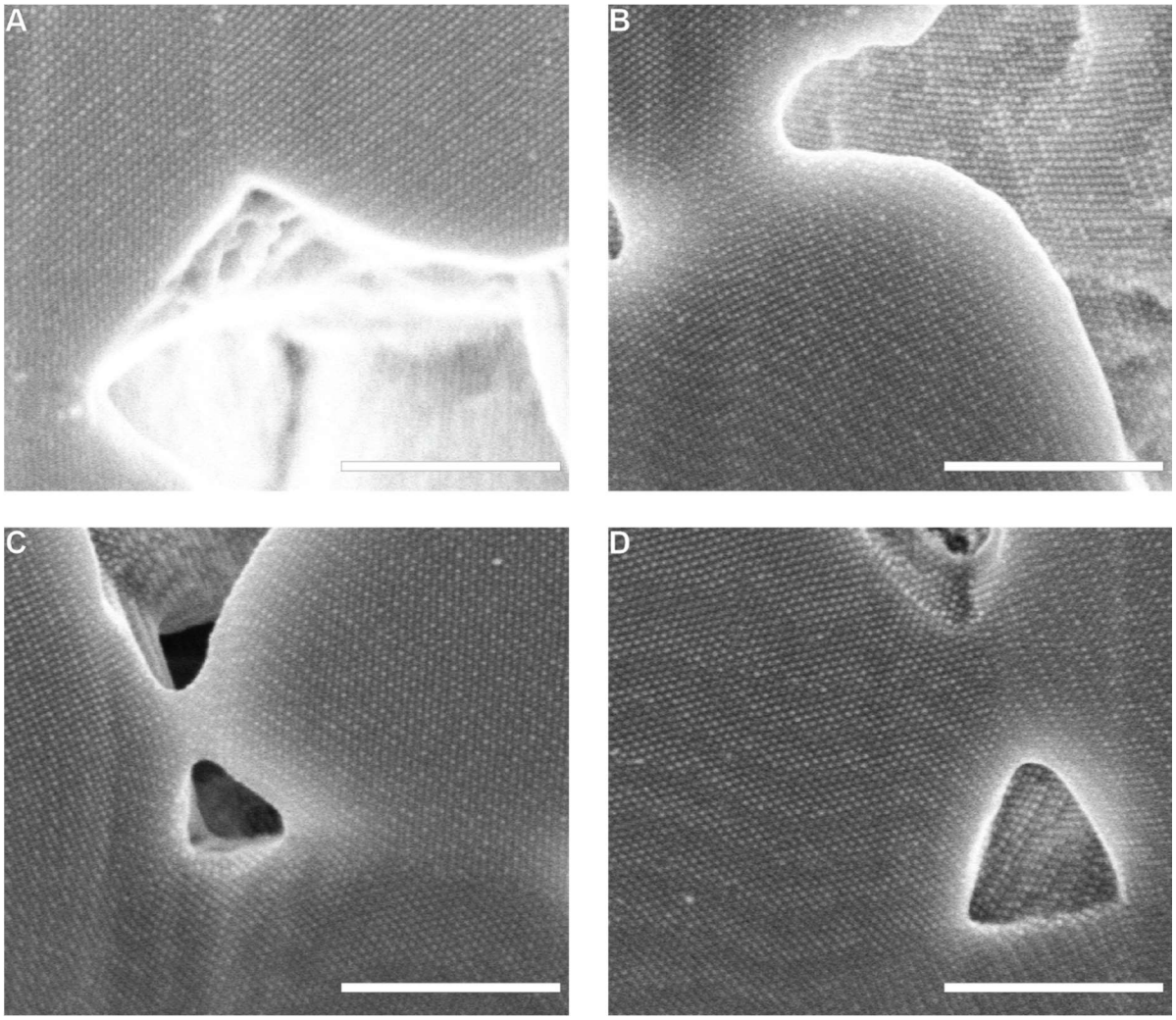

Figure S5-33. Examples of necking and crystallite deformation observed in the "slower cooled" sintered sample with larger grain sizes. Scale bars for all images are 500 nm.

A5.7.1 Cross-Sections

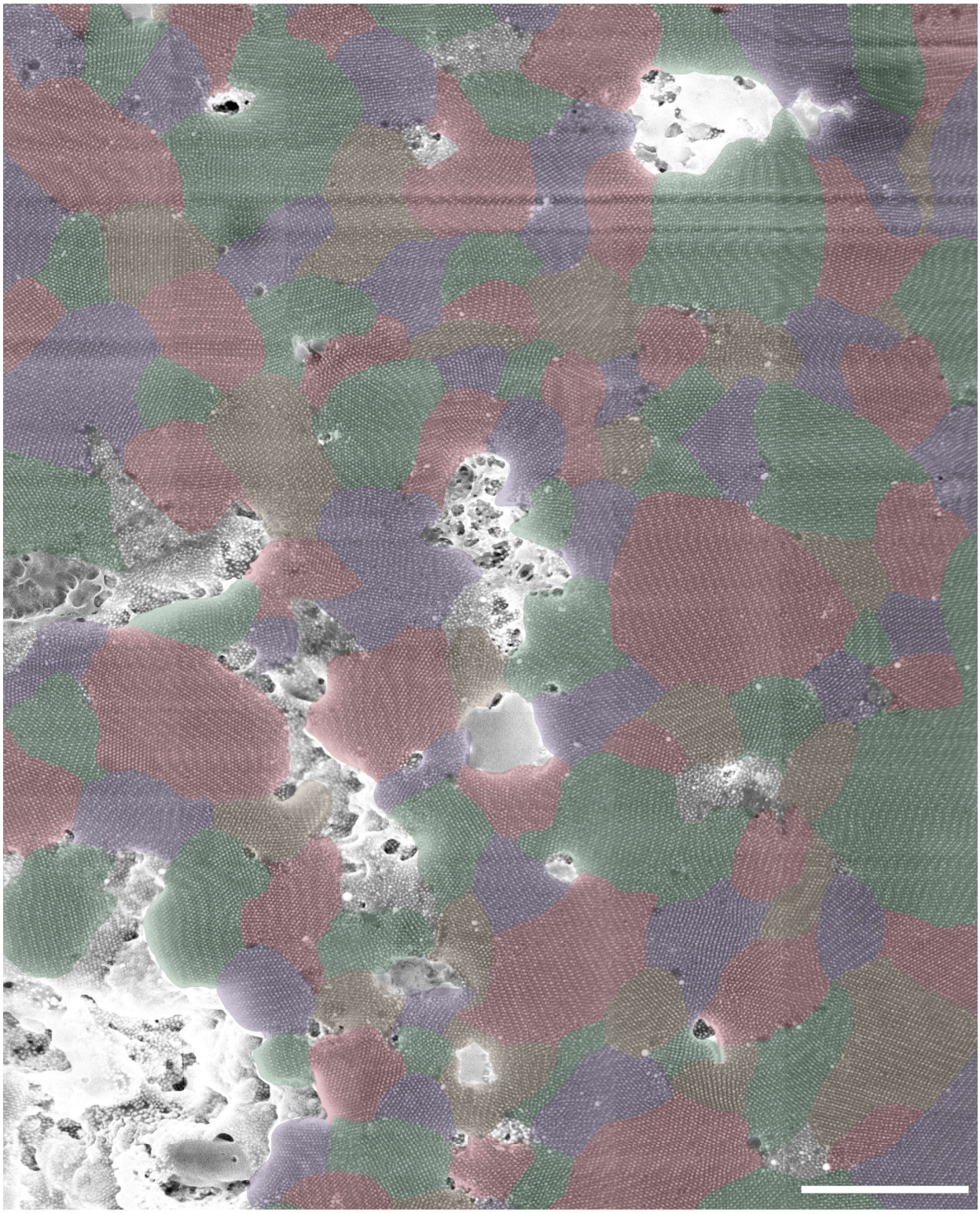

Figure S5-34. FIB cross-section of Au-NCTs rapidly cooled (15s / 0.1°C) and sintered into solids. Overlaid colors highlight grains of different orientations. Scale bar is 1 micron.

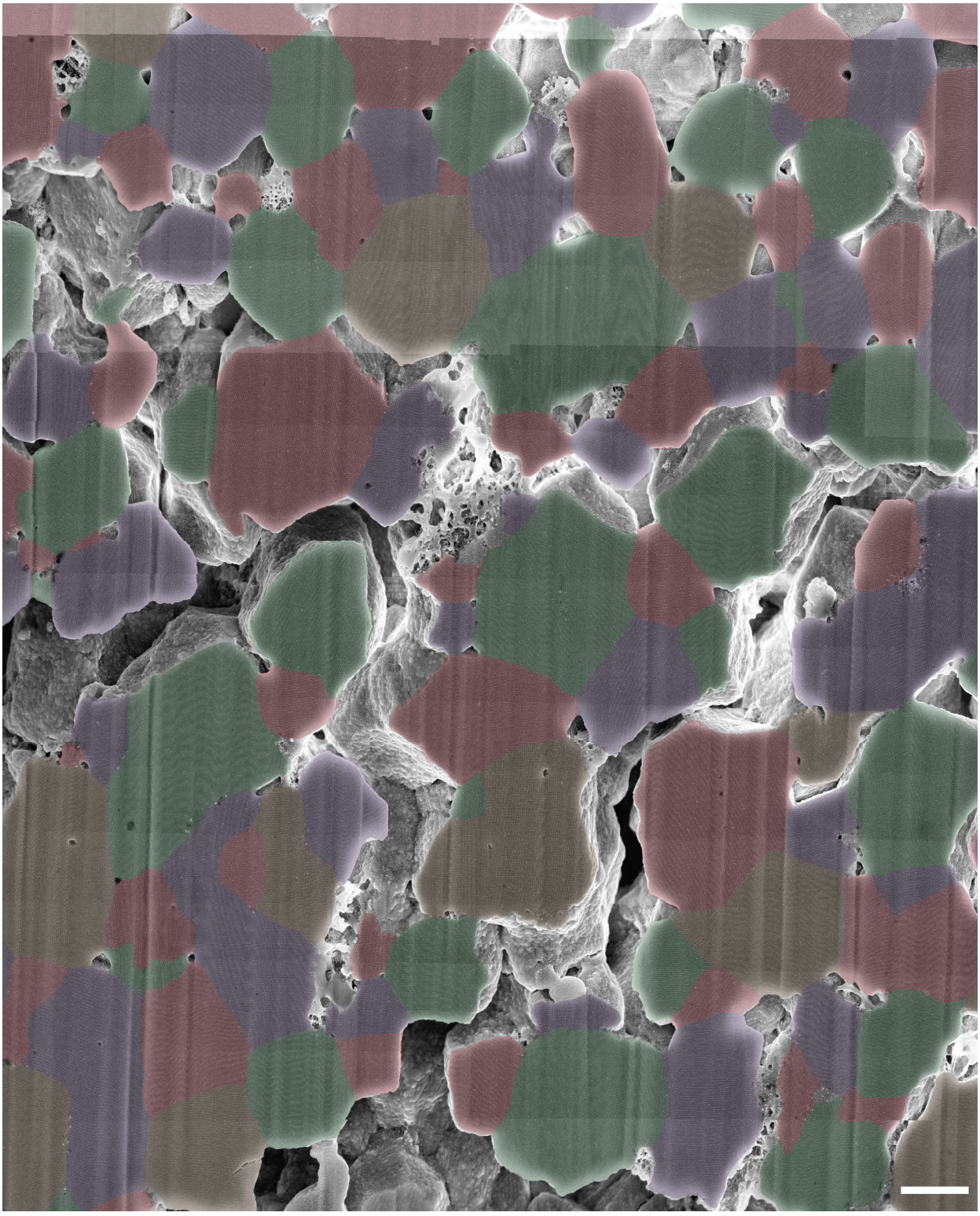

Figure S5-35. FIB cross-section of Au-NCTs slowly cooled (4 min/ 0.1°C) and sintered into solids. Overlaid colors highlight grains of different orientations. Scale bar is 1 micron.

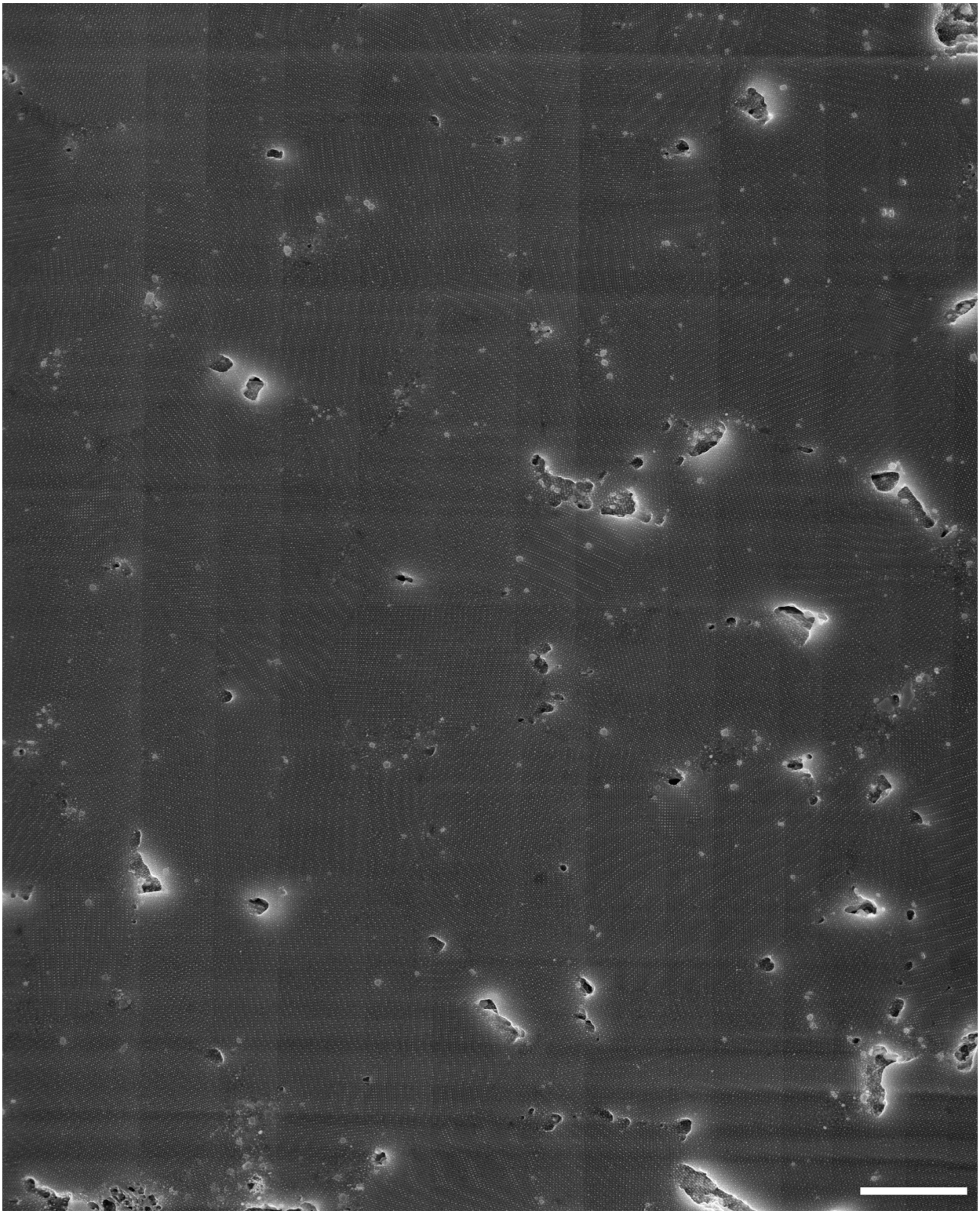

Figure S5-36. FIB cross-section of Au-NCTs and IO-NCTs coassembled into a CsCl lattice and sintered into solids. Light particles are Au-NCTs, dark ones are IO-NCTs. Scale bar is 1 micron.

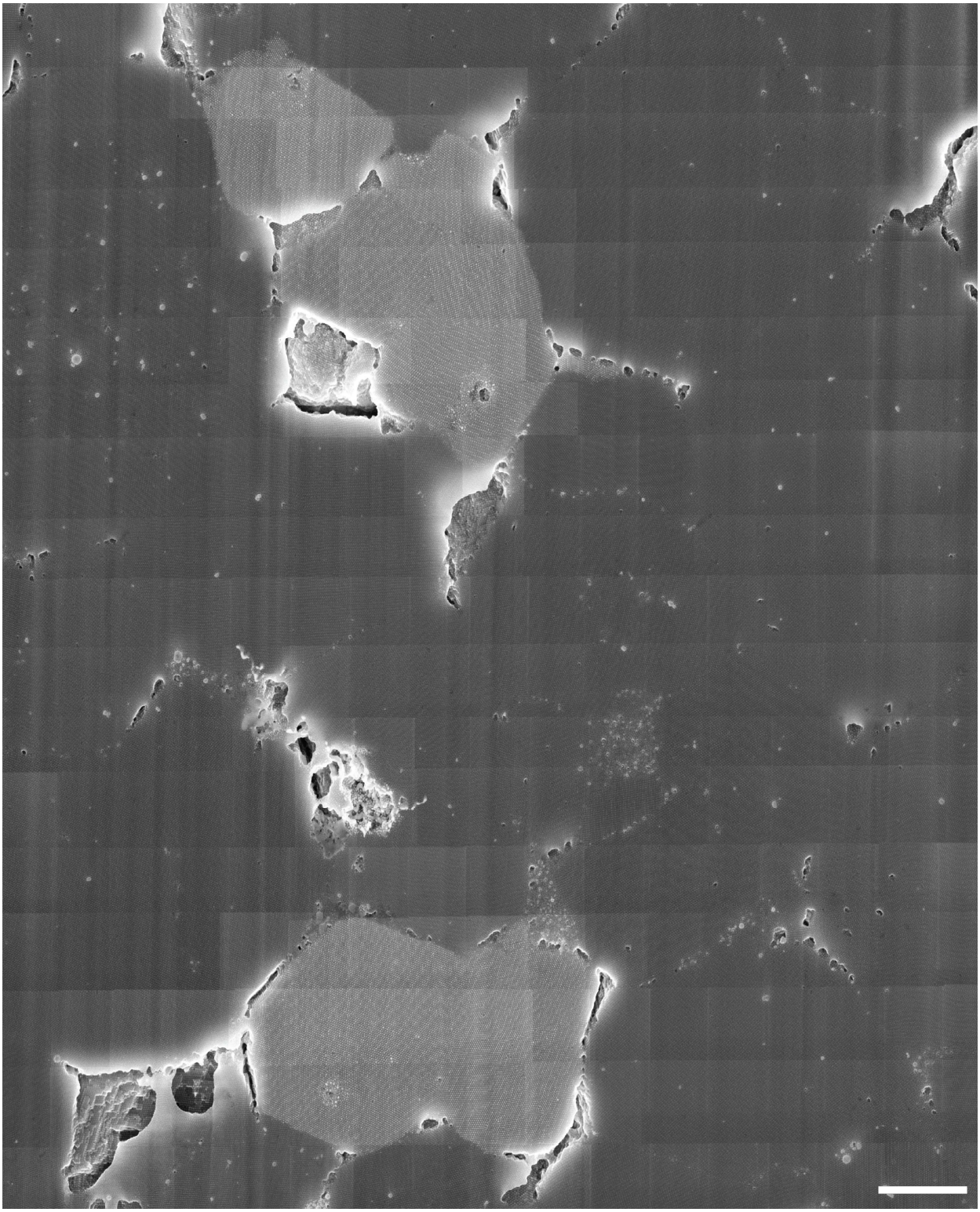

Figure S5-37. FIB cross-section of Au-NCTs and IO-NCTs assembled into bcc lattices, blended together, and sintered into solids. Dark regions are IO-NCTs, bright regions are Au-NCTs. Scale bar is 1 micron.

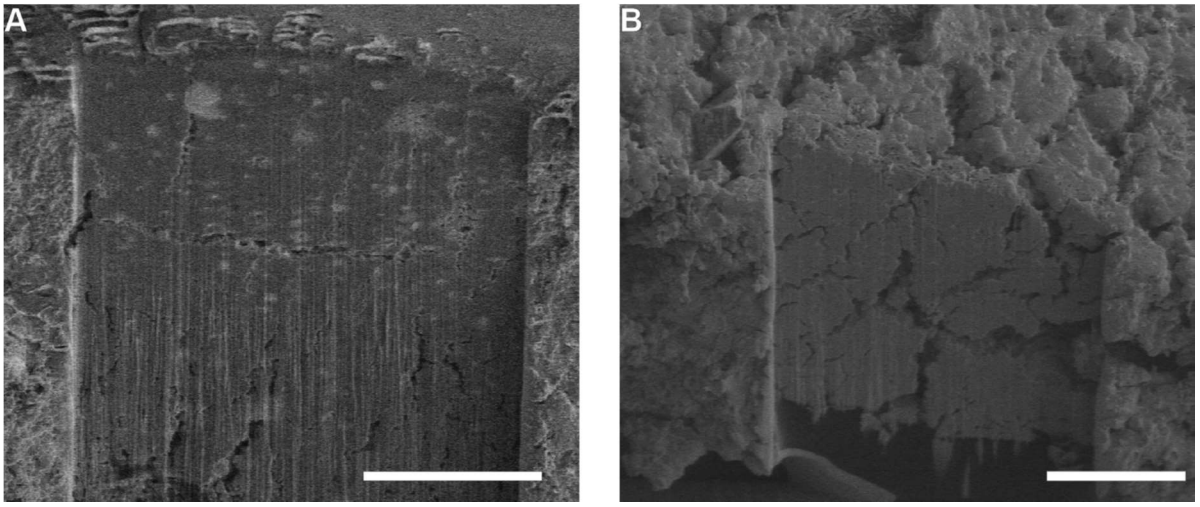

Figure S5-38. Lower magnification images of the FIB cross sections of the fast cooled (A) and slow cooled (B) sinter NCT samples featured in Figure 3. Scale bar for each image is 20 microns.

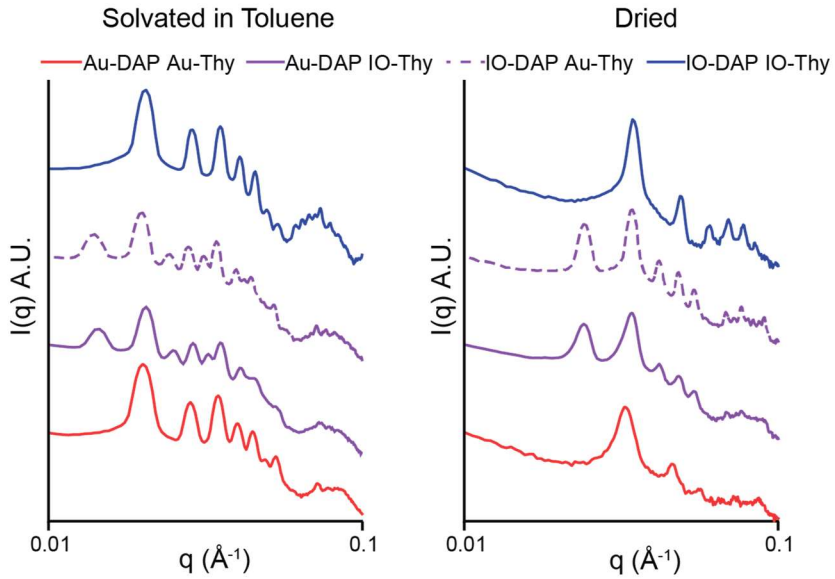

Figure S5-39. SAXS of NCT crystallites prepared with Au-NCTs (red), IO-NCTs (blue), or mixtures of Au and IO-NCTs (purple). Note that the mixed samples show a larger number of peaks, indicating they have formed a CsCl lattice. These samples were then used to prepare the sintered solids in the main text.

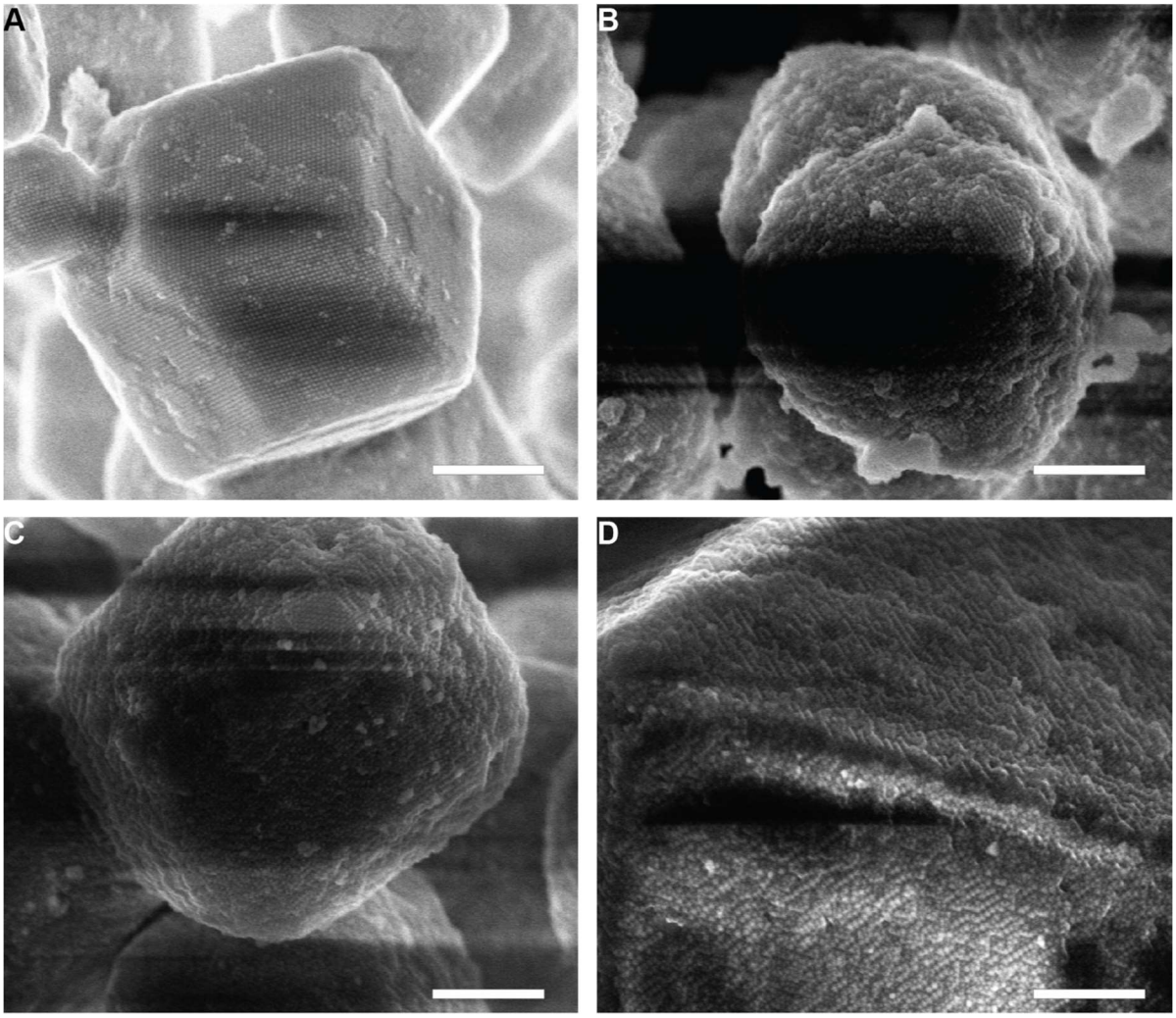

Figure S5-40. NCTs prepared with different nanoparticle cores, before they were sintered together in the experiments featured in **Figure 6-3** in the main text. (A) NCT crystals prepared entirely with AuNPs. (B) NCT crystals made from DAP functionalized AuNPs and Thy functionalized IONPs. (C) NCT crystals made from the coassembly of DAP functionalized IONPs and Thy functionalized AuNPs. (D) NCT crystals made entirely of IONPs. All scale bars are 500 nm.

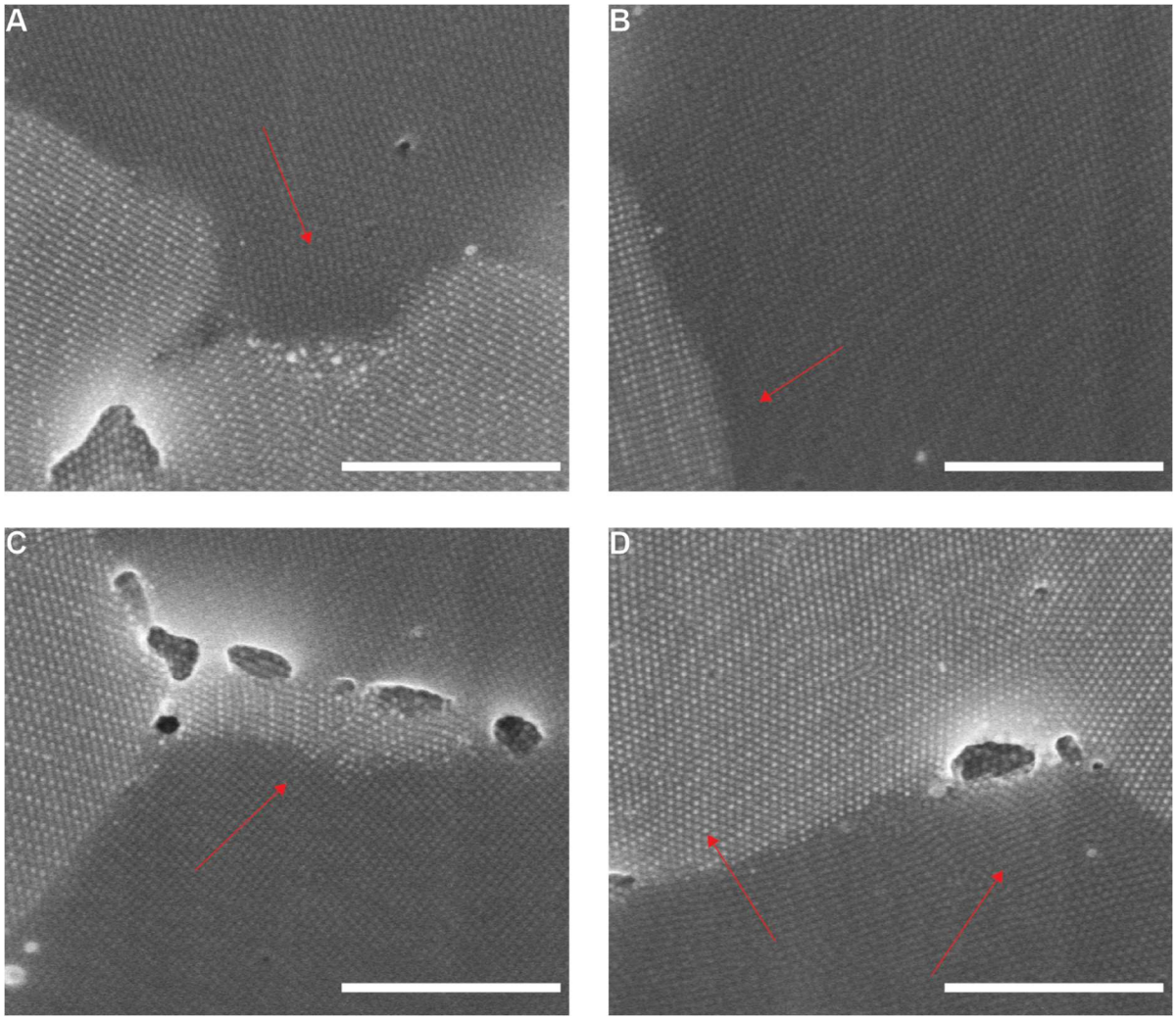

Figure S5-41. The experiments in this work did not provide conclusive evidence for grain boundary diffusion during sintering, but experiments with blended IO and Au NCTs allowed for visualization of the interface between crystallites. In several regions, significant distortions of the lattice were observed, suggesting some degree of grain boundary diffusion may be possible under the correct processing conditions. (A) A small segment of IO-NCTs between two Au-NCT crystallites deforms to match the neighboring grains. (B) Lattice strain appears to orient the NCTs to align at the interface. (C) A small segment of Au-NCTs orienting to match the surrounding IO-NCTs. (D) Lattice strain in both IO and Au NCTs. Scale bars for all images are 500 nm.

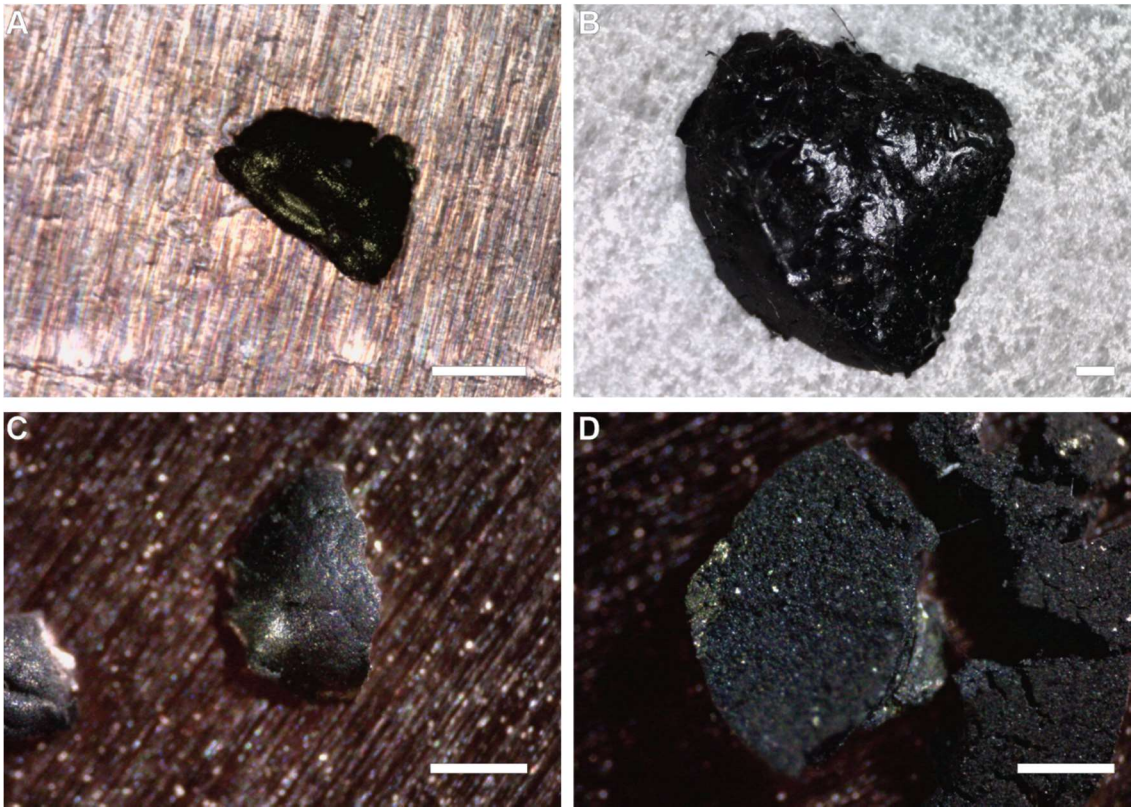

Figure S5-42. Optical images of sintered NCTs with different compositions. (A) Gold NCTs in a bcc lattice (B) Iron oxide NCTs in a bcc lattice (C) Gold and Iron Oxide NCTs in a CsCl Lattice (D) Blend of Gold NCTs in a bcc lattice and Iron Oxide NCTs in a bcc lattice. All scale bars are 0.5 mm.

A5.8 Mechanically Shaping NCTs

To prepare the mechanically shaped NCTs, first a sintered solid was prepared from IO-NCTs using the abovementioned procedure (**Figure S5-43**). The sample was then placed into a polyoxymethylene mold (**Figure S5-44**), cut with a laser cutter, and 500 Newtons applied to it for 1 hour.

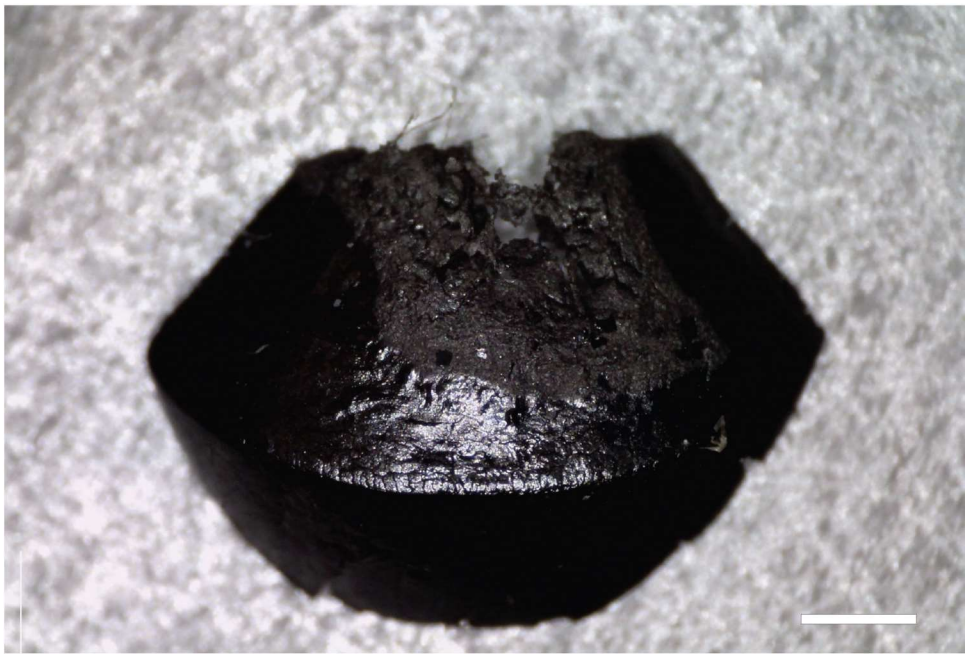

Figure S5-43. Optical image of a sintered IO-NCT solid that was then pressed into a mold to form the mechanically shaped NCT materials. Scale bar is 1 mm.

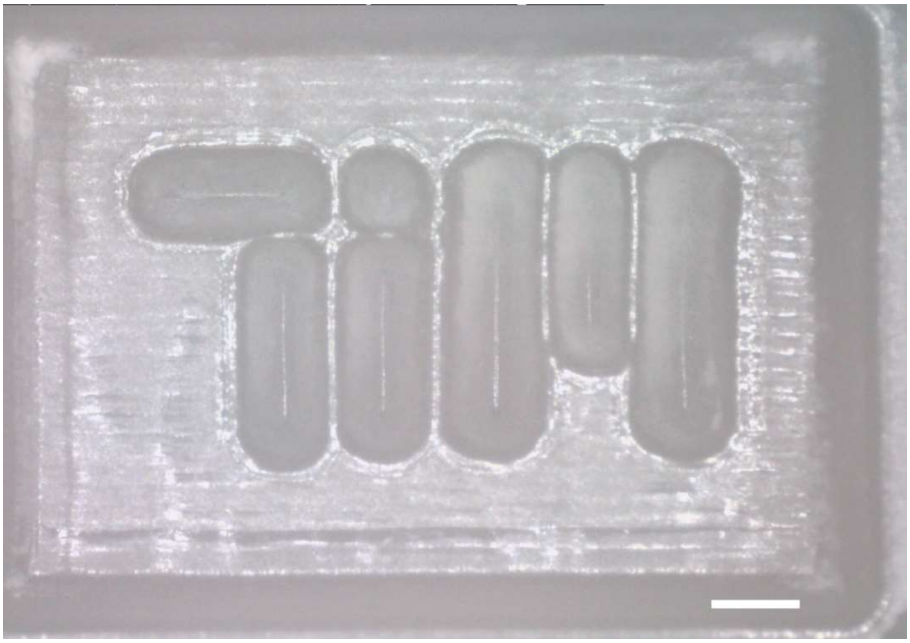

Figure S5-44. Optical image of the mold used to mechanically shape the NCT solids. Scale bar is 0.5 mm.

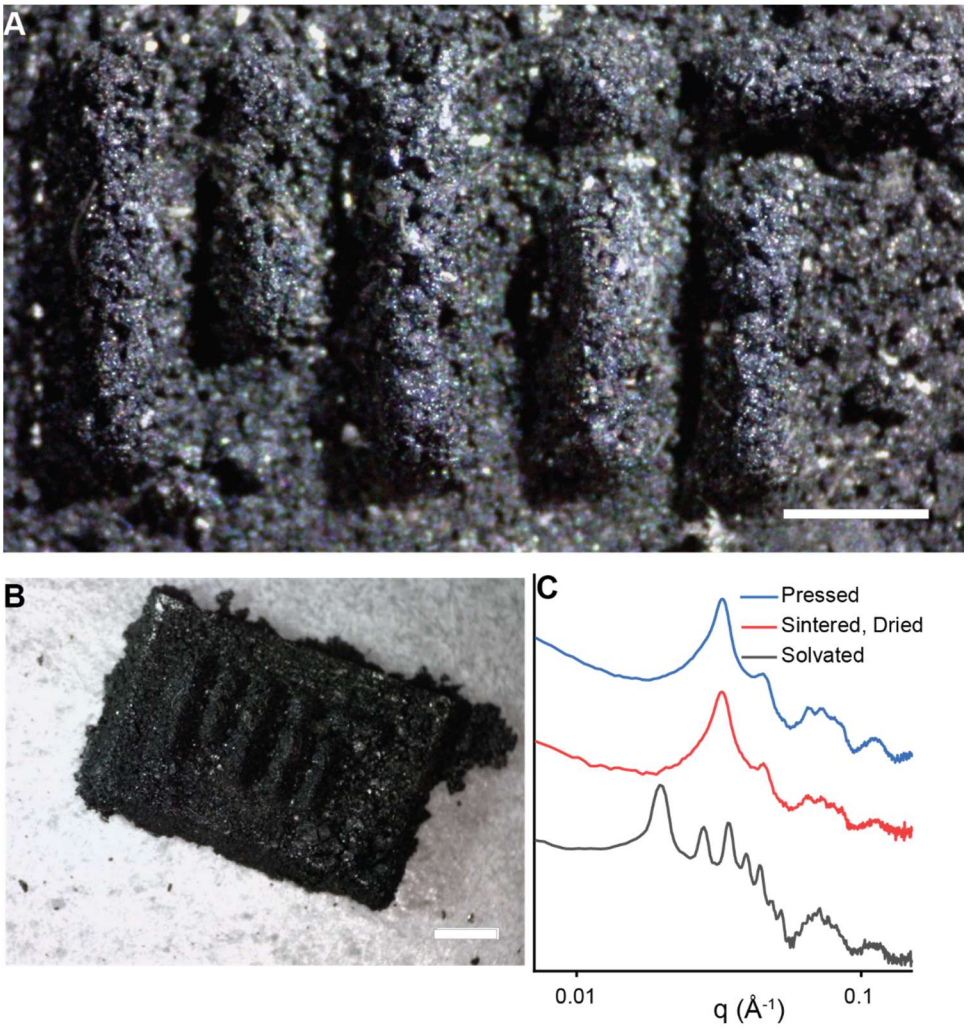

Figure S5-45. Mechanically processed NCT solids can also be created from NCTs with 13 kDa polymers. (A and B) Optical images of the NCT solid. Scale bars are (A) 0.5 mm and (B) 1 mm. (C) SAXS demonstrating the material retains its crystallinity throughout its processing. Ordering was slightly less well maintained in this sample than ones prepared with a shorter polymer brush, likely because the softer NCTs are more capable of deforming during sintering.

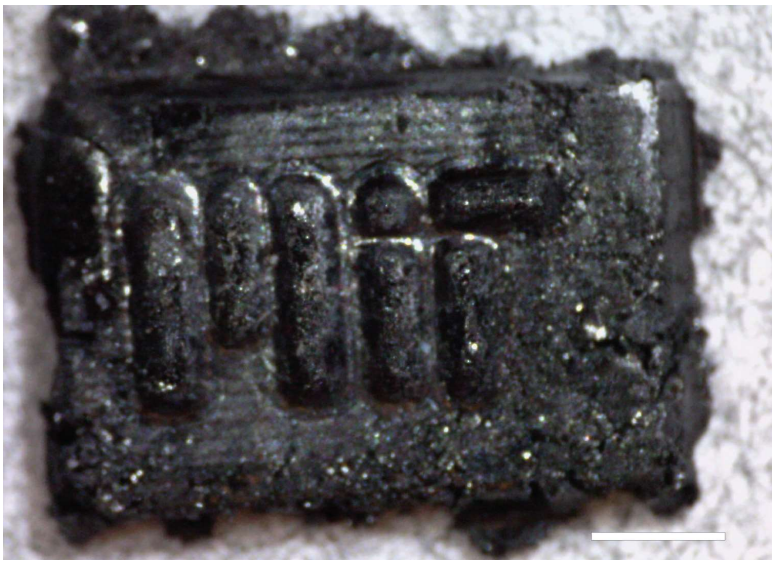

Figure S5-46. Optical image of a mechanically processed NCT solid made with 16 nm IO NPs and 8 kDa polymer. This is a lower magnification image of the picture used in Figure 1 of the main text. Scale bar is 1 mm.

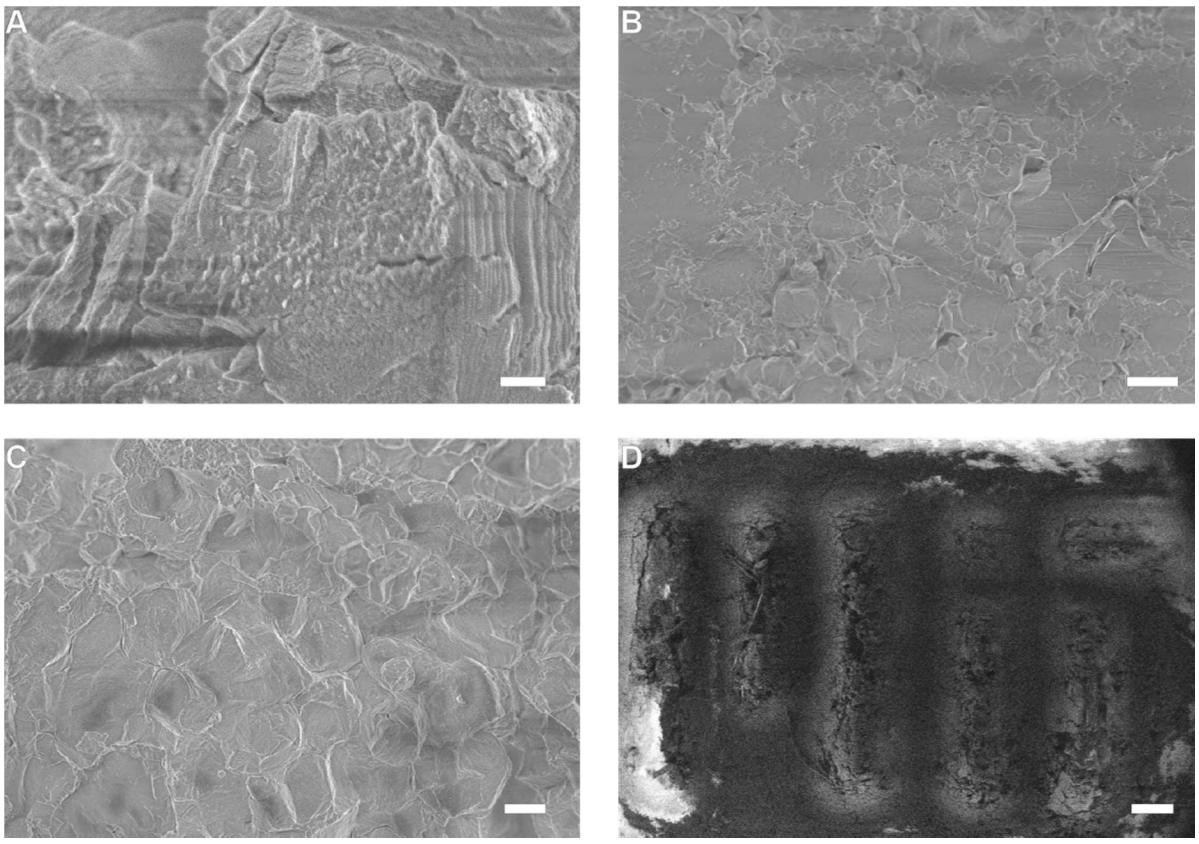

Figure S5-47. SEM micrographs of the mechanically processed NCT solid. (A) High magnification image with visible particles. Scale bar 400 nm. (B) Lower magnification image of the area in (A). Scale bar 10 microns. (C) Image of a rougher region where Wulff polyhedra are still visible. Scale bar 4 microns. (D) SEM image of the MIT school logo. Scale bar 200 microns.

Appendix 6. References

(1) Balazs, A. C.; Emrick, T.; Russell, T. P. Nanoparticle Polymer Composites: Where Two Small Worlds Meet. *Science* **2006**, *314* (5802), 1107–1110. https://doi.org/10.1126/science.1130557.

(2) Beniash, E. Biominerals—Hierarchical Nanocomposites: The Example of Bone. *Wiley Interdiscip. Rev. Nanomed. Nanobiotechnol.* **2011**, *3* (1), 47–69. https://doi.org/10.1002/wnan.105.

(3) Reznikov, N.; Bilton, M.; Lari, L.; Stevens, M. M.; Kröger, R. Fractal-like Hierarchical Organization of Bone Begins at the Nanoscale. *Science* **2018**, *360* (6388), eaao2189. https://doi.org/10.1126/science.aao2189.

(4) Gong, T.; Xie, J.; Liao, J.; Zhang, T.; Lin, S.; Lin, Y. Nanomaterials and Bone Regeneration. *Bone Res.* **2015**, *3*, 15029. https://doi.org/10.1038/boneres.2015.29.

(5) Snow, M. R.; Pring, A. The Mineralogical Microstructure of Shells: Part 2. The Iridescence Colors of Abalone Shells. *Am. Mineral.* **2005**, *90* (11–12), 1705–1711. https://doi.org/10.2138/am.2005.1788.

(6) Rousseau, M.; Lopez, E.; Stempflé, P.; Brendlé, M.; Franke, L.; Guette, A.; Naslain, R.; Bourrat, X. Multiscale Structure of Sheet Nacre. *Biomaterials* **2005**, *26* (31), 6254–6262. https://doi.org/10.1016/j.biomaterials.2005.03.028.

(7) Finnemore, A.; Cunha, P.; Shean, T.; Vignolini, S.; Guldin, S.; Oyen, M.; Steiner, U. Biomimetic Layer-by-Layer Assembly of Artificial Nacre. *Nat. Commun.* **2012**, *3* (1), 1–6. https://doi.org/10.1038/ncomms1970.

(8) Xia, Y.; Gates, B.; Li, Z.-Y. Self-Assembly Approaches to Three-Dimensional Photonic Crystals. *Adv. Mater.* **2001**, *13* (6), 409–413. https://doi.org/10.1002/1521-4095(200103)13:6<409::AID-ADMA409>3.0.CO;2-C.

(9) Ghosh, S. K.; Pal, T. Interparticle Coupling Effect on the Surface Plasmon Resonance of Gold Nanoparticles: From Theory to Applications. *Chem. Rev.* **2007**, *107* (11), 4797–4862. https://doi.org/10.1021/cr0680282.

(10) Begley, M. R.; Gianola, D. S.; Ray, T. R. Bridging Functional Nanocomposites to Robust Macroscale Devices. *Science* **2019**, *364* (6447), eaav4299. https://doi.org/10.1126/science.aav4299.

(11) Miles, A.; Gai, Y.; Gangopadhyay, P.; Wang, X.; Norwood, R. A.; Watkins, J. J. Improving Faraday Rotation Performance with Block Copolymer and FePt Nanoparticle Magneto-Optical Composite. *Opt. Mater. Express* **2017**, *7* (6), 2126–2140. https://doi.org/10.1364/OME.7.002126.

(12) Qin, J.; Deng, L.; Kang, T.; Nie, L.; Feng, H.; Wang, H.; Yang, R.; Liang, X.; Tang, T.; Shen, J.; Li, C.; Wang, H.; Luo, Y.; Armelles, G.; Bi, L. Switching the Optical Chirality in Magnetoplasmonic Metasurfaces Using Applied Magnetic Fields. *ACS Nano* **2020**. https://doi.org/10.1021/acsnano.9b05062.

(13) Naskar, A. K.; Keum, J. K.; Boeman, R. G. Polymer Matrix Nanocomposites for Automotive Structural Components. *Nat. Nanotechnol.* **2016**, *11* (12), 1026–1030. https://doi.org/10.1038/nnano.2016.262.

(14) Chevigny, C.; Dalmas, F.; Di Cola, E.; Gigmes, D.; Bertin, D.; Boué, F.; Jestin, J. Polymer-Grafted-Nanoparticles Nanocomposites: Dispersion, Grafted Chain Conformation, and Rheological Behavior. *Macromolecules* **2011**, *44* (1), 122–133. https://doi.org/10.1021/ma101332s.

(15) Cheng, S.; Xie, S.-J.; Carrillo, J.-M. Y.; Carroll, B.; Martin, H.; Cao, P.-F.; Dadmun, M. D.; Sumpter, B. G.; Novikov, V. N.; Schweizer, K. S.; Sokolov, A. P. Big Effect of Small Nanoparticles: A Shift in Paradigm for Polymer Nanocomposites. *ACS Nano* **2017**. https://doi.org/10.1021/acsnano.6b07172.

(16) Vaia, R. A.; Maguire, J. F. Polymer Nanocomposites with Prescribed Morphology: Going beyond Nanoparticle-Filled Polymers. *Chem. Mater.* **2007**, *19* (11), 2736–2751. https://doi.org/10.1021/cm062693+.
(17) Sajjayanukul, T.; Saeoui, P.; Sirisinha, C. Experimental Analysis of Viscoelastic Properties in Carbon Black-Filled Natural Rubber Compounds. *J. Appl. Polym. Sci.* **2005**, *97* (6), 2197–2203. https://doi.org/10.1002/app.21855.
(18) Shekar, K. C.; Prasad, B. A.; Prasad, N. E. Interlaminar Shear Strength of Multi-Walled Carbon Nanotube and Carbon Fiber Reinforced, Epoxy – Matrix Hybrid Composite. *Procedia Mater. Sci.* **2014**, *6*, 1336–1343. https://doi.org/10.1016/j.mspro.2014.07.112.
(19) Peng, S.; Zhang, R.; Chen, V. H.; Khabiboulline, E. T.; Braun, P.; Atwater, H. A. Three-Dimensional Single Gyroid Photonic Crystals with a Mid-Infrared Bandgap. *ACS Photonics* **2016**, *3* (6), 1131–1137. https://doi.org/10.1021/acsphotonics.6b00293.
(20) Meza, L. R.; Das, S.; Greer, J. R. Strong, Lightweight, and Recoverable Three-Dimensional Ceramic Nanolattices. *Science* **2014**, *345* (6202), 1322–1326. https://doi.org/10.1126/science.1255908.
(21) Whitesides, G. M.; Grzybowski, B. Self-Assembly at All Scales. *Science* **2002**, *295* (5564), 2418–2421. https://doi.org/10.1126/science.1070821.
(22) Rossi, L. M.; Shi, L.; Quina, F. H.; Rosenzweig, Z. Stöber Synthesis of Monodispersed Luminescent Silica Nanoparticles for Bioanalytical Assays. *Langmuir* **2005**, *21* (10), 4277–4280. https://doi.org/10.1021/la0504098.
(23) Eustis, S.; A. El-Sayed, M. Why Gold Nanoparticles Are More Precious than Pretty Gold: Noble Metal Surface Plasmon Resonance and Its Enhancement of the Radiative and Nonradiative Properties of Nanocrystals of Different Shapes. *Chem. Soc. Rev.* **2006**, *35* (3), 209–217. https://doi.org/10.1039/B514191E.
(24) Daruich De Souza, C.; Ribeiro Nogueira, B.; Rostelato, M. E. C. M. Review of the Methodologies Used in the Synthesis Gold Nanoparticles by Chemical Reduction. *J. Alloys Compd.* **2019**, *798*, 714–740. https://doi.org/10.1016/j.jallcom.2019.05.153.
(25) Zhao, P.; Li, N.; Astruc, D. State of the Art in Gold Nanoparticle Synthesis. *Coord. Chem. Rev.* **2013**, *257* (3–4), 638–665. https://doi.org/10.1016/j.ccr.2012.09.002.
(26) Schulz, F.; Homolka, T.; Bastús, N. G.; Puntes, V.; Weller, H.; Vossmeyer, T. Little Adjustments Significantly Improve the Turkevich Synthesis of Gold Nanoparticles. *Langmuir* **2014**, *30* (35), 10779–10784. https://doi.org/10.1021/la503209b.
(27) Turkevich, J.; Stevenson, P. C.; Hillier, J. A Study of the Nucleation and Growth Processes in the Synthesis of Colloidal Gold. *Discuss. Faraday Soc.* **1951**, *11* (0), 55–75. https://doi.org/10.1039/DF9511100055.
(28) Bastús, N. G.; Merkoçi, F.; Piella, J.; Puntes, V. Synthesis of Highly Monodisperse Citrate-Stabilized Silver Nanoparticles of up to 200 Nm: Kinetic Control and Catalytic Properties. *Chem. Mater.* **2014**, *26* (9), 2836–2846. https://doi.org/10.1021/cm500316k.
(29) Bastús, N. G.; Comenge, J.; Puntes, V. Kinetically Controlled Seeded Growth Synthesis of Citrate-Stabilized Gold Nanoparticles of up to 200 Nm: Size Focusing versus Ostwald Ripening. *Langmuir* **2011**, *27* (17), 11098–11105. https://doi.org/10.1021/la201938u.
(30) Brust, M.; Gordillo, G. J. Electrocatalytic Hydrogen Redox Chemistry on Gold Nanoparticles. *J. Am. Chem. Soc.* **2012**, *134* (7), 3318–3321. https://doi.org/10.1021/ja2096514.
(31) Prasad, B. L. V.; Stoeva, S. I.; Sorensen, C. M.; Klabunde, K. J. Digestive Ripening of Thiolated Gold Nanoparticles: The Effect of Alkyl Chain Length. *Langmuir* **2002**, *18* (20), 7515–7520. https://doi.org/10.1021/la020181d.
(32) Prasad, B. L. V.; Stoeva, S. I.; Sorensen, C. M.; Klabunde, K. J. Digestive-Ripening Agents for Gold Nanoparticles: Alternatives to Thiols. *Chem. Mater.* **2003**, *15* (4), 935–942. https://doi.org/10.1021/cm0206439.

(33) Jana, N. R.; Gearheart, L.; Murphy, C. J. Seeding Growth for Size Control of 5−40 Nm Diameter Gold Nanoparticles. *Langmuir* **2001**, *17* (22), 6782–6786. https://doi.org/10.1021/la0104323.
(34) Millstone, J. E.; Wei, W.; Jones, M. R.; Yoo, H.; Mirkin, C. A. Iodide Ions Control Seed-Mediated Growth of Anisotropic Gold Nanoparticles. *Nano Lett.* **2008**, *8* (8), 2526–2529. https://doi.org/10.1021/nl8016253.
(35) Grzelczak, M.; Pérez-Juste, J.; Mulvaney, P.; M. Liz-Marzán, L. Shape Control in Gold Nanoparticle Synthesis. *Chem. Soc. Rev.* **2008**, *37* (9), 1783–1791. https://doi.org/10.1039/B711490G.
(36) O'Brien, M. N.; Jones, M. R.; Brown, K. A.; Mirkin, C. A. Universal Noble Metal Nanoparticle Seeds Realized Through Iterative Reductive Growth and Oxidative Dissolution Reactions. *J. Am. Chem. Soc.* **2014**, *136* (21), 7603–7606. https://doi.org/10.1021/ja503509k.
(37) González-Rubio, G.; Kumar, V.; Llombart, P.; Díaz-Núñez, P.; Bladt, E.; Altantzis, T.; Bals, S.; Peña-Rodríguez, O.; Noya, E. G.; MacDowell, L. G.; Guerrero-Martínez, A.; Liz-Marzán, L. M. Disconnecting Symmetry Breaking from Seeded Growth for the Reproducible Synthesis of High Quality Gold Nanorods. *ACS Nano* **2019**. https://doi.org/10.1021/acsnano.8b09658.
(38) Ross, M. B.; Ku, J. C.; Lee, B.; Mirkin, C. A.; Schatz, G. C. Plasmonic Metallurgy Enabled by DNA. *Adv. Mater.* **2016**, n/a-n/a. https://doi.org/10.1002/adma.201505806.
(39) Wang, G.; Chen, X.; Liu, S.; Wong, C.; Chu, S. Mechanical Chameleon through Dynamic Real-Time Plasmonic Tuning. *ACS Nano* **2016**. https://doi.org/10.1021/acsnano.5b07472.
(40) Ding, X.; Liow, C. H.; Zhang, M.; Huang, R.; Li, C.; Shen, H.; Liu, M.; Zou, Y.; Gao, N.; Zhang, Z.; Li, Y.; Wang, Q.; Li, S.; Jiang, J. Surface Plasmon Resonance Enhanced Light Absorption and Photothermal Therapy in the Second Near-Infrared Window. *J. Am. Chem. Soc.* **2014**, *136* (44), 15684–15693. https://doi.org/10.1021/ja508641z.
(41) Hung, W. H.; Aykol, M.; Valley, D.; Hou, W.; Cronin, S. B. Plasmon Resonant Enhancement of Carbon Monoxide Catalysis. *Nano Lett.* **2010**, *10* (4), 1314–1318. https://doi.org/10.1021/nl9041214.
(42) Zhong, L.-B.; Yin, J.; Zheng, Y.-M.; Liu, Q.; Cheng, X.-X.; Luo, F.-H. Self-Assembly of Au Nanoparticles on PMMA Template as Flexible, Transparent, and Highly Active SERS Substrates. *Anal. Chem.* **2014**, *86* (13), 6262–6267. https://doi.org/10.1021/ac404224f.
(43) Frey, N. A.; Peng, S.; Cheng, K.; Sun, S. Magnetic Nanoparticles: Synthesis, Functionalization, and Applications in Bioimaging and Magnetic Energy Storage. *Chem. Soc. Rev.* **2009**, *38* (9), 2532–2542. https://doi.org/10.1039/B815548H.
(44) Lu, A.-H.; Salabas, E. L.; Schüth, F. Magnetic Nanoparticles: Synthesis, Protection, Functionalization, and Application. *Angew. Chem. Int. Ed.* **2007**, *46* (8), 1222–1244. https://doi.org/10.1002/anie.200602866.
(45) Boal, A. K.; Frankamp, B. L.; Uzun, O.; Tuominen, M. T.; Rotello, V. M. Modulation of Spacing and Magnetic Properties of Iron Oxide Nanoparticles through Polymer-Mediated "Bricks and Mortar" Self-Assembly. *Chem. Mater.* **2004**, *16* (17), 3252–3256. https://doi.org/10.1021/cm0495865.
(46) Majetich, S. A.; Wen, T.; Booth, R. A. Functional Magnetic Nanoparticle Assemblies: Formation, Collective Behavior, and Future Directions. *ACS Nano* **2011**, *5* (8), 6081–6084. https://doi.org/10.1021/nn202883f.
(47) Fernández, J. F.; Alonso, J. J. Ordering of Dipolar Ising Crystals. *Phys. Rev. B* **2000**, *62* (1), 53–56. https://doi.org/10.1103/PhysRevB.62.53.
(48) Wu, L.; Mendoza-Garcia, A.; Li, Q.; Sun, S. Organic Phase Syntheses of Magnetic Nanoparticles and Their Applications. *Chem. Rev.* **2016**, *116* (18), 10473–10512. https://doi.org/10.1021/acs.chemrev.5b00687.
(49) Hou, Y.; Yu, J.; Gao, S. Solvothermal Reduction Synthesis and Characterization of Superparamagnetic Magnetite Nanoparticles. *J. Mater. Chem.* **2003**, *13* (8), 1983–1987. https://doi.org/10.1039/B305526D.

(50) Kemp, S. J.; Ferguson, R. M.; Khandhar, A. P.; Krishnan, K. M. Monodisperse Magnetite Nanoparticles with Nearly Ideal Saturation Magnetization. *RSC Adv.* **2016**, *6* (81), 77452–77464. https://doi.org/10.1039/C6RA12072E.
(51) Li, D.; Yun, H.; Diroll, B. T.; Doan-Nguyen, V. V. T.; Kikkawa, J. M.; Murray, C. B. Synthesis and Size-Selective Precipitation of Monodisperse Nonstoichiometric MxFe3–XO4 (M = Mn, Co) Nanocrystals and Their DC and AC Magnetic Properties. *Chem. Mater.* **2016**, *28* (2), 480–489. https://doi.org/10.1021/acs.chemmater.5b03280.
(52) Schällibaum, J.; Torre, F. H. D.; Caseri, W. R.; Löffler, J. F. Large-Scale Synthesis of Defined Cobalt Nanoparticles and Magnetic Metal–Polymer Composites. *Nanoscale* **2009**, *1* (3), 374–381. https://doi.org/10.1039/B9NR00230H.
(53) Sun, S.; Murray, C. B.; Weller, D.; Folks, L.; Moser, A. Monodisperse FePt Nanoparticles and Ferromagnetic FePt Nanocrystal Superlattices. *Science* **2000**, *287* (5460), 1989–1992. https://doi.org/10.1126/science.287.5460.1989.
(54) Noh, H.-J.; Park, J.-H.; Kim, J.-Y.; Park, J.-G.; Park, J.; An, K.; Hwang, N.-M.; Hyeon, T.; Hwang, Y. Ultra-Large-Scale Syntheses of Monodisperse Nanocrystals. *Nat. Mater.* **2004**, *3* (12), 891. https://doi.org/10.1038/nmat1251.
(55) Puglisi, A.; Mondini, S.; Cenedese, S.; Ferretti, A. M.; Santo, N.; Ponti, A. Monodisperse Octahedral α-MnS and MnO Nanoparticles by the Decomposition of Manganese Oleate in the Presence of Sulfur. *Chem. Mater.* **2010**, *22* (9), 2804–2813. https://doi.org/10.1021/cm903735e.
(56) Bronstein, L. M.; Huang, X.; Retrum, J.; Schmucker, A.; Pink, M.; Stein, B. D.; Dragnea, B. Influence of Iron Oleate Complex Structure on Iron Oxide Nanoparticle Formation. *Chem. Mater.* **2007**, *19* (15), 3624–3632. https://doi.org/10.1021/cm062948j.
(57) Kinge, S.; Gang, T.; Naber, W. J. M.; van der Wiel, W. G.; Reinhoudt, D. N. Magnetic Nanoparticle Assembly on Surfaces Using Click Chemistry. *Langmuir* **2011**, *27* (2), 570–574. https://doi.org/10.1021/la103715y.
(58) Jishkariani, D.; D. Lee, J.; Yun, H.; Paik, T.; M. Kikkawa, J.; R. Kagan, C.; Donnio, B.; B. Murray, C. The Dendritic Effect and Magnetic Permeability in Dendron Coated Nickel and Manganese Zinc Ferrite Nanoparticles. *Nanoscale* **2017**, *9* (37), 13922–13928. https://doi.org/10.1039/C7NR05769E.
(59) Kataja, M.; Hakala, T. K.; Julku, A.; Huttunen, M. J.; van Dijken, S.; Törmä, P. Surface Lattice Resonances and Magneto-Optical Response in Magnetic Nanoparticle Arrays. *Nat. Commun.* **2015**, *6*, 7072. https://doi.org/10.1038/ncomms8072.
(60) Kobayashi, T. Cancer Hyperthermia Using Magnetic Nanoparticles. *Biotechnol. J.* **2011**, *6* (11), 1342–1347. https://doi.org/10.1002/biot.201100045.
(61) Hihath, S.; Kiehl, R. A.; Benthem, K. van. Interface Composition between Fe3O4 Nanoparticles and GaAs for Spintronic Applications. *J. Appl. Phys.* **2014**, *116* (8), 084306. https://doi.org/10.1063/1.4893958.
(62) Karmakar, S.; Kumar, S.; Rinaldi, R.; Maruccio, G. Nano-Electronics and Spintronics with Nanoparticles. *J. Phys. Conf. Ser.* **2011**, *292*, 012002. https://doi.org/10.1088/1742-6596/292/1/012002.
(63) Bera, D.; Qian, L.; Tseng, T.-K.; Holloway, P. H. Quantum Dots and Their Multimodal Applications: A Review. *Materials* **2010**, *3* (4), 2260–2345. https://doi.org/10.3390/ma3042260.
(64) Jang, Y.; Shapiro, A.; Isarov, M.; Rubin-Brusilovski, A.; Safran, A.; K. Budniak, A.; Horani, F.; Dehnel, J.; Sashchiuk, A.; Lifshitz, E. Interface Control of Electronic and Optical Properties in IV–VI and II–VI Core/Shell Colloidal Quantum Dots: A Review. *Chem. Commun.* **2017**, *53* (6), 1002–1024. https://doi.org/10.1039/C6CC08742F.
(65) Guan, J.; Sagar, L. K.; Li, R.; Wang, D.; Bappi, G.; Wang, W.; Watkins, N.; Bourgeois, M. R.; Levina, L.; Fan, F.; Hoogland, S.; Voznyy, O.; de Pina, J. M.; Schaller, R. D.; Schatz, G. C.; Sargent, E. H.; Odom, T. W. Quantum Dot-Plasmon Lasing with Controlled Polarization Patterns. *ACS Nano* **2020**. https://doi.org/10.1021/acsnano.9b09466.

(66) Carey, G. H.; Abdelhady, A. L.; Ning, Z.; Thon, S. M.; Bakr, O. M.; Sargent, E. H. Colloidal Quantum Dot Solar Cells. *Chem. Rev.* **2015**, 150624090720003. https://doi.org/10.1021/acs.chemrev.5b00063.
(67) Liu, W.; Choi, H. S.; Zimmer, J. P.; Tanaka, E.; Frangioni, J. V.; Bawendi, M. Compact Cysteine-Coated CdSe(ZnCdS) Quantum Dots for in Vivo Applications. *J. Am. Chem. Soc.* **2007**, *129* (47), 14530–14531. https://doi.org/10.1021/ja073790m.
(68) Murray, C. B.; Norris, D. J.; Bawendi, M. G. Synthesis and Characterization of Nearly Monodisperse CdE (E = Sulfur, Selenium, Tellurium) Semiconductor Nanocrystallites. *J. Am. Chem. Soc.* **1993**, *115* (19), 8706–8715. https://doi.org/10.1021/ja00072a025.
(69) Zhang, Q.; Yin, Y. All-Inorganic Metal Halide Perovskite Nanocrystals: Opportunities and Challenges. *ACS Cent. Sci.* **2018**, *4* (6), 668–679. https://doi.org/10.1021/acscentsci.8b00201.
(70) Tong, Y.; Bladt, E.; Aygüler, M. F.; Manzi, A.; Milowska, K. Z.; Hintermayr, V. A.; Docampo, P.; Bals, S.; Urban, A. S.; Polavarapu, L.; Feldmann, J. Highly Luminescent Cesium Lead Halide Perovskite Nanocrystals with Tunable Composition and Thickness by Ultrasonication. *Angew. Chem. Int. Ed.* **2016**, *55* (44), 13887–13892. https://doi.org/10.1002/anie.201605909.
(71) González-Carrero, S.; Galian, R. E.; Pérez-Prieto, J. Organometal Halide Perovskites: Bulk Low-Dimension Materials and Nanoparticles. *Part. Part. Syst. Charact.* **2015**, *32* (7), 709–720. https://doi.org/10.1002/ppsc.201400214.
(72) Gonzalez-Carrero, S.; E. Galian, R.; Pérez-Prieto, J. Maximizing the Emissive Properties of CH 3 NH 3 PbBr 3 Perovskite Nanoparticles. *J. Mater. Chem. A* **2015**, *3* (17), 9187–9193. https://doi.org/10.1039/C4TA05878J.
(73) Yoon, Y. J.; Chang, Y.; Zhang, S.; Zhang, M.; Pan, S.; He, Y.; Lin, C. H.; Yu, S.; Chen, Y.; Wang, Z.; Ding, Y.; Jung, J.; Thadhani, N.; Tsukruk, V. V.; Kang, Z.; Lin, Z. Enabling Tailorable Optical Properties and Markedly Enhanced Stability of Perovskite Quantum Dots by Permanently Ligating with Polymer Hairs. *Adv. Mater.* **2019**, *31* (32), 1901602. https://doi.org/10.1002/adma.201901602.
(74) Hou, S.; Guo, Y.; Tang, Y.; Quan, Q. Synthesis and Stabilization of Colloidal Perovskite Nanocrystals by Multidentate Polymer Micelles. *ACS Appl. Mater. Interfaces* **2017**, *9* (22), 18417–18422. https://doi.org/10.1021/acsami.7b03445.
(75) Liu, Y.; Wang, Z.; Liang, S.; Li, Z.; Zhang, M.; Li, H.; Lin, Z. Polar Organic Solvent-Tolerant Perovskite Nanocrystals Permanently Ligated with Polymer Hairs via Star-like Molecular Bottlebrush Trilobe Nanoreactors. *Nano Lett.* **2019**. https://doi.org/10.1021/acs.nanolett.9b04047.
(76) A. Hore, M. J. Polymers on Nanoparticles: Structure & Dynamics. *Soft Matter* **2019**, *15* (6), 1120–1134. https://doi.org/10.1039/C8SM02110D.
(77) Kim, B. J.; Bang, J.; Hawker, C. J.; Kramer, E. J. Effect of Areal Chain Density on the Location of Polymer-Modified Gold Nanoparticles in a Block Copolymer Template. *Macromolecules* **2006**, *39* (12), 4108–4114. https://doi.org/10.1021/ma060308w.
(78) Na, H. B.; Palui, G.; Rosenberg, J. T.; Ji, X.; Grant, S. C.; Mattoussi, H. Multidentate Catechol-Based Polyethylene Glycol Oligomers Provide Enhanced Stability and Biocompatibility to Iron Oxide Nanoparticles. *ACS Nano* **2012**, *6* (1), 389–399. https://doi.org/10.1021/nn203735b.
(79) Kim, P.; Jones, S. C.; Hotchkiss, P. J.; Haddock, J. N.; Kippelen, B.; Marder, S. R.; Perry, J. W. Phosphonic Acid-Modified Barium Titanate Polymer Nanocomposites with High Permittivity and Dielectric Strength. *Adv. Mater.* **2007**, *19* (7), 1001–1005. https://doi.org/10.1002/adma.200602422.
(80) Liu, Y.; Li, Y.; Li, X.-M.; He, T. Kinetics of (3-Aminopropyl)Triethoxylsilane (APTES) Silanization of Superparamagnetic Iron Oxide Nanoparticles. *Langmuir* **2013**, *29* (49), 15275–15282. https://doi.org/10.1021/la403269u.
(81) Neouze, M.-A.; Schubert, U. Surface Modification and Functionalization of Metal and Metal Oxide Nanoparticles by Organic Ligands. *Monatshefte Für Chem. - Chem. Mon.* **2008**, *139* (3), 183–195. https://doi.org/10.1007/s00706-007-0775-2.

(82) Hui, C. M.; Pietrasik, J.; Schmitt, M.; Mahoney, C.; Choi, J.; Bockstaller, M. R.; Matyjaszewski, K. Surface-Initiated Polymerization as an Enabling Tool for Multifunctional (Nano-)Engineered Hybrid Materials. *Chem. Mater.* **2014**, *26* (1), 745–762. https://doi.org/10.1021/cm4023634.
(83) Hasanzadeh, R.; Moghadam, P. N.; Bahri-Laleh, N.; Sillanpää, M. Effective Removal of Toxic Metal Ions from Aqueous Solutions: 2-Bifunctional Magnetic Nanocomposite Base on Novel Reactive PGMA-MAn Copolymer@Fe3O4 Nanoparticles. *J. Colloid Interface Sci.* **2017**, *490*, 727–746. https://doi.org/10.1016/j.jcis.2016.11.098.
(84) Tang, E.; Cheng, G.; Ma, X. Preparation of Nano-ZnO/PMMA Composite Particles via Grafting of the Copolymer onto the Surface of Zinc Oxide Nanoparticles. *Powder Technol.* **2006**, *161* (3), 209–214. https://doi.org/10.1016/j.powtec.2005.10.007.
(85) Jagur-Grodzinski, J. Functional Polymers by Living Anionic Polymerization. *J. Polym. Sci. Part Polym. Chem.* **2002**, *40* (13), 2116–2133. https://doi.org/10.1002/pola.10291.
(86) Sawamoto, M.; Aoshima, S.; Higashimura, T. Synthesis of New Functional Polymers by Living Cationic Polymerization. *Makromol. Chem. Macromol. Symp.* **1988**, *13–14* (1), 513–526. https://doi.org/10.1002/masy.19880130137.
(87) Grubbs, R. B. Nitroxide-Mediated Radical Polymerization: Limitations and Versatility. *Polym. Rev.* **2011**, *51* (2), 104–137. https://doi.org/10.1080/15583724.2011.566405.
(88) Matyjaszewski, K.; Xia, J. Atom Transfer Radical Polymerization. *Chem. Rev.* **2001**, *101* (9), 2921–2990. https://doi.org/10.1021/cr940534g.
(89) Moad, G.; Rizzardo, E.; Thang, S. H. Living Radical Polymerization by the RAFT Process. *Aust. J. Chem.* **2005**, *58* (6), 379–410.
(90) Matyjaszewski, K.; Tsarevsky, N. V. Nanostructured Functional Materials Prepared by Atom Transfer Radical Polymerization. *Nat. Chem.* **2009**, *1* (4), 276–288. https://doi.org/10.1038/nchem.257.
(91) Willcock, H.; K. O'Reilly, R. End Group Removal and Modification of RAFT Polymers. *Polym. Chem.* **2010**, *1* (2), 149–157. https://doi.org/10.1039/B9PY00340A.
(92) Zoppe, J. O.; Ataman, N. C.; Mocny, P.; Wang, J.; Moraes, J.; Klok, H.-A. Surface-Initiated Controlled Radical Polymerization: State-of-the-Art, Opportunities, and Challenges in Surface and Interface Engineering with Polymer Brushes. *Chem. Rev.* **2017**, *117* (3), 1105–1318. https://doi.org/10.1021/acs.chemrev.6b00314.
(93) Matyjaszewski, K.; Dong, H.; Jakubowski, W.; Pietrasik, J.; Kusumo, A. Grafting from Surfaces for "Everyone": ARGET ATRP in the Presence of Air. *Langmuir* **2007**, *23* (8), 4528–4531. https://doi.org/10.1021/la063402e.
(94) Wilczewska, A. Z.; Markiewicz, K. H. Surface-Initiated RAFT/MADIX Polymerization on Xanthate-Coated Iron Oxide Nanoparticles. *Macromol. Chem. Phys.* **2014**, *215* (2), 190–197. https://doi.org/10.1002/macp.201300400.
(95) Chevigny, C.; Gigmes, D.; Bertin, D.; Jestin, J.; Boué, F. Polystyrene Grafting from Silica Nanoparticles via Nitroxide-Mediated Polymerization (NMP): Synthesis and SANS Analysis with the Contrast Variation Method. *Soft Matter* **2009**, *5* (19), 3741–3753. https://doi.org/10.1039/B906754J.
(96) de Gennes, P. G. Conformations of Polymers Attached to an Interface. *Macromolecules* **1980**, *13* (5), 1069–1075. https://doi.org/10.1021/ma60077a009.
(97) Alexander, S. Adsorption of Chain Molecules with a Polar Head a Scaling Description. *J. Phys.* **1977**, *38* (8), 983–987. https://doi.org/10.1051/jphys:01977003808098300.
(98) Milner, S. T. Polymer Brushes. *Science* **1991**, *251* (4996), 905–914. https://doi.org/10.1126/science.251.4996.905.
(99) Milner, S. T.; Witten, T. A.; Cates, M. E. Theory of the Grafted Polymer Brush. *Macromolecules* **1988**, *21* (8), 2610–2619. https://doi.org/10.1021/ma00186a051.

(100) Daoud, M.; Cotton, J. P. Star Shaped Polymers : A Model for the Conformation and Its Concentration Dependence. *J. Phys.* **1982**, *43* (3), 531–538. https://doi.org/10.1051/jphys:01982004303053100.
(101) Ohno, K.; Morinaga, T.; Takeno, S.; Tsujii, Y.; Fukuda, T. Suspensions of Silica Particles Grafted with Concentrated Polymer Brush: Effects of Graft Chain Length on Brush Layer Thickness and Colloidal Crystallization. *Macromolecules* **2007**, *40* (25), 9143–9150. https://doi.org/10.1021/ma071770z.
(102) Ohno, K. Colloidal Crystals Formed by Polymer Brush-Afforded Fine Particles. *Polym. Chem.* **2010**, *1* (10), 1545–1551. https://doi.org/10.1039/B9PY00378A.
(103) Ohno, K.; Morinaga, T.; Takeno, S.; Tsujii, Y.; Fukuda, T. Suspensions of Silica Particles Grafted with Concentrated Polymer Brush: A New Family of Colloidal Crystals. *Macromolecules* **2006**, *39* (3), 1245–1249. https://doi.org/10.1021/ma0521708.
(104) Dukes, D.; Li, Y.; Lewis, S.; Benicewicz, B.; Schadler, L.; Kumar, S. K. Conformational Transitions of Spherical Polymer Brushes: Synthesis, Characterization, and Theory. *Macromolecules* **2010**, *43* (3), 1564–1570. https://doi.org/10.1021/ma901228t.
(105) Yi, C.; Yang, Y.; Liu, B.; He, J.; Nie, Z. Polymer-Guided Assembly of Inorganic Nanoparticles. *Chem. Soc. Rev.* **2020**, *49* (2), 465–508. https://doi.org/10.1039/C9CS00725C.
(106) Moffitt, M. G. Self-Assembly of Polymer Brush-Functionalized Inorganic Nanoparticles: From Hairy Balls to Smart Molecular Mimics. *J. Phys. Chem. Lett.* **2013**, *4* (21), 3654–3666. https://doi.org/10.1021/jz401814s.
(107) Kumar, S. K.; Jouault, N.; Benicewicz, B.; Neely, T. Nanocomposites with Polymer Grafted Nanoparticles. *Macromolecules* **2013**, *46* (9), 3199–3214. https://doi.org/10.1021/ma4001385.
(108) Moll, J. F.; Akcora, P.; Rungta, A.; Gong, S.; Colby, R. H.; Benicewicz, B. C.; Kumar, S. K. Mechanical Reinforcement in Polymer Melts Filled with Polymer Grafted Nanoparticles. *Macromolecules* **2011**, *44* (18), 7473–7477. https://doi.org/10.1021/ma201200m.
(109) Akcora, P.; Liu, H.; Kumar, S. K.; Moll, J.; Li, Y.; Benicewicz, B. C.; Schadler, L. S.; Acehan, D.; Panagiotopoulos, A. Z.; Pryamitsyn, V.; Ganesan, V.; Ilavsky, J.; Thiyagarajan, P.; Colby, R. H.; Douglas, J. F. Anisotropic Self-Assembly of Spherical Polymer-Grafted Nanoparticles. *Nat. Mater.* **2009**, *8* (4), 354–359. https://doi.org/10.1038/nmat2404.
(110) Srivastava, S.; Agarwal, P.; Archer, L. A. Tethered Nanoparticle–Polymer Composites: Phase Stability and Curvature. *Langmuir* **2012**, *28* (15), 6276–6281. https://doi.org/10.1021/la2049234.
(111) Maillard, D.; Kumar, S. K.; Fragneaud, B.; Kysar, J. W.; Rungta, A.; Benicewicz, B. C.; Deng, H.; Brinson, L. C.; Douglas, J. F. Mechanical Properties of Thin Glassy Polymer Films Filled with Spherical Polymer-Grafted Nanoparticles. *Nano Lett.* **2012**, *12* (8), 3909–3914. https://doi.org/10.1021/nl301792g.
(112) Li, Y.; Tao, P.; Viswanath, A.; Benicewicz, B. C.; Schadler, L. S. Bimodal Surface Ligand Engineering: The Key to Tunable Nanocomposites. *Langmuir* **2013**, *29* (4), 1211–1220. https://doi.org/10.1021/la3036192.
(113) Bombalski, L.; Dong, H.; Listak, J.; Matyjaszewsk, K.; Bockstaller, M. R. Null-Scattering Hybrid Particles Using Controlled Radical Polymerization. *Adv. Mater.* **2007**, *19* (24), 4486–4490. https://doi.org/10.1002/adma.200700928.
(114) Choi, J.; Hui, C. M.; Pietrasik, J.; Dong, H.; Matyjaszewski, K.; Bockstaller, M. R. Toughening Fragile Matter: Mechanical Properties of Particle Solids Assembled from Polymer-Grafted Hybrid Particles Synthesized by ATRP. *Soft Matter* **2012**, *8* (15), 4072–4082. https://doi.org/10.1039/C2SM06915F.
(115) Choi, J.; Dong, H.; Matyjaszewski, K.; Bockstaller, M. R. Flexible Particle Array Structures by Controlling Polymer Graft Architecture. *J. Am. Chem. Soc.* **2010**, *132* (36), 12537–12539. https://doi.org/10.1021/ja105189s.

(116) Voudouris, P.; Choi, J.; Gomopoulos, N.; Sainidou, R.; Dong, H.; Matyjaszewski, K.; Bockstaller, M. R.; Fytas, G. Anisotropic Elasticity of Quasi-One-Component Polymer Nanocomposites. *ACS Nano* **2011**, *5* (7), 5746–5754. https://doi.org/10.1021/nn201431w.
(117) Midya, J.; Cang, Y.; Egorov, S. A.; Matyjaszewski, K.; Bockstaller, M. R.; Nikoubashman, A.; Fytas, G. Disentangling the Role of Chain Conformation on the Mechanics of Polymer Tethered Particle Materials. *Nano Lett.* **2019**. https://doi.org/10.1021/acs.nanolett.9b00817.
(118) Gu, X. W.; Ye, X.; Koshy, D. M.; Vachhani, S.; Hosemann, P.; Alivisatos, A. P. Tolerance to Structural Disorder and Tunable Mechanical Behavior in Self-Assembled Superlattices of Polymer-Grafted Nanocrystals. *Proc. Natl. Acad. Sci.* **2017**, 201618508. https://doi.org/10.1073/pnas.1618508114.
(119) N. Israelachvili, J.; John Mitchell, D.; W. Ninham, B. Theory of Self-Assembly of Hydrocarbon Amphiphiles into Micelles and Bilayers. *J. Chem. Soc. Faraday Trans. 2 Mol. Chem. Phys.* **1976**, *72* (0), 1525–1568. https://doi.org/10.1039/F29767201525.
(120) Jones, J. B.; Sanders, J. V.; Segnit, E. R. Structure of Opal. *Nature* **1964**, *204* (4962), 990–991. https://doi.org/10.1038/204990a0.
(121) Alfrey, T.; Bradford, E. B.; Vanderhoff, J. W.; Oster, G. Optical Properties of Uniform Particle-Size Latexes*. *JOSA* **1954**, *44* (8), 603–609. https://doi.org/10.1364/JOSA.44.000603.
(122) Busch, K.; John, S. Photonic Band Gap Formation in Certain Self-Organizing Systems. *Phys. Rev. E* **1998**, *58* (3), 3896–3908. https://doi.org/10.1103/PhysRevE.58.3896.
(123) Vos, W. L.; Megens, M.; van Kats, C. M.; Bösecke, P. X-Ray Diffraction of Photonic Colloidal Single Crystals. *Langmuir* **1997**, *13* (23), 6004–6008. https://doi.org/10.1021/la970423n.
(124) Jiang, P.; Bertone, J. F.; Hwang, K. S.; Colvin, V. L. Single-Crystal Colloidal Multilayers of Controlled Thickness. *Chem. Mater.* **1999**, *11* (8), 2132–2140. https://doi.org/10.1021/cm990080+.
(125) Reculusa, S.; Ravaine, S. Synthesis of Colloidal Crystals of Controllable Thickness through the Langmuir−Blodgett Technique. *Chem. Mater.* **2003**, *15* (2), 598–605. https://doi.org/10.1021/cm021242w.
(126) Davis, K. E.; Russel, W. B.; Glantschnig, W. J. Settling Suspensions of Colloidal Silica: Observations and X-Ray Measurements. *J. Chem. Soc., Faraday Trans.* **1991**, *87* (3), 411–424. https://doi.org/10.1039/FT9918700411.
(127) Arcos, C.; Kumar, K.; González-Viñas, W.; Sirera, R.; Poduska, K. M.; Yethiraj, A. Orientationally Correlated Colloidal Polycrystals without Long-Range Positional Order. *Phys. Rev. E* **2008**, *77* (5), 050402. https://doi.org/10.1103/PhysRevE.77.050402.
(128) Amos, R. M.; Rarity, J. G.; Tapster, P. R.; Shepherd, T. J.; Kitson, S. C. Fabrication of Large-Area Face-Centered-Cubic Hard-Sphere Colloidal Crystals by Shear Alignment. *Phys. Rev. E* **2000**, *61* (3), 2929–2935. https://doi.org/10.1103/PhysRevE.61.2929.
(129) Honda, M.; Kataoka, K.; Seki, T.; Takeoka, Y. Confined Stimuli-Responsive Polymer Gel in Inverse Opal Polymer Membrane for Colorimetric Glucose Sensor. *Langmuir* **2009**, *25* (14), 8349–8356. https://doi.org/10.1021/la804262b.
(130) Yu, X.; Lee, Y.-J.; Furstenberg, R.; White, J. O.; Braun, P. V. Filling Fraction Dependent Properties of Inverse Opal Metallic Photonic Crystals. *Adv. Mater.* **2007**, *19* (13), 1689–1692. https://doi.org/10.1002/adma.200602792.
(131) Braun, P. V.; Wiltzius, P. Macroporous Materials—Electrochemically Grown Photonic Crystals. *Curr. Opin. Colloid Interface Sci.* **2002**, *7* (1–2), 116–123. https://doi.org/10.1016/S1359-0294(02)00009-2.
(132) Fang, Y.; Ni, Y.; Leo, S.-Y.; Taylor, C.; Basile, V.; Jiang, P. Reconfigurable Photonic Crystals Enabled by Pressure-Responsive Shape-Memory Polymers. *Nat. Commun.* **2015**, *6*, 7416. https://doi.org/10.1038/ncomms8416.

(133) Shevchenko, E. V.; Talapin, D. V.; Kotov, N. A.; O'Brien, S.; Murray, C. B. Structural Diversity in Binary Nanoparticle Superlattices. *Nature* **2006**, *439* (7072), 55–59. https://doi.org/10.1038/nature04414.
(134) Dong, A.; Chen, J.; Vora, P. M.; Kikkawa, J. M.; Murray, C. B. Binary Nanocrystal Superlattice Membranes Self-Assembled at the Liquid-Air Interface. *Nature* **2010**, *466* (7305), 474–477. https://doi.org/10.1038/nature09188.
(135) Ye, X.; Chen, J.; Eric Irrgang, M.; Engel, M.; Dong, A.; Glotzer, S. C.; Murray, C. B. Quasicrystalline Nanocrystal Superlattice with Partial Matching Rules. *Nat. Mater.* **2016**, *advance online publication*. https://doi.org/10.1038/nmat4759.
(136) Nagaoka, Y.; Tan, R.; Li, R.; Zhu, H.; Eggert, D.; Wu, Y. A.; Liu, Y.; Wang, Z.; Chen, O. Superstructures Generated from Truncated Tetrahedral Quantum Dots. *Nature* **2018**, *561* (7723), 378–382. https://doi.org/10.1038/s41586-018-0512-5.
(137) Nagaoka, Y.; Zhu, H.; Eggert, D.; Chen, O. Single-Component Quasicrystalline Nanocrystal Superlattices through Flexible Polygon Tiling Rule. *Science* **2018**, *362* (6421), 1396–1400. https://doi.org/10.1126/science.aav0790.
(138) Cargnello, M.; Johnston-Peck, A. C.; Diroll, B. T.; Wong, E.; Datta, B.; Damodhar, D.; Doan-Nguyen, V. V. T.; Herzing, A. A.; Kagan, C. R.; Murray, C. B. Substitutional Doping in Nanocrystal Superlattices. *Nature* **2015**, *524* (7566), 450–453. https://doi.org/10.1038/nature14872.
(139) Paik, T.; Diroll, B. T.; Kagan, C. R.; Murray, C. B. Binary and Ternary Superlattices Self-Assembled from Colloidal Nanodisks and Nanorods. *J. Am. Chem. Soc.* **2015**, *137* (20), 6662–6669. https://doi.org/10.1021/jacs.5b03234.
(140) Jishkariani, D.; Diroll, B. T.; Cargnello, M.; Klein, D. R.; Hough, L. A.; Murray, C. B.; Donnio, B. Dendron-Mediated Engineering of Interparticle Separation and Self-Assembly in Dendronized Gold Nanoparticles Superlattices. *J. Am. Chem. Soc.* **2015**, *137* (33), 10728–10734. https://doi.org/10.1021/jacs.5b06306.
(141) Ye, X.; Zhu, C.; Ercius, P.; Raja, S. N.; He, B.; Jones, M. R.; Hauwiller, M. R.; Liu, Y.; Xu, T.; Alivisatos, A. P. Structural Diversity in Binary Superlattices Self-Assembled from Polymer-Grafted Nanocrystals. *Nat. Commun.* **2015**, *6*, 10052. https://doi.org/10.1038/ncomms10052.
(142) Kang, Y.; Li, M.; Cai, Y.; Cargnello, M.; Diaz, R. E.; Gordon, T. R.; Wieder, N. L.; Adzic, R. R.; Gorte, R. J.; Stach, E. A.; Murray, C. B. Heterogeneous Catalysts Need Not Be so "Heterogeneous": Monodisperse Pt Nanocrystals by Combining Shape-Controlled Synthesis and Purification by Colloidal Recrystallization. *J. Am. Chem. Soc.* **2013**, *135* (7), 2741–2747. https://doi.org/10.1021/ja3116839.
(143) Nijs, B. de; Dussi, S.; Smallenburg, F.; Meeldijk, J. D.; Groenendijk, D. J.; Filion, L.; Imhof, A.; Blaaderen, A. van; Dijkstra, M. Entropy-Driven Formation of Large Icosahedral Colloidal Clusters by Spherical Confinement. *Nat. Mater.* **2015**, *14* (1), 56–60. https://doi.org/10.1038/nmat4072.
(144) Montanarella, F.; Geuchies, J. J.; Dasgupta, T.; Prins, P. T.; van Overbeek, C.; Dattani, R.; Baesjou, P.; Dijkstra, M.; Petukhov, A. V.; van Blaaderen, A.; Vanmaekelbergh, D. Crystallization of Nanocrystals in Spherical Confinement Probed by in Situ X-Ray Scattering. *Nano Lett.* **2018**. https://doi.org/10.1021/acs.nanolett.8b00809.
(145) Wang, D.; Hermes, M.; Kotni, R.; Wu, Y.; Tasios, N.; Liu, Y.; Nijs, B. de; Wee, E. B. van der; Murray, C. B.; Dijkstra, M.; Blaaderen, A. van. Interplay between Spherical Confinement and Particle Shape on the Self-Assembly of Rounded Cubes. *Nat. Commun.* **2018**, *9* (1), 1–10. https://doi.org/10.1038/s41467-018-04644-4.
(146) Jiao, Y.; Han, D.; Ding, Y.; Zhang, X.; Guo, G.; Hu, J.; Yang, D.; Dong, A. Fabrication of Three-Dimensionally Interconnected Nanoparticle Superlattices and Their Lithium-Ion Storage Properties. *Nat. Commun.* **2015**, *6*, 6420. https://doi.org/10.1038/ncomms7420.

(147) Choi, J.-H.; Wang, H.; Oh, S. J.; Paik, T.; Sung, P.; Sung, J.; Ye, X.; Zhao, T.; Diroll, B. T.; Murray, C. B.; Kagan, C. R. Exploiting the Colloidal Nanocrystal Library to Construct Electronic Devices. *Science* **2016**, *352* (6282), 205–208. https://doi.org/10.1126/science.aad0371.
(148) Zhang, S. Fabrication of Novel Biomaterials through Molecular Self-Assembly. *Nat. Biotechnol.* **2003**, *21* (10), 1171–1178. https://doi.org/10.1038/nbt874.
(149) Faul, C. f. j.; Antonietti, M. Ionic Self-Assembly: Facile Synthesis of Supramolecular Materials. *Adv. Mater.* **2003**, *15* (9), 673–683. https://doi.org/10.1002/adma.200300379.
(150) Pauling, L. THE PRINCIPLES DETERMINING THE STRUCTURE OF COMPLEX IONIC CRYSTALS. *J. Am. Chem. Soc.* **1929**, *51* (4), 1010–1026. https://doi.org/10.1021/ja01379a006.
(151) Kalsin, A. M.; Fialkowski, M.; Paszewski, M.; Smoukov, S. K.; Bishop, K. J. M.; Grzybowski, B. A. Electrostatic Self-Assembly of Binary Nanoparticle Crystals with a Diamond-Like Lattice. *Science* **2006**, *312* (5772), 420–424. https://doi.org/10.1126/science.1125124.
(152) Kalsin, A. M.; Grzybowski, B. A. Controlling the Growth of "Ionic" Nanoparticle Supracrystals. *Nano Lett.* **2007**, *7* (4), 1018–1021. https://doi.org/10.1021/nl0701915.
(153) Yang, L.; Tan, X.; Wang, Z.; Zhang, X. Supramolecular Polymers: Historical Development, Preparation, Characterization, and Functions. *Chem. Rev.* **2015**, *115* (15), 7196–7239. https://doi.org/10.1021/cr500633b.
(154) Fouquey, C.; Lehn, J.-M.; Levelut, A.-M. Molecular Recognition Directed Self-Assembly of Supramolecular Liquid Crystalline Polymers from Complementary Chiral Components. *Adv. Mater.* **1990**, *2* (5), 254–257. https://doi.org/10.1002/adma.19900020506.
(155) Elacqua, E.; Lye, D. S.; Weck, M. Engineering Orthogonality in Supramolecular Polymers: From Simple Scaffolds to Complex Materials. *Acc. Chem. Res.* **2014**, *47* (8), 2405–2416. https://doi.org/10.1021/ar500128w.
(156) Mirkin, C. A.; Letsinger, R. L.; Mucic, R. C.; Storhoff, J. J. A DNA-Based Method for Rationally Assembling Nanoparticles into Macroscopic Materials. *Nature* **1996**, *382* (6592), 607–609. https://doi.org/10.1038/382607a0.
(157) Alivisatos, A. P.; Johnsson, K. P.; Peng, X.; Wilson, T. E.; Loweth, C. J.; Bruchez, M. P.; Schultz, P. G. Organization of "nanocrystal Molecules" Using DNA. *Nature* **1996**, *382* (6592), 609–611. https://doi.org/10.1038/382609a0.
(158) Jin, R.; Wu, G.; Li, Z.; Mirkin, C. A.; Schatz, G. C. What Controls the Melting Properties of DNA-Linked Gold Nanoparticle Assemblies? *J. Am. Chem. Soc.* **2003**, *125* (6), 1643–1654. https://doi.org/10.1021/ja021096v.
(159) Seo, S. E.; Li, T.; Senesi, A. J.; Mirkin, C. A.; Lee, B. The Role of Repulsion in Colloidal Crystal Engineering with DNA. *J. Am. Chem. Soc.* **2017**, *139* (46), 16528–16535. https://doi.org/10.1021/jacs.7b06734.
(160) Gabrys, P. A.; Zornberg, L. Z.; Macfarlane, R. J. Programmable Atom Equivalents: Atomic Crystallization as a Framework for Synthesizing Nanoparticle Superlattices. *Small* **2019**, *15* (26), 1805424. https://doi.org/10.1002/smll.201805424.
(161) Park, S. Y.; Lytton-Jean, A. K. R.; Lee, B.; Weigand, S.; Schatz, G. C.; Mirkin, C. A. DNA-Programmable Nanoparticle Crystallization. *Nature* **2008**, *451* (7178), 553–556. https://doi.org/10.1038/nature06508.
(162) Macfarlane, R. J.; Lee, B.; Jones, M. R.; Harris, N.; Schatz, G. C.; Mirkin, C. A. Nanoparticle Superlattice Engineering with DNA. *Science* **2011**, *334* (6053), 204–208. https://doi.org/10.1126/science.1210493.
(163) Lin, H.; Lee, S.; Sun, L.; Spellings, M.; Engel, M.; Glotzer, S. C.; Mirkin, C. A. Clathrate Colloidal Crystals. *Science* **2017**, *355* (6328), 931–935. https://doi.org/10.1126/science.aal3919.
(164) Macfarlane, R. J.; Jones, M. R.; Lee, B.; Auyeung, E.; Mirkin, C. A. Topotactic Interconversion of Nanoparticle Superlattices. *Science* **2013**, *341* (6151), 1222–1225. https://doi.org/10.1126/science.1241402.

(165) Jones, M. R.; Macfarlane, R. J.; Prigodich, A. E.; Patel, P. C.; Mirkin, C. A. Nanoparticle Shape Anisotropy Dictates the Collective Behavior of Surface-Bound Ligands. *J. Am. Chem. Soc.* **2011**, *133* (46), 18865–18869. https://doi.org/10.1021/ja206777k.
(166) Lu, F.; Vo, T.; Zhang, Y.; Frenkel, A.; Yager, K. G.; Kumar, S.; Gang, O. Unusual Packing of Soft-Shelled Nanocubes. *Sci. Adv.* **2019**, *5* (5), eaaw2399. https://doi.org/10.1126/sciadv.aaw2399.
(167) Girard, M.; Wang, S.; Du, J. S.; Das, A.; Huang, Z.; Dravid, V. P.; Lee, B.; Mirkin, C. A.; Cruz, M. O. de la. Particle Analogs of Electrons in Colloidal Crystals. *Science* **2019**, *364* (6446), 1174–1178. https://doi.org/10.1126/science.aaw8237.
(168) Liu, W.; Tagawa, M.; Xin, H. L.; Wang, T.; Emamy, H.; Li, H.; Yager, K. G.; Starr, F. W.; Tkachenko, A. V.; Gang, O. Diamond Family of Nanoparticle Superlattices. *Science* **2016**, *351* (6273), 582–586. https://doi.org/10.1126/science.aad2080.
(169) Wang, Y.; Wang, Y.; Zheng, X.; Ducrot, É.; Yodh, J. S.; Weck, M.; Pine, D. J. Crystallization of DNA-Coated Colloids. *Nat. Commun.* **2015**, *6*, 7253. https://doi.org/10.1038/ncomms8253.
(170) Auyeung, E.; Li, T. I. N. G.; Senesi, A. J.; Schmucker, A. L.; Pals, B. C.; de la Cruz, M. O.; Mirkin, C. A. DNA-Mediated Nanoparticle Crystallization into Wulff Polyhedra. *Nature* **2014**, *505* (7481), 73–77. https://doi.org/10.1038/nature12739.
(171) O'Brien, M. N.; Lin, H.-X.; Girard, M.; Olvera de la Cruz, M.; Mirkin, C. A. Programming Colloidal Crystal Habit with Anisotropic Nanoparticle Building Blocks and DNA Bonds. *J. Am. Chem. Soc.* **2016**. https://doi.org/10.1021/jacs.6b09704.
(172) Seo, S. E.; Girard, M.; Olvera de la Cruz, M.; Mirkin, C. A. Non-Equilibrium Anisotropic Colloidal Single Crystal Growth with DNA. *Nat. Commun.* **2018**, *9* (1), 1–8. https://doi.org/10.1038/s41467-018-06982-9.
(173) Wang, M. X.; Seo, S. E.; Gabrys, P. A.; Fleischman, D.; Lee, B.; Kim, Y.; Atwater, H. A.; Macfarlane, R. J.; Mirkin, C. A. Epitaxy: Programmable Atom Equivalents Versus Atoms. *ACS Nano* **2016**. https://doi.org/10.1021/acsnano.6b06584.
(174) Hellstrom, S. L.; Kim, Y.; Fakonas, J. S.; Senesi, A. J.; Macfarlane, R. J.; Mirkin, C. A.; Atwater, H. A. Epitaxial Growth of DNA-Assembled Nanoparticle Superlattices on Patterned Substrates. *Nano Lett.* **2013**, *13* (12), 6084–6090. https://doi.org/10.1021/nl4033654.
(175) Gabrys, P. A.; Macfarlane, R. J. Controlling Crystal Texture in Programmable Atom Equivalent Thin Films. *ACS Nano* **2019**, *13* (7), 8452–8460. https://doi.org/10.1021/acsnano.9b04333.
(176) Gabrys, P. A.; Seo, S. E.; Wang, M. X.; Oh, E.; Macfarlane, R. J.; Mirkin, C. A. Lattice Mismatch in Crystalline Nanoparticle Thin Films. *Nano Lett.* **2018**, *18* (1), 579–585. https://doi.org/10.1021/acs.nanolett.7b04737.
(177) Leonardo Z. Zornberg; Gabrys, P. A.; Macfarlane, R. J. Optical Processing of DNA-Programmed Nanoparticle Superlattices. *Nano Lett.* **2019**, *19* (11), 8074–8081. https://doi.org/10.1021/acs.nanolett.9b03258.
(178) Lewis, D. J.; Zornberg, L. Z.; Carter, D. J. D.; Macfarlane, R. J. Single-Crystal Winterbottom Constructions of Nanoparticle Superlattices. *Nat. Mater.* **2020**, 1–6. https://doi.org/10.1038/s41563-020-0643-6.
(179) Abdilla, A.; Dolinski, N. D.; de Roos, P.; Ren, J. M.; van der Woude, E.; Seo, S. E.; Zayas, M. S.; Lawrence, J.; Read de Alaniz, J.; Hawker, C. J. Polymer Stereocomplexation as a Scalable Platform for Nanoparticle Assembly. *J. Am. Chem. Soc.* **2020**. https://doi.org/10.1021/jacs.9b10156.
(180) Ha, J.-M.; Lim, S.-H.; Dey, J.; Lee, S.-J.; Lee, M.-J.; Kang, S.-H.; Jin, K. S.; Choi, S.-M. Micelle-Assisted Formation of Nanoparticle Superlattices and Thermally Reversible Symmetry Transitions. *Nano Lett.* **2019**. https://doi.org/10.1021/acs.nanolett.8b04817.
(181) Kango, S.; Kalia, S.; Celli, A.; Njuguna, J.; Habibi, Y.; Kumar, R. Surface Modification of Inorganic Nanoparticles for Development of Organic–Inorganic Nanocomposites—A Review. *Prog. Polym. Sci.* **2013**, *38* (8), 1232–1261. https://doi.org/10.1016/j.progpolymsci.2013.02.003.

(182) Kim, C. R.; Uemura, T.; Kitagawa, S. Inorganic Nanoparticles in Porous Coordination Polymers. *Chem. Soc. Rev.* **2016**, *45* (14), 3828–3845. https://doi.org/10.1039/C5CS00940E.
(183) Talapin, D. V.; Lee, J.-S.; Kovalenko, M. V.; Shevchenko, E. V. Prospects of Colloidal Nanocrystals for Electronic and Optoelectronic Applications. *Chem. Rev.* **2010**, *110* (1), 389–458. https://doi.org/10.1021/cr900137k.
(184) Rybtchinski, B. Adaptive Supramolecular Nanomaterials Based on Strong Noncovalent Interactions. *ACS Nano* **2011**, *5* (9), 6791–6818. https://doi.org/10.1021/nn2025397.
(185) Boles, M. A.; Engel, M.; Talapin, D. V. Self-Assembly of Colloidal Nanocrystals: From Intricate Structures to Functional Materials. *Chem. Rev.* **2016**, *116* (18), 11220–11289. https://doi.org/10.1021/acs.chemrev.6b00196.
(186) Tang, C.; Lennon, E. M.; Fredrickson, G. H.; Kramer, E. J.; Hawker, C. J. Evolution of Block Copolymer Lithography to Highly Ordered Square Arrays. *Science* **2008**, *322* (5900), 429–432. https://doi.org/10.1126/science.1162950.
(187) Bates, C. M.; Seshimo, T.; Maher, M. J.; Durand, W. J.; Cushen, J. D.; Dean, L. M.; Blachut, G.; Ellison, C. J.; Willson, C. G. Polarity-Switching Top Coats Enable Orientation of Sub–10-Nm Block Copolymer Domains. *Science* **2012**, *338* (6108), 775–779. https://doi.org/10.1126/science.1226046.
(188) Sing, C. E.; Zwanikken, J. W.; Olvera de la Cruz, M. Electrostatic Control of Block Copolymer Morphology. *Nat. Mater.* **2014**, *13* (7), 694–698. https://doi.org/10.1038/nmat4001.
(189) Adler-Abramovich, L.; Gazit, E. The Physical Properties of Supramolecular Peptide Assemblies: From Building Block Association to Technological Applications. *Chem. Soc. Rev.* **2014**, *43* (20), 6881–6893. https://doi.org/10.1039/C4CS00164H.
(190) Jones, M. R.; Seeman, N. C.; Mirkin, C. A. Programmable Materials and the Nature of the DNA Bond. *Science* **2015**, *347* (6224). https://doi.org/10.1126/science.1260901.
(191) Talapin, D. V.; Shevchenko, E. V.; Murray, C. B.; Titov, A. V.; Král, P. Dipole−Dipole Interactions in Nanoparticle Superlattices. *Nano Lett.* **2007**, *7* (5), 1213–1219. https://doi.org/10.1021/nl070058c.
(192) Yan, W.; Xu, L.; Xu, C.; Ma, W.; Kuang, H.; Wang, L.; Kotov, N. A. Self-Assembly of Chiral Nanoparticle Pyramids with Strong R/S Optical Activity. *J. Am. Chem. Soc.* **2012**, *134* (36), 15114–15121. https://doi.org/10.1021/ja3066336.
(193) Zhao, Y.; Thorkelsson, K.; Mastroianni, A. J.; Schilling, T.; Luther, J. M.; Rancatore, B. J.; Matsunaga, K.; Jinnai, H.; Wu, Y.; Poulsen, D.; Fréchet, J. M. J.; Paul Alivisatos, A.; Xu, T. Small-Molecule-Directed Nanoparticle Assembly towards Stimuli-Responsive Nanocomposites. *Nat. Mater.* **2009**, *8* (12), 979–985. https://doi.org/10.1038/nmat2565.
(194) Heo, K.; Miesch, C.; Emrick, T.; Hayward, R. C. Thermally Reversible Aggregation of Gold Nanoparticles in Polymer Nanocomposites through Hydrogen Bonding. *Nano Lett.* **2013**, *13* (11), 5297–5302. https://doi.org/10.1021/nl402813q.
(195) Hashemi, A.; Jouault, N.; Williams, G. A.; Zhao, D.; Cheng, K. J.; Kysar, J. W.; Guan, Z.; Kumar, S. K. Enhanced Glassy State Mechanical Properties of Polymer Nanocomposites via Supramolecular Interactions. *Nano Lett.* **2015**, *15* (8), 5465–5471. https://doi.org/10.1021/acs.nanolett.5b01859.
(196) Williams, G. A.; Ishige, R.; Cromwell, O. R.; Chung, J.; Takahara, A.; Guan, Z. Mechanically Robust and Self-Healable Superlattice Nanocomposites by Self-Assembly of Single-Component "Sticky" Polymer-Grafted Nanoparticles. *Adv. Mater.* **2015**, *27* (26), 3934–3941. https://doi.org/10.1002/adma.201500927.
(197) Macfarlane, R. J.; O'Brien, M. N.; Petrosko, S. H.; Mirkin, C. A. Nucleic Acid-Modified Nanostructures as Programmable Atom Equivalents: Forging a New "Table of Elements." *Angew. Chem. Int. Ed.* **2013**, *52* (22), 5688–5698. https://doi.org/10.1002/anie.201209336.

(198) Wang, X.; Simard, M.; Wuest, J. D. Molecular Tectonics. Three-Dimensional Organic Networks with Zeolitic Properties. *J. Am. Chem. Soc.* **1994**, *116* (26), 12119–12120. https://doi.org/10.1021/ja00105a089.
(199) Hosseini, M. W. Molecular Tectonics: From Simple Tectons to Complex Molecular Networks. *Acc. Chem. Res.* **2005**, *38* (4), 313–323. https://doi.org/10.1021/ar0401799.
(200) Storhoff, J. J.; Lazarides, A. A.; Mucic, R. C.; Mirkin, C. A.; Letsinger, R. L.; Schatz, G. C. What Controls the Optical Properties of DNA-Linked Gold Nanoparticle Assemblies? *J. Am. Chem. Soc.* **2000**, *122* (19), 4640–4650. https://doi.org/10.1021/ja9938251.
(201) Matyjaszewski, K. Atom Transfer Radical Polymerization (ATRP): Current Status and Future Perspectives. *Macromolecules* **2012**, *45* (10), 4015–4039. https://doi.org/10.1021/ma3001719.
(202) Bertrand, A.; Lortie, F.; Bernard, J. Routes to Hydrogen Bonding Chain-End Functionalized Polymers. *Macromol. Rapid Commun.* **2012**, *33* (24), 2062–2091. https://doi.org/10.1002/marc.201200508.
(203) Goulet, P. J. G.; Bourret, G. R.; Lennox, R. B. Facile Phase Transfer of Large, Water-Soluble Metal Nanoparticles to Nonpolar Solvents. *Langmuir* **2012**, *28* (5), 2909–2913. https://doi.org/10.1021/la2038894.
(204) Jones, M. R.; Macfarlane, R. J.; Lee, B.; Zhang, J.; Young, K. L.; Senesi, A. J.; Mirkin, C. A. DNA-Nanoparticle Superlattices Formed from Anisotropic Building Blocks. *Nat. Mater.* **2010**, *9* (11), 913–917. https://doi.org/10.1038/nmat2870.
(205) Macfarlane, R. J.; Jones, M. R.; Senesi, A. J.; Young, K. L.; Lee, B.; Wu, J.; Mirkin, C. A. Establishing the Design Rules for DNA-Mediated Programmable Colloidal Crystallization. *Angew. Chem. Int. Ed.* **2010**, *49* (27), 4589–4592. https://doi.org/10.1002/anie.201000633.
(206) Li, T. I. N. G.; Sknepnek, R.; Olvera de la Cruz, M. Thermally Active Hybridization Drives the Crystallization of DNA-Functionalized Nanoparticles. *J. Am. Chem. Soc.* **2013**, *135* (23), 8535–8541. https://doi.org/10.1021/ja312644h.
(207) Beaulieu, M. R.; Hendricks, N. R.; Watkins, J. J. Large-Area Printing of Optical Gratings and 3D Photonic Crystals Using Solution-Processable Nanoparticle/Polymer Composites. *ACS Photonics* **2014**, *1* (9), 799–805. https://doi.org/10.1021/ph500078f.
(208) Crosby, A. J.; Lee, J.-Y. Polymer Nanocomposites: The "Nano" Effect on Mechanical Properties. *Polym. Rev.* **2007**, *47* (2), 217–229. https://doi.org/10.1080/15583720701271278.
(209) Badjić, J. D.; Nelson, A.; Cantrill, S. J.; Turnbull, W. B.; Stoddart, J. F. Multivalency and Cooperativity in Supramolecular Chemistry. *Acc. Chem. Res.* **2005**, *38* (9), 723–732. https://doi.org/10.1021/ar040223k.
(210) Kuna, J. J.; Voïtchovsky, K.; Singh, C.; Jiang, H.; Mwenifumbo, S.; Ghorai, P. K.; Stevens, M. M.; Glotzer, S. C.; Stellacci, F. The Effect of Nanometre-Scale Structure on Interfacial Energy. *Nat. Mater.* **2009**, *8* (10), 837–842. https://doi.org/10.1038/nmat2534.
(211) Huang, M.; Hsu, C.-H.; Wang, J.; Mei, S.; Dong, X.; Li, Y.; Li, M.; Liu, H.; Zhang, W.; Aida, T.; Zhang, W.-B.; Yue, K.; Cheng, S. Z. D. Selective Assemblies of Giant Tetrahedra via Precisely Controlled Positional Interactions. *Science* **2015**, *348* (6233), 424–428. https://doi.org/10.1126/science.aaa2421.
(212) Xia, Y.; Nguyen, T. D.; Yang, M.; Lee, B.; Santos, A.; Podsiadlo, P.; Tang, Z.; Glotzer, S. C.; Kotov, N. A. Self-Assembly of Self-Limiting Monodisperse Supraparticles from Polydisperse Nanoparticles. *Nat. Nanotechnol.* **2011**, *6* (9), 580. https://doi.org/10.1038/nnano.2011.121.
(213) laRica, R. de; Fratila, R. M.; Szarpak, A.; Huskens, J.; Velders, A. H. Multivalent Nanoparticle Networks as Ultrasensitive Enzyme Sensors. *Angew. Chem. Int. Ed.* **2011**, *50* (25), 5704–5707. https://doi.org/10.1002/anie.201008189.
(214) Prasad Thelu, H. V.; K. Albert, S.; Golla, M.; Krishnan, N.; Ram, D.; Murty Srinivasula, S.; Varghese, R. Size Controllable DNA Nanogels from the Self-Assembly of DNA Nanostructures through Multivalent Host–Guest Interactions. *Nanoscale* **2018**, *10* (1), 222–230. https://doi.org/10.1039/C7NR06985E.

(215) Fu, J.-H.; Lee, Y.-H.; He, Y.-J.; Chan, Y.-T. Facile Self-Assembly of Metallo-Supramolecular Ring-in-Ring and Spiderweb Structures Using Multivalent Terpyridine Ligands. *Angew. Chem. Int. Ed.* **2015**, *54* (21), 6231–6235. https://doi.org/10.1002/anie.201501507.
(216) Vial, S.; Nykypanchuk, D.; Yager, K. G.; Tkachenko, A. V.; Gang, O. Linear Mesostructures in DNA–Nanorod Self-Assembly. *ACS Nano* **2013**, *7* (6), 5437–5445. https://doi.org/10.1021/nn401413b.
(217) Deyev, S. M.; Lebedenko, E. N. Multivalency: The Hallmark of Antibodies Used for Optimization of Tumor Targeting by Design. *BioEssays* **2008**, *30* (9), 904–918. https://doi.org/10.1002/bies.20805.
(218) Gouin, S. G. Multivalent Inhibitors for Carbohydrate-Processing Enzymes: Beyond the "Lock-and-Key" Concept. *Chem. – Eur. J.* **2014**, *20* (37), 11616–11628. https://doi.org/10.1002/chem.201402537.
(219) Pieters, R. J. Intervention with Bacterial Adhesion by Multivalent Carbohydrates. *Med. Res. Rev.* **2007**, *27* (6), 796–816. https://doi.org/10.1002/med.20089.
(220) Zhao, H.; Sen, S.; Udayabhaskararao, T.; Sawczyk, M.; Kučanda, K.; Manna, D.; Kundu, P. K.; Lee, J.-W.; Král, P.; Klajn, R. Reversible Trapping and Reaction Acceleration within Dynamically Self-Assembling Nanoflasks. *Nat. Nanotechnol.* **2016**, *11* (1), 82–88. https://doi.org/10.1038/nnano.2015.256.
(221) Walker, D. A.; Leitsch, E. K.; Nap, R. J.; Szleifer, I.; Grzybowski, B. A. Geometric Curvature Controls the Chemical Patchiness and Self-Assembly of Nanoparticles. *Nat. Nanotechnol.* **2013**, *8* (9), 676–681. https://doi.org/10.1038/nnano.2013.158.
(222) Zhang, J.; Santos, P. J.; Gabrys, P. A.; Lee, S.; Liu, C.; Macfarlane, R. J. Self-Assembling Nanocomposite Tectons. *J. Am. Chem. Soc.* **2016**, *138* (50), 16228–16231. https://doi.org/10.1021/jacs.6b11052.
(223) Simundza, G.; Sakore, T. D.; Sobell, H. M. Base-Pairing Configurations between Purines and Pyrimidines in the Solid State: V. Crystal and Molecular Structure of Two 1:1 Hydrogen-Bonded Complexes, 1-Methyluracil: 9-Ethyl-8-Bromo-2,6-Diaminopurine and 1-Ethylthymine: 9-Ethyl-8-Bromo-2,6-Diaminopurine. *J. Mol. Biol.* **1970**, *48* (2), 263–278. https://doi.org/10.1016/0022-2836(70)90160-9.
(224) Lehn, J.-M. Supramolecular Chemistry — Molecular Information and the Design of Supramolecular Materials. *Makromol. Chem. Macromol. Symp.* **1993**, *69* (1), 1–17. https://doi.org/10.1002/masy.19930690103.
(225) Mammen, M.; Choi, S.-K.; Whitesides, G. M. Polyvalent Interactions in Biological Systems: Implications for Design and Use of Multivalent Ligands and Inhibitors. *Angew. Chem. Int. Ed.* **1998**, *37* (20), 2754–2794. https://doi.org/10.1002/(SICI)1521-3773(19981102)37:20<2754::AID-ANIE2754>3.0.CO;2-3.
(226) Huskens, J.; Mulder, A.; Auletta, T.; Nijhuis, C. A.; Ludden, M. J. W.; Reinhoudt, D. N. A Model for Describing the Thermodynamics of Multivalent Host−Guest Interactions at Interfaces. *J. Am. Chem. Soc.* **2004**, *126* (21), 6784–6797. https://doi.org/10.1021/ja049085k.
(227) Guo, P.; Sknepnek, R.; Olvera de la Cruz, M. Electrostatic-Driven Ridge Formation on Nanoparticles Coated with Charged End-Group Ligands. *J. Phys. Chem. C* **2011**, *115* (14), 6484–6490. https://doi.org/10.1021/jp201598k.
(228) Donakowski, M. D.; Godbe, J. M.; Sknepnek, R.; Knowles, K. E.; Olvera de la Cruz, M.; Weiss, E. A. A Quantitative Description of the Binding Equilibria of Para-Substituted Aniline Ligands and CdSe Quantum Dots. *J. Phys. Chem. C* **2010**, *114* (51), 22526–22534. https://doi.org/10.1021/jp109381r.
(229) Choueiri, R. M.; Galati, E.; Thérien-Aubin, H.; Klinkova, A.; Larin, E. M.; Querejeta-Fernández, A.; Han, L.; Xin, H. L.; Gang, O.; Zhulina, E. B.; Rubinstein, M.; Kumacheva, E. Surface Patterning of Nanoparticles with Polymer Patches. *Nature* **2016**, *538* (7623), 79–83. https://doi.org/10.1038/nature19089.

(230) Narumi, A.; Miura, Y.; Otsuka, I.; Yamane, S.; Kitajyo, Y.; Satoh, T.; Hirao, A.; Kaneko, N.; Kaga, H.; Kakuchi, T. End-Functionalization of Polystyrene by Malto-Oligosaccharide Generating Aggregation-Tunable Polymeric Reverse Micelle. *J. Polym. Sci. Part Polym. Chem.* **2006**, *44* (16), 4864–4879. https://doi.org/10.1002/pola.21582.
(231) Zhang, Z.; Glotzer, S. C. Self-Assembly of Patchy Particles. *Nano Lett.* **2004**, *4* (8), 1407–1413. https://doi.org/10.1021/nl0493500.
(232) Travesset, A. Soft Skyrmions, Spontaneous Valence and Selection Rules in Nanoparticle Superlattices. *ACS Nano* **2017**, *11* (6), 5375–5382. https://doi.org/10.1021/acsnano.7b02219.
(233) Batista, C. A. S.; Larson, R. G.; Kotov, N. A. Nonadditivity of Nanoparticle Interactions. *Science* **2015**, *350* (6257), 1242477. https://doi.org/10.1126/science.1242477.
(234) Liepold, C.; Smith, A.; Lin, B.; de Pablo, J.; Rice, S. A. Pair and Many-Body Interactions between Ligated Au Nanoparticles. *J. Chem. Phys.* **2019**, *150* (4), 044904. https://doi.org/10.1063/1.5064545.
(235) Beijer, F. H.; Sijbesma, R. P.; Vekemans, J. A. J. M.; Meijer, E. W.; Kooijman, H.; Spek, A. L. Hydrogen-Bonded Complexes of Diaminopyridines and Diaminotriazines: Opposite Effect of Acylation on Complex Stabilities. *J. Org. Chem.* **1996**, *61* (18), 6371–6380. https://doi.org/10.1021/jo960612v.
(236) Li, C.-P.; Du, M. Role of Solvents in Coordination Supramolecular Systems. *Chem. Commun.* **2011**, *47* (21), 5958–5972. https://doi.org/10.1039/C1CC10935A.
(237) Amenta, V.; Cook, J. L.; Hunter, C. A.; Low, C. M. R.; Vinter, J. G. Influence of Solvent Polarity on Preferential Solvation of Molecular Recognition Probes in Solvent Mixtures. *J. Phys. Chem. B* **2012**, *116* (49), 14433–14440. https://doi.org/10.1021/jp310379h.
(238) Bagno, A.; Campulla, M.; Pirana, M.; Scorrano, G.; Stiz, S. Preferential Solvation of Organic Species in Binary Solvent Mixtures Probed by Intermolecular 1H NOESY NMR Spectroscopy. *Chem. – Eur. J.* **1999**, *5* (4), 1291–1300. https://doi.org/10.1002/(SICI)1521-3765(19990401)5:4<1291::AID-CHEM1291>3.0.CO;2-M.
(239) Thaner, R. V.; Eryazici, I.; Macfarlane, R. J.; Brown, K. A.; Lee, B.; Nguyen, S. T.; Mirkin, C. A. The Significance of Multivalent Bonding Motifs and "Bond Order" in DNA-Directed Nanoparticle Crystallization. *J. Am. Chem. Soc.* **2016**, *138* (19), 6119–6122. https://doi.org/10.1021/jacs.6b02479.
(240) Wang, M. X.; Brodin, J. D.; Millan, J. A.; Seo, S. E.; Girard, M.; Olvera de la Cruz, M.; Lee, B.; Mirkin, C. A. Altering DNA-Programmable Colloidal Crystallization Paths by Modulating Particle Repulsion. *Nano Lett.* **2017**, *17* (8), 5126–5132. https://doi.org/10.1021/acs.nanolett.7b02502.
(241) Zhu, H.; Fan, Z.; Yu, L.; Wilson, M. A.; Nagaoka, Y.; Eggert, D.; Cao, C.; Liu, Y.; Wei, Z.; Wang, X.; He, J.; Zhao, J.; Li, R.; Wang, Z.; Grünwald, M.; Chen, O. Controlling Nanoparticle Orientations in the Self-Assembly of Patchy Quantum Dot-Gold Heterostructural Nanocrystals. *J. Am. Chem. Soc.* **2019**. https://doi.org/10.1021/jacs.9b01033.
(242) Pileni, M.-P. Self-Assembly of Inorganic Nanocrystals: Fabrication and Collective Intrinsic Properties. *Acc. Chem. Res.* **2007**, *40* (8), 685–693. https://doi.org/10.1021/ar6000582.
(243) Freymann, G. von; Kitaev, V.; V. Lotsch, B.; A. Ozin, G. Bottom-up Assembly of Photonic Crystals. *Chem. Soc. Rev.* **2013**, *42* (7), 2528–2554. https://doi.org/10.1039/C2CS35309A.
(244) Bishop, K. J. M.; Wilmer, C. E.; Soh, S.; Grzybowski, B. A. Nanoscale Forces and Their Uses in Self-Assembly. *Small* **2009**, *5* (14), 1600–1630. https://doi.org/10.1002/smll.200900358.
(245) Elacqua, E.; Zheng, X.; Shillingford, C.; Liu, M.; Weck, M. Molecular Recognition in the Colloidal World. *Acc. Chem. Res.* **2017**, *50* (11), 2756–2766. https://doi.org/10.1021/acs.accounts.7b00370.
(246) O'Brien, M. N.; Jones, M. R.; Mirkin, C. A. The Nature and Implications of Uniformity in the Hierarchical Organization of Nanomaterials. *Proc. Natl. Acad. Sci.* **2016**, *113* (42), 11717–11725. https://doi.org/10.1073/pnas.1605289113.

(247) Kotov, N. A.; Meldrum, F. C.; Wu, C.; Fendler, J. H. Monoparticulate Layer and Langmuir-Blodgett-Type Multiparticulate Layers of Size-Quantized Cadmium Sulfide Clusters: A Colloid-Chemical Approach to Superlattice Construction. *J. Phys. Chem.* **1994**, *98* (11), 2735–2738. https://doi.org/10.1021/j100062a006.
(248) Zheng, N.; Fan, J.; Stucky, G. D. One-Step One-Phase Synthesis of Monodisperse Noble-Metallic Nanoparticles and Their Colloidal Crystals. *J. Am. Chem. Soc.* **2006**, *128* (20), 6550–6551. https://doi.org/10.1021/ja0604717.
(249) Tao, A.; Sinsermsuksakul, P.; Yang, P. Tunable Plasmonic Lattices of Silver Nanocrystals. *Nat. Nanotechnol.* **2007**, *2* (7), 435–440. https://doi.org/10.1038/nnano.2007.189.
(250) Lo, P. K.; Karam, P.; Aldaye, F. A.; McLaughlin, C. K.; Hamblin, G. D.; Cosa, G.; Sleiman, H. F. Loading and Selective Release of Cargo in DNA Nanotubes with Longitudinal Variation. *Nat. Chem.* **2010**, *2* (4), 319–328. https://doi.org/10.1038/nchem.575.
(251) McMillan, J. R.; Brodin, J. D.; Millan, J. A.; Lee, B.; Olvera de la Cruz, M.; Mirkin, C. A. Modulating Nanoparticle Superlattice Structure Using Proteins with Tunable Bond Distributions. *J. Am. Chem. Soc.* **2017**, *139* (5), 1754–1757. https://doi.org/10.1021/jacs.6b11893.
(252) McMillan, R. A.; Paavola, C. D.; Howard, J.; Chan, S. L.; Zaluzec, N. J.; Trent, J. D. Ordered Nanoparticle Arrays Formed on Engineered Chaperonin Protein Templates. *Nat. Mater.* **2002**, *1* (4), 247. https://doi.org/10.1038/nmat775.
(253) Medalsy, I.; Dgany, O.; Sowwan, M.; Cohen, H.; Yukashevska, A.; Wolf, S. G.; Wolf, A.; Koster, A.; Almog, O.; Marton, I.; Pouny, Y.; Altman, A.; Shoseyov, O.; Porath, D. SP1 Protein-Based Nanostructures and Arrays. *Nano Lett.* **2008**, *8* (2), 473–477. https://doi.org/10.1021/nl072455t.
(254) Lynd, N. A.; Meuler, A. J.; Hillmyer, M. A. Polydispersity and Block Copolymer Self-Assembly. *Prog. Polym. Sci.* **2008**, *33* (9), 875–893. https://doi.org/10.1016/j.progpolymsci.2008.07.003.
(255) Si, K. J.; Chen, Y.; Shi, Q.; Cheng, W. Nanoparticle Superlattices: The Roles of Soft Ligands. *Adv. Sci.* **2018**, *5* (1), 1700179. https://doi.org/10.1002/advs.201700179.
(256) Jishkariani, D.; Elbert, K. C.; Wu, Y.; Lee, J. D.; Hermes, M.; Wang, D.; van Blaaderen, A.; Murray, C. B. Nanocrystal Core Size and Shape Substitutional Doping and Underlying Crystalline Order in Nanocrystal Superlattices. *ACS Nano* **2019**, *13* (5), 5712–5719. https://doi.org/10.1021/acsnano.9b01107.
(257) Macfarlane, R. J.; Thaner, R. V.; Brown, K. A.; Zhang, J.; Lee, B.; Nguyen, S. T.; Mirkin, C. A. Importance of the DNA "Bond" in Programmable Nanoparticle Crystallization. *Proc. Natl. Acad. Sci.* **2014**, *111* (42), 14995–15000. https://doi.org/10.1073/pnas.1416489111.
(258) Humphreys, F. J. A Unified Theory of Recovery, Recrystallization and Grain Growth, Based on the Stability and Growth of Cellular Microstructures—I. The Basic Model. *Acta Mater.* **1997**, *45* (10), 4231–4240. https://doi.org/10.1016/S1359-6454(97)00070-0.
(259) Brown, R. A. Theory of Transport Processes in Single Crystal Growth from the Melt. *AIChE J.* **1988**, *34* (6), 881–911. https://doi.org/10.1002/aic.690340602.
(260) Fukuda, T.; Ma, Y. D.; Inagaki, H. Free-Radical Copolymerization. 3. Determination of Rate Constants of Propagation and Termination for Styrene/Methyl Methacrylate System. A Critical Test of Terminal-Model Kinetics. *Macromolecules* **1985**, *18* (1), 17–26. https://doi.org/10.1021/ma00143a003.
(261) Milner, S. T.; Witten, T. A.; Cates, M. E. Effects of Polydispersity in the End-Grafted Polymer Brush. *Macromolecules* **1989**, *22* (2), 853–861. https://doi.org/10.1021/ma00192a057.
(262) Bentz, K. C.; Savin, D. A. Chain Dispersity Effects on Brush Properties of Surface-Grafted Polycaprolactone-Modified Silica Nanoparticles: Unique Scaling Behavior in the Concentrated Polymer Brush Regime. *Macromolecules* **2017**. https://doi.org/10.1021/acs.macromol.7b00608.
(263) Dodd, P. M.; Jayaraman, A. Monte Carlo Simulations of Polydisperse Polymers Grafted on Spherical Surfaces. *J. Polym. Sci. Part B Polym. Phys.* **2012**, *50* (10), 694–705. https://doi.org/10.1002/polb.23057.

(264) Jiang, X.; Zhao, B.; Zhong, G.; Jin, N.; Horton, J. M.; Zhu, L.; Hafner, R. S.; Lodge, T. P. Microphase Separation of High Grafting Density Asymmetric Mixed Homopolymer Brushes on Silica Particles. *Macromolecules* **2010**, *43* (19), 8209–8217. https://doi.org/10.1021/ma101518a.
(265) Phillips, C. L.; Glotzer, S. C. Effect of Nanoparticle Polydispersity on the Self-Assembly of Polymer Tethered Nanospheres. *J. Chem. Phys.* **2012**, *137* (10), 104901. https://doi.org/10.1063/1.4748817.
(266) Choi, J.; Hui, C. M.; Schmitt, M.; Pietrasik, J.; Margel, S.; Matyjazsewski, K.; Bockstaller, M. R. Effect of Polymer-Graft Modification on the Order Formation in Particle Assembly Structures. *Langmuir* **2013**, *29* (21), 6452–6459. https://doi.org/10.1021/la4004406.
(267) Bolhuis, P. G.; Kofke, D. A. Monte Carlo Study of Freezing of Polydisperse Hard Spheres. *Phys. Rev. E* **1996**, *54* (1), 634–643. https://doi.org/10.1103/PhysRevE.54.634.
(268) Pusey, P. N. The Effect of Polydispersity on the Crystallization of Hard Spherical Colloids. *J. Phys.* **1987**, *48* (5), 709–712. https://doi.org/10.1051/jphys:01987004805070900.
(269) Thünemann, A. F.; Rolf, S.; Knappe, P.; Weidner, S. In Situ Analysis of a Bimodal Size Distribution of Superparamagnetic Nanoparticles. *Anal. Chem.* **2009**, *81* (1), 296–301. https://doi.org/10.1021/ac802009q.
(270) Hatton, B.; Mishchenko, L.; Davis, S.; Sandhage, K. H.; Aizenberg, J. Assembly of Large-Area, Highly Ordered, Crack-Free Inverse Opal Films. *Proc. Natl. Acad. Sci.* **2010**, *107* (23), 10354–10359. https://doi.org/10.1073/pnas.1000954107.
(271) Feld, A.; Koll, R.; Fruhner, L. S.; Krutyeva, M.; Pyckhout-Hintzen, W.; Weiß, C.; Heller, H.; Weimer, A.; Schmidtke, C.; Appavou, M.-S.; Kentzinger, E.; Allgaier, J.; Weller, H. Nanocomposites of Highly Monodisperse Encapsulated Superparamagnetic Iron Oxide Nanocrystals Homogeneously Dispersed in a Poly(Ethylene Oxide) Melt. *ACS Nano* **2017**, *11* (4), 3767–3775. https://doi.org/10.1021/acsnano.6b08441.
(272) Cheon, J.; Park, J.-I.; Choi, J.; Jun, Y.; Kim, S.; Kim, M. G.; Kim, Y.-M.; Kim, Y. J. Magnetic Superlattices and Their Nanoscale Phase Transition Effects. *Proc. Natl. Acad. Sci.* **2006**, *103* (9), 3023–3027. https://doi.org/10.1073/pnas.0508877103.
(273) Yang, Z.; Wei, J.; Bonville, P.; Pileni, M.-P. Engineering the Magnetic Dipolar Interactions in 3D Binary Supracrystals Via Mesoscale Alloying. *Adv. Funct. Mater.* **2015**, *25* (30), 4908–4915. https://doi.org/10.1002/adfm.201501499.
(274) Yeom, J.; Santos, U. S.; Chekini, M.; Cha, M.; Moura, A. F. de; Kotov, N. A. Chiromagnetic Nanoparticles and Gels. *Science* **2018**, *359* (6373), 309–314. https://doi.org/10.1126/science.aao7172.
(275) Nayak, S.; Horst, N.; Zhang, H.; Wang, W.; Mallapragada, S.; Travesset, A.; Vaknin, D. Interpolymer Complexation as a Strategy for Nanoparticle Assembly and Crystallization. *J. Phys. Chem. C* **2019**, *123* (1), 836–840. https://doi.org/10.1021/acs.jpcc.8b09647.
(276) Zhang, C.; Macfarlane, R. J.; Young, K. L.; Choi, C. H. J.; Hao, L.; Auyeung, E.; Liu, G.; Zhou, X.; Mirkin, C. A. A General Approach to DNA-Programmable Atom Equivalents. *Nat. Mater.* **2013**, *12* (8), 741–746. https://doi.org/10.1038/nmat3647.
(277) Singh, G.; Chan, H.; Baskin, A.; Gelman, E.; Repnin, N.; Král, P.; Klajn, R. Self-Assembly of Magnetite Nanocubes into Helical Superstructures. *Science* **2014**, *345* (6201), 1149–1153. https://doi.org/10.1126/science.1254132.
(278) Nonappa; Haataja, J. S.; Timonen, J. V. I.; Malola, S.; Engelhardt, P.; Houbenov, N.; Lahtinen, M.; Häkkinen, H.; Ikkala, O. Reversible Supracolloidal Self-Assembly of Cobalt Nanoparticles to Hollow Capsids and Their Superstructures. *Angew. Chem. Int. Ed.* **2017**, *56* (23), 6473–6477. https://doi.org/10.1002/anie.201701135.
(279) Ahniyaz, A.; Sakamoto, Y.; Bergström, L. Magnetic Field-Induced Assembly of Oriented Superlattices from Maghemite Nanocubes. *Proc. Natl. Acad. Sci.* **2007**, *104* (45), 17570–17574. https://doi.org/10.1073/pnas.0704210104.

(280) Yang, Y.; Wang, B.; Shen, X.; Yao, L.; Wang, L.; Chen, X.; Xie, S.; Li, T.; Hu, J.; Yang, D.; Dong, A. Scalable Assembly of Crystalline Binary Nanocrystal Superparticles and Their Enhanced Magnetic and Electrochemical Properties. *J. Am. Chem. Soc.* **2018**, *140* (44), 15038–15047. https://doi.org/10.1021/jacs.8b09779.
(281) Lalatonne, Y.; Richardi, J.; Pileni, M. P. Van Der Waals versus Dipolar Forces Controlling Mesoscopic Organizations of Magnetic Nanocrystals. *Nat. Mater.* **2004**, *3* (2), 121. https://doi.org/10.1038/nmat1054.
(282) Chen, J.; Dong, A.; Cai, J.; Ye, X.; Kang, Y.; Kikkawa, J. M.; Murray, C. B. Collective Dipolar Interactions in Self-Assembled Magnetic Binary Nanocrystal Superlattice Membranes. *Nano Lett.* **2010**, *10* (12), 5103–5108. https://doi.org/10.1021/nl103568q.
(283) Frankamp, B. L.; Boal, A. K.; Tuominen, M. T.; Rotello, V. M. Direct Control of the Magnetic Interaction between Iron Oxide Nanoparticles through Dendrimer-Mediated Self-Assembly. *J. Am. Chem. Soc.* **2005**, *127* (27), 9731–9735. https://doi.org/10.1021/ja051351m.
(284) Yang, Z.; Wei, J.; Bonville, P.; Pileni, M.-P. Beyond Entropy: Magnetic Forces Induce Formation of Quasicrystalline Structure in Binary Nanocrystal Superlattices. *J. Am. Chem. Soc.* **2015**, *137* (13), 4487–4493. https://doi.org/10.1021/jacs.5b00332.
(285) Santos, P. J.; Cao, Z.; Zhang, J.; Alexander-Katz, A.; Macfarlane, R. J. Dictating Nanoparticle Assembly via Systems-Level Control of Molecular Multivalency. *J. Am. Chem. Soc.* **2019**, *141* (37), 14624–14632. https://doi.org/10.1021/jacs.9b04999.
(286) Wang, Y.; Santos, P. J.; Kubiak, J. M.; Guo, X.; Lee, M. S.; Macfarlane, R. J. Multistimuli Responsive Nanocomposite Tectons for Pathway Dependent Self-Assembly and Acceleration of Covalent Bond Formation. *J. Am. Chem. Soc.* **2019**, *141* (33), 13234–13243. https://doi.org/10.1021/jacs.9b06695.
(287) Santos, P. J.; Cheung, T. C.; Macfarlane, R. J. Assembling Ordered Crystals with Disperse Building Blocks. *Nano Lett.* **2019**, *19* (8), 5774–5780. https://doi.org/10.1021/acs.nanolett.9b02508.
(288) Turcheniuk, K.; V. Tarasevych, A.; P. Kukhar, V.; Boukherroub, R.; Szunerits, S. Recent Advances in Surface Chemistry Strategies for the Fabrication of Functional Iron Oxide Based Magnetic Nanoparticles. *Nanoscale* **2013**, *5* (22), 10729–10752. https://doi.org/10.1039/C3NR04131J.
(289) Majetich, S. A.; Sachan, M. Magnetostatic Interactions in Magnetic Nanoparticle Assemblies: Energy, Time and Length Scales. *J. Phys. Appl. Phys.* **2006**, *39* (21), R407–R422. https://doi.org/10.1088/0022-3727/39/21/R02.
(290) Bruvera, I. J.; Mendoza Zélis, P.; Pilar Calatayud, M.; Goya, G. F.; Sánchez, F. H. Determination of the Blocking Temperature of Magnetic Nanoparticles: The Good, the Bad, and the Ugly. *J. Appl. Phys.* **2015**, *118* (18), 184304. https://doi.org/10.1063/1.4935484.
(291) Dey, M.; Moritz, F.; Grotemeyer, J.; Schlag, E. W. Base Pair Formation of Free Nucleobases and Mononucleosides in the Gas Phase. *J. Am. Chem. Soc.* **1994**, *116* (20), 9211–9215. https://doi.org/10.1021/ja00099a042.
(292) Levchenko, I.; Bazaka, K.; Keidar, M.; Xu, S.; Fang, J. Hierarchical Multicomponent Inorganic Metamaterials: Intrinsically Driven Self-Assembly at the Nanoscale. *Adv. Mater.* **2018**, *30* (2), 1702226. https://doi.org/10.1002/adma.201702226.
(293) Kao, J.; Thorkelsson, K.; Bai, P.; Zhang, Z.; Sun, C.; Xu, T. Rapid Fabrication of Hierarchically Structured Supramolecular Nanocomposite Thin Films in One Minute. *Nat. Commun.* **2014**, *5*, 4053. https://doi.org/10.1038/ncomms5053.
(294) Grzelczak, M.; M. Liz-Marzán, L.; Klajn, R. Stimuli-Responsive Self-Assembly of Nanoparticles. *Chem. Soc. Rev.* **2019**, *48* (5), 1342–1361. https://doi.org/10.1039/C8CS00787J.
(295) Kundu, P. K.; Samanta, D.; Leizrowice, R.; Margulis, B.; Zhao, H.; Börner, M.; Udayabhaskararao, T.; Manna, D.; Klajn, R. Light-Controlled Self-Assembly of Non-

Photoresponsive Nanoparticles. *Nat. Chem.* **2015**, *7* (8), 646–652. https://doi.org/10.1038/nchem.2303.
(296) Steimle, B. C.; Fenton, J. L.; Schaak, R. E. Rational Construction of a Scalable Heterostructured Nanorod Megalibrary. *Science* **2020**, *367* (6476), 418–424. https://doi.org/10.1126/science.aaz1172.
(297) Chen, W.; Talreja, D.; Eichfeld, D.; Mahale, P.; Nova, N. N.; Cheng, H. Y.; Russell, J. L.; Yu, S.-Y.; Poilvert, N.; Mahan, G.; Mohney, S. E.; Crespi, V. H.; Mallouk, T. E.; Badding, J. V.; Foley, B.; Gopalan, V.; Dabo, I. Achieving Minimal Heat Conductivity by Ballistic Confinement in Phononic Metalattices. *ACS Nano* **2020**. https://doi.org/10.1021/acsnano.9b09487.
(298) Dreyer, A.; Feld, A.; Kornowski, A.; Yilmaz, E. D.; Noei, H.; Meyer, A.; Krekeler, T.; Jiao, C.; Stierle, A.; Abetz, V.; Weller, H.; Schneider, G. A. Organically Linked Iron Oxide Nanoparticle Supercrystals with Exceptional Isotropic Mechanical Properties. *Nat. Mater.* **2016**, *15* (5), 522–528. https://doi.org/10.1038/nmat4553.
(299) Quan, Z.; Xu, H.; Wang, C.; Wen, X.; Wang, Y.; Zhu, J.; Li, R.; Sheehan, C. J.; Wang, Z.; Smilgies, D.-M.; Luo, Z.; Fang, J. Solvent-Mediated Self-Assembly of Nanocube Superlattices. *J. Am. Chem. Soc.* **2014**, *136* (4), 1352–1359. https://doi.org/10.1021/ja408250q.
(300) Birshtein, T. M.; Lyatskaya, Yu. V. Theory of the Collapse-Stretching Transition of a Polymer Brush in a Mixed Solvent. *Macromolecules* **1994**, *27* (5), 1256–1266. https://doi.org/10.1021/ma00083a028.
(301) Samanta, D.; Iscen, A.; Laramy, C. R.; Ebrahimi, S. B.; Bujold, K. E.; Schatz, G. C.; Mirkin, C. A. Multivalent Cation-Induced Actuation of DNA-Mediated Colloidal Superlattices. *J. Am. Chem. Soc.* **2019**, *141* (51), 19973–19977. https://doi.org/10.1021/jacs.9b09900.
(302) Mason, J. A.; Laramy, C. R.; Lai, C.-T.; O'Brien, M. N.; Lin, Q.-Y.; Dravid, V. P.; Schatz, G. C.; Mirkin, C. A. Contraction and Expansion of Stimuli-Responsive DNA Bonds in Flexible Colloidal Crystals. *J. Am. Chem. Soc.* **2016**, *138* (28), 8722–8725. https://doi.org/10.1021/jacs.6b05430.
(303) Auyeung, E.; Macfarlane, R. J.; Choi, C. H. J.; Cutler, J. I.; Mirkin, C. A. Transitioning DNA-Engineered Nanoparticle Superlattices from Solution to the Solid State. *Adv. Mater.* **2012**, *24* (38), 5181–5186. https://doi.org/10.1002/adma.201202069.
(304) Lee, S.; Zheng, C. Y.; Bujold, K. E.; Mirkin, C. A. A Cross-Linking Approach to Stabilizing Stimuli-Responsive Colloidal Crystals Engineered with DNA. *J. Am. Chem. Soc.* **2019**. https://doi.org/10.1021/jacs.9b06106.
(305) Oh, T.; Park, S. S.; Mirkin, C. A. Stabilization of Colloidal Crystals Engineered with DNA. *Adv. Mater.* **2019**, *31* (1), 1805480. https://doi.org/10.1002/adma.201805480.
(306) Yoreo, J. J. D.; Gilbert, P. U. P. A.; Sommerdijk, N. A. J. M.; Penn, R. L.; Whitelam, S.; Joester, D.; Zhang, H.; Rimer, J. D.; Navrotsky, A.; Banfield, J. F.; Wallace, A. F.; Michel, F. M.; Meldrum, F. C.; Cölfen, H.; Dove, P. M. Crystallization by Particle Attachment in Synthetic, Biogenic, and Geologic Environments. *Science* **2015**, *349* (6247). https://doi.org/10.1126/science.aaa6760.
(307) Seo, S. E.; Girard, M.; de la Cruz, M. O.; Mirkin, C. A. The Importance of Salt-Enhanced Electrostatic Repulsion in Colloidal Crystal Engineering with DNA. *ACS Cent. Sci.* **2019**, *5* (1), 186–191. https://doi.org/10.1021/acscentsci.8b00826.
(308) Chaim, R.; Levin, M.; Shlayer, A.; Estournes, C. Sintering and Densification of Nanocrystalline Ceramic Oxide Powders: A Review. *Adv. Appl. Ceram.* **2008**, *107* (3), 159–169. https://doi.org/10.1179/174367508X297812.
(309) Jayaraman, G. S.; Wallace, J. F.; Geil, P. H.; Baer, E. Cold Compaction Molding and Sintering of Polystyrene. *Polym. Eng. Sci.* **1976**, *16* (8), 529–536. https://doi.org/10.1002/pen.760160802.
(310) Fang, Z. Z.; Wang, H. Densification and Grain Growth during Sintering of Nanosized Particles. *Int. Mater. Rev.* **2008**, *53* (6), 326–352. https://doi.org/10.1179/174328008X353538.

(311) Santos, P. J.; Macfarlane, R. J. Reinforcing Supramolecular Bonding with Magnetic Dipole Interactions to Assemble Dynamic Nanoparticle Superlattices. *J. Am. Chem. Soc.* **2020**, *142* (3), 1170–1174. https://doi.org/10.1021/jacs.9b11476.
(312) Feld, A.; Weimer, A.; Kornowski, A.; Winckelmans, N.; Merkl, J.-P.; Kloust, H.; Zierold, R.; Schmidtke, C.; Schotten, T.; Riedner, M.; Bals, S.; Weller, H. Chemistry of Shape-Controlled Iron Oxide Nanocrystal Formation. *ACS Nano* **2018**. https://doi.org/10.1021/acsnano.8b05032.
(313) Serantes, D.; Simeonidis, K.; Angelakeris, M.; Chubykalo-Fesenko, O.; Marciello, M.; Morales, M. del P.; Baldomir, D.; Martinez-Boubeta, C. Multiplying Magnetic Hyperthermia Response by Nanoparticle Assembling. *J. Phys. Chem. C* **2014**, *118* (11), 5927–5934. https://doi.org/10.1021/jp410717m.
(314) Myrovali, E.; Maniotis, N.; Makridis, A.; Terzopoulou, A.; Ntomprougkidis, V.; Simeonidis, K.; Sakellari, D.; Kalogirou, O.; Samaras, T.; Salikhov, R.; Spasova, M.; Farle, M.; Wiedwald, U.; Angelakeris, M. Arrangement at the Nanoscale: Effect on Magnetic Particle Hyperthermia. *Sci. Rep.* **2016**, *6*, 37934. https://doi.org/10.1038/srep37934.
(315) Park, S. S.; Urbach, Z. J.; Brisbois, C. A.; Parker, K. A.; Partridge, B. E.; Oh, T.; Dravid, V. P.; Olvera de la Cruz, M.; Mirkin, C. A. DNA- and Field-Mediated Assembly of Magnetic Nanoparticles into High-Aspect Ratio Crystals. *Adv. Mater.* **2019**, *n/a* (n/a), 1906626. https://doi.org/10.1002/adma.201906626.
(316) Moya, C.; Abdelgawad, A. M.; Nambiar, N.; Majetich, S. A. Magnetic Properties of Cube-Shaped Fe3O4 Nanoparticles in Dilute, 2D, and 3D Assemblies. *J. Phys. Appl. Phys.* **2017**, *50* (32), 325003. https://doi.org/10.1088/1361-6463/aa7b11.
(317) Jog, J. P. Solid State Processing of Polymers: A Review. *Adv. Polym. Technol.* **1993**, *12* (3), 281–289. https://doi.org/10.1002/adv.1993.060120306.
(318) Coessens, V.; Matyjaszewski, K. Synthesis of Polymers with Hydroxyl End Groups by Atom Transfer Radical Polymerization. *Macromol. Rapid Commun.* **1999**, *20* (3), 127–134. https://doi.org/10.1002/(SICI)1521-3927(19990301)20:3<127::AID-MARC127>3.0.CO;2-2.
(319) Yan, J.; Kristufek, T.; Schmitt, M.; Wang, Z.; Xie, G.; Dang, A.; Hui, C. M.; Pietrasik, J.; Bockstaller, M. R.; Matyjaszewski, K. Matrix-Free Particle Brush System with Bimodal Molecular Weight Distribution Prepared by SI-ATRP. *Macromolecules* **2015**, *48* (22), 8208–8218. https://doi.org/10.1021/acs.macromol.5b01905.
(320) Riter, R. E.; Kimmel, J. R.; Undiks, E. P.; Levinger, N. E. Novel Reverse Micelles Partitioning Nonaqueous Polar Solvents in a Hydrocarbon Continuous Phase. *J. Phys. Chem. B* **1997**, *101* (41), 8292–8297. https://doi.org/10.1021/jp971732p.
(321) Frenkel, D.; Smit, B. *Understanding Molecular Simulation, Second Edition: From Algorithms to Applications*, 2 edition.; Academic Press: San Diego, 2001.
(322) Kremer, K.; Grest, G. S. Dynamics of Entangled Linear Polymer Melts: A Molecular-dynamics Simulation. *J. Chem. Phys.* **1990**, *92* (8), 5057–5086. https://doi.org/10.1063/1.458541.
(323) Plimpton, S. Fast Parallel Algorithms for Short-Range Molecular Dynamics. *J. Comput. Phys.* **1995**, *117*, 1–19.
(324) Lloyd, S. Least Squares Quantization in PCM. *IEEE Trans. Inf. Theory* **1982**, *28* (2), 129–137. https://doi.org/10.1109/TIT.1982.1056489.
(325) Rousseeuw, P. J. Silhouettes: A Graphical Aid to the Interpretation and Validation of Cluster Analysis. *J. Comput. Appl. Math.* **1987**, *20*, 53–65. https://doi.org/10.1016/0377-0427(87)90125-7.
(326) Thordarson, P. Determining Association Constants from Titration Experiments in Supramolecular Chemistry. *Chem. Soc. Rev.* **2011**, *40* (3), 1305–1323. https://doi.org/10.1039/C0CS00062K.
(327) Smilgies, D.-M. Scherrer Grain-Size Analysis Adapted to Grazing-Incidence Scattering with Area Detectors. *J. Appl. Crystallogr.* **2009**, *42* (6), 1030–1034. https://doi.org/10.1107/S0021889809040126.

(328) Thompson, P.; Cox, D. E.; Hastings, J. B. Rietveld Refinement of Debye–Scherrer Synchrotron X-Ray Data from Al2O3. *J. Appl. Crystallogr.* **1987**, *20* (2), 79–83. https://doi.org/10.1107/S0021889887087090.
(329) Lee, L. V.; Mitchell, M. L.; Huang, S.-J.; Fokin, V. V.; Sharpless, K. B.; Wong, C.-H. A Potent and Highly Selective Inhibitor of Human α-1,3-Fucosyltransferase via Click Chemistry. *J. Am. Chem. Soc.* **2003**, *125* (32), 9588–9589. https://doi.org/10.1021/ja0302836.
(330) Huh, J.-H.; Lee, J.; Lee, S. Soft Plasmonic Assemblies Exhibiting Unnaturally High Refractive Index. *Nano Lett.* **2020**. https://doi.org/10.1021/acs.nanolett.0c00422.